DFG Graduate School of Earth Sciences
Interactions between Tectonics, Climate and the Biosphere in the African-Asian Monsoonal Region

LANDSCAPE EVOLUTION IN THE WESTERN INDIAN HIMALAYA SINCE THE MIOCENE

Kumulative Dissertation
zur Erlangung des akademischen Grades
Doktor der Naturwissenschaften (Dr. rer. nat.)

in der Wissenschaftsdisziplin Geologie

eingereicht an der
Mathematisch-Naturwissenschaftlichen Fakultät
UNIVERSITÄT POTSDAM

von

PATRICIA EUGSTER
M.Sc. in Erdwissenschaften, ETH Zürich

im August, 2017

Summary

The Himalayan arc stretches >2500 km from east to west at the southern edge of the Tibetan Plateau, representing one of the most important Cenozoic continent-continent collisional orogens, and is sometimes called a perfect natural laboratory. Internal deformation processes and climatic factors, which drive weathering, denudation, and transport, influence the growth and erosion of the orogen. During glacial times wet-based glaciers sculpted the mountain range and left overdeepend and U-shaped valleys, which were backfilled during interglacial times with paraglacial sediments over several cycles. These sediments partially still remain within the valleys because of insufficient evacuation capabilities into the foreland. The high peaks of the Himalaya represent the orographic barrier to precipitation mainly delivered by the Indian Summer Monsoon from the east and by the westerlies from the west mainly to the westernmost peaks of the Himalaya. Therefore, precipitation along the arc shows north-south and east-west gradients influencing the present day vegetation density but also part the presence of glaciers. The climatic processes overlay long-term tectonic processes responsible for uplift and exhumation caused by convergence. Possible processes accommodating convergence within the orogenic wedge along the main Himalayan faults, which divide the range into four major lithologic units, are debated. In this context, the identification of processes shaping the Earth's surface on short- and on long-term are crucial to understand the growth of the orogen and implications for landscape development in various sectors along the arc.

To study the western Himalaya is outstanding because 1) even though highly dynamic erosional processes are occurring, bedrock surfaces on ridges and along valley walls still exhibit well-preserved glacial polish and striations; 2) it is fed from moisture by the westerlies as well as the Indian Summer Monsoon, which is not capable to transport the sedimentary valley fill deposits towards the foreland; 3) it is situated at the western edge of the Central Himalayan rapid exhumation belt, which runs from central Nepal westwards to the Sutlej-Beas region in India. This thesis focuses on both surface and tectonic processes that shape the landscape in this dynamic region since late Miocene.

There is a long debate when and how extensive the High Himalaya has been glaciated during the late Pleistocene. In my first study, I dated well-preserved glacially polished bedrock on high-elevated ridges and valley walls in the upper of the Chandra Valley the by means of ^{10}Be terrestrial cosmogenic radionuclides (TCN). I used these ages and mapped glacial features to reconstruct the extent and timing of glaciation at the southern front of the Himalaya; also by testing various online provided calculators for cosmogenic exposure ages. I was able to reconstruct an extensive valley glacier of ~200 km length and >1000 m thickness. Ice thickness was high enough that it spilled over the valley bounding crestlines at two locations. Therefore ice was flowing into the uppermost Spiti and the Beas valleys prior to 20 ka. Deglaciation of the Chandra Valley glacier started subsequently to insolation increase on the Northern Hemisphere and thus responded to temperature increase. I showed that the timing this deglaciation onset was coeval with retreat of further midlatitude glaciers on the Northern and Southern Hemispheres. These comparisons also showed that the post-LGM deglaciation very rapid, occurred within a few thousand years, and was nearly finished prior to the Bølling/Allerød interstadial.

A second study (co–authorship) investigates how glacial advances and retreats in high mountain environments impact the landscape. It is not only important to know glacial extents, it is also important to decipher processes that lead to aggradation and incision in proglacial environments. By dating terrace surfaces and depth profiles by ^{10}Be TCN dating and geomorphic mapping, we obtained maximal length of the Siachen Glacier of >180 km and the height of the Siachen Glacier within the Nubra Valley. Today the Shyok and Nubra confluence is backfilled with sedimentary deposits, which are attributed to the valley blocking of the Siachen Glacier 900 m above the present day river level. A glacial dam of the Siachen Glacier blocked the Shyok River and lead to the evolution of >20 km long lake. Fluvial and lacustrine deposits in the valley document alternating draining and filling cycles of the lake dammed by the Siachen Glacier. In this study, we can show that glacial incision was outpacing fluvial incision.

In the third study, which spans the million-year timescale, I focus on exhumation and erosion within the Chandra and Beas valleys. In this study the position and discussed possible reasons of rapidly exhuming rocks, several 100-km away from one of the main Himalayan faults (MFT), but in close vicinity of the inactive South Tibetan Detachment (STD) using Apatite Fission Track (AFT) thermochronometry. The newly gained AFT ages indicate rapid exhumation of 0.75-2 mm/yr and confirm earlier studies in the Chandra Valley. I assume that the rapid exhumation is most likely related to uplift, when rocks move over a subsurface fault-ramp found within the neighboring Sutlej area. I tested this hypothesis by combining further low-temperature thermochronometers from areas east and west of my study area. By comparing two neighboring transects, each parallel to the Beas/Chandra Valley transect, I demonstrate similarities in the exhumation pattern to transects across the Sutlej region to the east, and strong dissimilarities in the transect crossing the Dhauladar Range to the west. I conclude that the belt of rapid exhumation terminates at the western end of the Kullu-Rampur window. Therewith, I corroborate earlier studies suggesting changes in exhumation behavior in the western Himalaya. Furthermore, I discussed several causes responsible for the pronounced change in exhumation patterns along strike: 1) the role of inherited pre-collisional features such as the Proterozoic sedimentary cover of the Indian basement, former ridges and geological structures, and 2) the variability of convergence rates along the Himalayan arc due to an increased oblique component towards the syntaxis.

The combination of field observations (geological and geomorphological mapping) and methods to constrain short- and long-term processes (^{10}Be, AFT) help to understand the role of the individual contributors to exhumation and erosion in the western Indian Himalaya. With the results of this thesis, I emphasize the importance of glacial and tectonic processes in shaping the landscape by driving exhumation and erosion in the studied areas.

Zusammenfassung

Der Himalaja, eines der wichtigsten känozoischen Kontinent-Kontinent Kollisionsgebirgen, erstreckt sich über 2500 km entlang des südlichen Randes des Tibetischen Plateaus von West nach Ost. Auf Grund der Möglichkeit dort sämtliche Disziplinen der Geowissenschaften zu studieren wird er oft auch als perfektes natürliches Labor bezeichnet. Die Gebirgsbildung wird durch interne Deformationsprozesse und klimatische Faktoren, welche auf Verwitterung, Abtragung und Transport wirken, beeinflusst. In einem Zyklus von Eis- und Warmzeiten wurde die Landschaft durch temperierte Gletscher geformt. U-Täler sind noch heute erhaltene Spuren der Gletscher, die in den Warmzeiten durch abgetragene Sedimente verfüllt wurden. Diese Sedimente befinden sich teilweise bis heute in diesen übertieften Tälern, weil es an Kapazitäten zur Ausräumung der Täler ins Vorland mangelt. Die hohen Gipfel des Himalajas dienen, dem aus Osten herziehenden Regen des indischen Sommermonsuns, als Barriere, während die Westwinde Feuchtigkeit hauptsächlich in den westlichen Teil des Gebirges liefern. Daraus resultiert eine von Ost nach West und von Süd nach Nord abfallende Niederschlagsmenge, welche sich auch in der heutigen Vegetationsdichte und dem Gletschervorkommen wiederspiegelt. Die kurz-skaligen klimatischen Prozesse überlagern sich mit langzeitlichen tektonischen Prozessen wie Hebung und Exhumation, die durch Konvergenz verursacht werden. Über die Prozesse, welche die Verkürzung entlang der Verwerfungen innerhalb himalajischen Gebirgskeils aufnehmen, wird debattiert. Im Zusammenhang mit dem Gebirgswachstum ist es entscheidend die Prozesse, welche die Erdoberfläche sowohl über kurze wie auch über längere Zeiträume formen zu bestimmen und damit auch deren Auswirkungen auf die Landschaftsentwicklung in den einzelnen Abschnitten des Gebirgsbogens.

Der westliche Himalaja zeichnet sich als ausgezeichnetes Forschungsgebiet aus: 1) Obwohl dynamische Erosionsprozesse stattfinden, beispielsweise durch Massenbewegungen, findet man entlang der Talflanken und auf Gebirgsrücken gut erhaltene durch Gletscher polierte Oberflächen. 2) Es wird sowohl vom Westwindsystem als auch durch den indischen Sommermonsun mit Feuchtigkeit versorgt, die jedoch nicht ausreicht um die verfüllten alpinen Täler auszuräumen. 3) Es am westlichen Ende des sogenannten „rapid exhumation belt“ gelegen ist, welcher vom zentralen Himalaja in Zentralnepal westlich bis in die Sutlej-Beas Region in Indien verläuft. Diese Dissertation fokussiert auf tektonische und Erdoberflächenprozesse, welche diese Landschaft in ihrer dynamischen Umgebung seit dem Miozän geprägt und beeinflusst haben.

Seit langem wird darüber diskutiert, wie und wann der Hohe Himalaja (High Himalaya) im Pleistozän vergletschert war. In der ersten Studie, habe ich im oberen Chandratal mittels ^{10}Be terrestrischen kosmogenen Nukliden (TCN) gut erhaltene vom Gletscher geschliffene und polierte Gesteinsoberflächen auf höher gelegenen Bergrücken und entlang der Talseiten datiert. Das Alter der Freilegung wurde mit verschiedenen online zur Verfügung stehenden Rechnern für kosmogene Nuklidalter berechnet. Basierend auf diesen Altern und kartierten glazialen Landformen habe ich nicht nur die Ausdehnung, sondern auch den Zeitpunkt einer Vergletscherung an der südlichen Front des Himalajas rekonstruiert. Dieser rekonstruierte Gletscher hat im Chandratal eine maximale Länge von etwa 200 km und mehr als 1000 m Dicke erreicht und floss vor 20 000 Jahren sogar in die benachbarten Täler Spiti und Beas. Die Entei-

sung des Chandratales folgte dem Anstieg der Sonneneinstrahlung und somit der Temperaturerwärmung auf der nördlichen Hemisphäre. Der Zeitpunkt des Enteisungsbeginns stimmt mit dem Rückgang weiterer Gletscher der mittleren Breiten auf der südlichen wie auch auf der nördlichen Hemisphäre überein. Diese Vergleiche zeigen auch, dass die Enteisung der letzteiszeitlichen Vergletscherung schon vor dem Bølling/Allerød Stadium nahezu abgeschlossen war.

In einer zweiten Studie (Ko-Autorenschaft) wird untersucht, wie Gletscher die Erdoberfläche formen und wie Gletschervorstöße und -rückzüge die Landschaft in alpinen Regionen beeinflussen. Daher ist es nicht nur wichtig die Ausdehnung von Gletschern zu kennen, sondern auch die Prozesse zu entschlüsseln, welche Aggradation und Einschneiden lenken. Die maximale Länge des Siachen Gletschers im Nubratal wurde in dieser Studie, an der ich beteiligt war, durch die Datierung von Terrassenoberflächen und Tiefenprofilen mittels ^{10}Be TCN und der Kartierung geomorphologischer Merkmale auf mehr als 180 km rekonstruiert. Heute ist der Zusammenfluss der Flüsse Shyok und Nubra mit Sedimenten verfüllt, deren Ablagerung mit einer Blockierung des Tales durch den Siachen Gletscher bis zu 900 m über der heutigen Flusshöhe zusammenhängen. Demzufolge, staute der Siachen Gletscher den Fluss Shyok. Hinter dem Damm bildete sich ein Stausee von über 20 km Länge. Fluviatile und lakustrine Ablagerungen im Tal dokumentieren sich wechselnde Entleerungs- und Auffüllungszyklen dieses Gletscherstausees. In dieser Studie, konnte ebenso gezeigt werden, dass fluviatile Erosion durch die glaziale Erosion überholt wird.

Über den längeren Zeitraum (Jahrmillionen) fokussiere ich auf Exhumation und Erosion in den Tälern Chandra und Beas. In dieser dritten Studie war es mir möglich mittels Apatit-Spaltspurdatierung (AFT) die Lage und Gründe der schnellen Exhumation in diesem Bereich zu beschreiben, einige hundert Kilometer entfernt einer der Hauptstörungen des Himalajas (MFT) und in der Nähe des inaktiven South Tibetan Detachment (STD). Die neuen AFT Alter deuten auf schnelle Exhumationsraten von etwa 0.75-2 mm/yr hin und bestätigen frühere Studien aus dem Chandratal. Ich vermute, dass diese schnelle Exhumation mit einer Bewegung über eine krustale Rampe im Zusammenhang steht, welche auch im östlich anschließenden Sutlej Tal ausgeprägt ist. Diese Hypothese wurde durch die Kombination weiterer tieftemperatur Thermochronometer aus benachbarten Gebieten untersucht. Durch den Vergleich zweier Profile, welche parallel zum Chandra/Beas-Profil laufen wurden im Sutlej Gebiet östlich des Studiengebietes ähnliche Exhumationsmuster gefunden. Das Exhumationsmuster über die Dhauladar Range unterscheidet sich hingegen von den anderen. Daraus schließe ich, das Ende es „rapid exhumation belt“ östlich des Kullu-Rampur Fensters im Beastal und bestätige damit auch frühere Studien, die einen Wechsel des Exhumationsverhaltens im westlichen Himalaja diskutieren. Im Weiteren wurden verschiedene Gründe wie ehemalige prä-kollisionale Strukturen und Sedimentbecken oder die abnehmende frontale Konvergenz gegen Westen diskutiert, welche sich Möglicherweise verantwortlich zeichnen für den Wechsel des Exhumationsverhaltens entlang des Streichens des Himalaja.

Die Kombination aus Feldbeobachtungen (geologische und geomorphologische Kartierung) und Methoden, die über kurze und längere Zeiträume Prozesse auflösen (^{10}Be, AFT), unterstützen die Erkenntnisse über die Rollenverteilung der einzelnen Akteure bezüglich Exhumation und Erosion im westlichen indischen Himalaja. Die Ergebnisse dieser Doktorarbeit heben die Wichtigkeit glazialer als auch tektonischer Prozesse als Steuerelemente von Exhumation und Erosion im Studiengebiet hervor.

Contents

MAIN PART OF THESIS

APPENDICES

List of Figures

List of Tables

Thesis organisation and author contributions

Chapters 2 – 4 of this thesis constitute papers that have been submitted and/or published as individual papers in peer–reviewed journals. All of these chapters are organised in subchapters including introduction, methods, results, discussion and conclusions. All references are provided at the end of this main thesis. Material published as supplementary information is given in the corresponding appendices (Appendices A – C). In the following sections an overview of the chapters and the contribution of the co-authors to the study are listed.

Chapter 2 presents a study from the Chandra Valley in northwestern India, where newly obtained ^{10}Be exposure ages of glacially polished and well-preserved surfaces point toward a large alpine valley glacier during the global Last Glacial Maximum (23-19 ka) and the subsequent deglaciation, which was similar in pace to those of global midlatitude glaciers. P. Eugster outlined and designed the study with D. Scherler and R. Thiede. Samples were collected during three field-seasons by 1) D. Scherler, R. Thiede, P. Eugster, 2) R. Thiede, P. Eugster and 3) P. Eugster. The samples were processed and analyzed by P. Eugster. A. T. Codilean introduced, helped and managed sample processing (extraction, analyzing of the ^{10}Be) in the clean lab of the GFZ in Potsdam. P. Eugster performed the data interpretation and glacial reconstruction model and wrote the manuscript and designed the figures. All co-authors were involved in the discussion of the manuscript.

Chapter 3 presents a study from from the Karakoram area in NW India where large valley fills and glacial remnants document the length, thickness and timing of the Siachen Glacier within the Shoyk and Nubra valleys. P. Eugster conducted fieldwork with D. Scherler and J. Mey. P. Eugster processed the TCN samples (^{10}Be samples) and analyzed the samples in the clean lab of the GFZ in Potsdam.

Chapter 4 presents a study from the northwestern Himalaya (from the Sutlej area to the Dhauladar Range), were I document and analyze the exhumation pattern at the transition zone between the Central Himalayan and the Western Himalayan by comparing low temperature thermochronometers and the morphological features of the area. P. Eugster, R. Thiede and D. Scherler outlined and designed the study. Apatite Fission track samples were collected during three field-seasons by 1) D. Scherler, R. Thiede, P. Eugster, 2) R. Thiede and P. Eugster and 3) K. Stübner. Samples were processed and analyzed by P. Eugster and K. Stübner. P. Eugster interpreted the data, wrote the manuscript and designed the figures. D. Scherler and R. Thiede guided writing up the results. All co-authors were involved in the discussion of the manuscript.

Chapter 5 is a discussion of the most relevant results of this thesis. It synthesizes and discusses the different relationships of the results from the different principal chapters 2 – 4.

Chapter 6 summarizes the general conclusions of this thesis.

Appendix A contains the supplementary information for chapter 2 that was published in 2015 in Geophysical Research Letters in 2016. It includes field photographs, a comparison of ^{10}Be exposure ages recalculated with the CRONUS online calculator hosted at the University of Kansas, data of the glacier reconstruction, and glacial striations measurements.

Appendix B contains the supplementary material of chapter 3, which was published in 2014 in Geological Society of America Bulletin. It includes additional figures, recalculated ^{10}Be exposure ages and glacial striation measurements.

Appendix C contains the apatite fission track data, erosion rate and advection calculation of chapter 4.

Declaration of Authorship

This work has not been submitted to any other institution of higher education, and it was prepared independently and exclusively wit the specified funds, the graduate school GRK1364 *Shaping Earth's Surface in a Variable Environment: Interactions between tectonics, climate and biosphere in the African-Asian monsoonal region* of the German Science Foundation (DFG, Deutsche Forschungsgemeinschaft; Projekt GRK1364/2) funded by DFG (STR 373/27-1 and 28/1).

MAIN PART OF THESIS

1 Introduction

1.1. Overview

1.1.1. Background

The Himalayan orogen, home of the world's highest summits, is shaped by the interaction between tectonics and climate on different timescales. While on long timescales the ongoing collision between India and Eurasia leads to shortening, deformation and uplift of the orogenic belt, on shorter timescales fluctuations in climate cause varying degrees of erosion and degradation.

Effects of tectonic uplift, the removal of rocks by weathering and fluvial or glacial erosion control exhumation [e.g., Willett, 1999] (Figure 1.1). In steady-state orogens uplift and erosion are balanced, which means that the material flux into an orogen by shortening processes (accretion) equals flux out of the orogen (erosion) [e.g., Willett and Brandon, 2002]. On the one hand, the orogen reacts on changes of the tectonic setting and on the other hand, the climate (precipitation, temperature) also triggers changes in topography, such as high and low relief or steep and shallow channel slopes. This can ultimately even lead to changes in the deformation style [e.g., Willett and Brandon, 2002; Willett, 2010]. This hypothetical concept is based on the critical taper theory. The critical taper theory, explains based on physical parameters such as the stress state through the orogenic taper, how an orogenic wedge is maintained by shifting the locus of deformation balancing mass removal by erosion [e.g., Dahlen and Suppe, 1988; Dahlen, 1990; Willett and Brandon, 2002].

Whether or not the material eroded by theses processes is transported out of the orogen depends on the available amounts of sediment and water as well as on the slope [e.g., Lane, 1955; Bull, 1991].

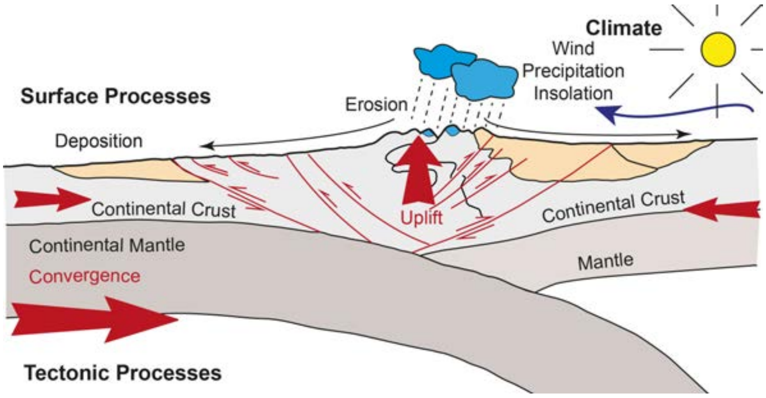

Figure 1.1: Schematic model of the interaction between tectonic processes, surface processes and climate. The mountain range is uplifted and the surface is exhumed. External factors such as precipitation, insolation and wind force erosion. Sediments are stored and deposited in intermontane valleys and foreland basins. Figure modified after Willett [1999].

For example, sediments will be stored as archives in alluvial deposits of intermontane basins or in the foreland [e.g., Hinderer, 2001; Otto et al., 2009].

Whereas evidence of tectonic processes i.e., uplift is hard to see in the landscape, alternating fluvial and glacial dominance of erosion leads to diverse and impressive traces. These include U-shaped valleys and valley overdeepenings, filled with hundreds of meters of sedimentary deposits (Figure 1.2) [Haeberli, 1983; Preusser et al., 2010; Mey et al., 2016]. Even though the erosional potential of glaciers is unclear, they are proposed to act as principal erosional agents and are thought to be the cause for increasing topographic relief in mountain belts [e.g., Egholm et al., 2009; Braun, 2010; Ward and Anderson, 2012; Herman et al., 2013]. Apart from their role as erosional agents glaciers also interact with tectonic processes on smaller scale by impeding thrusting due to their weight [Hampel and Hetzel, 2006; Turpeinen et al., 2008] and on a larger scale by the adjustment of the lithosphere to removed ice mass by the glacial rebound as seen in the formerly glaciated Fennoscandian/Baltic Shield or after LGM deglaciation of the Alps [Mey et al., 2016]. Such isostatic adjustments also occur due to the removal and unloading of material out of the orogen, e.g., due to protracted erosive periods [Molnar and England, 1990]. Tectonics may also trigger mass wasting events [e.g., Hovius et al., 2011; Qiu, 2016] and react to erosion by reorganizing deformation [Willett, 2010]. In the Himalaya the tectonic processes of the ongoing collision that lead to exhumation and deformation are controversially debated [e.g., Webb et al., 2007; Larson et al., 2010; Ader et al., 2012].

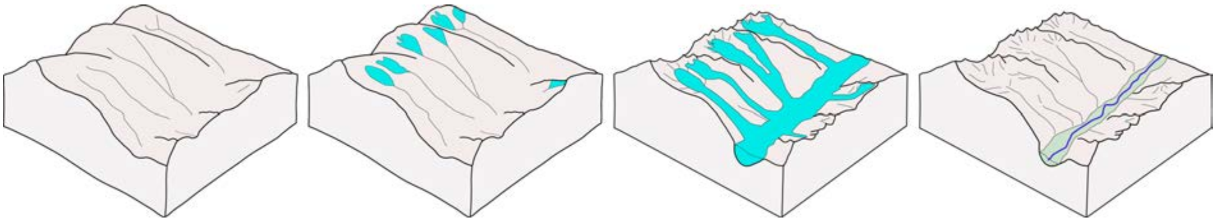

Figure 1.2: Dynamic model of fluvially and glacially influenced landscape development. Figure after Flint [1971].

Usually, short-term denudation is well quantified by ^{10}Be basin-wide erosion rates [e.g., von Blanckenburg, 2005; Wittmann et al., 2007], nonetheless erosion rates in formerly glaciated areas are suggested to be biased due to variable erosion over time [Ganti et al., 2016]. In the Himalaya it is suggested that short-term fluvial and long-term denudation rates vary between 0.5-3 mm/yr, while glacial erosion rates are estimated at around 5 mm/yr [Godard et al., 2012; Thiede and Ehlers, 2013; Olen et al., 2016]. Long-term erosion (exhumation) is quantified by low-temperature thermochronometry, e.g., fission-track dating of apatites or zircons.

In the following paragraphs I introduce glacial processes in detail as they are a focus of this thesis. In addition, the methods I used to address the research questions are explained in brief. In chapter 1.2 the tectonic and climatic characteristics of the Himalaya are introduced.

1.1.2. Glacial processes

Glaciers move and therefore transfer of incorporated components (e.g., boulders or gravel) from higher to lower elevations [Benn and Evans, 2010]. In the upper parts snow and ice are accumulated (accumulation area) and in the lower part of an active glacier this ice melts (ablation area). The movement of glaciers down-valley leads to the abrasion, and with the help of rocks frozen to the lower parts of a glacier, deformation of the underlying bedrock [Benn and Evans, 2010]. The style of deformation and erosion depends in this context on the characteristics of the substratum, mainly on the lithology and the periglacial weathering conditions [Benn and Evans, 2010]. The main glacial erosional processes have been described as abrasion, quarrying and subglacial fluvial meltwater erosion [Herman and Braun, 2008; Benn and Evans, 2010]. Both processes, abrasion and quarrying are not well understood and quantified; however preliminary results assume that they are proportional to the sliding velocity of ice [Herman and Braun, 2008]. Besides erosional processes along the base of the glacier Ward and Anderson [2011] identified frost cracking as dominant mechanical weathering mechanism along steep valley slopes and mountain fronts, in addition rockfalls on glaciers and snow avalanches that supply loose sediments to the top of glaciers play a major role in erosion.

A fundamental concept important for the understanding of glacial dynamics is the equilibrium line altitude (ELA), which defines the altitude where accumulation is equal to ablation (mass balance = 0). The ELA reflects the climatic conditions and is defined annually. The snowline of glaciers with a negative mass balance lies above the firnline; for temperate glaciers the snowline is the firnline. There exist diverse methods to estimate the former ELA, these include: accumulation-area ratio (AAR), maximum elevation of lateral moraines (MELM), toe-to-headwall altitude ratios (THAR), toe-to-summit altitude method (TSAM), cirque-floor altitudes) [Benn and Lehmkuhl, 2000]. Benn and Lehmkuhl [2000] suggest for these methods a more general term the Glacier Elevation Index (GEI). Other easily employable methods to determine former ice cover are for example based on the physics of glaciers by applying a perfect plasticity model [Benn and Evans, 2010; Benn and Hulton, 2010]. Simulations that included the hydrology at the bottom of the glacier show an increase of erosion at low altitudes and also the slowing down of erosion when the topography does not allow further ablation [Herman et al., 2011].

In addition, besides glacial carving and incision additional growth in relief has been explained by a variety of processes. For example, permafrost-related mechanisms may stabilize a fractured mountain front, preventing its collapse as summarized in the Teflon Peaks Hypothesis [Anderson, 2005]. This hypothesis proposes that glaciers erode the landscapes while sliding over bedrock and consequently steepen the valley walls. On these steep valley walls and peaks only little ice or snow sticks, which protects the mountain from the direct impact of glacial erosion, promoting the growth of relief. Hence, Teflon peaks enhance the effects of rapid rock uplift [Ward et al., 2012]. In contrast, the shield hypothesis of Thomson et al. [2010], proposes that in areas where the climatic and geologic conditions are feasible, glaciers do not slide as wet-based glaciers because they are frozen to the bedrock. Therefore, these cold-based glaciers protect the mountain peaks from erosion and the effect on topography depends on the temperature at the base of the glacial ice [e.g., Sudgen and John, 1976; Kleman and Hättestrand, 1999].

Although, erosion due to these mechanisms have been proven challenging until recent to quantify, the enormous masses of ice and meltwater certainly leave traces in the landscape, such as U-shaped valleys, moraines, trimlines, polished bedrock ridges, large outwash plaines etc. These features provide an opportunity to reconstruct incision and the overall glacial history. As glaciers are sensitive to temperature and precipitation we are able to relate their advances and retreats to hemispheric or global oscillations in these parameters. Herman et al. [2011] confirm that climatic oscillations control and rapidly modify erosion patterns through time. It is important to note, that the time a glacier needs to readjust to a new equilibrium (= reaction time) depends on its size and is defined by $\tau_v = \Delta V / \Delta B$ = volume change/mass balance, where τ_v is the volume timescale [Jóhannesson and Raymond, 1989a; 1989b; Benn and Evans, 2010]. Table 1.1 shows scaling numbers for different types of glaciers, suggesting that for larger glaciers it takes longer to adjust to external influences [Kuhn, 1995; Lüthi and Funk, 2011].

Table 1.1: Typical scales and reaction times of different glacier types [Kuhn, 1995; Lüthi and Funk, 2011].

Size	Thickness	Length	Thickness/Length	Reaction time
Ice sheets	1000 m	1000 km	0.001	1000 years
Valley glaciers	100 m	10 km	0.01	100 years
Cirque glaciers	10 m	0.1 km	0.1	10 years

During or after their retreat information about the extent of disappearing glaciers is provided by the exposed landforms; while depositional landforms (e.g., moraines) take 1-10 ka to develop, erosional bedrock landforms develop from weeks to millions of years (e.g., roches moutonnées) [Fredin et al., 2013]. In the alpine foreland the glacial series, a succession of glacial landforms and deposits serves as a classical base glacial stratigraphy (Figure 1.3) [Penck and Brückner, 1909]. In the high Himalayan realm not all of these features are found. Mostly U-shaped, sometimes overdeepened valleys are most prominent. At the terminus of some glaciers outwash plains are established that may incise into older alluvial plains. Terminal moraines containing debris and rock fragments, formerly incorporated in the ice, define its maximal extent. Lateral moraines and trimlines that separated rugged bedrock ridges from glacially polished hillslopes mark glacier elevations at the side walls. Where the ice retreats, often streamlined, elongated and asymmetric bedrock roches moutonnées and/or drumlins occur. The polished bedrock surfaces of the roche moutonnées sometimes show grooves of several centimeters depth that indicate flow directions (e.g., rat tails). In addition, fluvio-lacustrine remnants of glacial lakes dammed by ice or moraines demonstrate the dimension of glacial processes and their profound impact on landscape evolution. Subsequent glacial lake outburst floods (GLOFs) related to moraine-dam breaks are documented worldwide and are hazardous for people living in the downstream valleys [Kääb et al., 2005; Bolch et al., 2012].

1.1.3. Terrestrial Cosmogenic Radionuclides (TCN)

The measurement of Terrestrial Cosmogenic Nuclides is a well established method to obtain ages and/or rates for short-term ($\sim 10^4$-10^6 yr) geologic and geomorphic processes [Brown et al., 1995; Bierman and Steig, 1996; Granger et al., 1996]. For the quantification of denudation rates and/or exposure ages of glacial landforms, such as moraines, glacially polished surfaces or fluvial terraces, the ^{10}Be concentration accumulated in quartz sand, boulders or bedrock are key to use the TCN method. In this study I used ^{10}Be accumulated on glacially polished surfaces and boulders to obtain exposure ages. In the following sections, I will focus on ^{10}Be TCN method to date glacial landforms.

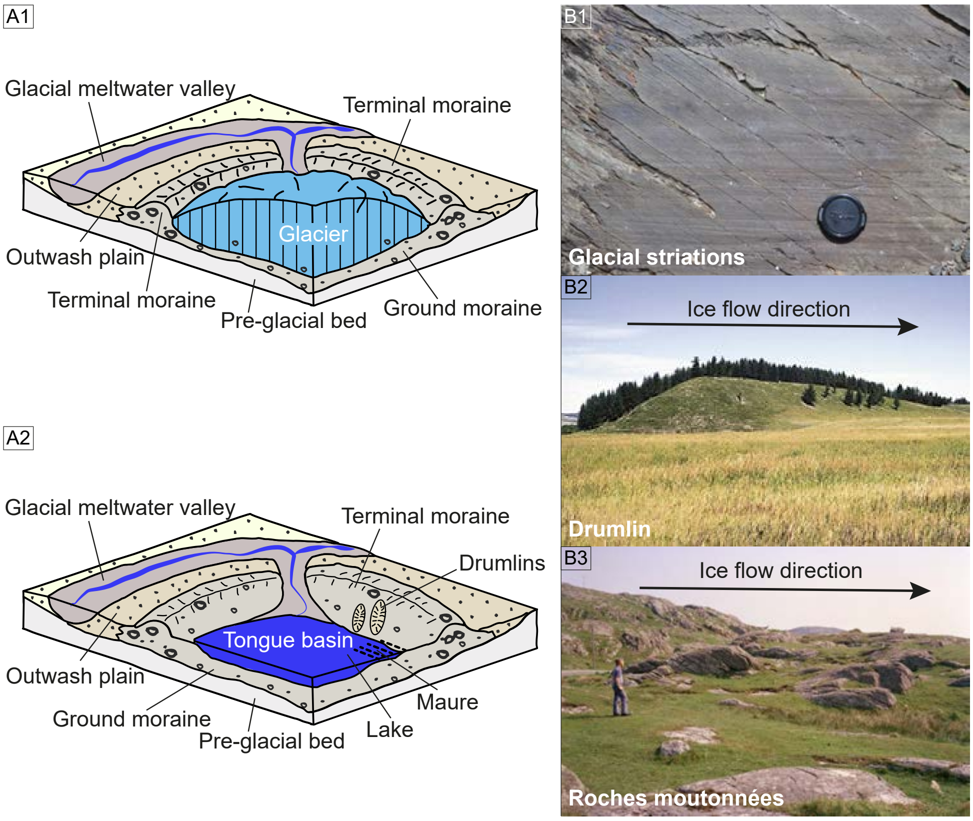

Figure 1.3: Glacial series and geomorphic examples. Left: the glacial series after Penck and Brückner [1909]. A1) indicates a situation during glaciation and A2) shows a situation after ice retreat. Right: photographs of glacial landforms identified in the Indian Himalaya. B1) Groove marks on glacially polished bedrock in the Lahul area, India. B2) Drumlin; ice flow direction is to the right. Stoss side is the steep side and gently sloping sector is the lee side (Photo: University of Toronto Scarborough). B3) Roches moutonnées. Ice flow direction is to the right. The stoss side is left and the plucking side is on the right (Photo: British Geological Survey, P008317).

Terrestrial Cosmogenic Nuclides are *in situ* produced at the Earth's surface. Nuclide reactions caused by the interaction of high-energy particles from space with atmospheric particles (particles when penetrating the atmosphere) lead to a secondary cosmic ray cascade descending to the Earth's surface with a decreasing energy level of the particles [Dunai, 2001; Blanckenburg, 2005]. The remaining neutrons interact with the atmosphere (*meteoric*) or with the atoms at the surface (*in situ*) and produce cosmogenic nuclides [Dunai, 2001; Blanckenburg and Willenbring, 2014]. The penetration depth is only ∼4-5 m with decreasing TCN concentration, accordingly to the attenuation length (Λ_{sp}) or absorption mean free path [Desilets and Zreda, 2001]. When attempting to obtain exposure ages from bedrock the samples only stem from the uppermost ∼<5 cm. From these samples the ^{10}Be has to be extracted and the ^{10}Be/^{9}Be ratio is measured using Accelerator Mass Spectrometry (AMS), from which the ^{10}Be concentrations are calculated.

It is crucial to note that TCNs are only accumulated at surface when exposed and uncovered; consequently, the longer a surface is exposed to cosmic rays, the higher the ^{10}Be concentration is. Therefore, older ages are obtained, when, for example, a previously exposed surface is covered again by ice and the accrued *in situ* ^{10}Be accumulation cannot be removed e.g., by erosion or decay. The measured ^{10}Be concentration of these samples is then higher due to the inherited ^{10}Be. Conversely, covering a surface by ice or a turn-over of a boulder leads to lower ^{10}Be accumulation and to underestimation of exposure ages (Figure 1.4).

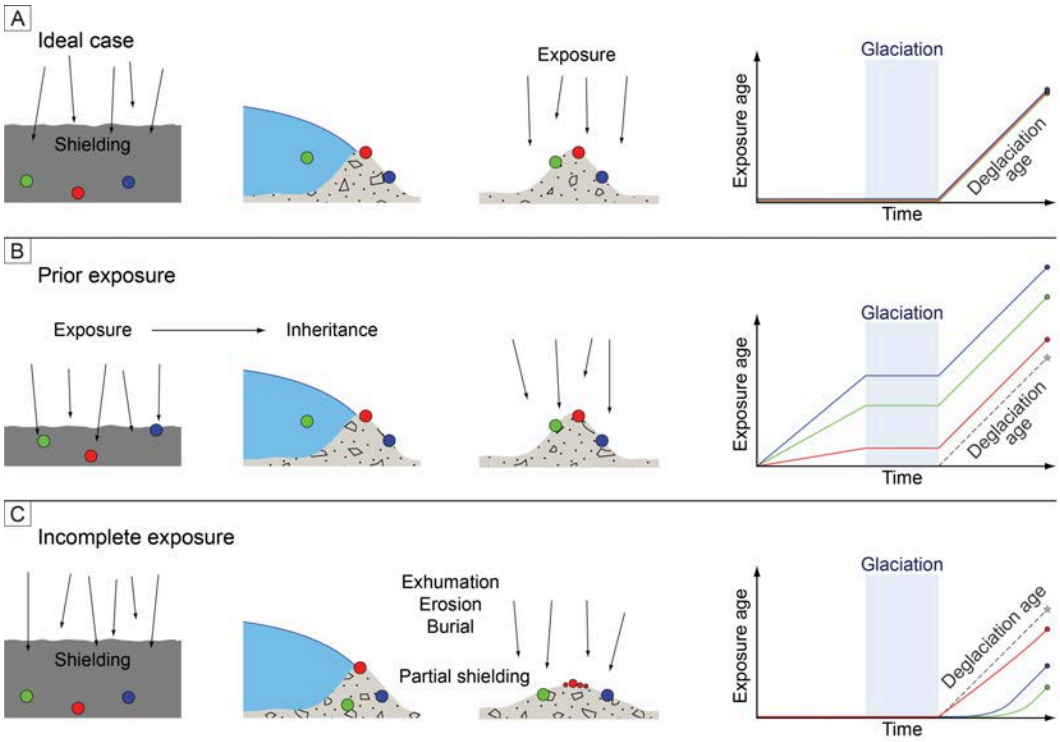

Figure 1.4: Overview of possible relationships from exposure ages on boulders from a moraine (green, red, blue) in three different examples. A) In the ideal case the surface has been covered and was then exposed in one single event. This means that the samples reflect the real exposure age. B) Samples were exposed to the surface before they were incorporated into the moraine and contain inherited ^{10}Be. Therefore, they yield exposure ages that are too old. C) Boulders were exhumed after the deposition of the moraine e.g., due to the degradation of the moraine. The resulting ^{10}Be concentration is lower due to the partial shielding and yields younger ages for the moraine deposition. Figure from Heyman et al. [2011].

Equation 1.1 has to be solved to obtain exposure ages and is also embedded in the commonly used cosmo online calculators formerly known as CRONUS earth online calculators [http://hess.ess.washington.edu/] hosted by the University of Washington.

$$N = S_{thick} S_G P_{ref,sp,Xx} \int_0^T S_{Xx}(t) exp(-\lambda t) exp \frac{-\varepsilon t}{\Lambda_{sp}} \, \mathrm{d}t + \tag{1.1}$$

$$P_{mu} \int_0^T exp(-\lambda t) exp \frac{-\varepsilon t - z/2}{\Lambda_{sp}} \, \mathrm{d}t$$

In this equation T is the exposure age, N the measured nuclide concentration (atoms/g), S_{thick} the nondimensional thickness correction, S_G the nondimensional geometric shielding correction, $P_{\mathrm{ref,\ sp,\ Xx}}$ the reference production rate due to spallation for the specific scaling scheme (see Table 1.2), λ is the nuclide specific decay constant (1/yr), ε is the assumed erosion rate (g/(cm^{2}yr)), Λ_{sp} is the effective attenuation length for spallogenic production (g/cm^2), P_μ is the muonic surface production rate (atoms/(g yr)), z is the sample thickness, Λ_μ effective attenuation length for production by muons [Balco et al., 2008].

The cosmic rays interact with the Earth's magnetic field, the atmosphere and the Earth's surface, so the local TCN production is influenced by external factors. These scaling factors need to be considered when calculating exposure ages. The scaling factors that are taken into account are altitude and latitude, topographic shielding, and overburden due to snow or vegetation. While topographic shielding can be measured in the field by a hand-held compass [Dunne et al., 1999] and the overburden due to snow or vegetation cover can be calculated [Masarik and Reedy, 1995], scaling frameworks have been developed to address altitude and latitude TCN production rate dependencies [e.g., Lal, 1991; Stone ,2000; Dunai ,2001; Desilets et al. ,2006; Balco et al., 2006]. In table 1.2 an overview of the different scaling frameworks that have been developed for the spallogenic production are listed [Balco et al., 2008 Table 4 therein; Lifton et al., 2014; Marrero et al., 2016; Borchers et al., 2016; Phillips et al., 2016].

Table 1.2: Overview on scaling frameworks developed for spallogenic production

ID	References	Scaling factor is function of...	time-dependent due to
St	Lal [1991], Stone [2000]	...geographic latitude and atmospheric pressure.	not time-dependent
De	Desilets et al. [2006]	...cutoff rigidity[a] and atmospheric pressure.	magnetic field changes
Du	Dunai [2001]	...cutoff rigidity[a] and atmospheric pressure.	magnetic field changes
Li	Lifton et al., [2005]	...cutoff rigidity[a], atmospheric pressure and solar modulation.	solar output, magnetic field changes
Lm	Lal [1991], Stone [2000], Nishiizumi et al. [1998]	Based on St, but with paleomagnetic corrections.	magnetic field changes
Sf	Lifton et al. [2014]	...cutoff rigidity[a], atmospheric pressure, solar modulation influencing the total flux of neutrons and protons.	solar output, magnetic field changes
Sa	Lifton et al. [2014]	...cutoff rigidity[a], atmospheric pressure, solar modulation and specific nuclide	solar output, magnetic field changes

[a] A major function of the geomagnetic field is the cut-off rigidity (R_c), a filter that defines the required energy of a particle to enter the atmosphere [Balco et al., 2008] and stronlgy depends on the latitude (currently 0 GV near poles, 15 GV at the equator) [Dunai, 2001; Balco et al., 2008; Lifton et al., 2014].

Several attempts have to be made to define globally valid calibrations for the ^{10}Be production [e.g., Balco et al., 2008 and Heyman, 2014] or regionally valid calibrations, e.g. for North America [Balco et al., 2009] or New Zealand [Putnam et al., 2010]. The production rate of *in situ* produced ^{10}Be nuclides is 4-5 atoms/(g yr) and a half-life time is 1.358±0.012 Ma [Balco et al., 2008; Chmeleff et al., 2010; Korschinek et al., 2010]. More recent studies suggest that the production rate might lower [Borchers et al., 2016; Phillips et al., 2016] resulting in age differences of up to 30% [Lifton et al., 2014]. However, when dealing with TCN it is necessary to keep in mind that the production rate varies temporally and spatially [Lifton et al., 2014].

1.1.4. Low-temperature thermochronometry

Low-temperature thermochronometers are used to study exhumation processes of the Earth's crust and the near surface, because they allow to reconstruct time-temperature paths of minerals moving towards the Earth's surface due to a combination of tectonics and erosion [Chew and Spikings, 2015 and authors therein]. Apatites and zircons are minerals found in igneous rocks, but especially apatites can also be found in metamorphic sediments (pelites, carbonates) or mafic rocks [Chew and Spikings, 2015]. In low-temperature thermochronometry apatites and zircons are used for (U-Th)/He and Fission Track analysis. (U-Th)/He dating measures the helium that accumulates due to radioactive decay of ^{238}U, ^{235}U, ^{232}Th and the α-decay of ^{147}Sm resulting in ^{4}He in a single mineral grain. Closure temperatures for apatite is 75±5 °C [Wolf et al., 1998; Farley, 2000] and for zircon is 170 °C [Reiners et al., 2002]. In this study I performed apatite fission track (AFT) analysis.

The fission track technique allows one to date the time of a rock exposed at the surface became exhumed since it passed through a closure temperature (for apatite ∼110±10 °C, for zircon ∼240±10 °C) [Gallagher et al., 1998; Barbarand et al., 2003]. Fission, either occurring spontaneously or induced by irradiation, leaves zones of damage within the crystal lattice; these tracks are called fission tracks. The ^{238}U isotope of uranium splits into two daughter fragments with a strong positive charge that catapult into different directions through the apatite grain. Alternative models are suggested to explain their occurrence. The two daughter fragments travel through the mineral lattice where the damage occurs because of electron stripping or ionization in the "ion explosion model" leaving vacancies [Fleischer et al., 1975] or because of heat conduction away from the damaged zone in the "thermal spike model" [Seitz, 1949; Bonfiglioli et al., 1961; Chadderton and Montagu-Pollock, 1963]. In any case, the resulting damage will disappear and anneal when apatite is subjected higher temperatures and therefore a sample then resets. Tracks remain in the mineral when passing the lower boundary of the partial annealing zone (PAZ). Within the PAZ of apatite, between 60-∼110 °C and of zircons ∼180-240 °C fission tracks may shorten and disappear [Gleadow and Duddy, 1981; Brandon et al., 1998], if the rock is rapidly exhuming the tracks will remain in the rock. Samples with older exhumation histories, which also means slower exhumation, usually record a higher track density than younger samples with higher exhumation rates.

In the external detector method (EDM) the fission track ages are calculated by counting the spontaneous tracks in a the apatite grain and the tracks induced by irradiation on a piece of muscovite, indicating the amount of ^{238}U [Chew and Spikings, 2015]. The spontaneous apatite tracks do not show any preferred orientation and are randomly oriented. Unetched tracks can only be viewed by transmitted electron microscopy (TEM); to make them visible under an optical microscope the samples need to get etched in 5.5 mol nitric acid for 20 seconds. With this step the already damaged areas in the grain dissolve more rapidly than the "healthy" areas and the etch pits become visible. In the hexagonal apatite the lattice is asymmetric, which leads to anisotropic etching behavior. This means that the etching rate in the c-axis is the highest whereas it etches more slowly into the a- and b-axis. Where a track hits the surface the etch pit helps to identify the orientation of the surface. The external detectors (muscovites) are etched in 40%-hydrofluoric acid (HF) at 21 °C for 45 minutes. Finally, to obtain fission track ages it is necessary to include a ζ-calibration in the age calibration [Hurford and Green, 1983], where Fish Canyon Tuff and Durango Tuff apatites of known ages are counted and compared.

In addition, information about the annealing behavior can be extracted. Estimates about the resistance of tracks to annealing is given by the D_{par} value that is the measured etch pit parallel to the c-axis (D_{par}) [Ketcham et al., 1999]. D_{par} depends on the etching conditions [Sobel and Seward, 2010] and the mineral composition [Ketcham et al., 1999]. Lower D_{par} values indicate etching at low temperatures and low resistance to anneal [Ketcham et al., 1999].

One way to obtain exhumation rates is by age-elevation relationships (AER). Usually, the ages get older with elevation and hence the slope of the relationship yields an estimate on the exhumation rate (Figure 1.5A) [Huntington et al., 2007]. This approach assumes non-disturbed isotherms and regular vertical exhumation otherwise the closure temperature (Tc) varies in elevation (Figure 1.5B) [Stüwe et al., 1994; Mancktelow and Grasemann, 1997; Ehlers, 2005]. Therefore, this assumption is not fully valid or applicable as isotherms can be disturbed by faults (Figure 1.5C) [Huntington et al., 2007], geothermal heat [Mancktelow and Grasemann, 1997] and, topography [Braun, 2002; Ehlers, 2005] and has to be taken into consideration when interpreting low-temperature thermochronometer ages.

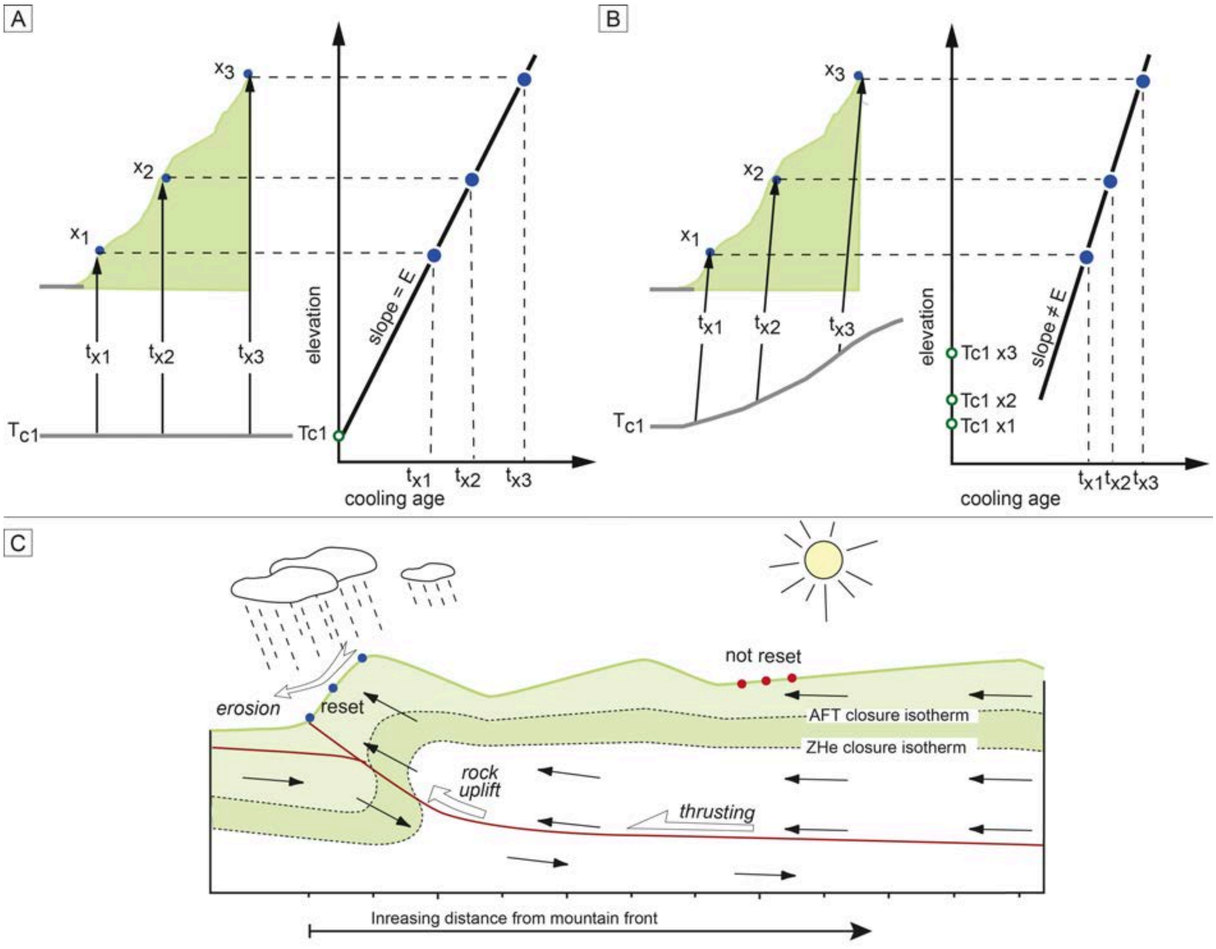

Figure 1.5: A) Age-elevation relationship within an undisturbed system, where rock move vertically to the surface. The slope represents the exhumation rate E. B) Age-elevation relationship in a disturbed system. The isotherms follow the topography resulting in a variation of Tc elevation. Because of different closure temperatures the slope is not equal to the exhumation rate E. C) Exhumation situation above a thrust at the southern front of the Himalaya. Samples that exhume vertically from below the Tc are reset and yield cooling ages. Samples transported laterally are not reset and it is unclear when they passed the PAZ. Figures modified from Ehlers [2005], Huntington et al. [2007], Deeken et al. [2011].

1.2. Geologic and climatic setting

1.2.1. Of hot and cold rocks

Over time, the collision of India and Eurasia 50 million years ago lead to the evolution of the Tibetan plateau (>5 km elevation), the Himalayan orogen of 3000 km length (>8 km elevation), and the disappearance of the Tethys ocean (Figure 1.6) [Le Fort, 1975; Avouac, 2003; Royden et al., 2008]. Subsequent to the collision, 2000 km of shortening has been accommodated by accretion of sediments and internal deformation [e.g., Royden et al., 2008].

First, the different units distinguished by Gansser [1964] and then the evolutionary stages of the the orogeny subsequent to the collision are described (Figure 1.6B). Rocks from the former Eurasian plate are mainly magmatic (e.g., Ladakh batholith) and separated from the Indian northernmost passive margin and its Tethyan sediments by the Indus-Tsanpo Suture Zone (ITSZ). The ITSZ consists of ophiolithes, marine sediments, and volcanic rocks [Le Fort, 1975]. To the south of the ITSZ the corresponding units can be traced along the entire length of the Himalayan arc. From north to south the Tethyan units comprise deformed sediments of the passive north Indian margin, separated from the High Himalayan sequences (HHS) by the north dipping South Tibetan Detachment (STD) normal fault [Le Fort, 1975; Burg et al., 1984]. The High Himalaya sequence comprises the metamorphosed granites and metasediments, such as the Haimantas that are separated from the Lesser Himalaya by the north dipping Main Central Thrust (MCT). The Main Boundary Thrust (MBT) marks the boundary between the Lesser Himalaya and the Himalayan foreland also known as the Sub-Himalaya, which mainly consists of the fluvial and marine Siwalik sequences. The Main Frontal Thrust (MFT) marks the boundary between the foreland fold-and-thrust belt and the undeformed Indo-Gangetic foreland basin.

Subsequent to the collision the following orogenic stages are distinguished 1) Alpine phase (intracontinental subduction) and 2) the Himalayan phase. Whereas 1) is characterized by nappe formation and the crustal shearing resulting doubling involving rocks from the suture area [Le Fort, 1975], the Himalayan phase is characterized by deformation along the evolving MCT, magmatism, and metamorphism [Le Fort, 1975]. During this phase the High Himalaya reached its metamorphic peak conditions around $\sim$23 Ma and high exhumation continued until $\sim$19-16 Ma. The southward propagation of deformation continued at the front after the cessation of high exhumation around $\sim$16 Ma, burying the Lesser Himalaya while exhuming the High Himalaya [Najman et al., 2009; Thiede et al., 2009]. Around 6 Ma rocks of the Lesser Himalaya were exhumed to the surface, which led to the disruption of drainage patterns [DeCelles et al., 1998; Najman et al., 2009]. In the foreland basin an increased accumulation of sediments at $\sim$11 Ma is attributed to the development of erosional topography due to activity of MBT, which was associated with the deposition of the Siwalik Group [Brozovic and Burbank, 2000; Najman et al., 2009].

The most striking faults can be traced along strike of the Himalayan arc but also across-strike structures are observed. For example, Pleistocene grabens have been described from 78°E to the east by Armijo et al. [1986] (Figure 1.7). Crustal stresses associated with the ongoing collision are attributed to cause the orientation of these grabens (Figure 1.7) [Armijo et al., 1986]. In addition, surface expressions of

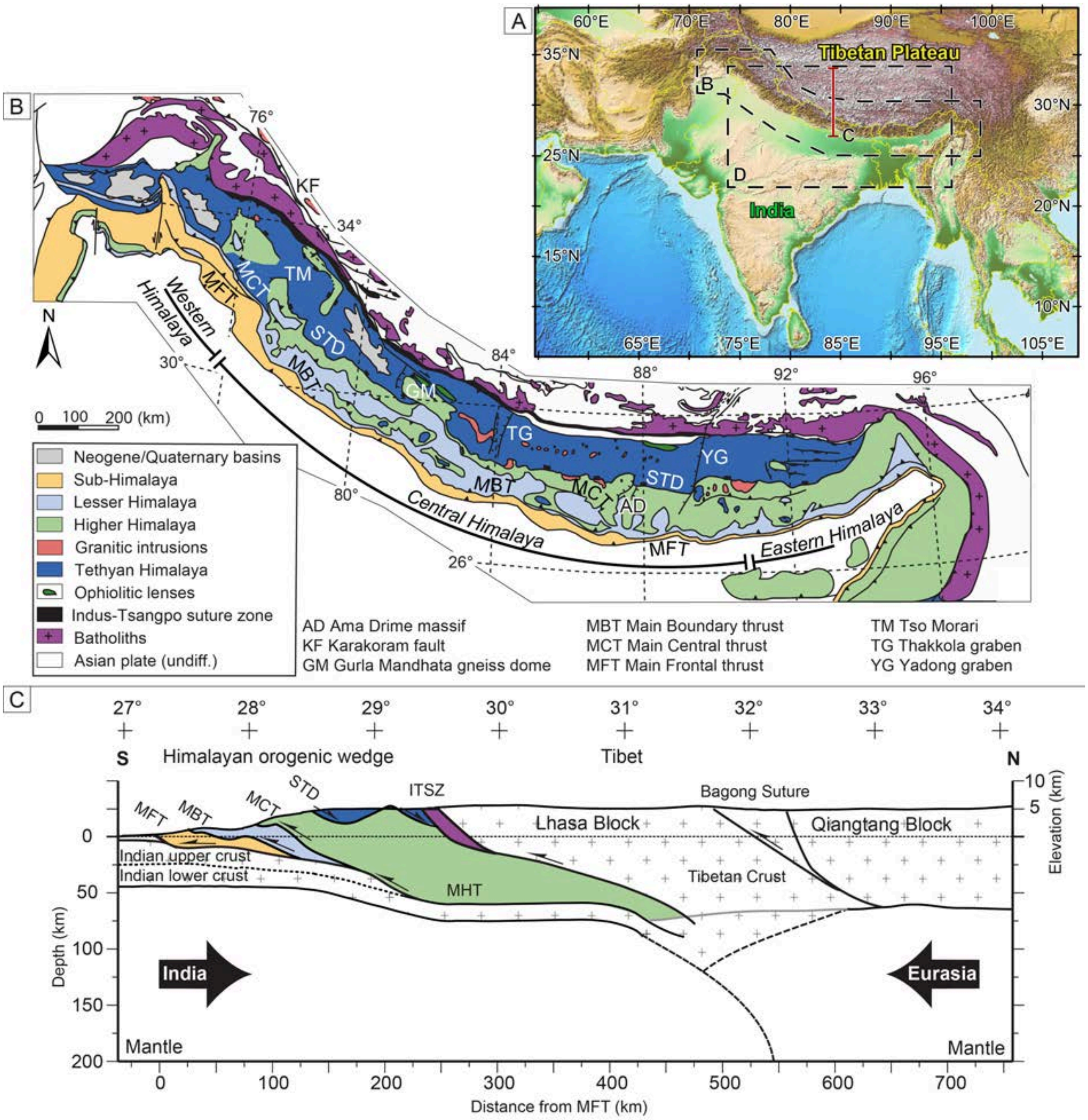

Figure 1.6: A) The Indian subcontinent and its bordering mountain chains and the outlines of figures B and C and the transect D are represented [Amante and Eakins, 2009]. B) The main geologic units, fault systems and Himalayan division [Hodges, 2000] between 74°E to ∼98°E. C) Cross-section across strike in the Kathmandu area illustrates the southward extruding units of the Himalayan orogenic wedge. Figure 1.6 is continued in figure 1.7. Figures modified from Yin [2006], Hintersberger et al. [2011], Godin and Harris [2014].

the Yadong cross structure mac correspond to possible graben structures attributed to inherited structures related to pre-collisional geology [Wu et al., 1998]. Furthermore, culminations and domal uplift are related to magmatic intrusions or thrusts evolving during the orogeny [e.g., Johnson, 1994]. However, tracing the main units along the orogenic arc results in a non-uniform distribution. While the Tethyan sediments show a constant width, the High, Lesser and Sub-Himalayan sequences show a discontinuous distribution along arc. Tectonic windows consisting of Lesser Himalayan material are exposed in High Himalayan sequences, including the Rampur and Kisthwar windows, but also klippen of High Himalayan or Tethyan Himlayan thrusts are superposed on the Lesser Himalaya along arc, including the Shimla, Karnali or Kathmandu klippen [DiPietro and Pogue, 2004].

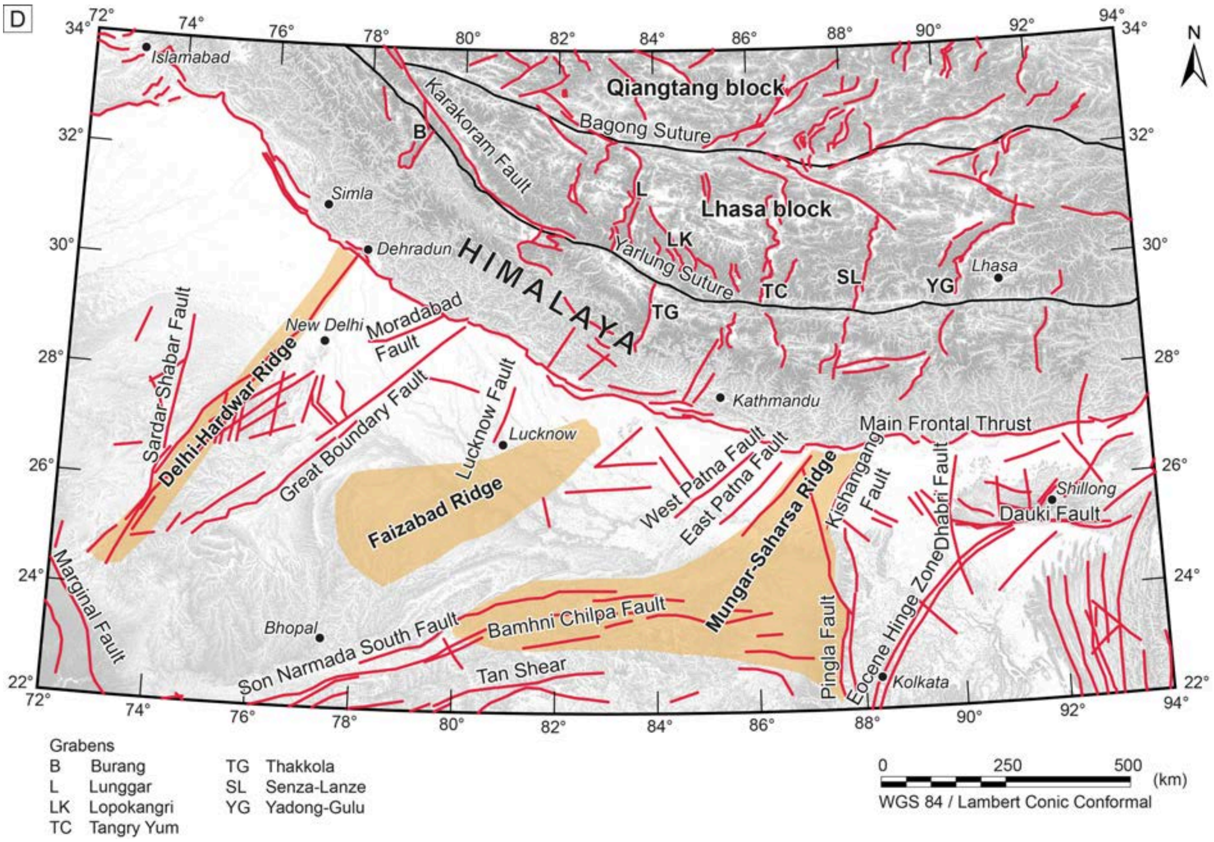

Figure 1.7: Continuation of Figure 1.6. Introduction to the Himalayan region. D) The Himalayan orogen and the Tibetan plateau host north to south striking grabens. On the Indian plate, subducting under the Eurasian plate, several pre-collisional rifts and ridges are indicated. Map modified from Godin and Harris [2014].

The alignment of the tectonic units before the Miocene, especially the emplacement of the High Himalayan units or nappes to the north is still being discussed and possible models may include: wedge extrusion, channel flow and, tectonic wedging. In the wedge extrusion model the Higher Himalayan sequence in the footwall of the STD is extruded to the south [e.g., Hodges, 2000; Webb et al., 2011]. The channel-flow model postulates that the High Himalayan sequence consists of a lower-viscosity than the surrounding Tethyan and Lesser Himalayan sequences, and is flowing to the south [Beaumont et al., 2001; Webb et al., 2011]. In the eastern syntaxis magnetotelluric investigations propose the existence of crustal flow [Bai et al., 2010]. Channel flow as well as wedge extrusion posit an active STD [Webb et al., 2011]. The tectonic wedging model does not require an active STD, here the emplacement occurs in depth and backthrusting of the units has been proposed [Webb et al., 2011].

Since the Miocene, emplacement of thrusts and exhumation have been proposed to occur over a mid-crustal ramp by duplexing or underplating or because of out-of-sequence thrusting [e.g., Bollinger et al., 2004; Herman et al., 2010]. Studies combining thermochronometery and 1- to 3-D modeling suggest different scenarios e.g., 1) in Bhutan, the absence of a mid-crustal ramp [Robert et al., 2011] or the presence of two small ramps [McQuarrie and Ehlers, 2015]; 2) in central Nepal a mid-crustal ramp several tens of kilometers away from the MFT [Robert et al., 2011]; 3) in the Sutlej area in India the presence of a mid-crustal ramp located beneath the Rampur Window is proposed [Thiede et al., 2009].

A two-step topography is observed along the Himalayan arc for ∼400 km (Nepal-Garhwal India), separating the physiographic Lesser Himalaya and the High Himalaya. The transition is from low to high elevations, from low to high slopes, and from low to high channel steepness, is called the physiographic transition 2 (PT_2) and is located between the MBT and the STD not strictly corresponding to the MCT [e.g., Morell et al., 2015]. The PT_2 is suggested to be associated with tectonic activity [e.g., Hodges, 2000].

Along the Himalayan arc erosion and exhumation have been shown as temporally and spatially variable distributed and decoupled exhumation/erosion rates have been proposed [e.g., Thiede and Ehlers, 2013; Olen et al., 2015; Abrahami et al., 2016]. Most of the recent studies suggest that in the Himalaya at least on the short-term, tectonics is the dominant driver of erosion [e.g., Godard et al., 2014; Scherler, 2014; Olen et al., 2015]. However, an unifying model for the overall morphological evolution of the orogen is still missing.

1.2.2. Of wind, water and ice

The Asian region is strongly influenced by the Asian Monsoon system, which is divided into the South Asia Monsoon, which is also called Indian Monsoon, East Asia Monsoon and South-East Asia Monsoon [e.g., Li et al., 2014]. The Indian Monsoon (ISM) only develops in summer and delivers around 78% of the annual rainfall to the Indian subcontinent [Gadgil, 2003; Ding and Sikka, 2006; Li et al., 2014]. The simplest view of the ISM is to imagine its development due to heating and movement of air masses above the Indian subcontinent and the Tibetan Plateau during summer. As warm air masses rise, low pressure areas are generated in which converging air masses from the Bay of Bengal flow towards the Himalayan mountain chain [Flohn, 1957; Gadgil, 2003]. Related to the monsoon is the seasonally migrating Inter Tropical Convergence Zone (ITCZ), which is formed where northern and southern hemisphere tradewinds converge [e.g., Gadgil, 2003]. It is suggested that the monsoon is caused by the ITCZ [Charney, 1967; Gadgil, 2003]. However, throughout the monsoon season there are alternating phases of intense and no rainfall [e.g., Annamalai and Slingo, 2001; Gadgil, 2003]. The intensity of the ISM is coupled to the evolution of the Himalayan arc and the Tibetan Plateau, but on longer timescales the monsoon also affects the exhumation of the orogen since it enhances erosion and exhumation [Clift et al., 2008; 2010]. Reorganization of river systems north of the collision and loess on the Chinese loess plateau indicate establishment of the East and South Asia Monsoon around ∼24 Ma [Clift et al., 2008] and recent studies have identified Quaternary (monsoonal) conditions even as early as the late Eocene [Licht et al., 2014; 2016].

The northwest Himalaya is influenced by the ISM, bringing moisture along strike from the Bay of Bengal to the northwest during summer; during winter by the midlatitude westerlies, supply moisture from the Mediterranean, Caspian and Black Seas to the western flanks, but also to the central sectors of the High Himalaya (Figure 1.8) [e.g., Benn and Owen, 1998]. Both moisture drivers are influenced by the Northern Hemisphere insolation and by changes in the climate system such as the Eurasian snow cover [e.g., Kripalani, 2003] and El Niño Southern Oscillation [e.g., Webster et al., 1998].

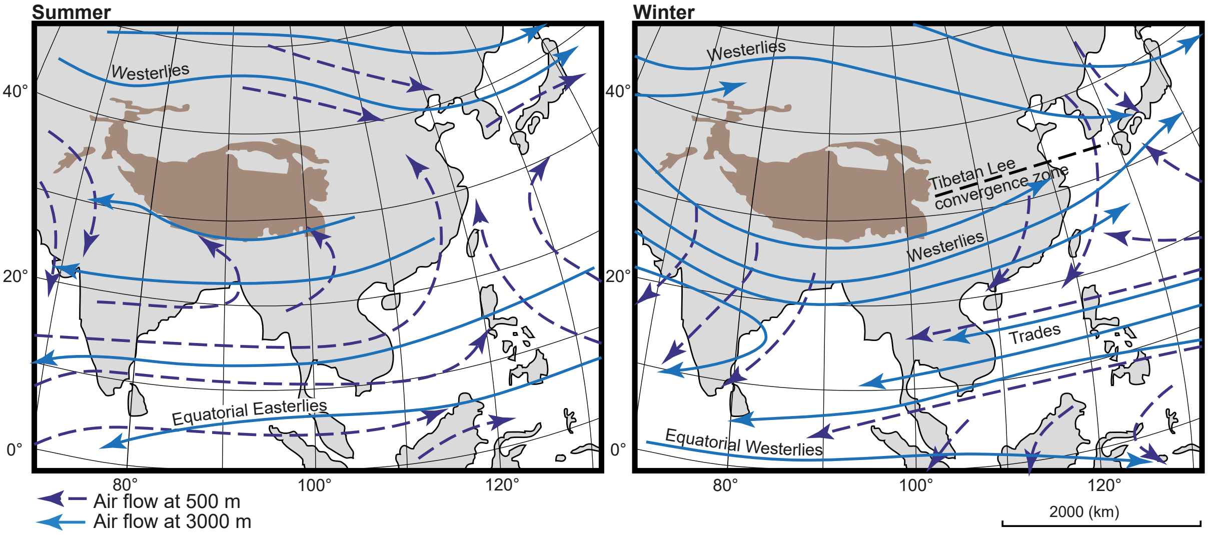

Figure 1.8: Overview on Asian wind systems. Shown in brown color are mountains and orogenic plateau areas in excess of 5000 m. Solid lines show winds at 3000 m and at 500 m elevation. Figure modified from Owen and Dortch [2014].

Monsoon rainfall shows a decreasing gradient from east to west and from south to north, which is also reflected in the vegetation distribution [Bookhagen, 2010; Bookhagen and Burbank, 2010; Olen et al., 2016]. The high mountain chains serve as an orographic barrier to precipitation, leading to an arid Tibetan plateau. It is under debate how far the westerlies reach into the Himalayan arc. Several studies showed that the northwestern areas receives moisture from two circulation systems [e.g., Wagnon et al., 2007; Wulf et al., 2010; Azam et al., 2014]. Measurements of the Bhuntar Observatory confirm winter precipitation even south of the first orographic barrier [Azam et al., 2014]. Data from the orographic interior of Himachal Pradesh (Lahul) suggest that despite minor precipitation, the area receives a considerable amount of precipitation during the winter months from the mid-latitude westerlies [Wulf et al., 2010], while 60-80% of the annual rainfall falls during summer [Bookhagen and Burbank, 2010] (Figures 1.9-1.12). Due to the location north and south of the orographic barrier to precipitation the Chandra Valley (north) and the Beas Valley (south) show different characteristics. In the Chandra Valley hillslopes are steep and deeply incised. The upper Chandra Valley is characterized by a broad valley, where glacially overprinted surfaces either glacial deposits or bedrock are exposed and vegetation is sparse (grassland) [e.g., Olen et al., 2016]. There the Chandra River incises mainly into the alluvial flood plains. In the wide valley rockfall deposits, debris flows, alluvium, or remnants of moraines are found [e.g., Owen et al., 1995; Coxon et al., 1996]. In the lower part of the Chandra Valley, where it is narrower the river incises into bedrock. Where the river is joined by the Bhaga River flowing as Chenab River it incises again in alluvial deposits continuing its course westwards parallel to the strike of the Himalaya. In the Chenab Valley vegetation increases and the shallower dipping hillslopes are mantled with debris.

In the Chandra Valley and tributary valleys major knickpoints have been observed, that correspond to hanging valleys or to para-glacial alluvial plains. The Beas Valley lies on the southern side of the High Himalayan ranges and is exposed to the moisture bearing winds from the south, which is also reflected in a higher vegetation. The Beas River profile is convex only showing small knickzones. Because of frequently intense monsoon rainfall the areas at the mountain front are also hit by devastating flash floods destroying infrastructure and causing the loss of lives, and leading to intense erosion processes (Figures 1.9-1.12) [Bookhagen, 2010; Bookhagen and Burbank, 2010].

Snowmelt contribution to water discharge is 25-50% for the Chandra/Chenab River catchment and <25% for the Beas catchment [Bookhagen and Burbank, 2010]. Likewise, in central Nepal at elevations above 3000 m snowfall contributes 25-30% of the annual precipitation [Lang and Barros, 2004]. In this setting the major snowfall events occur due to trapped westerly waves in winter [Lang and Barros, 2004]. Mass balance models (1969 - 2000) from the Chhota Shigri (Figure 1.11), a 9-km-long and 15.7 km^2 valley glacier in the Chandra Valley show that winter precipitation and summer temperatures are comparable drivers of glacial mass balance [Wagnon et al., 2007; Azam et al., 2014].

Figure 1.9: Lower Chandra Valley. The glacially carved and sediment filled lower Chandra Valley is at the transition zone between the westerlies and the ISM. Southern side of the valley represents the orographic barrier to the ISM.

Figure 1.10: View of the Beas Valley. Beas River at Palchan with bouldery deposits after intense rainfall in the Rothang area in the night of August 3th to 4th, 2012. The resulting flood obliterated houses and roads at the riverside and a bridge between the Rothang and Manali.

Figure 1.11: View of the medial moraine of the Chhota Shigri Glacier in the Chandra Valley at $\sim$5000 m asl (south to the right). This glacier is located in the rain-shadow of the high peaks.

Figure 1.12: Uppermost Tos Valley on the southern flanks of the High Himalaya. View to the north. Glaciers located in the south of the orographic barrier are completely covered with gravel debris.

Multiple Quaternary glaciations are documented along the whole Himalayan arc and Tibetan Plateau [e.g., Owen et al., 2008 and authors therein]. Especially, in the arid northern parts of India and western parts of Tibet areally extensive glaciations around 300 ka are documented. However, not all areas along the arc show the same timing and frequency of glaciations over the last 100,000 years. For example, in the monsoon-influenced Himalaya glaciations older than Marine Isotope Stage 3 are missing, whereas in some parts of the Transhimalaya glacial features associated with the last glacial maximum of <25,000 years are not documented [Owen and Dortch, 2014]. Different authors have pointed out that the differentiation and unequivocal interpretation of glacial landforms is difficult due their destruction by mass movements, fluvial and glacial processes [Owen and Dortch, 2014]. Pronounced erosion in the wetter regions rapidly removes the depositional and geomorphic evidence and lowers thereby the preservation potential [Owen et al., 1996; 2005; Seong et al., 2009]. Present day, most of the Central Asian and adjacent areas ice cover (114,800 km^2) is situated in the Himalayas where it serves as a freshwater reservoir for the region important for human consumption, agriculture and energy production [Barnett et al., 2005; Dyurgerov and Meier, 2005].

1.3. Motivation

The enormous power and dynamic interplay between tectonics, climate and erosion has tragically been illustrated in 2015 when the Village of Langtang in Nepal was buried under a massive landslide of ice and rock, which was triggered by the Gorkha 7.9 magnitude earthquake [Qiu, 2016]. In this case, the loose material released by rapid glacial retreat, but also stored sediments in the high mountain valleys, suddenly fell due to mass wasting triggered by the earthquake. This emphasizes the vulnerability of mountain populations with respect to the inherent hazards of this dynamic region.

In this context, it is crucial to understand, which processes drive exhumation and erosion in the western Indian Himalaya. The area is exceptional to study as it is situated: 1) at the western edge of the rapid exhumation belt, which runs from central Nepal to the Sutlej-Beas region; 2) is under influence of the ISM and the westerlies; 3) even though, dynamic erosional processes are occurring, well-preserved evidence of former glaciations are found.

To study the influence of long-term exhumation and short-term erosion on geomorphic surface processes, I revisited the Chandra and Beas valleys in the western Indian Himalaya. The following research questions were assessed:

- Which geomorphic processes influence the northwestern Himalaya on the short timescales (100 ka)?
- What drives the geomorphic evolution since the Miocene?
- What are the consequences of short and long-term erosion in the western Indian Himalaya for landscape development?

2 Rapid Last Glacial Maximum deglaciation in the Indian Himalaya coeval with midlatitude glaciers: New insights from ^{10}Be-dating of ice-polished bedrock surfaces in the Chandra Valley, NW Himalaya

Abstract

Despite a large number of dated glacial landforms in the Himalaya, the ice extent during the global Last Glacial Maximum (LGM) from 19 to 23 ka is only known to first order. New cosmogenic ^{10}Be exposure ages from well-preserved glacially polished surfaces, combined with published data, and an improved production rate scaling model allow reconstruction of the LGM ice extent and subsequent deglaciation in the Chandra Valley of NW India. We show that a >1000 m thick valley glacier retreated >150 km within a few thousand years after the onset of LGM deglaciation. By comparing the recession of the Chandra Valley Glacier and other Himalayan glaciers with those of Northern and Southern Hemisphere glaciers,we demonstrate that post-LGM deglaciation was similar and nearly finished prior to the Bølling/Allerød interstadial. Our study supports the view that many Himalayan glaciers advanced during the LGM, likely in response to global variations in temperature.

This chapter was published in
Geophysical Research Letters 43 (2016)
co–authored by Patricia Eugster, Dirk Scherler, Rasmus C. Thiede, Alexandru T. Codilean, and Manfred R. Strecker

2.1. Introduction

The behavior of glaciers is an important climate proxy for changes in humidity and temperature in high mountain ranges, where other climate archives are generally limited. Because the response time of glaciers to varying climate conditions is on the order of tens to hundreds of years, glacial chronologies based on dated moraines are frequently used to infer paleoclimatic conditions [e.g., Putnam et al., 2010]. In the Himalaya, previous studies suggested strong sensitivity of glaciers to variations in precipitation and thus to orbitally driven monsoon intensity. Additional factors may constitute strong east-west gradients in moisture sources, with western areas being influenced by the midlatitude westerlies [e.g., Benn and Owen, 1998] and Northern Hemisphere climate oscillations [e.g., Dortch et al., 2013; Owen and Dortch, 2014]. However, despite a rich collection of >1800 cosmogenic exposure ages that mostly stem from moraines [Dortch et al., 2013; Murari et al., 2014; Owen and Dortch, 2014], it has proven difficult to unambiguously identify the nature of the climatic controls on glacier fluctuations during the late Quaternary period. For example, robust data on advances of Himalayan glaciers during the global Last Glacial Maximum (LGM), here defined as the time period of maximum global ice volume from 19 to 23 ka during Marine Isotope Stage 2 (MIS2) [Mix et al., 2001; Lisiecki and Raymo, 2005], are limited. This particularly applies to the monsoon-influenced sectors of the Himalaya where early last glacial, late glacial, and early Holocene advances are commonly recognized [e.g., Owen, 2009; Scherler et al., 2010; Murari et al., 2014]. Possible reasons for the conundrum of scarce LGM advances include (1) asynchronous or no glacial advances due to steep climatic gradients [Owen et al., 2005] or hypsometric effects [Pratt-Sitaula et al., 2011]; (2) glacial advance due to the impact of rock avalanches and transient increases in debris cover [e.g., Gardner and Hewitt, 1990; Tovar et al., 2008; Jamieson et al., 2015]; (3) large age uncertainties due to unstable till deposits [Applegate et al., 2009; Heyman et al., 2011]; and (4) lack of adequate calibration sites and variations between scaling schemes [Chevalier et al., 2011; Heyman, 2014]. Although asynchronous glacial advances due to topographic effects or steep climatic gradients may exist, it is not very likely that these effects exclusively occur in the Himalaya; yet, so far, there exists limited evidence from other regions. Rock avalanches could trigger asynchronous glacial advances, but these are likely short-lived, local, and subordinate for large glaciers. In contrast, it is well known that erosion rates in the Himalaya are high [Godard et al., 2014; Olen et al., 2015], which makes erosive degradation of moraines a reasonable explanation. Furthermore, there still exist no cosmogenic nuclide calibration sites in the Himalaya, leading to additional methodological age uncertainties. However, recently published new calibrations, including low-latitude and high-altitude sites elsewhere [e.g., Kelly et al., 2013], newly compiled calibration data sets [Heyman, 2014; Borchers et al., 2016], and improved insights into discrepancies between production rate scaling models [Lifton et al., 2014], furnish an improved framework for cosmogenic nuclide exposure dating in the Himalaya.

We revisited the Chandra Valley in the Lahul region, NW Himalaya, where pioneering work by Owen et al. [1995, 1996, 1997, 2001] has established the timing of Late Pleistocene glacial advances mainly based on dated boulders. By dating ice-polished, glacially striated bedrock surfaces and reconstructing former ice extents, we are able to refine the existing glacial chronology subsequent to the LGM and suggest that the timing and pace of LGM deglaciation in the Chandra Valley and other Himalayan regions is similar to midlatitude glaciers, and primarily a response to increased global temperatures.

2.2. Study Area

The Chandra Valley, a tributary of the Chenab Valley, lies at >3000 m elevation and is surrounded by peaks higher than 6000 m elevation. The bedrock in the Lahul area comprises Neoproterozoic to Permian granitic intrusions and metasedimentary rocks of the High Himalaya and Tethyan sequences [Steck, 2003]. Among numerous smaller glaciers, the most extensive glaciers in the upper Chandra Valley are Samundar Tapu (86 km^2) [Pfeffer et al., 2014] and Bara Shigri (130 km^2) [Pfeffer et al., 2014] (Figure 2.1). Trimlines, U-shaped valleys, and dated glacial features attest to a major trunk-valley glaciation, previously referred to as the pre- or syn-LGM Chandra and Batal Glacial stages. The latter stage is manifested by pronounced trimlines and landforms (Batal I) overlain by younger drumlins that indicate readvances (Batal II) along the Chandra and Bhaga Valleys [Owen et al., 1995, 1997, 2001], reassigned to 15.3±1.6 ka [Murari et al., 2014]. Subsequent advances during the Kulti glacial stage are related to tributary glaciers and have been attributed to the Early Holocene [Owen et al., 1995, 1997, 2001] but redefined to the Late Glacial [Murari et al., 2014] and are interpreted as evidence for climatic forcing by the South Asian summer monsoon [Owen et al., 2001] or the midlatitude westerlies [Murari et al., 2014].

2.3. Methods

We collected 15 bedrock samples from well-preserved glacially polished surfaces and three samples from boulders resting on these surfaces for cosmogenic ^{10}Be exposure dating (see Appendix A for field photographs and detailed description of sampling locations). After standard mineral separation steps [e.g., Kohl and Nishiizumi, 1992], we extracted Be by ion exchange chromatography at the German Research Centre for Geosciences GFZ in Potsdam. ^{10}Be/^{9}Be ratios were measured by accelerator mass spectroscopy at the University of Cologne [Dewald et al., 2013]. We used the CRONUS-Earth Web Calculator [http://web1.ittc.ku.edu:8888/1.0/] hosted at the University of Kansas, which is based on the calibration data set compiled by Borchers et al. [2016], for calculating exposure ages for both the new and previously published [Owen et al., 2001] ^{10}Be concentrations. This calculator uses a new scaling model by Lifton et al. [2014] (later also referred to as LSD scaling) that is specific to ^{10}Be and accounts for its production rate sensitivity on the incident cosmic ray energy spectrum, instead of the cosmic ray flux-based scaling utilized previously. The cosmic ray flux-based scaling schemes do not account for nuclide-specific differences in production rate sensitivities. The CRONUS-Earth Web Calculator (hosted by the University of Washington) was also used to recalculate all previously published ages discussed; this information is presented in Figures 2.1-2.3 (supporting information provides the references of Figure 2.3). The reported exposure ages are based on the production rate scaling model by Lifton et al. [2014] and a ^{10}Be half-life of 1.387±0.012 Ma [Chmeleff et al., 2010; Korschinek et al., 2010]. We used the nuclide-specific attenuation lengths described by Lifton et al. [2014] with 145 g/cm^2 for altitudes between 0 and 2 km and 160 g/cm^2 for >3 km elevations and the thickness correction included in the CRONUS-Earth Web Calculator [Marrero et al., 2016]. In addition, we also calculated all of our ages with the CRONUS online calculator v2.2 using the calibration of Balco et al. [2008] and a more extensive calibration data set compiled by Heyman [2014].

Topographic shielding was measured in the field with a hand-held compass using the model by Dunne et al. [1999]. Snow cover shielding was not accounted for because our sampling sites comprise steep valley flanks and wind-exposed ridges, where thick snow cover is unlikely to remain for long.

We reconstructed the surface profile of the former glacier stepwise from the terminus up-glacier with a simple model that assumes a perfectly plastic ice rheology and a constant driving stress [Benn and Hulton, 2010]: $h_{i+1}=h_i+(f\tau D/H)_i(\Delta x/\rho g)$, where h_i is the ice-surface elevation at node i, H is the ice thickness, τD is the driving stress, Δx is the node distance, ρ is the ice density (900 kg/m^2), g is acceleration by gravity (9.81 m/s^2), and f is a dimensionless shape factor that accounts for valley-side drag and is calculated from H, the cross-sectional area of the valley A, and the ice-covered perimeter p, according to $f=A/Hp$. This is a 2-D model that neglects tributary glaciers, allowing for the estimation of the ice surface profile of the former trunk glacier, constrained by ice-polished and dated surfaces, moraines, and trimlines. We tested different values of τD and obtained the best matches with our field constraints using τD = 50 kPa for the maximum ice extent. The longitudinal valley profile and the shape factors (0.4–0.5 in the Chandra Valley) were measured from a 90 m resolution Shuttle Radar Topography Mission digital elevation model [Jarvis et al., 2008] using MATLAB and the TopoToolbox v2 [Schwanghart and Scherler, 2013].

2.4. Results

2.4.1. Surface exposure dating

Our new exposure ages range between ~14 and ~20 ka (Table 2.1 and Figure 2.1b). Older ages are obtained from locations with elevations >700 m above the present-day valley floor, while younger ages are obtained from lower elevations. At the Kunzum La (La = pass) (Figure 2.2b, Profile a-a'), glacial striations indicate that ice was flowing eastward into the Spiti Valley [Owen et al., 1997; Saha et al., 2015], crossing the drainage divide of the Chenab and Sutlej watersheds. Ice-polished bedrock surfaces record ice-free conditions by approximately 17.6±1.2 ka (16.0±1.2 ka, 19.2±1.2 ka), which is consistent with striations in the upper Spiti Valley dated at 17.4±1.3 and 18.3±1.3 ka. While the previously dated and recalculated surface at the Kunzum La of 18.0±1.3 ka [Owen et al., 2001] is consistent with our data, the boulders dated in that study yield exposure ages of 19.7±1.2 ka, 19.0±1.2 ka, and 18.6±1.2 ka [Owen et al., 1996, 2001], indicating possibly minor inheritance or a readvance. On a bedrock ridge at the Bara Shigri/Chandra confluence (Figure 2.2b, Profile b-b') at ~4600 m elevation, glacial striations occur ~700 m above the present valley floor on extensive ice-polished surfaces. A trimline at 4800–4900 m elevation separates rugged hillslopes from ice-polished surfaces with a mean age of 17.6±2.4 ka (19.3±1.2 ka, 15.9±1.2 ka). Two boulders located on this ridge yield ages of 17.8±1.3 ka, consistent with the average surface age, and 32.5±2.3 ka, clearly indicating inheritance. Striated surfaces at lower elevation from the opposite valley side are located 30–150 m above the valley floor and yield a mean age of 15.8±1.5 ka (15.6±1.2 ka, 14.5±1.1 ka, 17.4±1.3 ka). These results reflect rapid glacier retreat, with the ice thinning by >500 m within ~2 ka. Finally, at a location ~15 km farther downvalley (Figure 2.2b, Profile c-c'), glacial striations are ~500 m above the valley floor and four samples collected over

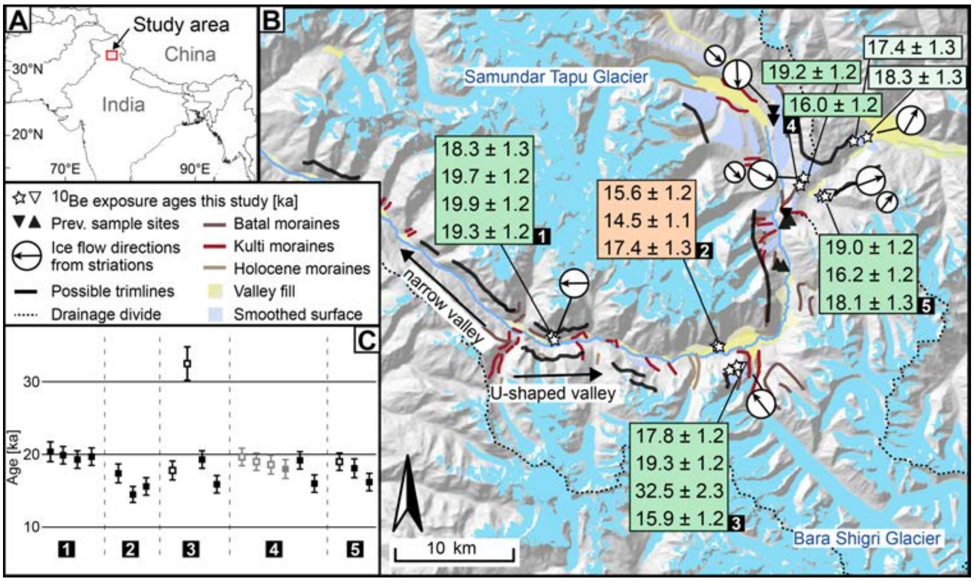

Figure 2.1: Sampling locations and ^{10}Be exposure ages of this study. (a) Study area. (b) Upper Chandra Valley with mapped landforms, flow directions of glacial striations [Owen et al., 1996, 2001; this study] and modern glaciers [Pfeffer et al., 2014]. White stars and white bottom up triangles indicate sampling locations and corresponding ^{10}Be exposure ages of this study. Black triangles indicate sampling locations of previous studies [Owen et al., 1996, 2001]. (c) Comparison of ^{10}Be exposure ages and uncertainties obtained from boulders (white squares) and from glacially polished surfaces black (this study)/grey [Owen et al., 2001]. The numbers correspond to the sampling location in Figure 2.1b.

∼100 m in elevation yield mean exposure ages of 19.3±1.2 ka (18.3±1.3 ka, 19.7±1.2 ka, 19.9±1.2 ka,19.3±1.2 ka). We found no more striations farther downstream.

Ages calculated with the CRONUS Earth web calculator using the scaling model by Lifton et al. [2014] are generally older than ages calculated with the CRONUS online calculator [Balco et al., 2008] and Heyman's [Heyman, 2014] calibrations. The ages are on average ∼25% older comparing Lal/Stone time-dependent ages by Balco et al. [2008] and on average ∼11% older comparing Lal/Stone time-dependent ages by Heyman [2014] with ages from Lifton et al. [2014] for the Himalayan glaciers (see also Table S2 and Figures S17 and S18 in Appendix A).

Table 2.1: CRN Data of this study

Sample				Location		Elevation	Thick-ness	Density	Production rate atoms (g qz)-1		Shielding Factor	Denu-da-tion	Sample Weight	Be Carrier	^{10}Be/^{9}Be [c]	^{10}Be Concentration [f, g g]	Exposure Age [f, h]
Nr.	Name	Type [a]	Trust [b]	N°	E°	masl	(cm)		Spallation [d]	Muons [e]		mm/yr	g	mg		atoms (g qz)-1	ka
1	WP051	pbs	1	32.4164	77.6308	4760	1.5	2.65	45.806	0.357	0.9767	0	33.2900	0.2765	1771±57.0	9.81E5±3.30E4	16.0±1.2
2	PE13_01	pbs	1	32.4237	77.6357	4819	3	2.6	45.685	0.355	0.9589	0	46.1187	0.1496	5588±174.0	1.21E6±3.94E4	19.2±1.2
3	PE12_013	pbs	0	32.2808	77.5779	4485	3	2.65	37.271	0.300	0.9215	0	40.0977	0.3063	1545±48.2	7.88E5±2.57E4	15.9±1.2
4	WP058	pbs	1	32.2822	77.5688	4491	4	2.8	39.933	0.321	0.9944	0	28.5550	0.2666	1705±53.2	1.06E6±0.47E4	19.3±1.2
5	WP059	bos	1	32.2823	77.5693	4499	3.5	2.8	40.258	0.324	0.9943	0	27.9600	0.2664	3211±98.6	2.04E6±6.56E4	32.5±2.3
6	WP057	bos	1	32.2806	77.5676	4483	3.5	2.8	39.949	0.322	0.9944	0	26.7800	0.2772	1387±43.1	9.58E5±3.12E4	17.8±1.3
7	WP052	pbs	1	32.2981	77.7738	3928	3.5	2.8	27.517	0.238	0.9048	0	28.1550	0.2746	981±30.8	6.38E5±2.10E4	17.4±1.3
8	WP053	pbs	1	32.2991	77.5531	4028	4	2.8	30.527	0.260	0.9575	0	26.5150	0.2752	828.6±26.9	5.73E5±1.94E4	14.5±1.1
9	WP054	pbs	1	32.2993	77.5534	4039	2	2.8	31.245	0.266	0.9578	0	28.3850	0.2752	993.2±31.6	6.42E5±2.13E4	15.6±1.2
10	PE12_061	pbs	1	32.3086	77.4058	4095	3	2.65	31.553	0.267	0.9460	0	40.1750	0.3068	1521±47.8	7.76E5±2.54E4	18.3±1.3
11	PE12_062	pbs	1	32.3066	77.4070	4011	3	2.65	30.078	0.257	0.9416	0	40.0993	0.3068	1615±50.1	8.25E5±2.67E4	19.9±1.2
12	PE12_063	pbs	1	32.3051	77.4072	3955	3	2.65	29.534	0.254	0.9520	0	40.4024	0.3068	1531±47.5	7.76E5±2.52E4	19.3±1.2
13	PE12_064	pbs	1	32.3083	77.4061	4072	3	2.65	31.700	0.269	0.9617	0	40.3521	0.3334	1554±48.3	8.57E5±2.79E4	19.7±1.2
14	PE12_056	pbs	1	32.4092	77.6498	4597	5	2.65	41.413	0.328	0.9815	0	40.0345	0.3062	1984±61.3	1.01E6±3.27E4	18.1±1.3
15	PE12_057	bos	1	32.4093	77.6515	4612	3	2.65	42.467	0.337	0.9831	0	19.3261	0.3072	1044±32.9	1.11E6±3.64E4	19.0±1.2
16	PE12_058	pbs	1	32.4085	77.6523	4608	3	2.65	42.079	0.334	0.9760	0	40.0975	0.3070	1782±55.2	9.11E5±2.83E4	16.2±1.2
17	PE13_02	pbs	1	32.4507	77.6801	4568	4	2.6	38.324	0.305	0.9114	0	16.7413	0.1519	1483±47.9	8.98E5±3.03E4	17.4±1.3
18	PE13_03	pbs	1	32.4540	77.6936	4184	4	2.6	33.755	0.281	0.9698	0	46.9540	0.1512	3857±120.0	8.29E5±2.70E4	18.3±1.3

[a] pbs = polished bedrock surface. bos = boulder on polished bedrock surface; all the tops were exposed at the surface

[b] Trust based on the quality of the sample and the possible earlier shielding due to e.g., till cover. 1 = very good. 0 = good.

[c] AMS ratios were normalised to 07KNSTD standard and corrected using full procedural blanks (n=5) with ^{10}Be/^{9}Be ratios ranging between 0.9±0.4 and 2.5±0.6 x 10^{-15}

[d] Production rate based on Lifton et al. [2014] as described in Borchers et al. [2016] and Marrero et al. [2016]

[e] Production rate calculated as described in Marrero et al. [2016] and Phillips et al. [2016]

[f] Uncertainties are reported in the 1σ confidence level

[g] Propagated uncertainties include error in the blank, carrier mass (1%), and counting statistics

[h] Propagated error in the model ages inclued a 6% uncertainty in the production rate of ^{10}Be and a 4% uncertainty in the ^{10}Be decay constant

2.4.2. Glacier reconstruction and deglaciation history

Based on the spatial distribution of our new and previously published exposure ages we were able to reconstruct the ice extent in the Chandra Valley between ∼20 ka and 15 ka. Our reconstruction suggests that during the LGM, the Chandra Valley was occupied by a glacier up to 1000 m thick (see Figure 2.2a), which we refer to as the Chandra Valley Glacier or CVG. Both our new ages and reconstruction confirm that glacial ice was crossing major drainage divides such as Kunzum La (∼600 m of ice thickness above the present drainage divide) eastward into the Spiti Valley [Saha et al., 2015] and the Rothang La (∼400 m ice thickness above the pass) southward into the Beas Valley, also supported by glacial striations [Owen et al., 2001] (Figure 2.1b). Although no terminal moraines of the former CVG are preserved, likely due to postglacial fluvial erosion in the narrow and deeply incised Chenab Valley, there is evidence that the glacier reached at least the village of Rape [Owen et al., 1997]. Our reconstruction of the ice surface suggests that the glacier extended even beyond Udaipur, reaching a length of ∼200 km. However, our reconstruction does not take into account the joining of the Bhaga arm (>100 km) [Owen et al., 1997, 2001] into the trunk valley glacier, which may have resulted in an even longer CVG.

Prior to 19–18 ka, the ice still occupied two drainage divides, but rapid melting had started (Figure 2.2). Between 17 and 15 ka, the trunk-valley glacier had retreated to a length of ∼70 km. After 15 ka, the main trunk valley must have been mostly ice-free, as organic sediments and peat started accumulating near Chandra Lake at ∼12.9±0.2 ka (radiocarbon age of 11.0±0.1 ka) [Owen et al., 1997; Rawat et al., 2015], which is close to the present terminus of the modern Samundar Tapu Glacier. At the Pleistocene-Holocene transition, tributary valley glaciers readvanced at least once into the trunk valley at around 13 ka (recalculated from Owen et al. [2001] and Murari et al. [2014]), but there exists no evidence of any trunk-valley glacier advance at this time or later. Well-preserved flood deposits in the Chandra River bed resulting from ice dam failure in the Upper Chandra Valley [Coxon et al., 1996; Owen et al., 2001] and preserved Holocene strath terraces [Adams et al., 2009] support this interpretation. Our reconstruction suggests a mean ice retreat rate of 37±11 m per year in the Chandra Valley beginning at the end of the LGM.

2.5. Discussion

Our new field and ^{10}Be exposure data and the reconstructed ice extent suggest that during the LGM the Chandra Valley and its tributaries were occupied by a ∼200 km long and ∼1 km thick glacier, supporting earlier observations by Owen et al. [1995, 1997]. Combining field observations of pronounced trimlines that separate ice-polished surfaces below from rugged bedrock ridges and hillslopes above and sample heights of our new ^{10}Be ages suggest that earlier advances during the last glacial cycle were either similar or not much more extensive than during the LGM. We favor this interpretation, given the excellent preservation of glacially polished surfaces at high elevation since ∼20 ka. Furthermore, our ice reconstruction and field evidence support significant overtopping (>500 m) into both the Spiti and Beas Valleys [Owen et al., 1995, 1997, 2001; Saha et al., 2015]. Thus, our reconstructed LGM glacier may not have corresponded to the most extensive glaciation during the last glacial cycle. Comparing

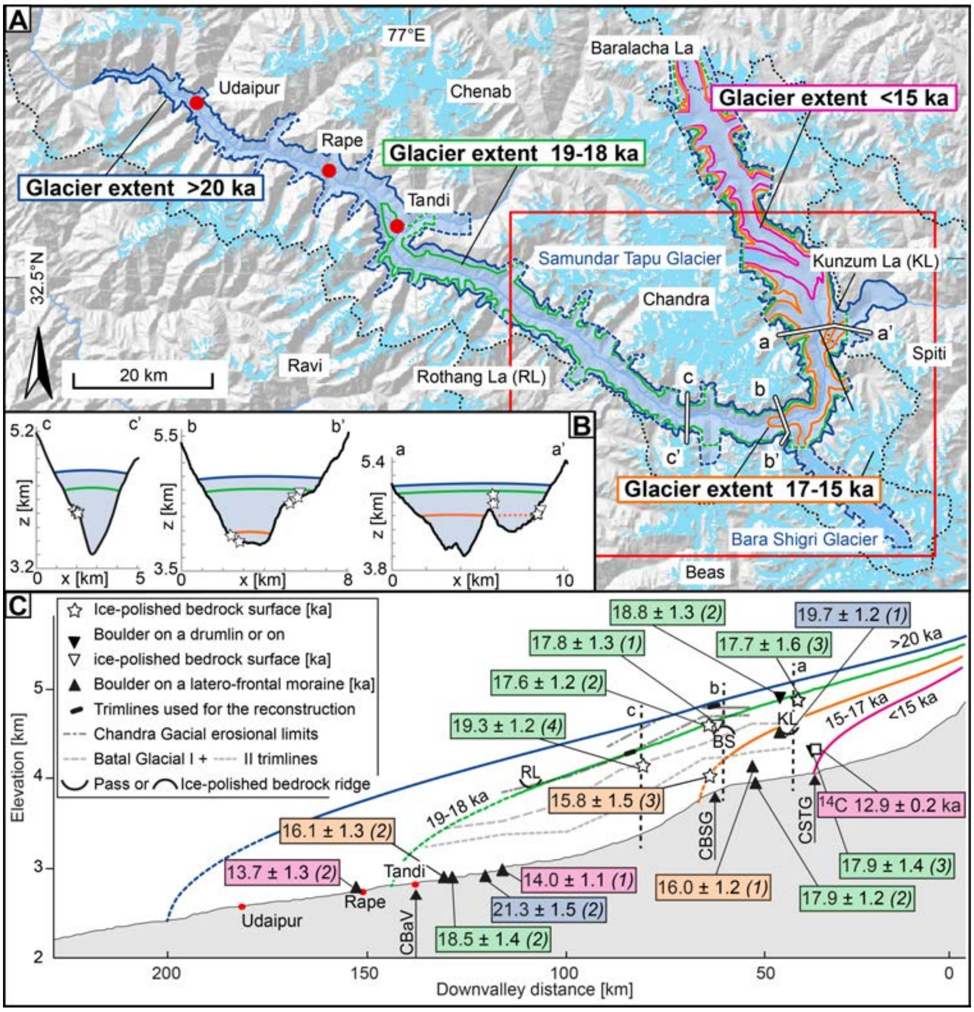

Figure 2.2: Chandra Valley glacier extent during LGM. (a) The Chandra Valley with reconstructed ice extents during the LGM and the subsequent deglaciation. Colors correspond to retreating positions in Figure 2.2c. White stars and white bottom up triangles indicate our sampling locations. Modern glaciers from Pfeffer et al. [2014] (b) Profiles a-a', b-b', and c-c' show sample locations above the present valley floor. The reconstructed ice thicknesses are shown according to colors in Figure 2.2c. We included samples from neighboring locations. (c) Retreat history of LGM glacier in the Chandra Valley from Udaipur to the Baralacha La from >20 ka to <15 ka, reconstructed by ^{10}Be data [Owen et al., 2001; this study] and ^{14}C data [Rawat et al., 2015]. Mean retreat ages are combined from different studies [Owen et al., 1996, 2001; this study] by the landform they stem from (in parentheses, the number of ages used for the mean age) and are color coded according to the retreating position they belong to. Broken lines in the reconstructions indicate the unclear terminus because of not taking the joining of the Bhaga Glacier and Bara Shigri Glacier into account. Confluence Chandra Valley with main tributary valleys or glaciers indicated by an arrow. CBaV = confluence with Bhaga Valley, CBSG = confluence with Bara Shigri Glacier, CSTG = confluence with Samundar Tapu Glacier.

our new data and earlier work [Owen et al., 1997, 2001] suggests that our reconstructed LGM ice extent is better correlated with the Chandra glacial stage than the Batal trimlines and, as supported by Murari et al.'s [2014] reanalysis, shifts the Batal glacial stage toward the LGM. More dedicated work near the identified trimlines is needed to resolve this issue.

Exposure ages of boulders and ice-polished bedrock surfaces from the same locations within the Chandra Valley are in good agreement with each other and show consistent ages between 19 and 16 ka with no systematic bias (Figure 2.1c). Because horizontal as well as near-vertical polished surfaces at locations 15–20 km apart from each other yield virtually identical ages, we suggest that in our study, cosmogenic nuclide inheritance is an issue for only one sample, a $\sim$33 ka boulder situated on a much younger surface. The similar ages between boulders and surfaces also suggest that glacial erosion has been sufficient to reset all surfaces and that postdepositional erosion of boulder surfaces is negligible.

The reconstructed CVG maintained its maximum vertical extent prior to or at 20 ka, during a weakened Indian Summer Monsoon (Figure 2.3b) [Herzschuh, 2006; Dutt et al., 2015]. After 20 ka, coeval with increasing temperatures, but also increasing monsoonal strength, the CVG rapidly receded. We thus argue that the retreat of the CVG was primarily driven by temperature; although tributary glaciers with shorter response times could still have reacted to changes in precipitation with minor readvances during a general phase of retreat [Scherler et al., 2011]. Such readvances of tributary glaciers are well documented by remnants of moraines and dated boulders on lateral and frontal moraines of the Kulti glacial stage [Owen et al., 2001].

The new scaling scheme by Lifton et al. [2014] affects estimated exposure ages significantly. In the Chandra Valley, recalculated LSD ages deviate from the exposure ages obtained from the CRONUS-Earth online calculator (v2.2) [Balco et al., 2008] by 25% and the calibration data set compiled by Heyman [2014] by 11%. Within the Himalaya the differences are 24% and 10%, respectively (see also Appendix A Data Set S2 and Figures S17 and S18). Differences within the scaling schemes remain at approximately 10%. In contrast to previous scaling models, the LSD scaling model uses analytical approximations to cosmic ray fluxes in the atmosphere and includes an updated geomagnetic and atmospheric framework [Lifton et al., 2014]. Although the lack of calibration sites within the Himalaya does not yet allow testing whether these improvements also result in more precise ages, a better understanding of the discrepancies between previous scaling models and the resulting bias [Lifton et al., 2014] suggests that some of the existing scaling models have deficiencies. In contrast to the Himalaya, however, the maximum increase of published middle- to high-latitude exposure ages in the Northern and Southern Hemispheres is merely 8% and some locations even show decreasing ages of the same order when using the LSD scaling model.

The new scaling scheme by Lifton et al. [2014] affects estimated exposure ages significantly. In the Chandra Valley, recalculated LSD ages deviate from the exposure ages obtained from the CRONUS-Earth online calculator [v2.2; Balco et al., 2008] by 25% and the calibration data set compiled by Heyman [2014] by 11%. Within the Himalaya the differences are 24% and 10%, respectively (see also Appendix A DS2, Fig. S17, S18). Differences within the scaling schemes remain at approximately 10%. In contrast to previous scaling models, the LSD scaling model uses analytical approximations to cosmic-ray fluxes in the atmosphere and includes an updated geomagnetic and atmospheric framework [Lifton

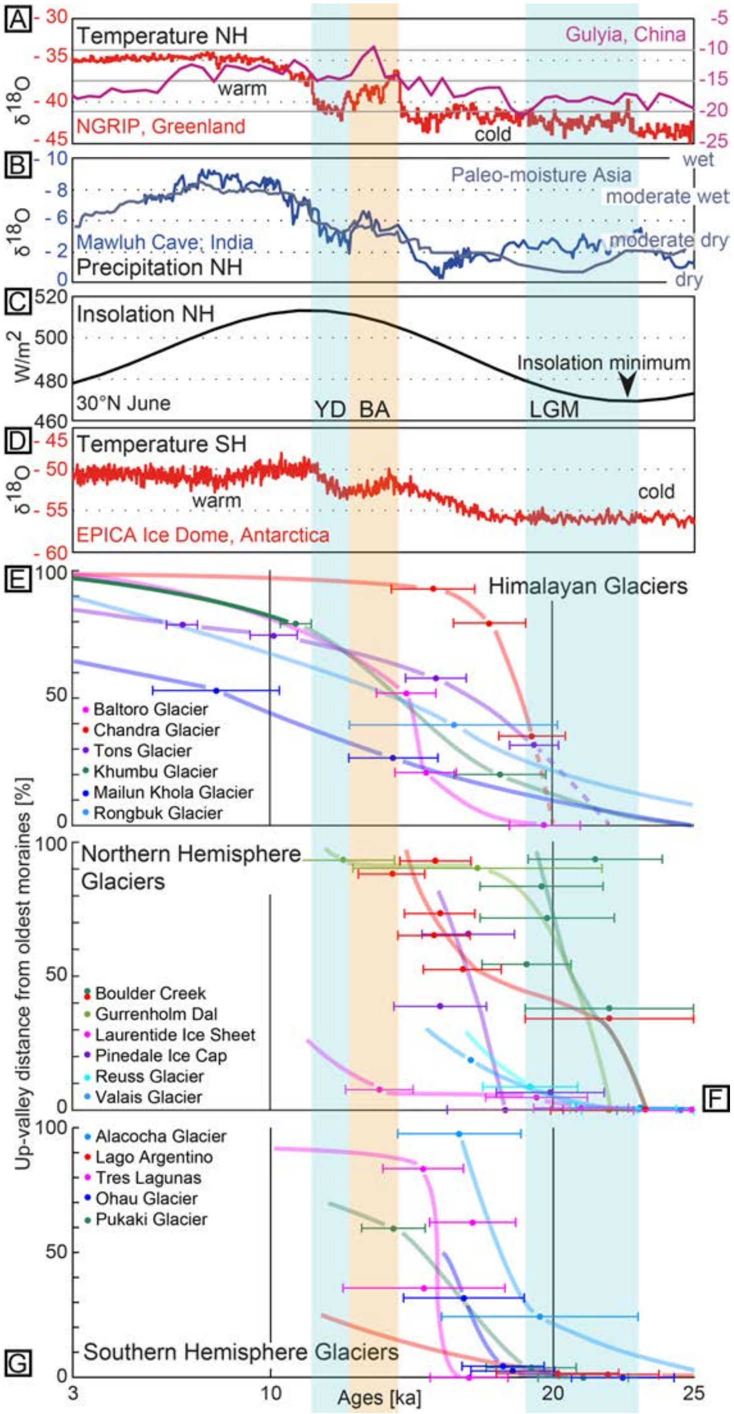

Figure 2.3: Comparison of deglaciation and climate proxies of the Northern and Southern Hemispheres. Glacier retreat indicated as up-valley distance in percent from location of oldest LGM record to the present-day glacier terminus or if vanished to the catchment boundary. Smooth line helps to identify the proposed long-term retreat, in which subtleties of minor glacial advances and retreats may be hidden. Exposure ages on the x-axis were recalculated using the CRONUS-Earth Web Calculator hosted at the University of Kansas. YD = Younger Dryas. BA = Bølling/Allerød. (a) NGRIP from Greenland project, Gulyia ice core, (b) Mamwluh Cave δ^{18}O record; effective moisture record (c) Northern insolation; (d) Epica ice dome; (e) Himalayan glacier retreat; (f) Northern Hemisphere glacier retreat; (g) Southern Hemisphere glacier retreat. Full reference list is provided in Appendix A.

et al., 2014]. Although the lack of calibration sites within the Himalaya does not yet allow testing whether these improvements also result in more precise ages, a better understanding of the discrepancies between previous scaling models and the resulting bias [Lifton et al., 2014] suggests that some of the existing scaling models have deficiencies. In contrast to the Himalaya, however, the maximum increase of published mid- to high-latitude exposure ages in the northern and southern hemispheres is merely 8% and some locations even show decreasing ages of the same order when using the LSD scaling model.

In light of our new observations and age constraints from the Chandra Valley and the older recalculated moraine ages, it is thus possible that many glacial advances, previously considered to be Late Glacial may be coeval with the LGM confirmed by Optically Stimulated Luminescence ages, e.g., in the Everest region [Richards et al., 2000; Owen et al., 2009]. Importantly, glaciation during the LGM and the pace of retreat in the Himalaya appear to have been more akin to midlatitude glaciers than previously thought and thus reflect hemisphere-scale processes rather than close regional links such as monsoonal forcing.

Acknowledgements

This research was funded by the graduate school GRK1364 (Shaping Earth's Surface in a Variable Environment) of the German Science Foundation to MS and DS (DFG, Deutsche Forschungsgemeinschaft, grant STR 373/19-2). RT is supported by DFG grant TH 1371/5-1 We are indebted to Dr. V. Jain and T. Tsering Longpo for logistical support during our fieldwork in India. We thank T. Schildgen and W. Düsing for help with sample preparation and discussions. We thank N. Lifton and L. Owen for constructive comments that improved the paper. Field photographs and additional information on calculation results are provided in the Supplementary Information of this manuscript

3 Ice dams, outburst floods, and glacial incision at the western margin of the Tibetan Plateau: A >100 kyr chronology from the Shyok Valley, Karakoram

Abstract

Some of the largest and most erosive floods on Earth result from the failure of glacial dams. While potentially cataclysmic ice dams are recognized to have repeatedly formed along ice-sheet margins, much less is known about the frequency and longevity of ice dams caused by mountain glaciers, and their impact on landscape evolution. Here we present field observations and results from cosmogenic nuclide dating that allow reconstructing a >100-kyr-long history of glacial damming in the Shyok Valley, eastern Karakoram (South Asia). Our field observations provide evidence that Asia's second-longest glacier, the Siachen, once extended for over 180 km and blocked the Shyok River during the penultimate glacial period, leading to upstream deposition of a more than 400-m-thick fluvio-lacustrine valley fill. ^{10}Be-depth profile modeling indicates that glacial damming ended with the onset of the Eemian interglacial and that the Shyok River subsequently incised the valley fill at an average rate of $\sim$4-7 m ka. Comparison with contemporary ice-dammed lakes in the Karakoram and elsewhere suggests recurring outburst floods during the aggradation period, while over 25 cycles of fining-upward lake deposits within the valley fill indicate impounding of floods from farther upstream. Despite prolonged damming, the net effect of this and probably earlier damming episodes by the Siachen Glacier is dominated by glacial erosion in excess of fluvial incision, as evidenced by a pronounced overdeepening that follows the glaciated valley reach. Strikingly similar overdeepened valleys at all major confluences of the Shyok and Indus Rivers with Karakoram tributaries indicate that glacial dams and subsequent outburst floods have been widespread and frequent in this region during the Quaternary. Our study suggests that the interaction of Karakoram glaciers with the Shyok and Indus Rivers promoted valley incision and headward erosion into the Icewestern margin of the Tibetan Plateau.

This chapter was published in
Geological Society of American Bulletin published online February 13, 2014
co–authored by Dirk Scherler, Henry Munack, Juergen Mey, Patricia Eugster, Hella Wittmann, Alexandru T. Codilean, Peter Kubik and Manfred R. Strecker

3.1. Introduction

The significance of rare but catastrophic events in Earth's history relative to steady but uniform processes is an important topic in the Earth sciences [e.g., Wolman and Miller, 1960]. Amongst the most impressive examples of catastrophic landscape-shaping events are dam-related megafloods, many of which appear to be intimately related to glacial climates and environments [e.g., Baker, 2002; O'Connor and Costa, 2010]. For example, the Missoula floods [northwestern U.S.; Bretz, 1969] and the flood that emptied Lake Agassiz [north-central North America; Barber et al., 1999] were due to failure of ice dams at the margins of the Laurentide ice sheet, and had far-reaching environmental consequences [e.g., Clarke et al., 2003]. In mountainous landscapes, and in response to present-day warming, moraine-dammed lakes frequently develop in front of retreating glaciers, and their catastrophic outbursts pose a significant hazard for downstream communities [e.g., Clague and Evans, 2000; Hewitt and Liu, 2010; Benn et al., 2012]. In contrast to moraine dammed lakes, ice-dammed lakes commonly form when a tributary glacier has detached from the main trunk glacier, and the resulting lakes commonly drain subglacially on a relatively frequent basis [Costa and Schuster, 1988]. Merzbacher Lake, for example, is an ice-dammed lake associated with the Inylchek Glacier, Tien Shan (Central Asia), which drains almost every summer [Ng and Liu, 2009]. More dangerous situations occur when the valley where damming occurs is largely ice free itself, so that a substantial amount of water can be impounded by the dam before failure [Costa and Schuster, 1988]. Clearly, the higher and more stable the dam and the shallower the dammed valley, the greater the ice-dammed lake volume and the potential flood discharge. Examples from the European Alps [Haeberli, 1983], Alaska [Post and Mayo, 1971], the Karakoram [South Asia; Hewitt and Liu, 2010], and many other regions worldwide [Costa and Schuster, 1988] underscore the importance of glacial dams on modulating flood frequency and peak discharges. Because these factors could be of primary importance for the long-term efficiency of sediment transport and bedrock incision [e.g., Wolman and Miller, 1960; Snyder et al., 2003; Tucker, 2004; Lague et al., 2005], glacial dams may have a far greater impact on landscape evolution in mountainous regions than their areal footprint and representation in the depositional record would suggest.

Depositional evidence for very large (up to 2835 km^2) glacially dammed Holocene lakes upstream of the Tsangpo River gorge, on the southeastern edge of the Tibetan Plateau, led Montgomery et al. [2004] to suggest that catastrophic failure of these lakes may have resulted in the most erosive events in recent Earth history. Furthermore, Korup and Montgomery [2008] argued that repeated glacial damming of major rivers in this region substantially impeded headward river incision into the Tibetan Plateau and has helped preserve a distinct plateau edge through protracted sediment accumulation and storage upstream from the barriers [e.g., Montgomery et al., 2004]. These studies bring glacial dams to the forefront of processes shaping the edges of Cenozoic orogenic plateaus that are impacted by glacial climates. However, the longevity of glacier dams and the damming frequency are generally not well constrained [Korup and Tweed, 2007], which makes assessing their geomorphic relevance in the long term difficult. Although historically active glacier dams tend to fail frequently [Costa and Schuster, 1988], examples of larger glacier dams are rare and their hydrology may be more complex, potentially rendering them more stable. We address these issues in our study of one of the most impressive examples of Pleistocene glacial damming in the Karakoram and demonstrate that ice dams and associated outburst floods were likely frequent and important processes in the Quaternary evolution of the Shyok and Indus Valleys.

3.1.1. Glacier Dams in the Karakoram Mountains

The Karakoram Mountains, at the northwestern edge of the Tibetan Plateau, have the greatest concentration of glaciers in the Himalayas and feature some of the longest glaciers in Central Asia (Figure 3.1). They also host one of the world's largest assemblages of presently or historically active glacier dams, many of which have failed catastrophically [Cunningham, 1854; Mason, 1929; Gunn et al., 1930; Hewitt, 1982; Korup et al., 2010]. The historically most devastating floods were related to lakes that formed in valleys blocked by glaciers coming from tributaries [Hewitt and Liu, 2010]. At present, there are more than 90 reports of ice dam related outburst floods that occurred during the past 200 years in rivers draining the Karakoram Mountains [Hewitt and Liu, 2010]. The Kyagar Glacier, for example, is blocking the upper Shaksgam River (Figure 3.1), a tributary of the Yarkand River that repeatedly forms an up to 7-km-long lake (Figure 3.2). During the past 50 years, this lake drained at least 19 times catastrophically, resulting in 7 major or destructive floods. Two times, peak discharges measured at Kaqun, China, located some 500 km downstream from the ice dam, exceeded 6000 m^3/s [Hewitt and Liu, 2010]. In other places without direct flood or lake reports, strandlines behind glaciers can be seen in satellite images [e.g., Google Earth http://www.google.com/earth/], and provide indirect evidence for the existence of ice-dammed lakes in the past.

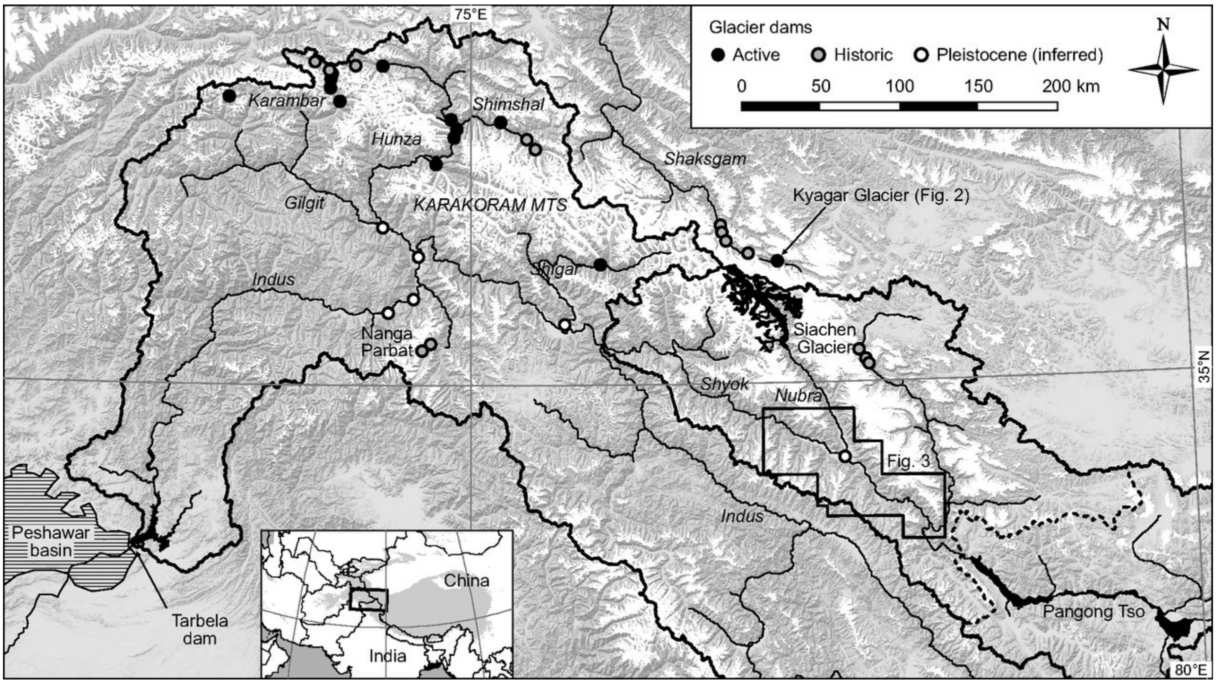

Figure 3.1: Study area in the eastern Karakoram Mountains (South Asia). Thick bold lines indicate the outline of the Shyok and Indus catchments. Dashed line in the Shyok catchment delimits the currently endorheic area, draining to Pangong Tso. River names are given in italic font. Glacier dams after Hewitt [1982], Dortch et al. [2010], Seong et al. [2008], Phillips et al. [2000], and inspection of satellite images. Active glacier dams are defined as places where a glacier confines the flood plain of a river to a width that is smaller than up- or downstream of the confinement. White areas are present-day glaciers after Arendt et al. [2012].

Several Karakoram valleys stand out with an unusual abundance of active or historic glacier dams: the Shaksgam, Shimshal, Karambar, and uppermost Shyok. All of these valleys are parallel to mountain ranges that host several large, ice-covered tributaries. On a larger spatial and longer temporal scale, the same applies to the entire Karakoram and its main drainages. While the aforementioned valleys have been ice covered, glacial morphology and deposits in the Gilgit, Hunza, Shigar, and Nubra Valleys (Figure 3.1) indicate that Pleistocene glaciers reached the Indus and Shyok Valleys [Derbyshire et al., 1984; Shroder et al., 1989; Phillips et al., 2000; Owen et al., 2006; Seong et al., 2007; Dortch et al., 2010], where they probably formed ice-dammed lakes. However, distinguishing between fluvio-lacustrine deposits related to glacial or landslide processes can be difficult, and it has been argued that many previously identified moraines and ice damĐrelated lake deposits are due to large rock avalanches [Hewitt, 1999; Hewitt et al., 2011]. Here, we report field observations that document one of the largest known glacier dams in the Karakoram. Cosmogenic nuclide exposure dating together with published data allow reconstruction of a >100-k.y.-long history of glacial damming, and associated upstream aggradation and subsequent incision in the upper Shyok River.

3.2. The Study Area

The Shyok River is the largest tributary of the upper Indus River and drains much of the high and rugged eastern Karakoram, the Transhimalaya, and low-relief areas on the western Tibetan Plateau (Figure 3.1). Its drainage area is currently ∼15,000 km^2, but may have been ∼80,000 km^2 when Lake Pangong Tso spilled over its northwestern edge and was hydrologically connected with the Shyok River in the early Holocene [Gasse et al., 1996] and probably during earlier times in the last glacial cycle [Shi et al., 2001]. In the heart of the eastern Karakoram lies the presently 70-km-long Siachen Glacier. Its terminus is at 3600 m above sea level (asl) and sources the Nubra River, which flows ∼80 km southeast along the Karakoram fault before it enters the Shyok suture zone and joins the WNW-flowing Shyok River [Rolland et al., 2000]. From the glacier terminus down to ∼3000 m asl, the Nubra and Shyok Valleys are wide and alluviated, with widths that reach >5 km at their confluence. At the mouths of most of their tributaries, large alluvial fans extend far into the valley and testify to a period of aggradation that appears to be still ongoing (Figure 3.3A) [Drew, 1873]. Active aggradation is also evident at the Shyok-Nubra confluence, where the Shyok River is currently building a fan that forces the Nubra River to the downstream side of the valley (Figure 3.3A).

Near the Shyok-Nubra confluence, well preserved wave-cut lake shorelines occur up to ∼150 m above the present-day valley bottom, and have been related to a lake that formed due to Siachen Glacier's damming of the Shyok River [Dortch et al., 2010]. Although the shorelines have not been dated chronometrically, based on regional stratigraphic and geomorphic relationships their formation has been bracketed by dated moraines to between 41±2 ka and 81±6 ka [Dortch et al., 2010]. Furthermore, till-mantled hillslopes that occur up to ∼900 m above the valley floor indicate that the Siachen Glacier may once have been much thicker, but these deposits have not been dated so far. In contrast, Phartiyal et al. [2005] assigned lake sediments at various elevations near the confluence to a phase when an extensive paleolake stretched for ∼100 km along the Shyok Valley and ∼30 km upstream into the Nubra Valley. Their interpretation, the stratigraphic relationship with dated moraines, and calibrated ^{14}C ages from these lake sediments of

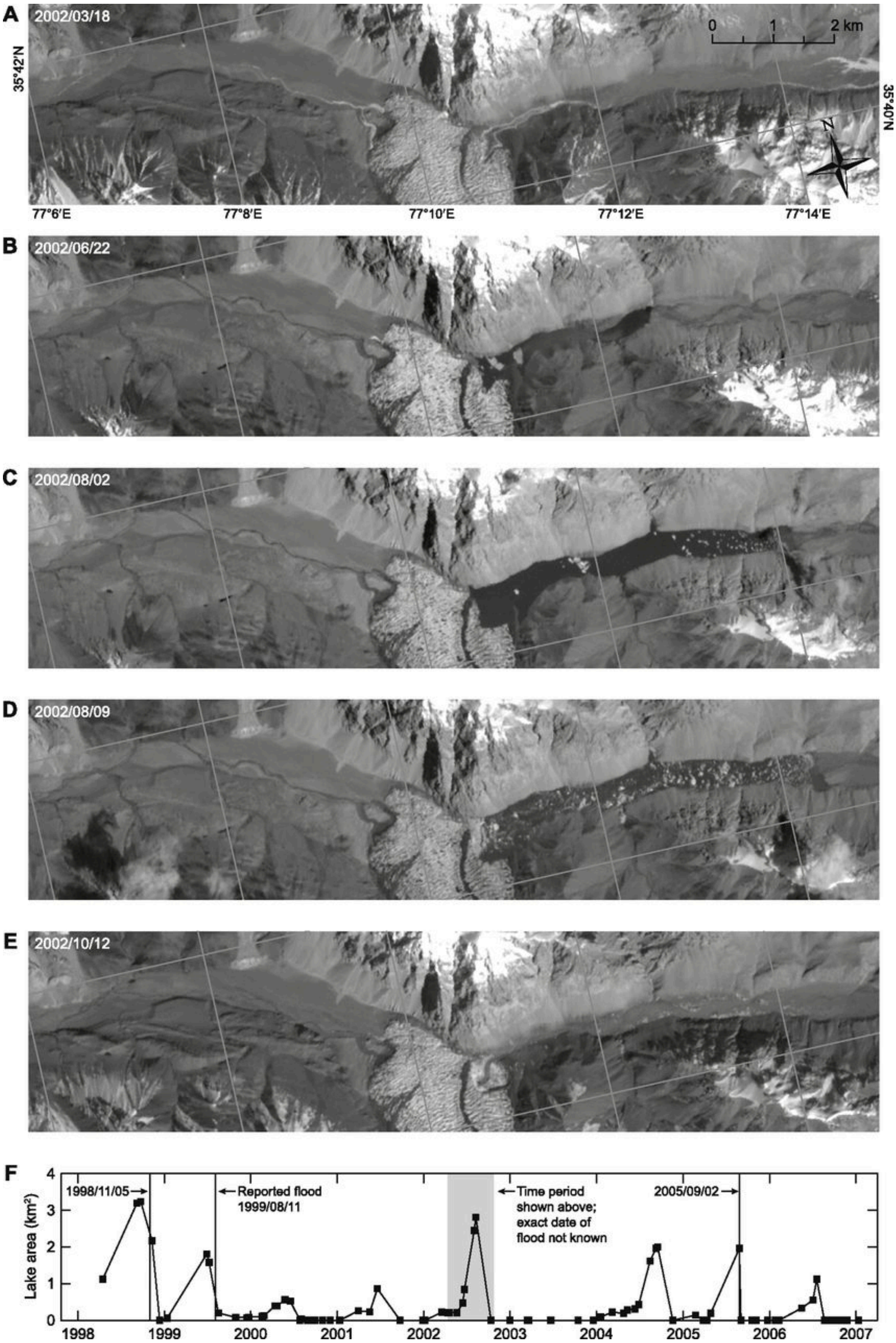

Figure 3.2: Kyagar Glacier terminus and lake in the upper Shaksgam River. (AE) Landsat ETM+ satellite images (band 8), acquired March to October 2002. (F) Evolution of lake area obtained from Landsat TM and ETM+ satellite images, together with reported flood dates from Hewitt and Liu [2010]. Estimated uncertainty in lake area is ∼15%, and up to ∼30% after 31 May 2003, when the scan line corrector instrument of the ETM sensor failed.

ca. 25±27 ka [Phartiyal and Sharma, 2009] are in conflict with the glacial-damming hypothesis and merit further investigation. We combine the previous results by Dortch et al. [2010] with our own field data and cosmogenic nuclide dating to decipher the glacial damming history at the Shyok-Nubra confluence.

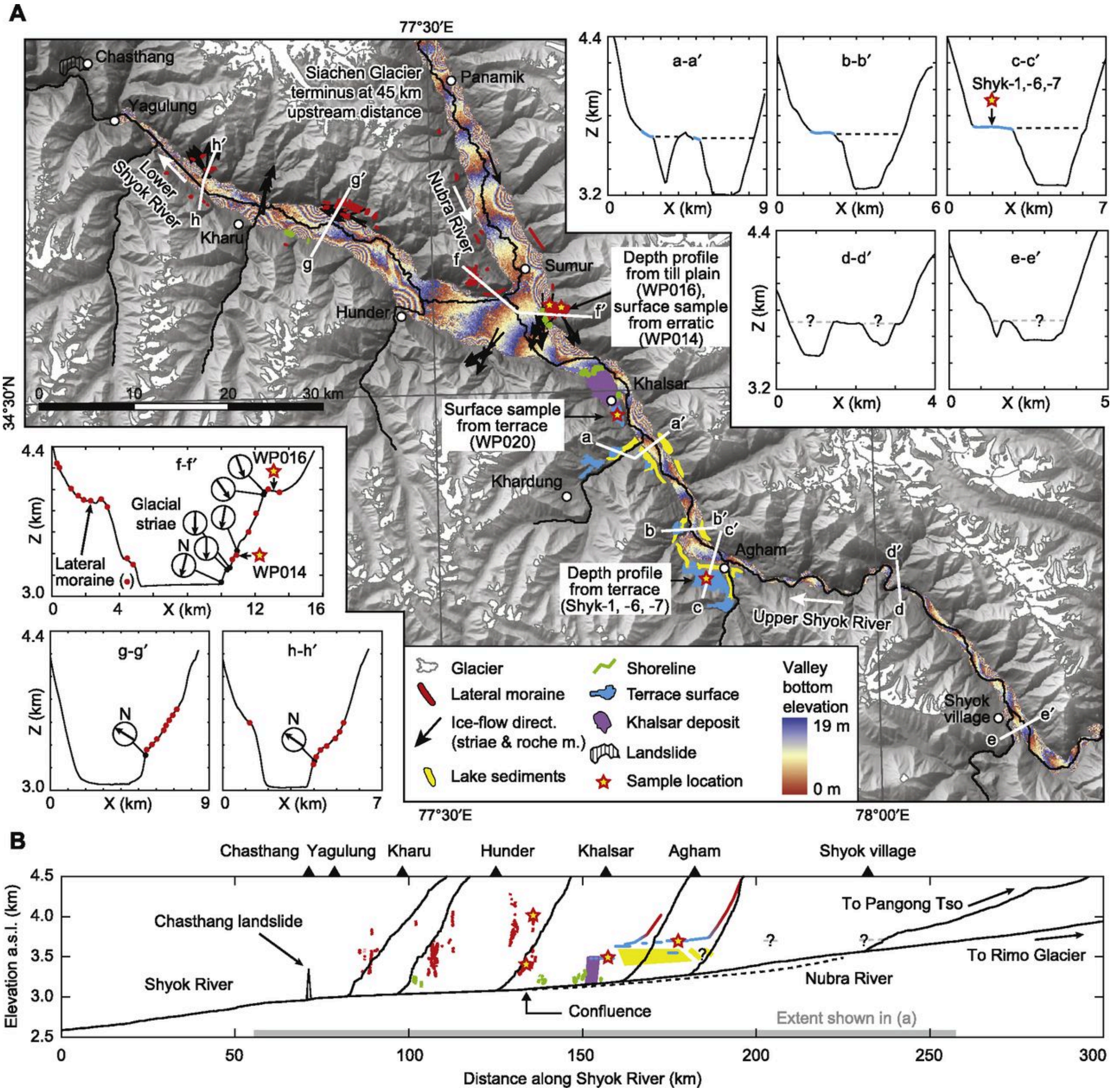

Figure 3.3: Geomorphology of the Shyok-Nubra confluence. (A) Hillshade image with glaciers (white), major depositional landforms (colored polygons), ice-flow directions from glacial striae and roches moutonnées (black arrows), sample locations (stars), and traces of surface elevation profiles (a-a' through h-h'). Dashed lines in profiles a-a' through e-e' give top of reconstructed valley fill. Elevations of Shyok and Nubra valley bottoms are colored, repeating every 20 m to highlight low gradients and alluvial fans. White arrows give flow direction of rivers. (B) Longitudinal profiles of the Shyok River and major tributaries (solid black lines); the Nubra River is dashed (a.s.l. above sea level). Colored lines and polygons give moraine ridges (red), terrace surfaces (blue), shorelines (green), and lake deposits (yellow). Triangle near Chasthang indicates a landslide.

3.3. Methods

3.3.1. Mapping and Remote-Sensing Analysis

We conducted field work in the Shyok Valley between the villages of Chasthang and Agham, and in the Nubra Valley up to the village of Panamik, where we mapped Quaternary deposits and landforms and collected samples for cosmogenic nuclide surface-exposure dating. Because there have been controversies about inferred glacial origins of Quaternary deposits in several parts of the Karakoram [Hewitt, 1999; Hewitt et al., 2011], we employed a conservative approach of mapping glacial deposits and looked specifically for glacial striations and their association with lateral moraine ridges. Spatial references were obtained using a handheld GPS and topographic maps. We supplemented our field mapping with analysis of optical satellite imagery and 90-m-resolution Shuttle Radar Topography Mission digital elevation models (DEM). Specifically, we identified and mapped terraces and moraines in areas we could not access in the field, e.g., farther upstream from Agham and on steep hillslopes, based on surface morphology, extent, appearance in high-resolution optical imagery in Google Earth, and similarity with landforms that we mapped in the field. We again used the same cautious mapping approach in the sense that any landform identified in this way would have to be between landforms of the same type that we mapped in the field.

3.3.2. Surface-Exposure Dating

We dated aggradation surfaces in the study area using in situ produced cosmogenic nuclides. Specifically, we measured ^{10}Be in amalgamated samples from two depth profiles and at one location from a surface sample alone. Each sample consisted of ∼30-40 well-rounded, granitic and gneissic pebbles of ∼5 cm diameter or equally sized chunks from slightly larger cobbles (<10 cm), which were taken from the same depth (±5 cm) or the surface. After standard physical and chemical preparatory steps [e.g., Kohl and Nishiizumi, 1992; von Blanckenburg et al., 2004], we measured the in situ produced ^{10}Be/^{9}Be ratios in our samples at the Ion Beam Facility of the ETH Zuerich, Switzerland, and the Centre for Accelerator Mass Spectrometry of the University of Cologne [CologneAMS; Dewald et al., 2013], Germany (Table 3.1).

We calculated exposure ages from ^{10}Be concentrations based on a time-dependent version of the production rate scaling model by Lal [1991], updated by Stone [2000], as provided in the CRONUS online calculator [v. 2.2; Balco et al., 2008; denoted there by Lm], and using a ^{10}Be half-life of 1.387±0.016 m.y. [Chmeleff et al., 2010; Korschinek et al., 2010]. At two sites, we modeled the total in situ ^{10}Be production as due to the fractional production by neutron spallation (n, 97.85 %), slow muons (m_1, 1.5%) and fast muons (m_2, 0.65%), with attenuation lengths of 160 g cm^{-2} (Λ_n), 1500 g cm^{-2} (Λm_1), and 5300 g cm^{-2} (Λm_2), respectively [Braucher et al., 2003, 2009]:

$$
\begin{aligned}
C(x,t) = \frac{P_0 n}{\varepsilon/\Lambda_n + \lambda}\, e^{(-x/\Lambda_n)} \left[1\, e^{-t(\varepsilon/\Lambda_n+\lambda)} \right] \\
+ \\
\frac{P_0 m_1}{\varepsilon/\Lambda_{m_1} + \lambda}\, e^{(-x/\Lambda_{m_1})} \left[1 - e^{t(\varepsilon/\Lambda_{m_1}+\lambda)} \right] \\
+ \\
\frac{P_0 m_2}{\varepsilon/\Lambda_{m_2} + \lambda}\, e^{(-x/\Lambda_{m_2})} \left[1 - e^{-t(\varepsilon/\Lambda_{m_2}+\lambda)} \right],
\end{aligned}
\tag{3.1}
$$

where C is the ^{10}Be concentration [atoms g^{-1}], x is depth below the surface [cm], t is the exposure time [yr], P_0 is the surface production rate [atoms g^{-1} yr^{-1}], ε is the erosion rate [g cm^{-2} yr^{-1}], and Λ is the decay constant. Note that ε used here reflects an erosion rate given in cm yr^{-1} multiplied by density, ρ [g cm^{-3}]. We derived the scalar surface production rate, P_0, by averaging the decay-weighted, time-dependent instantaneous surface production rates, $P_{0,\,i}$, over the model time according to:

$$
P_0 = \frac{\sum P_{0,i}\, e^{-\lambda t_i}}{\sum e^{-\lambda t_i}}. \tag{3.2}
$$

where the subscript i refers to the discrete times for which production rates are calculated, typically at increments of 1 k.y. Following Braucher et al. [2009] we obtained best-fit results with an estimated uncertainty for our depth-profile data using a Monte Carlo inversion method. For each depth profile, we randomly sampled 200 concentration profiles from our n samples, which lie within the range defined by the measured concentrations (Ci) plus/minus their uncertainties ($2\sigma_i$) and obtained the best-fit solution by minimizing the chi-squared misfit (χ^2) between the measured and modeled concentrations (Equation 3.1) for given exposure age-erosion rate or exposure age-density pairs, with the other parameters predefined, e.g., inheritance (C_0), density, erosion rate:

$$
\chi^2 = \sum_{i=1}^{n} \left(\frac{C_i - C(x_i, t, \rho, \varepsilon, C_0)}{2\sigma_i} \right)^2. \tag{3.3}
$$

We emphasize that ^{10}Be production rates are poorly constrained in the study area and that instantaneous production rates, calculated with different existing scaling models, vary by up to 60% during the past 100 k.y. [e.g., Balco et al., 2008]. The absolute ages presented in this study are therefore subject to greater uncertainty, with respect to chronologies obtained with other dating methods, than indicated by the analytical and modeling uncertainties that we provide. To allow comparison with our new ages, we recalculated the exposure ages published by Dortch et al. [2010] based on the same production-rate scaling model used for our samples and refer to the recalculated ages from here on and in all of our figures. Additional details on the ^{10}Be-depth profile modeling, the recalculated published ^{10}Be exposure ages, and data on glacial striation measurements are located in the online supplemental material (Appendix B).

3.4. Results

3.4.1. Fluvial and Lacustrine Deposits in the Upper Shyok Valley

The upper Shyok River, i.e., upstream of the Nubra confluence, flows mostly on >1-km wide alluviated valley bottoms, but approaches bedrock between the villages of Agham and Shyok, where the valley is more confined and steeper (Figure 3.3). Where valley bottoms are wide, the valley is riddled with remnants of an up to ∼400-m-thick sequence of fluvio-lacustrine deposits that are frequently topped by flat terrace surfaces. These terrace surfaces have top elevations between ∼3600 and ∼3700 m asl and can be traced >20 km along the upper Shyok Valley, and several kilometers into major tributaries (Figures 3.4A, 3.4B). Between Khalsar and Agham the top elevation drops ∼5.5 m per kilometer, which is similar to the present-day gradient of the Shyok River. We could not access areas much farther upstream from Agham, but subhorizontal surfaces, which could correspond to fill or strath terraces, can be identified in the DEM (Figure 3.3A).

Where accessible, the upper and lower parts of the valley fill are dominated by relatively homogenous cobble and gravel deposits with occasional boulders and sand lenses typical for a braided-river depositional environment (Figure 3.4A). The middle part comprises a ∼150-200-m-thick lacustrine unit (3.4B) that is exposed between Agham (∼3450-3600 m asl) and Khalsar (∼3400-3600 m asl) and easily visible on satellite images. No comparable lakesediment outcrops were seen farther upstream in satellite images or farther downstream in the field (Figure 3.3A). Within the tributary joining the Shyok at profile a-a’ in Figure 3A, the lake deposits pinch out at a distance of ∼4.5 km from the Shyok, whereas their extent appears to be more restricted in the tributary near Agham. In these two tributaries, the fluvio-lacustrine valley fills grade upstream into glacial facies at a distance of ∼10 and 7 km from the Shyok, respectively. At a well-exposed lake-sediment outcrop near Agham, we observed 25 upward-fining units, with a few more obscured by colluvium (Figure 3.4C). In this location, each unit is∼1-5 m thick and starts with rippled fine sands at the base that grade into massive silts, and finally laminated silty clays at the top. Throughout these deposits, isolated small dropstones can be found. Samples that were taken from these lake sediments (Figures 3.4C, 3.5) are devoid of any ostracods [S. Mischke, 2012, personal commun.], and unfortunately not suitable for optically stimulated luminescence (OSL) dating due to signal saturation [J. Bloethe, 2012, personal commun.].

3.4.2. The Khalsar Deposit

A conspicuous deposit occupies ∼10 km^2 in the upper Shyok Valley near Khalsar village, close to the Shyok-Nubra confluence (Figure 3.6; termed here the Khalsar deposit). At the downstream end of this deposit, well-developed lake shorelines that have been related to glacial damming at the Shyok-Nubra confluence occur up to an elevation of 3250 m asl, that is, ∼100 m above the present-day river, and less well developed shorelines occur up to ∼200 m above the present-day river [Dortch et al., 2010]. The origin and timing of deposition is important because of this stratigraphic relationship, but has been debated in previous studies. Pant et al. [2005] and Dortch et al. [2010] interpreted the Khalsar deposit

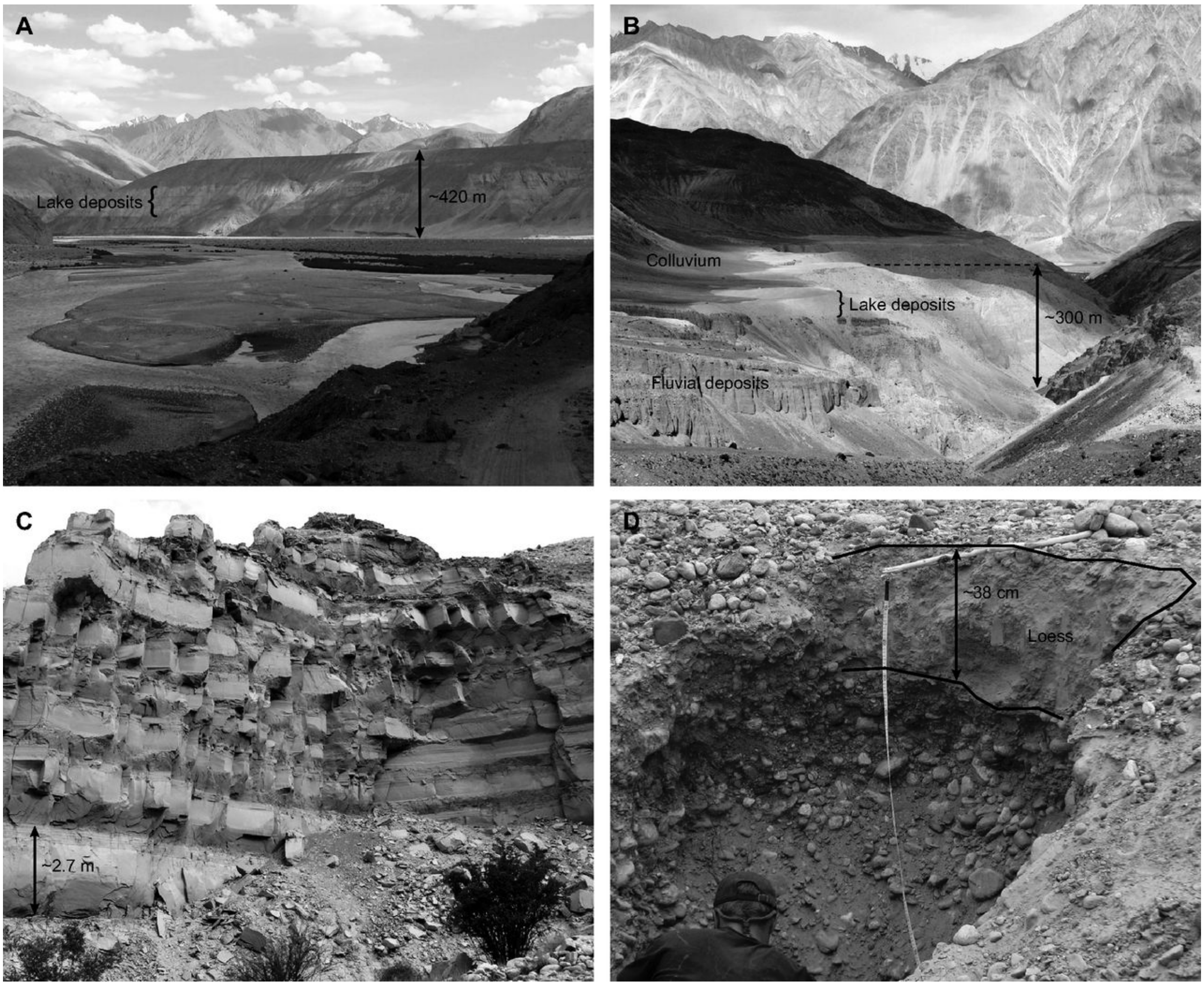

Figure 3.4: Field photographs of fluvial-lacustrine valley fill in the upper Shyok Valley. (A) Fill terrace near Agham village. Note bright colored lake sediments. View is southeast, upstream the Shyok River. (B) Valley fill in a tributary near Khardung. View is north, toward confluence with the Shyok River. (C) Lake sediments exposed at a terrace near Agham. Height of outcrop is ∼16 m. Note cyclic repetition of dark to light-colored sediments. (D) Pit for sampling ^{10}Be-depth profile on a terrace near Agham. Note fine-grained loess deposits between desert pavement and fluvial cobbles.

as a moraine and therefore as evidence for glaciers in the upper Shyok Valley reaching all the way to the confluence. We agree with Phartiyal et al. [2005], interpreting it as a landslide deposit, based on several criteria. Although most of the deposit is currently inaccessible for civilians, accessible outcrops near its downstream limit, and close to the present valley bottom, reveal a disturbed contact between monomict, intensely fragmented granitic material and convoluted fluvial cobble beds below, which resemble present-day Shyok cobbles (Figure 3.6, inset). A rock avalanche is furthermore corroborated by a large (>4 m) boulder with extension fractures that radiate from a point on its upper end and create a jigsaw pattern (Figure 3.6, inset), suggesting a large and sudden in situ loading, as well as clastic dikes of sand and pebbles that intrude several meters into the overlying material [cf. Shreve, 1987; Owen et al., 2008]. The tributary coming from the south makes a 1.8 km southeast, i.e., upstream, detour around most of the deposit before it flows northeast again and joins the northwest-flowing Shyok (Figure 3.6). The tributary dissects the deposit at Khalsar village and exposes a sharp basal contact with an up to 300-m-thick section of underlying fluvial cobbles that are identical to those previously described and in continuity with a terrace surface extending another $\sim$1 km upstream at an elevation of $\sim$3480 m asl. On the southwestern edge of the terrace surface, perched between the southern hillslopes and the monomict granitic deposits, are a few meters of exposed lake sediments. Our observations suggest that at least part of the deposit, if not all, is related to a rock avalanche that originated from the northern granitic valley walls and fell partly onto a fluvial terrace, causing upstream deflection and ponding of the tributary. We note that we found no indicators in the field or on satellite images that the $\sim$1.5 km offset of the tributary could be due to movement on a previously unrecognized strand of the Karakoram fault, which traces the northern side of the upper Shyok Valley in this location [Phillips, 2008].

3.4.3. Glacial Marks and Deposits in the Nubra and Lower Shyok Valleys

In the lower Shyok Valley, i.e., downstream of the Nubra confluence, terraces associated with fluvio-lacustrine deposits are absent. Instead, like in the adjoining Nubra Valley [Dortch et al., 2010], hillslopes are commonly mantled with glacial deposits that mostly consist of rounded to sub-angular, unsorted allochthonous boulders in a sand-silt matrix (Figure 3.7). These deposits are commonly capped with long, valley-parallel lateral moraines that occur on both sides of the Nubra confluence up to >4000 m asl (Figures 3.3A,3.7). At three locations in the lower Shyok Valley, where hillslope angles are relatively gentle, abundant and closely spaced lateral moraines can be observed (Figure 3.3A, profiles f-f', g-g', h-h'). The elevation of lateral moraines in the lower Shyok Valley systematically decreases downstream, for both individual moraines as well as sets of moraines (Figure 3.3B). Glacial striations and roches moutonnées are widespread in the Nubra and lower Shyok Valleys and consistently indicate down-valley ice movement (Figure 3.3A). On some bedrock ridges in front of confluences in the lower Shyok Valley we found striations documenting ice transport toward the tributaries. Yet, within these tributaries, close to their mouths, we also observed remnants of valley fills that appear to be of fluvial origin. Farther up in these tributaries, tills and moraines are widespread.

At the lower end of our study area, near the village of Yagulung, two large and smooth whaleback-shaped bedrock bumps protrude up to 200 m over the valley floor. These features closely resemble roches moutonnées, but we did not find any glacial striations on them. Yet farther downstream, at the

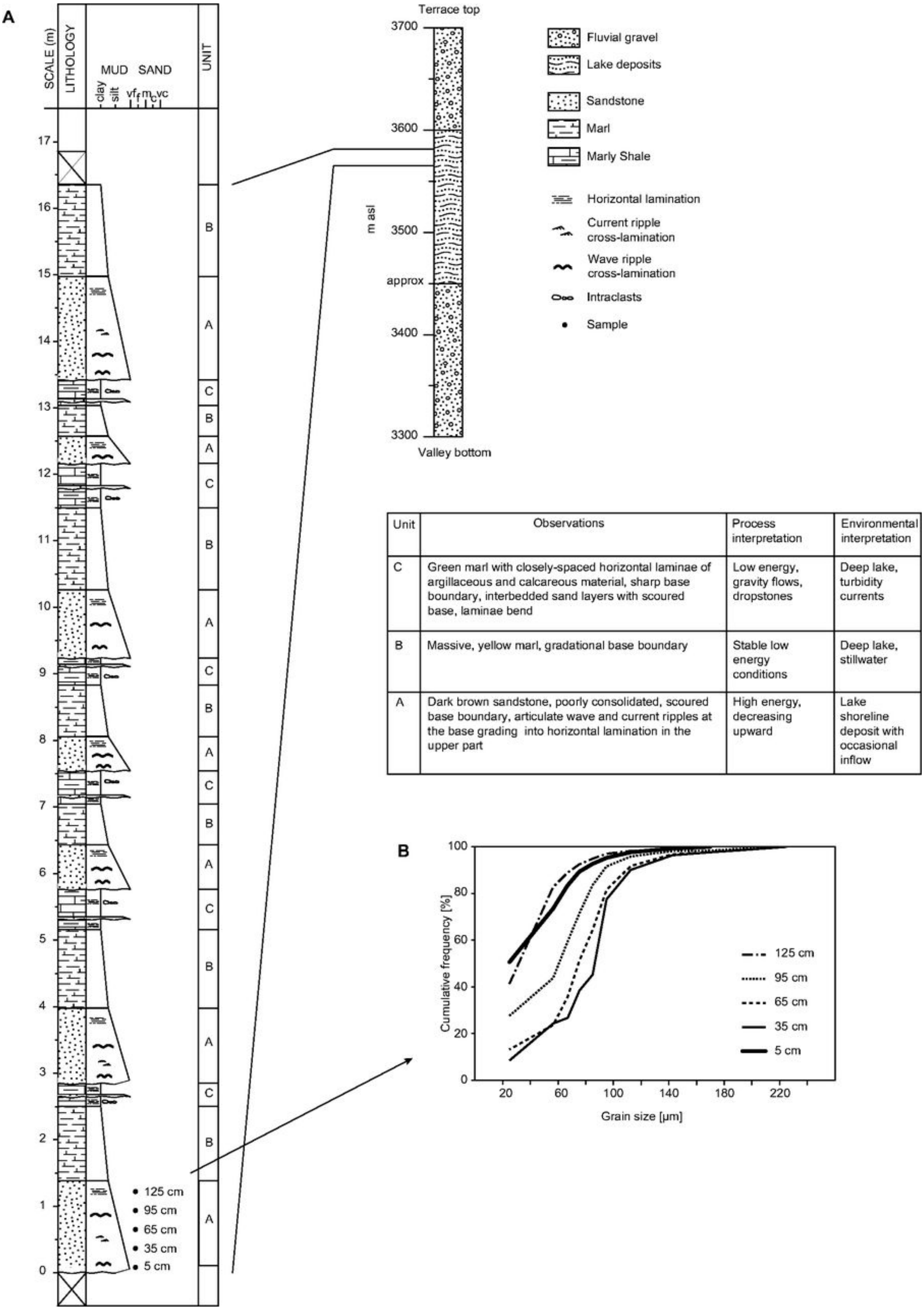

Unit	Observations	Process interpretation	Environmental interpretation
C	Green marl with closely-spaced horizontal laminae of argillaceous and calcareous material, sharp base boundary, interbedded sand layers with scoured base, laminae bend	Low energy, gravity flows, dropstones	Deep lake, turbidity currents
B	Massive, yellow marl, gradational base boundary	Stable low energy conditions	Deep lake, stillwater
A	Dark brown sandstone, poorly consolidated, scoured base boundary, articulate wave and current ripples at the base grading into horizontal lamination in the upper part	High energy, decreasing upward	Lake shoreline deposit with occasional inflow

Figure 3.5: Stratigraphic column of valley fill exposed at the terrace near Agham village (asl—above sea level). Lower-right plot shows cumulative grain-size distributions from lake sediment samples indicated at the lower end of the stratigraphic column.

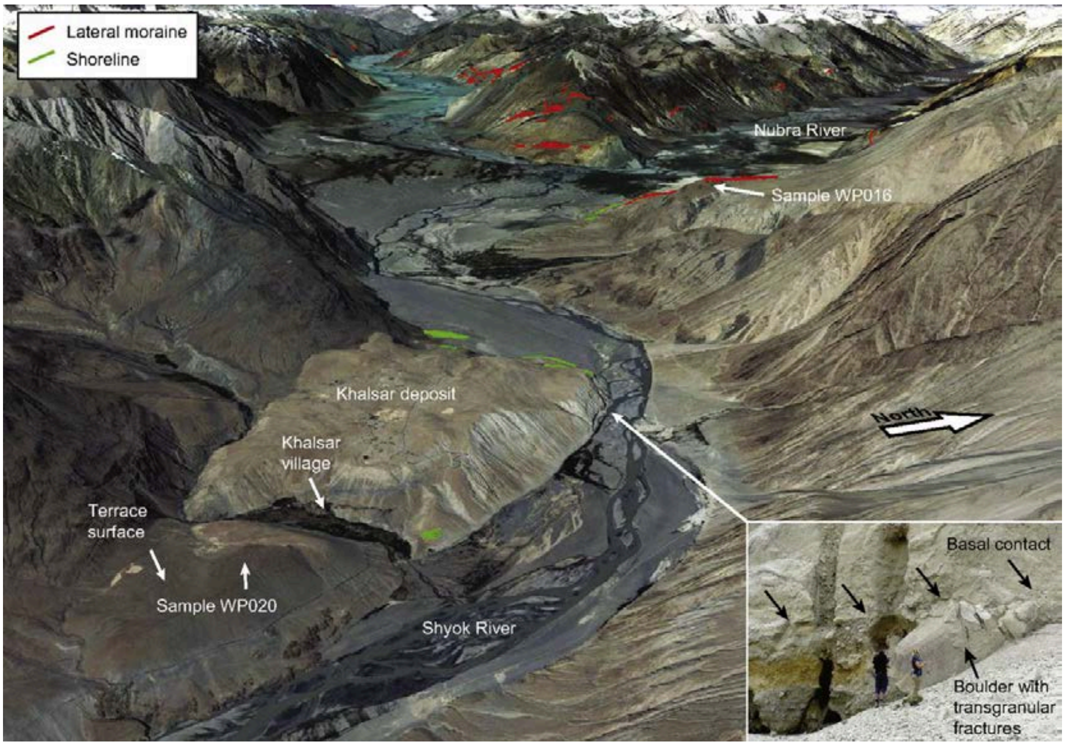

Figure 3.6: Perspective aerial Nubra River view of the Shyok Valley near Khalsar [Google Earth, http://www.google.com/earth/]. View to the northwest, downstream the Shyok Valley. Nubra Valley joins from the upper right corner. Field of view at the bottom of the figure is ∼ 5 km. Inset photo shows basal contact of granitic fragmented material (top) with fluvial cobbles and boulders (below). Note the >4-m-tall boulder with transgranular extension fractures radiating from a point on its upper end.

village of Chastang (34.822°N, 77.081°E), a landslide deposit with surface elevations between 3200 and 3500 m asl abuts the river (Figure 3.3). The northern hillslope above this landslide deposit appears to be still in motion. Apart from the well-developed shorelines near the confluence (Figure 3.7; Dortch et al., 2010], we also found shorelines between Kharu and Hunder, occurring up to an elevation of ∼3250 m asl, that is, ∼200 m above the presentday river (Figure 3.8). These shorelines and those at the confluence are characterized by staircase morphologies with rhythmic downhill variations in slope angle and grain size that can be laterally traced and appear perfectly horizontal.

3.4.4. Surface-Exposure Dating

We collected five samples along a depth profile that extends from the surface to a depth of 100 cm that we obtained from a relatively flat till plain found at ∼4000 m asl at the NubraShyok confluence (Figure 3.3A, site WP016). Because we were not able to measure densities in the field, and because density can vary spatially in tills over very short distances depending on the presence of boulders or fines, we applied Equations 3.1 and 3.2 and the previously described model with erosion rate and exposure age as free parameters and tested results for average densities of 1.9, 2.0, and 2.1 g cm^{-3} (Figure B.2). These densities are within the range of dry bulk densities (average ∼2.0 g cm^{-3}) that have been measured in tills from the UK [Fülöp, 2012] and Minnesota, South Dakota, and Iowa [http://depts.washington.edu/cosmolab/projects/summary_density.html] [Balco, 2004]. We refer to dry bulk densities, instead of wet bulk densities, because the environment in the Shyok Valley is arid and the

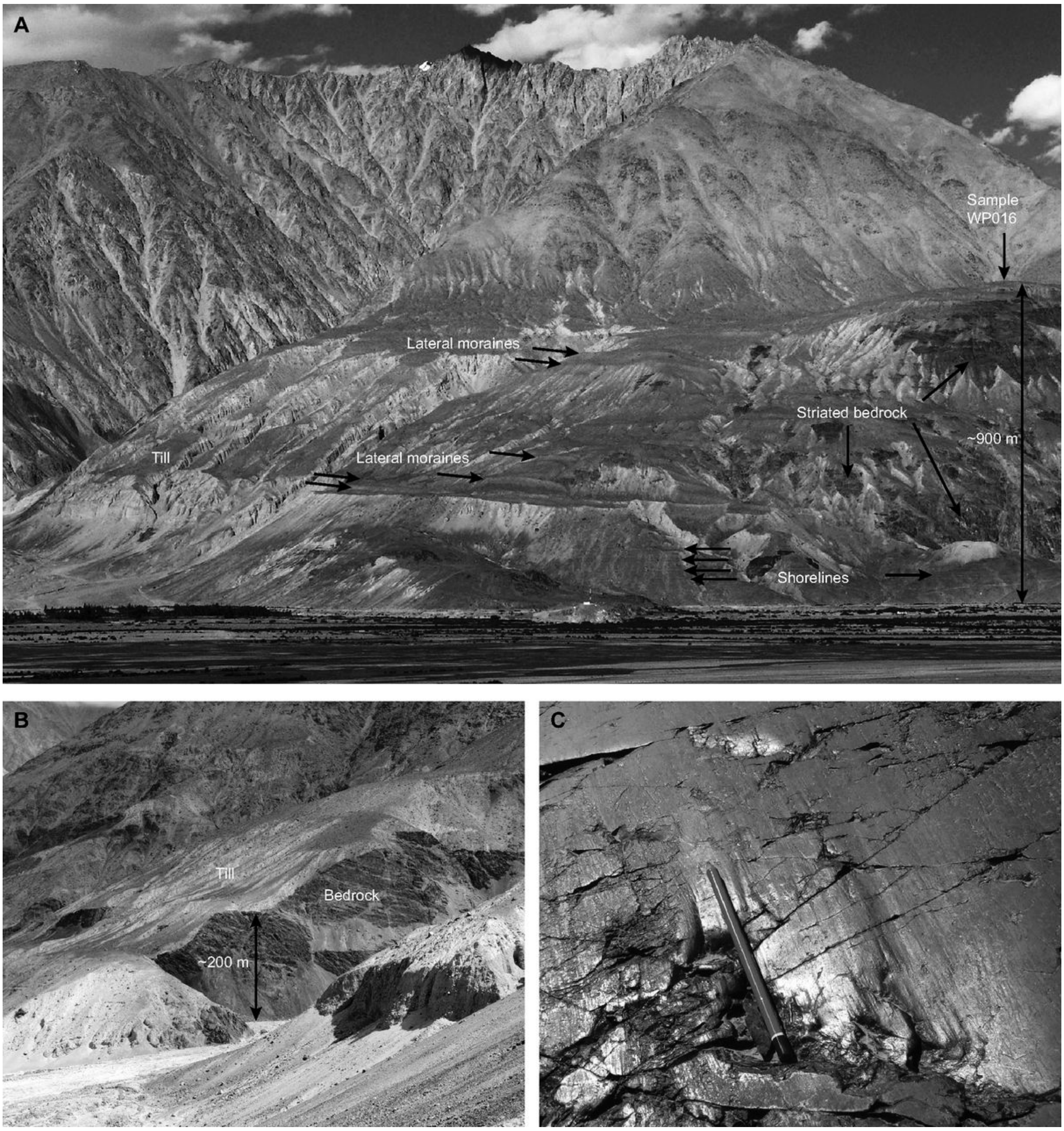

Figure 3.7: Field photographs of glacial deposits and marks. (A) Lateral moraines, till, and ice-polished bedrock at the Shyok-Nubra confluence. Note dissected, light-colored till covering dark-colored (striated) bedrock, with sub-horizontal lateral moraine ridges dipping from left to right. Note also horizontal shorelines near the valley bottom. Depth-profile samples (WP016) were collected from the till plain near the vertical arrow, ∼900 m above the valley bottom. View to the northeast. (B) Till-mantled hillslope near the Nubra-Shyok confluence, dissected by a tributary. Note light-colored tills on staircase-cut bedrock. View to the north. (C) Glacial striations on the upglacier side of a roche moutonnée in Nubra Valley.

Figure 3.8: Field photograph of shorelines near Kharu. View to the south.

sample location is located on a diffluent surface, rendering it unlikely that water stays in the uppermost 1 m of the ground for a long time period. Despite insufficient data to accurately model the exposure age or the amount of surface erosion, our results suggest a minimum exposure age of ca. 100 ka, assuming a dry bulk till density of 2.0 g cm^{-3} and no erosion (Figure 3.9A). For more likely erosion rates of 2-6 mm/k.y., best-fit exposure ages are between 124 and 200 ka. At erosion rates of ~7 mm/k.y., the modeled concentrations approach steady state and yield good fits with our measurements only for higher assumed densities (Figure B.2).

We further obtained ^{10}Be concentrations from two surface samples (>1 km apart) and seven samples along a 160-cm deep profile at an extensive terrace (~4-5 km^2) near the village of Agham (Figure 3.3, samples Shyk-1 to Shyk-7). On this terrace, dark-coated pebbles of the surficial desert pavement overlie a fine-grained layer, 38 cm thick at the sampling location, which we infer to be inflated loess (aeolian dust) that has buried the samples at depth while the surface samples were passively uplifted and continuously exposed [e.g., McFadden et al., 1987; Wells et al., 1995; Hancock et al., 1999]. We therefore included loess accumulation in our depth-profile modeling, while exposure age, density, and inheritance are free parameters. Because we have no constraints on loess-accumulation rates apart from its final thickness, we explore several scenarios. Assuming that no erosion has taken place before loess accumulation, the end-member scenarios are instant accumulation of the entire loess deposit either right after deposition of our samples, or just before our sampling. Both scenarios are unlikely and yield ^{10}Be concentration profiles that do not match the entire profile. In particular, the ^{10}Be concentrations of the surface samples are too low for an early rapid loess deposition, and too high for a late-stage rapid deposition.

The simplest reasonable scenario is continuous and constant loess accumulation, i.e., a negative erosion rate that is set by the exposure time divided by the thickness of the loess layer. The model results are in good agreement with our measurements (Figure 3.9B) and yield 107-116 ka surface-exposure ages, with an inheritance of 5,00 atoms/g and for densities of 1.85-2.0 g cm^{-3} (best fit: 112 ka and 1.9 g cm^{-3}). Tests with higher inherited concentrations show that best-fit densities vary within reasonable ranges (~1.9-2.1 g cm^{-3}) for inherited concentrations 70,00 atoms/g, whereas exposure age is relatively insensitive (107-117 ka; Figure B.3). We explored other, more variable loess-accumulation scenarios,

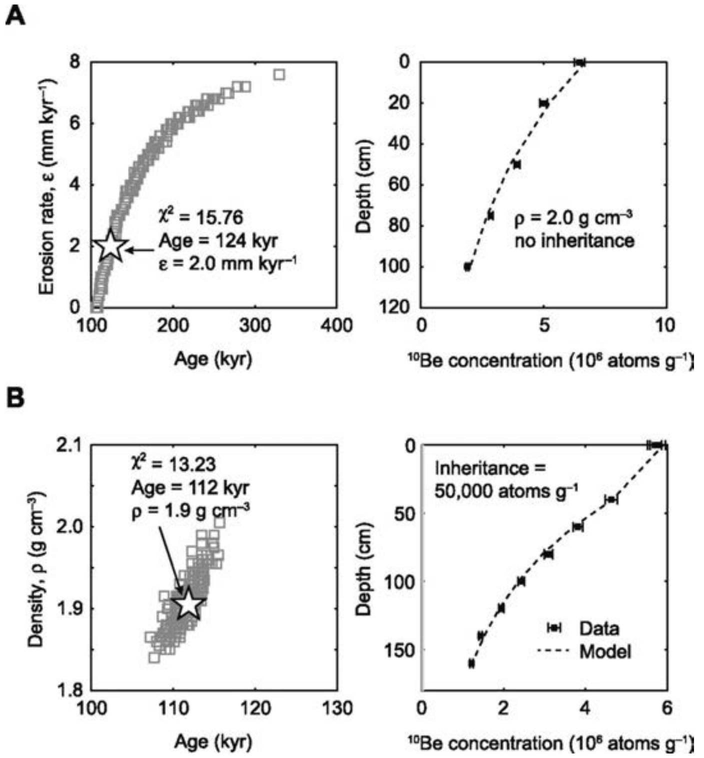

Figure 3.9: Best-fit ^{10}Be model results of depth-profile data. (A) Till plain at the Shyok-Nubra confluence. (B) Fill terrace near the village of Agham. Left panels show Monte Carlo best-fit results of exposure age–erosion rate (ε) (A) or exposure age–density (ρ) (B). Right panels show depth profiles of measured and best-fit modeled ^{10}Be concentrations. Error bars reflect 2σ analytical uncertainties.

by modeling the ^{10}Be accumulation (Equation 3.3) numerically (Figure 3.10). In these cases, we did not perform Monte Carlo experiments to estimate the uncertainties. We furthermore assumed 5,00 atoms/g inheritance and a fixed density equal to our best-fit density from the first scenario (1.9 g cm^{-3}), and varied the exposure duration manually until a visually good fit was obtained. We do not expect that a full parameter search would add any accuracy at this stage, because an unlimited number of possible dust-accumulation scenarios exist. While many scenarios yield model results that fit the samples at depth reasonably well, reproducing the surface-sample concentrations requires that accumulation of dust occurred mostly during the glacial period. Furthermore, variable loess accumulation scenarios that yield good fits with our data indicate an exposure age that is similar to the simple model of constant and continuous dust accumulation during the duration of exposure (~110 k.y.).

We also collected one amalgamated surface sample from a terrace near the village of Khalsar (sample WP020; cf. Figure 3.6). Because loess underlies the desert pavement on this flat terrace surface too, we assume a formation similar to the terrace surface at Agham, and obtained a maximum exposure age based on simple continuous exposure of the surface sample and zero inheritance. The resulting maximum exposure age, calculated with the CRONUS online calculator [v. 2.2; Balco et al., 2008], is 100.3±9.3 ka. For an assumed inheritance of 5,00 atoms/g, the exposure age would reduce to 99.3±9.2 ka. Finally, we collected one sample (WP014) from an erratic granitic boulder located on a moraine at an elevation of 3389 m asl at the confluence, which yielded an exposure age of 69.6±6.4 ka, assuming no surface erosion.

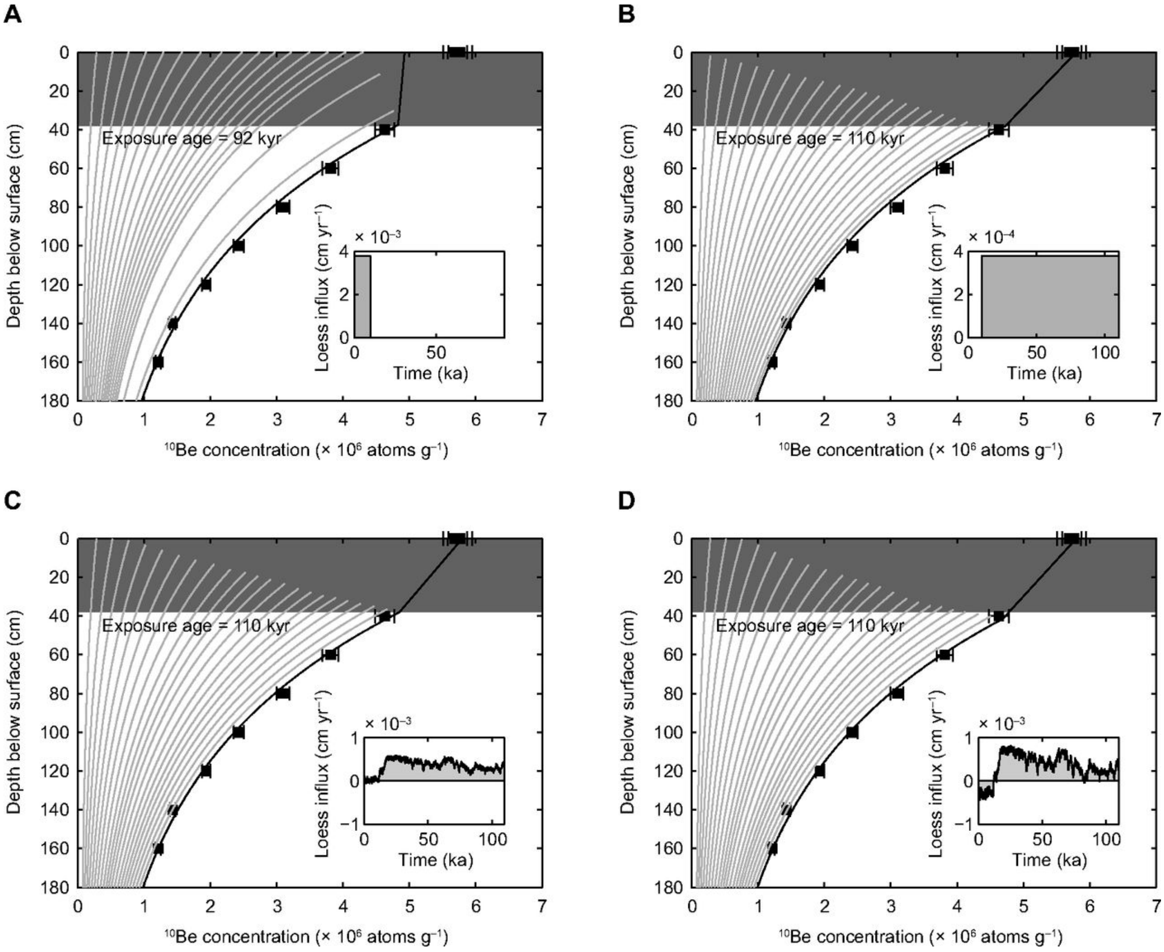

Figure 3.10: ^{10}Be depth-profile modeling results for different loess accumulation scenarios. (A) Constant accumulation during the interglacial. (B) Constant accumulation during the glacial. (C, D) Loess accumulation scaled by the Antarctic temperature record [Stenni et al., 2001]. Loess accumulation in D is more negative during interglacial periods and more positive during glacial periods. Data points give measured concentrations; error bars the 2σ analytical uncertainties. Black thick lines connect modeled concentrations. Thin gray lines give concentrations during the model run in 5000 yr time steps. Inset figures give loess influx rates (positive: inflation, negative: deflation) during the model run. Dark gray box covering the top 38 cm indicates thickness of the loess layer with unknown concentration. All models use a density of 1.9 g cm^{-3} and an inheritance of 50,000 atoms g^{-3}.

Table 3.1: Cosmogenic nuclide sample data

Sample name	Latitude	Longitude	Elevation above sea level	Depth below surface	Topographic shielding	Sample weight	^{10}Be concentration [a]	^{10}Be concentration uncertainty [b]
	(°N)	(°E)	(m)	(cm)		(g)	(atoms[g qz]$^{-1}$)	(atoms[g qz]$^{-1}$)
Shyk-1	34.3158	77.8185	3710	0	0.998	23.00	5.69E+06	1.80E+05
Shyk-6	34.3204	77.8187	3700	0	0.998	23.58	5.76E+06	1.83E+05
Shyk-7_40	34.3204	77.8187	3700	40	0.998	47.59	4.63E+06	1.47E+05
Shyk-7_0	34.3204	77.8187	3700	60	0.998	41.03	3.81E+06	1.21E+05
Shyk-7_80	34.3204	77.8187	3700	80	0.998	47.93	3.10E+06	9.82E+04
Shyk-7_100	34.3204	77.8187	3700	100	0.998	58.23	2.43E+06	7.70E+04
Shyk-7_120	34.3204	77.8187	3700	120	0.998	50.64	1.94E+06	6.15E+04
Shyk-7_140	34.3204	77.8187	3700	140	0.998	55.33	1.43E+06	4.56E+04
Shyk-7_160	34.3204	77.8187	3700	160	0.998	47.29	1.22E+06	3.88E+04
WP016-0cm	34.5699	77.6535	4048	0	0.997	28.31	6.48E+06	2.05E+05
WP016-20cm	34.5699	77.6535	4048	20	0.997	27.14	5.01E+06	1.59E+05
WP016-50cm	34.5699	77.6535	4048	50	0.997	30.19	3.93E+06	1.25E+05
WP016-75cm	34.5699	77.6535	4048	75	0.997	30.20	2.85E+06	9.08E+04
WP016-100cm	34.5699	77.6535	4048	100	0.997	30.45	1.90E+06	6.11E+04
WP014	34.5768	77.6307	3389	0	0.992	35.00	3.01E+06	9.54E+04
WP020	34.4853	77.7104	3483	0	0.992	29.42	4.57E+06	1.46E+05

[a] The subtracted average laboratory process blank ^{10}Be/^{9}Be ratios are 3.9 x 10^{-15}(Shyk-1 to Shyk-7; 0.02% – 0.09% of the measured ^{10}Be/^{9}Be ratios and 2.5 x 10^{-15}(WP014 to WP020; 0.02%–0.08% of the measured ^{10}Be/^{9}Be ratios. ^{10}Be/^{9}Be ratios were normalized to the ETH in-house standard S2007N (Shyk-1 to Shyk-7), and to the standard 07KNSTD that was used in Cologne(WP014 to WP020). Note that the two standards are equivalent within rounding error.

[b] ^{10}Be concentration uncertainties reflect total analytical uncertainties at the 1σ level.

3.5. Discussion

3.5.1. Timing and Extent of Glacial Damming

The distribution of glacial striations and deposits in the lower Shyok Valley indicate glacial coverage over a length of at least 45 km. When considering the highest occurrence of moraine ridges and extrapolating their downstream decrease in elevation, the ice may even have extended much farther. Although U-shaped valley morphologies suggest ice reaching farther downstream, we currently lack direct evidence based on striations and unequivocal deposits. Because glacial marks and deposits are highest near the confluence and extend down-valley but not up-valley, it appears most reasonable to connect this ice cover to the Siachen Glacier in the Nubra Valley, which would have extended over a total length of >180 km, that is, >120 km from its present-day terminus.

The fluvio-lacustrine deposits in the upper Shyok Valley adjoining the glacial marks and deposits in the lower Shyok Valley provide compelling evidence that the Siachen Glacier blocked the Shyok River at its confluence with the Nubra River, resulting in extensive upstream aggradation and lacustrine deposition. The mapped succession of fluvial and lacustrine deposits is similar to a 450-m-thick sequence of fluvial and lacustrine deposits in the French Alps, which have been related to aggradation behind glacial dams during the last glacial cycle [Brocard et al., 2003]. We found no direct contacts between glacial and fluviolacustrine deposits, but the highest glacial striations at the confluence suggest that the Siachen Glacier would have flowed a short distance up into the upper Shyok Valley (Figure 3.3A, profile f-f'), although certainly not farther than where the lacustrine deposits are found. The spatial distribution of our mapped deposits indicates that a continuous valley fill extended at least to the village of Agham. Horizontal, low-relief surfaces, which slightly increase in elevation farther upstream from the extensive fill terrace near Agham, indicate a possible extent close to the village of Shyok. However, this greater extent must not have prevailed throughout the entire aggradation period. Instead, given the extensive ice coverage in the headwaters of the Shyok today (Figure 3.1), it appears more plausible that these glaciers advanced farther downstream and temporarily occupied the more distal parts of the upper Shyok Valley.

Our ^{10}Be-depth profile data from the till plain above the Shyok-Nubra confluence suggest that the Siachen Glacier retreated from an elevation of more than 900 m above the present-day river (Figure 3.3B) most likely no later than ca. 124 ka, and probably at the beginning of the Eemian/Sangamon interglacial. Such an elevation is sufficient for the glacier to have blocked the Shyok River and to account for the observed valley fill. Furthermore, the timing is in accordance with cessation of damming and an onset of fluvial incision into the valley fill by ca. 107-116 ka, constrained by the terrace surface near Agham. However, for higher inferred erosion rates, it is possible that the till plain we dated is older than 124 ka and even unrelated to the valley fill. We note, however, that morpho-stratigraphically younger moraine ridges occurring at lower elevations at the confluence indicate ice elevations that would have been high enough (>3600 m asl) to block the Shyok and account for the observed valley fill (Figures 3.3, 3.7). These moraines must be older than the ca. 75±3 ka moraines that occur at elevations of $\sim$3250-3400 m asl [Dortch et al., 2010; and our sample WP014). The ca. 100±9 ka maximum surface-exposure age of

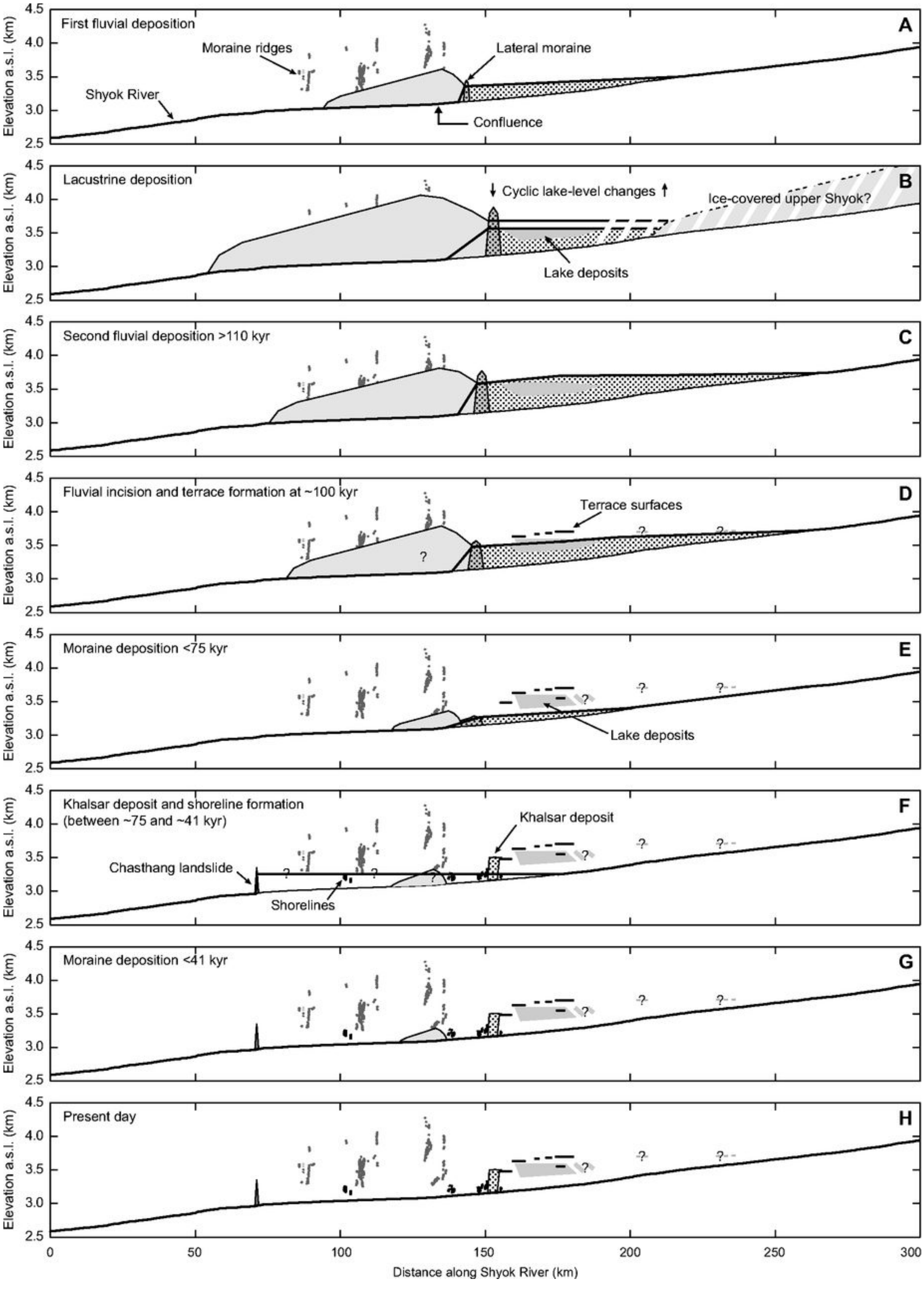

Figure 3.11: Conceptual model of the aggradation and incision history of the valley fill in the vicinity of the Shyok-Nubra confluence (a.s.l.—above sea level). See text for details and compare with Figure 3.3.

the terrace that hosts the Khalsar deposit and which is at an elevation of ∼3480 m asl is also compatible with an incision of the valley fill that started ca. 107-116 ka.

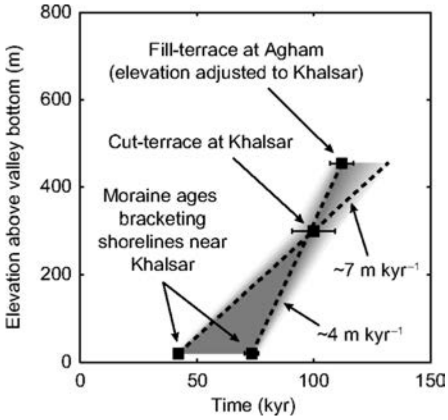

Figure 3.12: Incision history of the Shyok River into the valley fill. Error bars reflect Monte Carlo best-fit model results for the Agham terrace age and external uncertainties from CRONUS online calculator [Balco et al., 2008] for other ages. Shaded areas indicate likely incision paths. Dashed lines and numbers give possible average incision rates. See text for details.

Our interpretation contrasts with that of Dortch et al. [2010] who inferred that glaciers occupied the upper Shyok Valley down to the Shyok-Nubra confluence during the suggested aggradation period. Their argument for ice coverage is based on inferred roches moutonnées in the upper Shyok and a glacial origin of the Khalsar deposit, for which we do not find any supporting evidence. First, we could not find any glacial striations on bedrock in the area of the valley fill, and no observations to this extent are provided by Dortch et al. [2010]. This is in stark contrast to the many striated bedrock surfaces in the lower Shyok and at the Shyok-Nubra confluence. Second, as outlined above, we interpret the Khalsar deposit to have formed by a rock avalanche, which occurred after formation of the ca. 100±9 ka terrace that hosts part of the deposit. Third, the age constraints for ice coverage provided by Dortch et al. [2010] are based on exposure ages from cobbles, boulders, and a bedrock surface, located just upstream of the terrace near Khalsar, and range from ca. 100 to 140 ka. Because these samples stem from elevations (3534-3557 m asl) that would have been buried by the valley fill (top elevation >3600 m asl) and because we did not find any convincing evidence for a former glacier in this part of the upper Shyok Valley during the time of aggradation, we suggest that these ages most likely reflect a complex exposure history related to the time before burial and after excavation of the valley fill.

3.5.2. Aggradation and Incision History

The thick and extensive valley fill in the upper Shyok Valley testifies to a period of protracted upstream sediment deposition. Unfortunately, we were not able to date the onset or duration of the aggradation period, but with the geometry of the valley fill and published erosion-rate estimates, we can derive firstorder estimates of the time scales of aggradation. From the DEM and the topmost valley-fill surface, we calculated the minimum volume removed by erosion to be 30.7 km^3, corresponding to an extent of the valley fill just beyond Agham. Approximately 10 km^3 of this valley fill are lake sediments. Estimates of subglacial erosion rates beneath the Siachen Glacier that are based on proglacial river-gauging data span 0.11-0.46 mm/yr [Bhutiyani, 2000], whereas cosmogenic nuclide-derived catchment-wide erosion

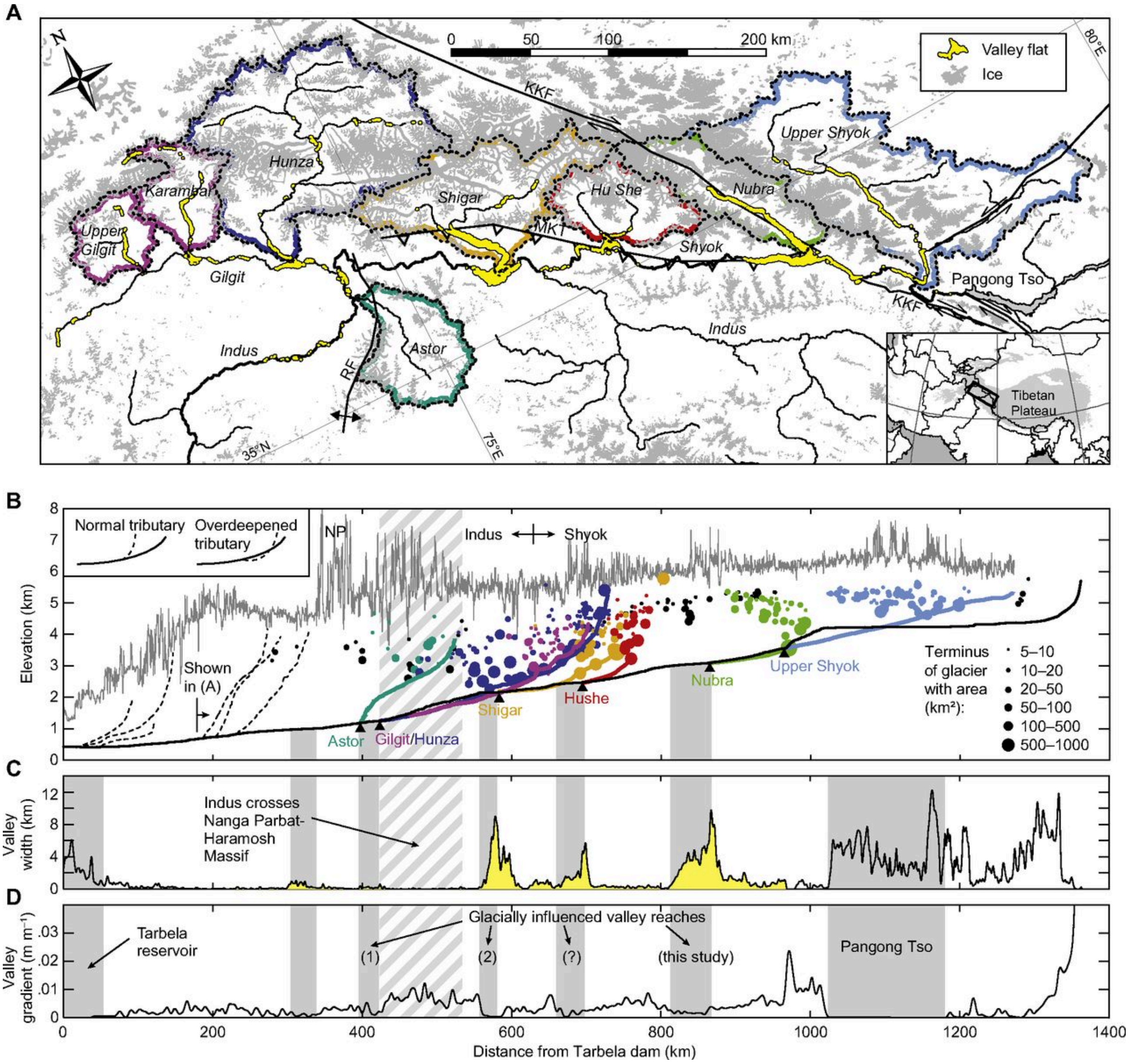

Figure 3.13: Morphologic characteristics of formerly glaciated confluences along the Shyok and Indus Rivers. (A) Catchments of major rivers that drain the Karakoram Mountains, along with the distribution of present-day glaciers (gray) and valley flats (yellow). RF—Raikhot fault; MKT—Main Karakoram thrust; KKF—Karakoram fault. (B) Longitudinal profiles following the Shyok and Indus Rivers (blackline) where they are adjacent to the Karakoram and major Karakoram tributaries (colored lines) shown in A (NP—Nanga Parbat). Filled circles show termini of glaciers >5 km^2. Size of circle indicates glacier area and color whether it drains into a Karakoram tributary (colored) or directly into the Shyok or Indus (black). Gray line shows maximum elevation within a 80-km-wide swath profile that follows the Shyok and Indus Rivers adjacent to the Karakoram. All positions along the x-axis refer to the distance from the Tarbela dam along the channel network, even if the channel network is not shown, as in the case of the glacier termini. (C) Valley width and (D) valley gradient along the trunk stream profile shown in B. Numbers in parenthesis refer to (1) Derbyshire et al. [1984], (2) Seong et al. [2007].

rates from Shyok tributaries draining the Ladakh batholith range from ∼0.05 to 0.07 mm/yr [Dortch et al., 2011a]. Hence, assuming erosion rates of 0.1-0.5 mm/yr across all areas upstream of the confluence but downstream of Pangong Tso (Figure 3.1), and acknowledging a lower density of sediment (2.0 g cm^{-3}) as compared to bedrock (2.7 g cm^{-3}), yields aggradation times of 6-27 k.y. This is based on the assumption that all incoming material is retained behind the dam. If we consider that the fluvial deposits reflect only the bedload, which is typically ∼10% [e.g., Hinderer, 2001] but could be as high as ∼33 % [Pratt-Sitaula et al., 2007] of the eroded material upstream, these numbers increase to ∼13-196 k.y., and include ∼2-9 k.y. of lacustrine deposition, during which trapping of all the bed and suspended load occurred.

Given these estimates and considering that they pertain only to the valley fill that has been eroded since incision, it is reasonable to assume that the aggradation of the valley fill occurred over several tens of thousands of years, most likely starting during the previous glacial period when glaciers south of the Ladakh Range [Owen et al., 2006], in Zanskar [Hedrick et al., 2010], and in the central Karakoram [Seong et al., 2007] were also more extensive than subsequently. The aggradation period was likely accompanied by concurrent changes in Siachen Glacier's length and thickness and thus the ice-dam height, which probably affected the depositional environments (Figures 3.11A- 3.11C). The apparent lack of lake deposits upstream of Agham, along with the recognition of terrace-like surfaces at elevations near 3700 m asl between Agham and the Shyok village (see Figure 3.3, profiles d-d' and e-e'), suggest that higher parts of the upper Shyok Valley had been ice covered during deposition of the lacustrine units, but may have been ice free thereafter (Figure 3.11B).

Our data show that the aggradation period ended at ca. 107-116 ka, when the Shyok River started to incise the valley fill. The ca. 100±9 ka exposure age of the terrace near Khalsar is statistically indistinguishable from this age, but its lower position argues that it is truly younger, possibly related to a period of lateral planation, which shaped this terrace and another cut terrace near Agham (Figure 3.3B). Such stalling of incision could be due to readvance of the Siachen Glacier and associated damming at the beginning of the last glacial period (Figure 3.11D). Further dissection of the valley fill might have halted again for some time during readvance of the Siachen Glacier that terminated at ca. 75±3 ka (Figure 3.11E) at the confluence [Dortch et al., 2010], but there is no indication in form of cut terraces.

The Khalsar deposit, which is stratigraphically younger than the ca. 100±9 ka terrace surface it partly rests on, is in contact with fluvial gravels 20 m above the present-day valley bottom (3180 m asl), and hosts well-developed shorelines at its northern edge (Figure 3.3). Dated nearby moraines with and without shorelines at the same elevation apparently constrain their formation to between ca. 41±2 and ca. 75±3 ka [Dortch et al., 2010], indicating that the Shyok had already incised to near its present-day level by this time (Figure 3.11F). Although the formation of these shorelines by a glacier-dammed lake appears reasonable [Dortch et al., 2010], the shorelines near Kharu (Figure 3.8) that also occur up to an elevation of 3250 m asl could be related to the same lake. In this case, the Siachen Glacier could not have impounded the lake. An alternative explanation links lake formation to the landslide near Chasthang, which may once have blocked the Shyok River (Figure 3.3), but this hypothesis needs further investigation. In any case, this lake period appears to have been brief, as no associated lacustrine deposits were found. Another readvance of the Siachen Glacier that ended at ca. 41±2 ka [Dortch et al., 2010] had the potential for further damming of the Shyok River, while thereafter the confluence appears to have been mostly ice free (Figures 3.11G, 3.11H).

The currently available age constraints therefore suggest that the Shyok River incised the valley fill with an average rate of ∼4-7 m/k.y. and reached its present level between ca. 41±2 and ca. 75±3 ka (Figure 3.12). Postglacial incision rates of a similarly thick glacially dammed valley fill in the French Alps were initially about an order of magnitude higher (>60 m/k.y.) but dropped to ∼10 m/k.y. after 5 ka [Brocard et al., 2003]. Because retreat of the Siachen Glacier would have exposed a steep knickpoint in the profile of the Shyok River, we expect that incision rates were also much higher initially, but were slowing down as the step in the profile got progressively leveled. Given the extent of damming before incision and the apparently incomplete dissection during the interglacial, it is quite likely that readvances of the Siachen Glacier during the earlier part of the last glacial period, e.g., ca. 75±3 ka, slowed or temporarily stopped incision of the valley fill.

3.5.3. Catastrophic Outburst Floods from Ice-Damned Lakes

Aggradation of the fluvial deposits in the Shyok valley fill was likely accompanied by frequent formation and drainage of an icedammed lake, perhaps resembling the lake that repeatedly forms and drains behind the Kyagar Glacier dam (Figure 3.2). Alternatively, the Shyok River could have passed by the ice laterally, without any ponding, similar to the Shimshal River, which currently passes the Khurdopin Glacier over a length of $\sim$3 km, in the eastern Hunza watershed (Figure 3.1). We do not know how the Shyok eventually discharged its waters past the ice-covered confluence, but lateral passage is more conceivable when the glacier's extent downstream from the confluence was short and the upglacier supply of ice low, so that the Shyok could have maintained connectivity with downstream areas. When the glacier stretched far beyond the confluence, however, and the upstream supply of ice was much higher due to thicker ice with higher velocities, keeping a passage open would have been more difficult, especially during winter when discharge is low.

In analogy to the dynamics of historically active glacier dams in the Karakoram (Figure 3.2) [Mason, 1929; Hewitt, 1982] and elsewhere [Roberts, 2005, and references therein], it therefore seems most likely that blocking of the Shyok River by the Siachen Glacier resulted in a hydraulically fragile system with high potential for frequent outburst flooding from ephemeral lakes. If lake drainage occurred through a subglacial tunnel, the discharge at the glacier terminus would be expected to increase exponentially over hours to days due to melt widening of the waterfilled conduit [e.g., Nye, 1976], resulting in peak-flood discharges that greatly exceed regular discharges. Yet ice dams formed by tributary glaciers often fail by subaerial breaching, which usually results in more rapid discharge increases [Walder and Costa, 1996] and more catastrophic outburst floods [Haeberli, 1983]. We note however that breaching of a very long ice dam would require greater work expenditure by the passing waters so that discharge increases may be slower, which would prolong flood duration at the expense of peak-flood discharges. We argue that the lake formation and most likely rapid lake drainage on an annual basis would not have provided conditions stable enough for continuous lacustrine deposition, while the resulting flood discharges upstream of the dam would still have allowed for transport and deposition of fluvial gravels up to the dam.

In contrast, the lacustrine deposits of the valley fill document the existence of a lake that must have stretched over at least 20 km, approximately between Khalsar and Agham. The cyclic fining-upward units are best explained by periodically changing water depths (Figure 3.5). Because the units are relatively thick ($\sim$1-5 m), and for the same argument as above, it appears unlikely that deposition occurred during lakelevel changes on a regular annual basis. On the other hand, the >25 units make a link with longterm climatic changes, e.g., due to orbital variations with 10^4-10^5 year periodicities, also unlikely. From the present-day discharge of the Shyok River at its confluence with the Indus River [Ali and deBoer, 2008; Table 3.2) we estimate the Shyok discharge upstream of its confluence with the Nubra to be $\sim$200 m^3/s, or $\sim$6 km^3/yr. For this discharge, for lake bottoms between 3450 and 3600 m asl elevation, and for an assumed maximum water depth of 100-200 m, lake volumes estimated from the DEM are between 9 and 48 km^3, assuming the lake extended just beyond the village of Agham. Given these estimates, it would have required from about one to eight years for filling up the lake if all water from upstream areas were retained in the lake. Considering modelbased estimates of annual evaporation from lake surfaces in the high and arid western part of Tibet [Avouac et al., 1996], we conclude that evaporation would have prolonged the infilling insignificantly, because of the relatively small area compared to the high inflow rate.

Table 3.2: Shyok River Water Discharge

Location	Mean discharge (m$^3/s$)	Upstream area[a] (km^2)
Shyok-Indus confluence [b]	333	33.383
Shyok-Nubra confluence [c]	199	14.941

[a] Mean discharge values from Ali and de Boer [2008].

[b] Mean discharge was back-calculated by assuming the same specific runoff as at the Shyok-Indus confluence.

[c] Upstream area excluding areas draining in Pagong Tso.

Despite our crude estimate, such short time periods for lake filling leave two basic alternatives of lake behavior. In the first scenario, lake sedimentation was relatively slow, perhaps occurring at rates of $\sim$10 mm/yr, resulting in a $\sim$15-k.y. lacustrine period. Deposition of the meter-thick lake units at gradually increasing water depths would thus have required a significant amount of leakage during lake-level rise in order to avoid flotation of the ice dam. Although we deem this scenario not very likely, we acknowledge that an ice dam rimmed by significant amounts of glacial sediments could have been more stable and allowed for a spillway between lateral moraines and the adjacent hillslopes. In this scenario, periodic lake-level changes on centennial time scales could have occurred due to final dam flotation or possibly glacier surges, i.e., recurring periods of rapid basal sliding that are particularly common amongst Karakoram glaciers [Copland et al., 2011] and which have surge periods of several decades to >100 years [Hewitt, 1998].

In the second scenario, the lake was ephemeral and sedimentation was rapid. In this case, each cyclic lake unit may represent the deposits of an individual flood event that initiated farther upstream and got ponded by the Siachen Glacier dam at the Shyok-Nubra confluence. An analogy can be made with the well-studied glacial Lake Missoula outburst-flood deposits that accumulated in back-flooded valleys of Washington, USA, and which are commonly referred to as rhythmites [Waitt, 1985]. These rhythmites are typically fining upwards, have thicknesses ranging from centimeters to several meters [Atwater, 1986], and were deposited at intervals spanning several decades [Waitt, 1985; Clague et al., 2003]. In the upper Shyok Valley, potential sources of catastrophic floods are located in the headwaters of the Shyok River, where historic failures of tributary ice dams (Figure 3.1) have repeatedly resulted in destructive catastrophic outburst floods [Mason, 1929]. During glacial periods, however, the upper Shyok glaciers most likely advanced farther down in the trunk valley and potentially reached the Shyok village (Figure 3.3), where they would have blocked the tributary that is coming from Pangong Tso. The ∼2 km downstream displacement of the confluence of this tributary may actually be the vestige of such blocking. Dortch et al. [2011b] reported evidence for catastrophic partial drainage of Pangong Tso at ca. 11±1 ka through this tributary, which they relate to lake spillover during a more humid period [Gasse et al., 1996]. When Pangong Tso is hydrologically connected to the Shyok River, the drainage area of this tributary increases from ∼2000 to 46,000 km^2. The resulting increase in discharge may very well increase the hydraulic pressure on any ice that blocks this tributary and initiate a period of outburst flooding that is archived in the lacustrine deposits. In light of these considerations, the scenario of upstream flood-related lake deposition appears to provide better support of the current data and observations.

3.5.4. Glacial Damming and the Quaternary Evolution of the Shyok Valley

The reconstructed period of glacial damming and associated upstream aggradation and incision occurred for several tens of thousands of years and directly affected ∼100 km of the Shyok Valley. Yet, the current landscape and morphodynamics in the Shyok Valley appear to be largely controlled by the results of glacial erosion. Numerous alluvial fans along the previously glaciated, kilometer-wide valley floors (Figure 3.3B) and active aggradation of the Shyok River at the confluence testify to the current incapacity of the Shyok and Nubra Rivers to evacuate the material that is supplied by their tributaries. The most obvious interpretation of this gentle-sloping valley reach is that of a glacial overdeepening that was carved by the Siachen Glacier and subsequently back-filled with alluvium [e.g., Penck, 1905; Gutenberg et al., 1956]. This interpretation is supported by tributaries to the Shyok and Nubra, which are often seen hanging above the main stem rivers, suggesting differential incision as is typical for glacial valleys [e.g., Amundson and Iverson, 2006]. Furthermore, simple backfilling behind a landslide dam [e.g., Hewitt et al., 2011] can be excluded, because no active dam exists near the downstream end of the alluviated valley reach, which is widest at the confluence as opposed to its downstream end. We also note that we found no evidence in the field or in published studies [Phillips, 2008; Taylor and Yin, 2009] that differential uplift along active tectonic structures contributes to this overdeepening, but it may be that the rocks in the lower Shyok and Nubra Valleys are more erodible than elsewhere, due to their proximity to the Shyok suture zone and Karakoram fault, respectively (Figure 3.13A). In this context it is also worth mentioning that we have not seen any obvious signs of recent deformation, e.g., disrupted or displaced depositional surfaces, along the Karakoram fault in our study area.

Our results furthermore show that the Siachen Glacier had been much more extensive prior to the last interglacial as compared to the last glacial period. A similar pattern has been observed in the Ladakh Range to the south, leading Owen et al. [2006] to speculate about a long-term aridification of the region. It is also conceivable, however, that progressive glacial incision during more extensive periods successively forced the Siachen Glacier to smaller extents [e.g., Oerlemans, 1984; Kaplan et al., 2008], because any lowering of the bed that is not sufficiently compensated by uplift would have led to a successively lower ablation area, smaller accumulation area, and thus a shorter glacier with time [Anderson et al., 2012]. This idea is compatible with the valley overdeepening as a product of subglacial erosion. But even if this were not the case and rock uplift did at least balance valley incision, unless previous times had been significantly drier, for which there is currently no evidence [cf. Owen et al., 2006], we see no reason why similar damming episodes would not have occurred during earlier times and possibly throughout much of the Quaternary. We therefore suggest that extensive glacial damming and associated processes have not been extraordinary, rare events, but occurred rather frequently during earlier episodes during the Quaternary period.

It has been recently argued that repeated glacial damming of the Tsangpo-Brahmaputra River during the Quaternary might have stabilized the Tibetan Plateau edge by impeding headward fluvial incision [Korup and Montgomery, 2008]. In the Shyok Valley, however, the inferred valley overdeepening suggests that incision by the Siachen Glacier has been higher than fluvial incision farther downstream, rendering the net effect of blocking fluvial incision not very important. It follows that the base level of the upper Shyok River is actually controlled by glacial erosion at the confluence and therefore decoupled from its downstream areas. This tributary control of local base level has prevailed for at least the last two glacial cycles, but likely much longer. Our reconstruction also suggests that the valley fill was not fully dissected before further, although minor, damming occurred, and that the upper Shyok River in our study area has probably not been flowing on bedrock for the same amount of time, i.e, the last two glacial cycles. However, no major knick zone is developed along the upper Shyok River, which could indicate either efficient glacial incision during periods when potentially the entire upper Shyok was ice covered or fluvial incision to below the current level whenever bedrock was exposed in between previous damming periods. In any case, our data suggest that the influence of glaciers in the Shyok Valley has been to promote rather than delay the incision of the plateau edge. Future studies should examine the apparent contrasting role of glaciers for the evolution of the Tibetan Plateau margins more closely.

3.5.5. Signatures of Glacial Damming and Erosion along the Karakoram

The courses of the Indus and Shyok Rivers, both of which have vast catchment areas in lowrelief regions of the Tibetan Plateau and run for hundreds of kilometers parallel to the Karakoram, make these rivers particularly prone to interacting with large glaciers that originate in the Karakoram. Indeed, signs of ice coverage have been identified at all major confluences of the Indus and Shyok with rivers draining the Karakoram [Bürgisser et al., 1982; Derbyshire et al., 1984; Shroder et al., 1989; Cornwell, 1998; Phillips et al., 2000; Seong et al., 2007; Hewitt et al., 2011], which suggests that the formation of ice dams, upstream aggradation, and catastrophic outburst flooding have been widespread in this region and probably common during much of the Quaternary. However, ample evidence as found at the Shyok-Nubra confluence is often missing from farther downstream, and some of the deposits previously cited as evidence for glacial dams along the Indus River may actually be related to younger rock avalanches [Hewitt, 1999; Hewitt et al., 2011].

There exist several accounts of historical floods related to glacier or landslide dams in the Shyok and Indus Valleys that had devastating effects on local communities [e.g., Cunningham, 1854; Shroder, 1998; Hewitt and Liu, 2010]. Cornwell and Hamidullah [1992] reported the distribution of boulder beds, plunge pools, and chutes along the middle Indus Valley (between Gilgit River and the Tarbela dam), which they interpret as geomorphic evidence of such floods. More evidence appears farther downstream in the Peshawar Basin, which is located just west of the Tarbela dam, where the Indus exits the mountains

(Figure 3.1). Throughout this basin, several tens of decimeterto meterscale rhythmites are interpreted to represent deposits of repeated catastrophic floods in the Indus Valley that occurred during the Bruhnes geomagnetic chron, i.e., <730 ka [Burbank and Tahirkheli, 1985]. Cornwell [1998] suggested that ice-dammed lakes located along the middle Indus Valley, downstream of Nanga Parbat, were the likely sources of such floods, but this is difficult to test and at least some historical floods are clearly related to landslide dams [e.g., Shroder, 1998].

Based on our discussion about the origin of the lacustrine deposits in the upper Shyok, and because Karakoram glaciers appear to respond synchronously to climatic changes [Hewitt, 2005; Scherler et al., 2011a], we emphasize that glacier-dammed lakes along the Indus and Shyok Valleys could have acted as both sources of outburst floods as well as impounding basins for floods from farther upstream. In general, the farther downstream the ice or landslide dam, the higher the annual discharge and the greater the likelihood of catastrophic floods from farther upstream. Moreover, the volume of ephemeral lakes and therefore the potential flood magnitude increase as valley gradients upstream of the dam decrease, which is expected for farther downstream reaches. To what extent this partly explains fewer well-preserved valley fills farther downstream is currently, due to the limited amount of data, difficult to tell. But it is notable that historical floods in the Indus Valley have scoured valley walls up to several tens of meters above the valley floor [Cunningham, 1854]. Instead of depositional evidence, we identify striking similarities between all other major confluences of the Indus and Shyok Rivers with Karakoram tributaries (i.e., Gilgit-Hunza-Indus, Shigar-Indus, Hushe-Shyok) and the ShyokNubra confluence that involve (Figure 3.13): (1) a high degree of present-day ice coverage in the tributaries that serves to source far-reaching glacier advances, (2) alluviated valley reaches that are widest at the confluence and extend far into the tributaries where they are commonly more gently sloping than the Indus or Shyok trunk streams (Figure 3.13B), and (3) a systematic pattern of valley gradients being low where the valleys are wide but the gradients gradually increase upstream of the confluences, concurrent with a valley narrowing. It is also worth noting that all major tributaries appear more deeply incised than the trunk Shyok or Indus valleys near the confluences, especially when considering that bedrock in these tributaries is most likely significantly lower than the alluviated valley floors. In addition, the fact that the alluviated reaches are gradually widening upstream, just to the confluences where they occur, argues against a single landslide origin, which would show the opposite pattern, i.e., widest at the barrier and narrowing upstream. Note, however, that this argument does not preclude landslides or rock avalanches from occurring within these reaches [e.g., Hewitt, 1999; Hewitt et al., 2011]. In fact, the glacial preconditioning of the landscape may enhance both the susceptibility to large slope failures [Hewitt, 2009] as well as the preservation potential due to the shallow valley floors.

3.5.6. Implications for the Quaternary Evolution of the Western Tibetan Plateau Margin

The glacial overdeepenings along the Shyok and Indus Valleys clearly testify to a greater longterm efficiency of glacial erosion compared to fluvial incision, which has been noted elsewhere [e.g., Brocklehurst and Whipple, 2002, 2006]. Although damming-related upstream aggradation locally protects the bedrock from erosion [Korup and Montgomery, 2008], the long-term effects of such shielding appear to be subordinate in these valleys, compared to either glacial incision during periods of more extensive glaciation or fluvial incision whenever bedrock was exposed. Areas located downstream of glacial dams, on the other hand, have likely been subjected to repeated outburst floods, whose main effect is to concentrate the total discharge into a few high-magnitude events. In the presence of thresholds for sediment transport [e.g., Snyder et al., 2003; Tucker, 2004] and considering that sediment provides the tools for bedrock erosion [e.g., Sklar and Dietrich, 1998], such floods are most likely highly erosive events that have the potential to incise valley fills, or bedrock in areas of no valley fill, at a higher rate than under non-flood discharge conditions [cf. Wulf et al., 2010].

We therefore suggest that glacially controlled local base-level lowering together with catastrophic outburst flooding are important processes in the Quaternary evolution of these valleys, and possibly the margins of the Tibetan Plateau in general [cf. Montgomery et al., 2004; Lang et al., 2013]. Variable glacial extents during the Quaternary could focus erosion along different segments of a glaciated catchment, thereby deepening the tributary valleys. Concurrently, the confluences with the Shyok and Indus Rivers would have alternated between periods of glacial incision and fluvial damming with associated outburst flooding, which would have promoted headward incision into the western margin of the Tibetan Plateau [van der Beek et al., 2009]. During this process, concurrent changes in catchment morphology and supraglacial debris cover [Scherler et al., 2011b] may influence glacial mass balances and extents such that flood-effective glacial dams could still occur long after a valley has been deeply incised. In the lower Indus Valley, for example, Nanga Parbat glaciers apparently reached the Indus at an altitude of ∼1200 m asl during the last glacial cycle [Phillips et al., 2000]. Similar processes may also operate along other orogenic plateaus, such as the Pamir Plateau with its deeply entrenched valley systems and extensive glaciers, glacial overprint of lower valley reaches, and stream captures along its western and northwestern flanks [Nšth, 1932; Strecker et al., 2003]. These examples emphasize the potentially destructive role of glacial systems with respect to the preservation and longevity of orogenic plateau margins, particularly in environments where snowlines and precipitation allow for the formation of extensive and fast-moving glaciers, such as in the Karakoram [Scherler et al., 2011a]. Where snowlines are higher and glaciers much smaller, as for instance along the eastern margin of Tibetan Plateau, the extent of glacial incision is certainly much lower, but the formation of glacial dams with associated outburst flooding may nevertheless be an important process [Lang et al., 2013].

3.5.7. Significance of Glacial Dams for Mountainous Landscape Evolution

The thick valley fill at the Shyok-Nubra confluence clearly shows that large glacial dams can be efficient barriers for sediment transport [e.g., Korup and Tweed, 2007], probably over time scales that are mostly dictated by glacial dynamics and mass balances, and thus climate. Therefore, glacial dams can strongly modulate the sediment dispersal from partly glaciated mountainous regions, which will inevitably affect the rates and patterns of sediment accumulation in intermontane or foreland depositional basins. At the same time, however, their tendency to fail catastrophically leads to concentrating the upstream available discharge into highly erosive flood events downstream [e.g., Haeberli, 1983; Costa and Schuster, 1988; Walder and Costa, 1996; Tweed and Russell, 1999; Roberts, 2005], which lowers the preservation potential of previous glacigenic deposits. It is important to realize that unless the climatic or topographic boundary conditions change, glacial dams will reform after each failure, thus resulting in recurring annual to decadal flood events. Although more depositional evidence is needed, the available data and observations suggest that in the Shyok and Indus Rivers, catastrophic flood discharges may have been frequent rather than exceptional events throughout much of the Quaternary period.

The impact of glacial dams on modulating discharge is in contrast to that of landslide or moraine dams, which in most cases will fail only once or, as in the case of voluminous landslides, may have long recurrence intervals when they affect slopes repeatedly. In addition, a fraction of the ice itself can contribute to elevating the flood discharge, whereas the material of debris dams tends to be spread out downstream during and after dam failure, often leading to longlasting valley floor aggradation [Korup, 2004; Korup and Tweed, 2007] on the order of several thousands of years [Trauth et al., 2000; Bookhagen et al., 2005; Ouimet et al., 2007]. The coarse material, typical of many landslide dams, can subsequently also affect channel roughness and promote aggradation [Brummer and Montgomery, 2006]. We note, however, that bedrock erosion during floods may delicately depend on the availability of tools, in the form of boulders, which are certainly more abundant in debris dams as compared to ice dams. Whether tools are in short supply at repeatedly failing glacier dams, or whether the supply of debris by the glacier and from ice-free downstream reaches is sufficient, needs to be tested. The above differences between ice and debris dams have in any case important consequences for the erosive impact of catastrophic floods from natural dams that are so far poorly understood.

3.6. Conclusions

We presented evidence that the Siachen Glacier formed a long-lived glacier dam in the Shyok Valley, which resulted in aggradation of a thick valley fill. Cosmogenic nuclide dating constrains the damming episode to the penultimate glacial cycle with its incision starting during the last interglacial. Our new data allow refining the glacial chronology of the Shyok-Nubra confluence and demonstrate that the Siachen Glacier had been much more extensive during the pen-ultimate glacial cycle compared to the last glacial cycle, while the Shyok Valley upstream of the confluence with the Nubra had been ice free over at least 20 km. Frequent formation and catastrophic drainage of ice-dammed lakes during the time of aggradation is likely, whereas lake deposits within the valley fill suggest that the ice dam might also have impounded floods from farther upstream. Subglacial erosion by the Siachen Glacier has produced a pronounced valley overdeepening and suggests a glacial control of local base level along the Shyok River.

Existing glacial reconstructions and chronologies from other parts of the Karakoram allude to similar ice dams along the Indus and Shyok Rivers at confluences with major Karakoram tributaries. As a result, the present-day longitudinal profile of the Shyok and Indus Rivers adjacent to the Karakoram resembles a staircase of filled-up, overdeepened valleys that are separated by narrower and steeper valley reaches. Whereas the overdeepenings and the previously glaciated tributaries show that glacial incision has been outpacing fluvial incision along the trunk streams, the lack of significant knick zones upstream of the damming sites suggests that the net result of glacial interaction with the Shyok and Indus Rivers was to promote incision of these valleys into the western margin of the Tibetan Plateau. Key factors in this process have probably been widespread and frequent catastrophic outburst floods from glacially dammed lakes throughout much of the Quaternary.

Acknowledgements

This research was funded by the German Federal Ministry of Education and Research (BMBF, PROGRESS). D.S. was supported by the Alexander von Humboldt Foundation. H.M. was supported by DFG grant KO3937/2. P.E. was supported by DFG graduate school GK1364 (DFG grant STR373/21-2). We thank R. Thiede and T. Tsering Lonpo for supportduring fieldwork, S. Mischke for analyzing the fossil content of our lake samples, J. Bloethe for testing OSL dating on the lake sediments, T. Schildgen, D. Montgomery, J. Dortch, and D. Egholm for valuable comments on an earlier draft, B. Hallet for stimulating discussions, and D. Burbank for a constructive review that helped improve the manuscript.

4 Segmentation of the Main Himalayan Thrust revealed by low-temperature thermochronometry in the western Indian Himalaya

Abstract

Despite remarkable tectonostratigraphic similarities along the Himalayan arc, pronounced topographic and exhumational variability exists in different morphotectonic segments. The processes responsible for this segmentation are debated. Of particular interest is a 30 to 40-km-wide orogen-parallel belt of rapid exhumation that extends from central Nepal to the western Himalaya and its possible linkage to a mid-crustal ramp in the basal décollement, and the related growth of Lesser Himalayan duplex structures. Here we present 26 new apatite fission-track cooling ages from the Beas-Lahul region, at the transition from the Central to the Western Himalaya (∼77°-78°E) to investigate segmentation in the Himalayan arc from a thermochronologic perspective. Together with previously published data from this part of the orogen, we document significant lateral changes in exhumation between the Dhauladar Range to the west, the Beas-Lahul region, and the Sutlej area to the east of the study area. In contrast to the Himalayan front farther east, exhumation in the far western sectors is focused at the frontal parts of the mountain range, and associated with the hanging wall of the Main Boundary Thrust fault ramp. Our results allow us to spatially correlate the termination of the rapid exhumation belt with a mid-crustal ramp to the west. We suggest that a plunging anticline at the northwestern edge of the Larji-Kullu-Rampur window represents the termination of the Central Himalayan segment, which is related to the evolution of the Lesser Himalayan duplex.

This chapter was accepted by
Tectonics on July 19, 2018
co–authored by Patricia Eugster, Rasmus C. Thiede, Dirk Scherler, Konstanze Stübner, Edward R. Sobel
and, Manfred R. Strecker

4.1. Introduction

Since the onset of the India-Eurasia collision ~54 Ma ago, India has been moving northward relative to Tibet resulting in the growth of the Himalayan orogenic wedge, Tibet's southern plateau margin. The Himalaya is commonly described as cylindrical-shaped orogen with major along-strike tectono-stratigraphic similarities (Figure 4.1); this includes the lithologies and structures of the Lesser and Higher Himalaya, the southward-directed growth of the Lesser Himalayan duplex structures, and approximately synchronous deformation along major structural boundaries. These include the Southern Tibetan Detachment (STD), the Main Central Thrust (MCT), the Main Boundary Thrust (MBT), and the Main Frontal Thrust (MFT) [Gansser, 1964; Valdiya, 1980; Burg et al., 1984; Schelling and Arita, 1991; Srivastava and Mitra, 1994; Hodges, 2000; Bendick and Bilham, 2001; Kohn, 2014; DeCelles et al., 2016]. Despite many regional similarities, the orogen is characterized by significant lateral variations regarding the role of major structures [Yin, 2006], topography [Duncan et al., 2003, Bookhagen and Burbank, 2006], and exhumation rates [Thiede et al., 2009; Robert et al., 2011; Thiede and Ehlers, 2013, Harvey et al., 2015, van der Beek, et al., 2016]. In particular, segments of the belt that are characterized by a pronounced topographic step between Lesser and Higher Himalaya, are associated with a focused exhumation; they alternate with segments where topographic steps or major tectono-stratigraphic units are missing and exhumation rates are lower [Duncan et al., 2003; Robert et al., 2011, Thiede et al., 2017]. The potential structural and tectonic controls that determine these spatially variable topographic, deformation, and exhumation patterns have remained controversial.

One of the structurally most prominent segments of the orogen is the Central Himalaya, a region extending from central Nepal to Garhwal (77°E-91°E) [e.g., Hodges, 2000]; this sector of the range has been at

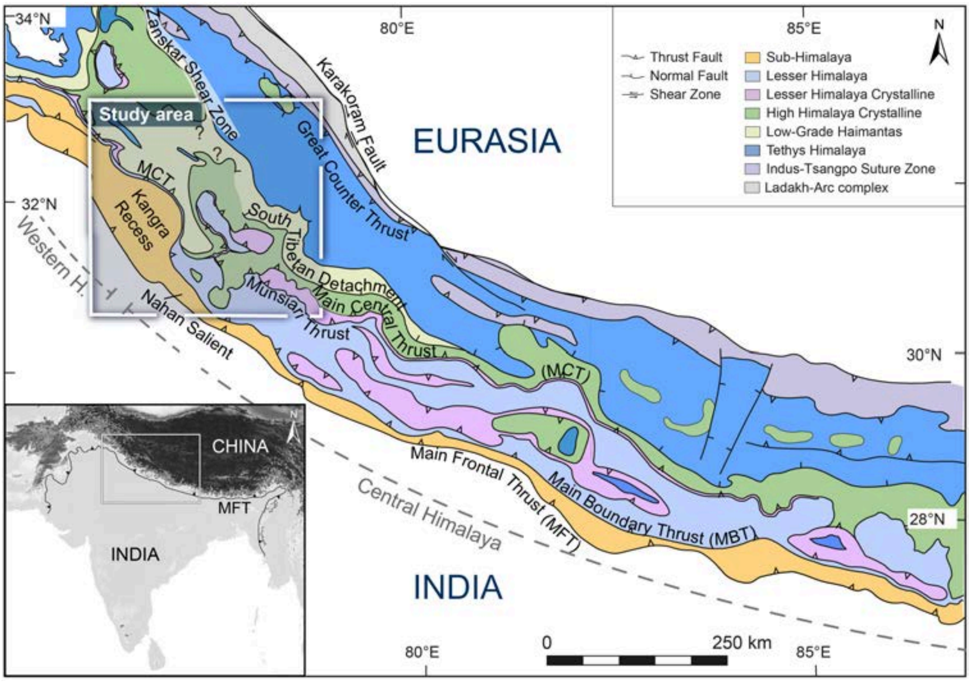

Figure 4.1: Geologic overview of the Himalaya between Pakistan and central Nepal. Subdivision into the Central (~91-78°E) and Western Himalaya (78-75°E) follows Hodges [2000]. Rectangle shows map extent of Figure 4.2. Map modified after DiPietro and Pogue [2004].

the center of discussions about the structural architecture and evolution of the entire mountain belt [e.g., Gansser, 1964; Hodges, 2000; Robinson et al., 2001; Avouac, 2003; Kohn, 2014].

In central Nepal, the southern exposures of rocks that constitute the High Himalaya are separated from the Lesser Himalaya by a pronounced change in topography known as the “physiographic transition two” (PT_2) [Figure 4.2C; Hodges et al., 2001, Wobus et al., 2006]. In most areas, the PT_2 spatially coincides with small to moderate-magnitude seismicity, and it is therefore thought to be associated with a structural and rheological change in the orogenic wedge that appears to correlate with a ramp in the Main Himalayan Thrust fault (MHT) at mid-crustal level (Figure 4.2) [Pandey et al., 1995; Mahesh et al., 2013; Elliott et al., 2016]. In close proximity to the PT_2, at a distance of $\sim$100-150 km north of the MFT, an $\sim$30 to 40-km-wide, relatively continuous belt of rapid exhumation extends from central Nepal in the east to the Sutlej area in the west (Figure 4.2) [e.g., Thiede et al., 2009; Herman et al., 2010; van der Beek et al., 2016]. Rapid exhumation on the order of 2-5 mm/yr [Jain et al., 2000, Thiede and Ehlers, 2013 and references therein] in this area has been related to the growth of a duplex structure in Lesser Himalayan rocks [e.g., Cattin and Avouac, 2000; DeCelles et al., 2001; Robinson et al., 2001; Bollinger et al., 2004; Herman et al., 2010], and/or to out-of-sequence thrusting [e.g., Wobus et al., 2005; Whipple et al., 2016]. However, along-strike disparities in topography, seismicity and convergence rates, suggest that orogenic growth and exhumation may not be as evenly distributed as suggested earlier. For example, there exist striking differences in topography, such as the disappearance of the PT_2 at the transition from the Central to the Western Himalaya at $\sim$77°E [e.g., Hodges, 2000; Bookhagen and Burbank, 2006; Deeken et al., 2011; Morrell et al., 2017]. Coincident with this topographic transition is a change towards more limited exposure of Lesser Himalayan units and more extensive exposure of High Himalayan units and, in particular, lower-grade metamorphic High Himalayan rocks (the "low-grade Haimantas", which correspond to the light-green unit in Figure 4.1). To date the underlying causes for the along-strike topographic and tectonic transition in this area has not been resolved.

In this study we document the regional exhumation patterns and their along-strike variations. We analyzed 26 new apatite fission-track samples from the Beas and Chandra valleys, Himachal Pradesh, India. We combined our new data with previously published low-temperature thermochronometry and geomorphic observations to better understand the temporal and spatial evolution of first-order fault systems such as STD since the Miocene. In addition, we attempted to unravel which mechanisms ultimately account for the change in exhumation style and pattern at the transition between the Western and the Central Himalaya, approximately at $\sim$77°E. By reviewing our new and previously published data, we were able to localize the spatial characteristics of rapid exhumation and detected significant gradients in exhumation since the Miocene, both along- and across-strike of the orogen.

4.2. Topographic and geologic setting of the study area

Our study area is located in the upper part of the Beas and Chandra valleys in the state of Himachal Pradesh, India (Figure 4.1, Figure 4.2A). The region constitutes a high-relief area, and elevations are mostly >2000 m above sea level (asl) (Figure 4.2B, Figure 4.3). Present-day annual rainfall decreases from >2000 mm/yr south of the Rohtang Pass to less than a few hundred mm/yr north of it. Moving along-strike of the orogen to the southeast and northwest from our study area, the topography and associated patterns of relief and rainfall change significantly (Figure 4.3). In the vicinity of the Sutlej Valley, elevation increases gradually from <1000 m in the foreland to ∼6000 m in the orogenic interior, where deep incision of the Sutlej River has created high local relief. Rainfall is more evenly distributed across the mountain range and decreases northward more gradually. In contrast, farther northwest, in the area of the Kangra recess, elevations increase more abruptly from the Sub-Himalaya at the mountain front to >5000 m over a very short distance, and so do rainfall and local relief.

The lower part of our study area straddles the Larji-Kullu-Rampur Window (LKRW), which exposes Lesser Himalayan Crystalline and meta-sedimentary units that are separated from the low-grade to unmetamorphosed Lesser Himalayan rocks by the Munsiari or Ramgarh Thrust faults (MT or RT) [e.g., Steck, 2003; Webb, 2013; Stübner et al., 2018]. Rocks exposed within the LKRW define an antiform [Steck, 2003; Webb, 2013] and are surrounded by the High Himalayan Crystalline complex that consists of meta-igneous and meta-sedimentary rocks [Steck, 2003]. During the Miocene, the STD (top-to-the-NE) and MCT (top-to-the-SW) exhumed the high-grade core of the Himalaya which is exposed in the High Himalayan Crystalline complex; this feature disappears towards the northwest [Vannay et al., 2004]. Deformation features exposed within the High Himalayan units are mostly ductile [e.g., Steck, 2003; Webb et al., 2011]. Previous work inferred that the STD, whose exact location is debated, runs

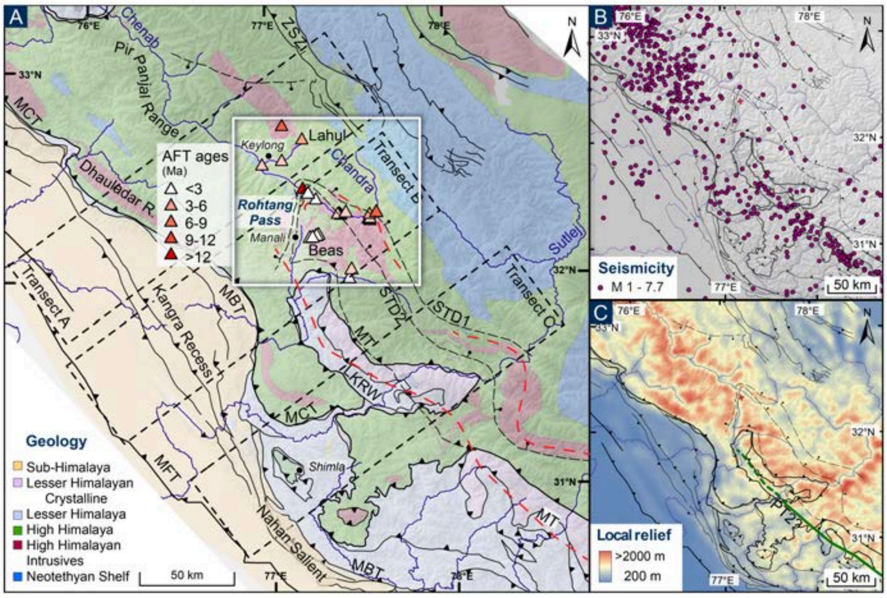

Figure 4.2: Geologic and physiographic overview of the study area. (A) Geological map after Steck [2003], Webb et al. [2007], Célérier et al. [2009], and Webb et al. [2011]. New sample locations presented as colored triangles. The dashed rectangular boxes show the location of three transects presented in Figure 4.3 and Figure 4.7. The dashed red lines indicate the extent of the belt of rapid exhumation as defined in text [Thiede et al., 2009]. The Rohtang Pass is shown by a saddle symbol. MFT = Main Frontal Thrust, MBT = Main Boundary Thrust, MCT = Main Central Thrust, MT = Munsiari Thrust, STD = South Tibetan Detachment; ZSZ = Zanskar Shear Zone; LKRW = Larji-Kullu-Rampur window. (B) Seismicity between 1964 and 2014; events 1<M<5 for locations 77°-81°E [Mahesh et al., 2013] and 4<M<7.7 for other areas from the NEIC Catalog. (C) Local relief calculated from an ASTER GDEM [a product of the NASA and METI] 30-m-resolution digital elevation model, using a circular moving window with a 4.5 km radius. The green line indicates the PT_2.

through the Beas and Chandra valleys; the temporal and spatial evolution of the STD has not been understood until now [e.g., Steck, 2003; Webb et al., 2007, Stübner et al., 2018]. To the south the MCT emerges in the vicinity of the MBT around the Kangra recess.

Previous studies [e.g., Kumar et al., 1995; Lal et al., 1999; Jain et al., 2000; Schlup, 2003; Thiede et al., 2004; Vannay et al., 2004; Thiede et al., 2005; Thiede et al., 2006; Adams et al., 2009; Adlakha et al., 2013; Thiede et al., 2017] have shown that the High Himalaya in the northwestern sector of the mountain belt has undergone rapid exhumation since the Late Miocene-Pliocene. Young apatite fission track (AFT) cooling ages (<3 Ma) have been reported from the Beas and Sutlej valleys and the Garhwal Himalaya [Thiede et al., 2009]. North of the Kangra recess, young AFT and zircon helium (ZHe) cooling ages have been documented in the Dhauladar Range, located in the hanging wall of the MBT [Deeken et al., 2011; Thiede et al., 2017].

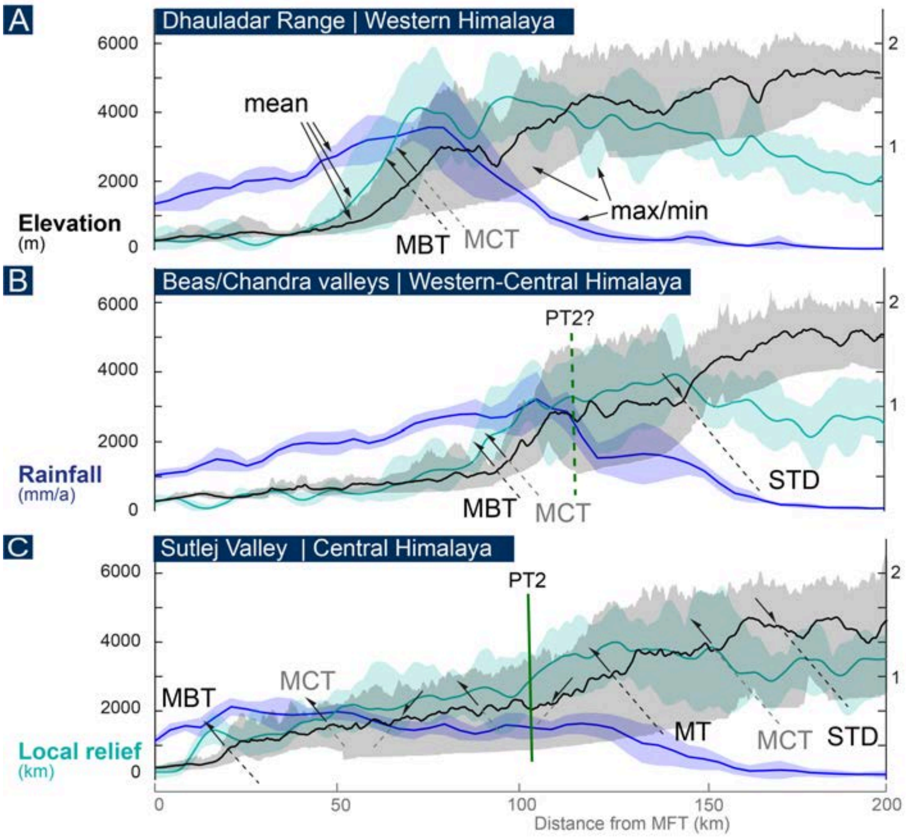

Figure 4.3: Swath profiles from the study area. Each panel shows elevation (black), local relief (green), and rainfall (blue) statistics (mean, min, max), calculated over a width of 50 km. The main faults cutting the transects are indicated by dashed lines [Steck, 2003]. For locations see Figure 4.2. PT$_2$ corresponds to its course in Figure 4.2C. Elevation data is based on ASTER GDEM [a product of NASA and METI], and rainfall is based on Tropical Rainfall Measuring Mission data [Bookhagen and Burbank, 2006].

4.3. Methods

We collected samples from meta-sedimentary and meta-igneous rocks. Apatite grains were recovered from whole-rock samples using standard magnetic and heavy-liquid separation procedures. Fission-track mounts were prepared and analyzed at the University of Potsdam and the University of Göttingen.

After etching spontaneous tracks in 5.5 M nitric acid for 20 seconds at 21°C, samples and Goodfellow mica external detectors were irradiated at the research reactor of the Oregon State University. Mica detectors were etched in 40%-hydrofluoric acid for 45 min as described in Sobel and Strecker [2003]. We determined zeta-ages [Hurford and Green, 1983]. Because of the young AFT ages, several samples contain grains of zero-track densities, which partly explains why the χ^2-values of some samples are below 5%, and these samples failed the χ^2-test. For these samples, we used central ages. Samples that passed the χ^2-test with values >5% are reported as pooled ages [Galbraith, 1981; Green, 1981]. All our ages listed in Table 4.1 were calculated with Trackkey [Dunkl, 2002].

We measured the diameter of the etch pit parallel to the c-axis (D_{par}: Table 4.1) to assess the resistance of tracks to thermal annealing. D_{par} depends primarily on kinetic characteristics of the crystal [Ketcham et al., 1999] and to a lesser extent on the etching conditions [Sobel and Seward, 2010]. Smaller D_{par} values (<1.75 μm) indicate low resistance to annealing; this means that annealing may occur even at lower temperatures, and relatively quickly [Donelick, 2005]. We corrected for our D_{par} values following the procedure outlined in Sobel and Seward [2010].

4.4. Results

We analyzed a total of 26 samples: 19 from the Chandra and Chenab valleys and 7 from the Beas Valley. Sample lithologies comprise meta-sediments, gneiss and leucogranites. 14 samples stem from three separate elevation transects; one elevation transect in the Beas Valley ranges from 2383 to 4145 m asl, two transects from the Chandra Valley range from 3130 to 4691 m asl. The latter include the proposed location of the STD [Webb, 2013]. All samples are from the MCT hanging wall. Except for the proposed STD, no significant faults have been documented in the sampling area in the past [e.g., Epard et al., 1995; Webb et al., 2007]. However, during fieldwork we were able to visit the Rohtang tunnel project where an approximately 1-km-wide cataclastic zone is exposed 3 km north of the tunnel entrance. Our new AFT cooling ages range from 1.7±0.2 to 13.6±1.7 Ma (Table 4.1, Figure 4.4; errors are quoted at the 1σ level). Dpar measurements of 1.46±0.16 to 1.85±0.37 μm indicate approximately homogenous track-pit sizes with little intra-sample variability. This indicates that most of our samples annealed relatively fast at low temperatures [Donelick, 2005].

Sample ages from the Beas and Parbati valleys range from 1.7±0.2 to 3.4±0.5 Ma with an increase in age with elevation of ~1.3 Myr/1600 m (~1.2 mm/yr) (Figure 4.5A). In the Chandra Valley, AFT ages range from 2.3±0.3 to 10.0±1.1 Ma (Figure 4.4). The youngest cooling ages in the Chandra Valley (<3 Ma) correspond to elevations of ~3200-3500 m asl, immediately north of the Rohtang Pass. In two elevation transects located in the Chandra Valley, the ages increase up to ~9 Ma with a gradient of ~5 Myr/1500 m (0.3 mm/yr) (Figure 4.5B); these data exhibit unusually pronounced age scatter and errors, compared to many other age-elevation transects in the northwestern Himalaya [Thiede et al., 2009]. Farther northwest and northeast, older (~5-10 Ma) AFT ages are also found at lower elevations (3100-3900 m asl; Figure 4.4).

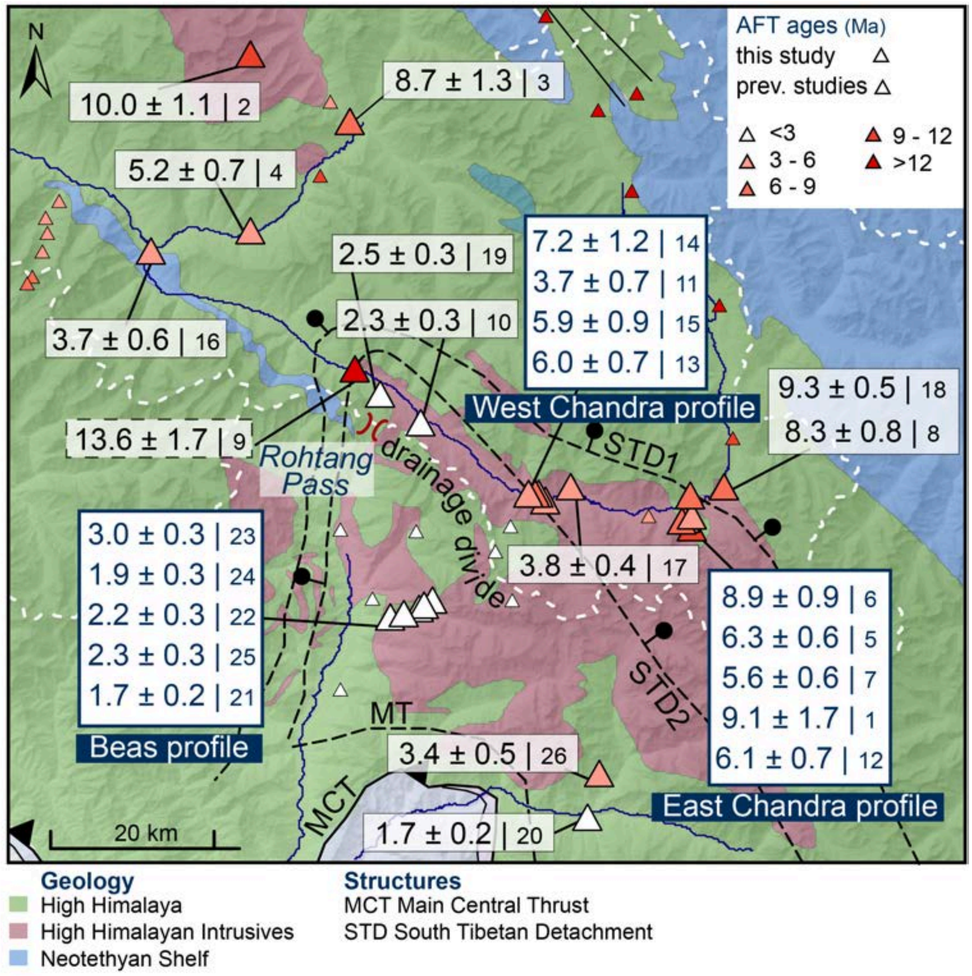

Figure 4.4: New and published apatite fission-track data from the upper Beas and Chandra valleys. Small boxes highlight the sample age (with uncertainties) and sample number (in small fonts; c.f., Table 4.1). The blue framed samples were collected along elevation transects shown in Figure 4.5. Geological map in the background is the same as in Figure 4.2 .

Sample #9 (PE12_047; 13.6±1.7 Ma) is significantly older than samples #19 and #10 (807A1 and PE12_053; 2.3±0.3 and 2.5±0.3 Ma) from similar elevations and at a distance of ∼400 m (Figure 4.4, Figure 4.5B). Because younger ages are also documented farther northwest (#4 and #16 – 3.7±0.6 and 5.2±0.7 Ma), we interpret sample #9 as an outlier, which we therefore did not include in Figure 4.7. Our new ages are in good agreement with previously published AFT ages from the Beas and Chandra valleys [Schlup, 2003] and help to better constrain existing regional age trends and the regional 3D-pattern of exhumation in this region.

Table 4.1: Apatite Fission-Track (AFT) data from the Beas and Chandra valleys

Sample	Lithology	Lat	Long	Altitude	XI[a]	Rho-S[b]	NS[c]	Rho-I[b]	NI [c]	$P(\chi^2)^d$	Rho-De	ND[f]	Age		Dpar	SD	Analyst[g]
		°N	°E	m asl		x10^6		x10^5		%	x10^6		Ma		μm	μm	
RT11-39	Two-mica gneisss	32.2755	77.5746	4330	16	0.775	62	16.179	1295	4	8.680	3661	9.1	1.7	1.50	0.19	PE
RT11-28	Two-mica gneisss	32.7339	77.0902	4770	33	1.427	289	24.666	4997	2	8.610	3661	10.0	1.1	1.55	0.16	PE
RT11-29	Sandy siltstone of the Haimantas	32.6677	77.2016	3410	26	0.673	67	12.688	1263	16	8.530	3661	8.7	1.3	1.57	0.17	PE
RT11-30	Sandy siltstone of the Haimantas	32.5662	77.0865	3240	36	0.516	70	16.142	2189	19	8.460	3661	5.2	0.7	1.62	0.29	PE
PE12_014	Metamorphic granite	32.2834	77.5665	4599	39	1.035	316	23.766	7257	14	7.460	2962	6.3	0.6	1.74	0.30	PE
PE12_015	Coarse gneiss	32.2816	77.5638	4691	34	1.451	200	23.322	3215	25	7.430	2962	8.9	0.9	1.64	0.30	PE
PE12_017	Coarse gneiss	32.2858	77.5742	4495	35	0.957	234	24.427	5975	18	7.370	2962	5.6	0.6	1.64	0.26	PE
PE12_021	Medium grained granite	32.3128	77.6110	3975	21	2.221	252	37.768	4286	14	7.310	2962	8.3	0.8	1.65	0.29	PE
PE12_047	Medium- to coarse grained gneiss	32.4334	77.2016	3124	41	0.407	104	4.204	1073	14	7.250	2962	13.6	1.7	1.48	0.28	PE
PE12_053	Medium- to coarse grained gneiss	32.3807	77.2729	3214	40	0.272	73	16.259	4364	81	7.220	2962	2.3	0.3	1.76	0.25	PE
PE12_054	Medium- to coarse grained gneiss	32.3042	77.4110	3505	26	0.248	37	9.367	1400	100	7.190	2962	3.7	0.7	1.50	0.36	PE
PE12_059	Schist	32.3055	77.5734	3786	34	0.806	155	17.477	3360	6	7.160	2962	6.1	0.7	1.65	0.31	PE
PE12_065	Meta-sediment and gneiss	32.3113	77.4049	3130	43	0.336	108	7.757	2494	43	7.130	2962	6.0	0.7	1.68	0.32	PE
PE12_066	Metasediment	32.3111	77.4003	3983	32	0.269	43	7.696	1232	60	10.682	4529	7.2	1.2	1.85	0.37	PE
PE12_068	Metasediment	32.3105	77.3935	3570	32	0.572	64	13.333	1491	6	7.070	2962	5.9	0.9	1.46	0.23	PE
RT11-31	Mica-rich sandstone of the Haimantas	32.5480	76.9756	2890	39	0.473	42	17.460	1549	96	7.040	2962	3.7	0.6	1.46	0.26	PE
B03B4	Hbl-bearing metasediment	32.3155	77.4400	3894	80	0.464	127	17.070	4671	54	7.215	7887	3.8	0.4	-	-	KS
804C1	Granite	32.3132	77.6109	4053	60	2.254	465	34.219	7060	41	7.267	7887	9.3	0.5	-	-	KS
807A1	Augengneiss	32.4079	77.2295	3474	136	0.178	119	10.500	7006	0	7.319	7887	2.5	0.3	-	-	KS
823G1	Leucogranite	32.0013	77.4511	2236	180	0.103	66	8.988	5766	72	7.424	7887	1.7	0.2	-	-	KS
010A1	Augengneiss	32.1972	77.2350	2383	120	0.139	120	11.947	10309	43	7.581	7887	1.7	0.2	-	-	KS
010D1	Augengneiss	32.2045	77.2674	3356	179	0.132	84	9.121	5819	0	7.633	7887	2.2	0.3	-	-	KS
011B1	Granitic augengneiss	32.2120	77.2828	4145	180	0.200	128	10.137	6503	0	7.685	7887	3.0	0.3	-	-	KS
011D1	Granitic augengneiss	32.2070	77.2734	3484	55	0.136	53	11.054	4303	12	7.738	7887	1.9	0.3	-	-	KS
011E1	Leucogranite	32.1999	77.2500	2851	80	0.228	65	15.295	4361	1	7.790	7887	2.3	0.3	-	-	KS
014B2	Quartzite	32.0429	77.4649	3443	125	0.073	42	3.328	1907	53	7.842	7887	3.4	0.5	-	-	KS

[a] the number of individual grains dated

[b] Rho-S and Rho-I are spontaneous and induced track densities measured in tracks/cm^2

[c] NS and NI are the number of spontaneous and induced tracks counted

[d] P(Chi)sq (%) is the chi-squared probability [Galbraith, 1981; Green, 1981]

[e] Rho-D is the induced track density in external detector adjacent to CN5 dosimetry glass in tracks/cm^2

[f] ND is the number of induced tracks counted on the U standard

[g] Zeta calibration use for apatite Patricia Eugster PE 386.1±27.8, Konstanze Stübner KS 389.1±6.8. The correction factor compared to Durango and Fish Canyon Tuff apatites [Sobel and Seward, 2010; Donelick et al., 1999] is 1.05 for PE.

4.5. Discussion

4.5.1. Age-elevation profiles and exhumation rates

In Figure 4.5, we combine our new AFT data from the Beas and Chandra valleys with ZHe ages from Stübner et al. [2018], which stem from the same sample locations. To better constrain the timing and magnitude of exhumation-rate changes in the High Himalaya, we constructed a composite vertical pseudo-elevation transect using AFT, ZHe, ZFT and ^{40}Ar/^{39}Ar data [Reiners et al., 2003] from the two valleys. In this transect, AFT ages are given with their true elevations, but for ZHe, ZFT and muscovite ^{40}Ar/^{39}Ar data elevations increase assuming closure temperatures of 120±10 and 200±10, 240±10, 350±50 °C for AFT, ZHe, ZFT, and muscovite ^{40}Ar/^{39}Arr, respectively [Gleadow and Duddy, 1981; Reiners et al., 2002; Reiners and Brandon, 2006]. We assume a high Pliocene geothermal gradient of 35°C/km in agreement with previous studies [Deeken et al., 2011; Stübner et al. 2018]. Although the analyzed zircons show high U and Th (eU) compositional variation, the repeated accuracy of similar ages of our samples documents that no systematic variation is recognized, most likely related to the rapid exhumation (>1 mm/yr). Ages from samples that were collected south of the Rohtang Pass (Figure 4.5A) display a relatively consistent trend of the combined ZHe and AFT ages (note that open symbols are from samples away from the elevation transect); the gradient of ∼0.65 Myr/km suggests exhumation with near-constant rates through this temperature range since at least ∼4 Ma. To facilitate regional comparison of exhumation rates, we estimate a first-order exhumation rate using the simple 1D-modeling AGE2EDOT approach [Brandon et al., 1998], and using the same parameters as in studies from adjacent areas (i.e., model thickness, 10-30 km; geothermal gradient, 35°C/km) [Deeken et al. 2011; Thiede et al., 2009]. Mean AFT ages of ∼2-3 Ma in the Beas-Parbati region imply erosion rates of ∼1-2 mm/yr, similar to erosion rates of ∼1-2 mm/yr obtained from mean ZHe ages of ∼3-5 Ma. The AGE2EDOT model is based on the assumption that erosion rates have been constant long enough that the thermal field achieved a dynamic equilibrium. We evaluate this assumption using RESPTIME, which calculates the advection velocity of closure isotherms, normalized to the assumed erosion rate, as a function of time since the onset of erosion [Brandon et al., 1998]. Using the same parameters as for AGE2EDOT, we find that after 4 Myr of erosion, the closure-temperature isotherms of AFT and ZHe advect at 10% and 20% of the imposed erosion rate, respectively, suggesting near-steady state thermal conditions [Reiners and Brandon, 2006]. Even though, in near-steady state, the closure-temperature isotherms were presumably not subhorizontal at the onset of erosion due to previous advection. Therefore, we propose that the High Himalaya south of the Rohtang Pass has been exhuming at ∼1-2 mm/yr since at least 4 Ma. The available data south of the Rohtang Pass do not provide any additional information, as to when this rapid exhumation began. However, the data from the north (see discussion below) and thermal modelling results of Stübner et al. [2018] suggest that the present-day pattern, has been established since 8-10 Ma. The overall cooling pattern across the Rohtang Pass is most likely controlled by oblique upward thrusting along several active out-of-sequence basement thrust, in the Beas region most likely related to faulting along the MT [Stübner et al., 2018].

AFT ages from the Chandra Valley, and corresponding ZHe ages [Stübner et al., 2018], are generally older than those from south of the pass, and especially the AFT chronometer shows significant variability

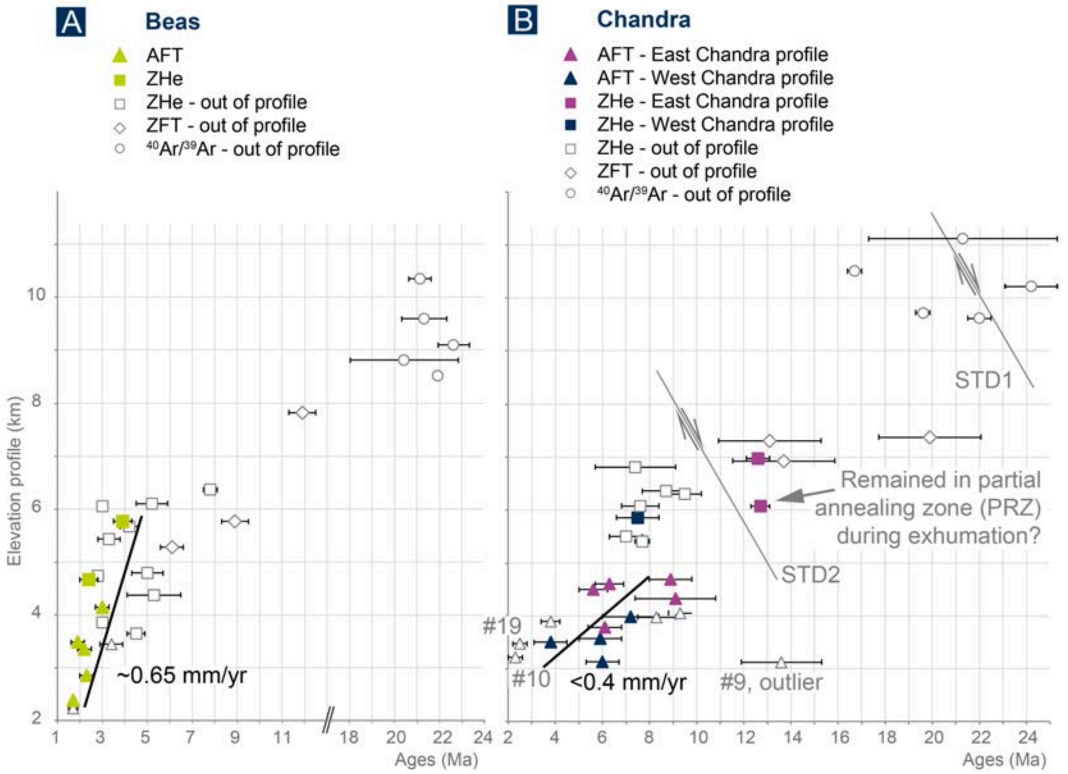

Figure 4.5: New AFT- and published ZHe- [Stübner et al., 2018], ZFT- [Schlup, 2003], ^{40}Ar/^{39}Ar- [Schlup, 2003; Stübner et al., 2014] cooling ages, plotted against their pseudo-elevation from (A) the Beas Valley and (B) the Chandra Valley; see Figure 4.4 for location. Figure 4.5B includes the suggested STD(1) and STD(2). Grey open symbols correspond to off-profile samples. See text for definition.

in the ages of samples from similar elevation. Within the Chandra Valley we observed two cooling stages: (a) rapid cooling between 13 and 7 Ma based on ZHe, ZFT cooling ages (Figure 4.6), and (b) slow cooling between 9 and 3 Ma based on the age patterns of the AFT data (∼0.3 mm/yr). During that time the large scatter of ages from the AFT samples indicate that they must have stayed within or moved slowing through the partial annealing zone. AFT ages <3 Ma near to, but north of the Rohtang Pass, indicate rapid cooling during the last 3 Ma (∼1 mm/yr). ZHe both to the north and west of Rohtang are >12 Ma and indicate slow exhumation rates of <0.5 mm/yr since the middle Miocene. One possible explanation for this cooling scenario is the movement of the rocks north of the Rohtang Pass over a ramp-flat-ramp structure, where rapid cooling occurs when the rocks pass over the ramps, while slow cooling occurs when the rocks move along the flat.

Whatever the true exhumation path is, the data show a strong increase of age with (pseudo-)elevation (∼10 Myr/4000 m; 0.4 mm/yr; Figure 4.5B), suggesting slower late Miocene to Pliocene erosion and exhumation compared to the Beas Valley. We use the slope of the age-elevation trend (∼0.3 mm/yr) as an apparent exhumation rate in the Chandra Valley. Because of the steep spatial gradients in AFT and ZHe ages in the upper Chandra Valley toward middle Miocene AFT ages over a distance of only a few kilometers [Schlup, 2003; this study; Figure 4.4]. For example, the >10 AFT,∼12-20 Ma ZHe, and >15 ZFT cooling ages, could reflect partially reset and non-reset ages since the middle Miocene and reflect a mean exhumation <0.3 mm/yr since that time. These cooling ages stem from the hanging wall of Zanskar shear zone and STD(1) and document no tectonic exhumation (fault activity) since the middle Miocene along the STD(1) or Zanskar Shear Zone (figures 5B, 6). We note that the present-day orographic barrier coincides with a pronounced northward increase of AFT and ZHe cooling ages from Pliocene to middle Miocene in the upper Chandra Valley and beyond. A possible conclusion is that the location of the topographic crest of the High Himalaya may have already existed here by the middle Miocene and that the orogenic interior (Lahul) may thus have been characterized by more arid conditions since then. However, we also note that during this time, the locus of active deformation and rock uplift was different from the present and thus the position of the high topography and the orographic barrier may have been quite different.

In contrast, samples and cooling patterns south of the Rohtang Pass exhibit continuous rapid denudation (AFT 1-3 Ma, ZHe 2-5 Ma, ZFT 6-9 Ma) since at least late Miocene time [Schlup et al., 2013; Stübner et al., 2018]. In contrast to the Chandra Valley, the cooling pattern suggests that rocks are moving continuously over deep-seated ramps from depths >6 km (assuming a thermal gradient 35°/km), most likely related to the MT [Vannay et al., 2004; Stübner et al., 2018]. This zone of rapid cooling along the Beas is exposed along a 20 to 30-km-long, NE-SW-oriented transect; this indicates that the area is too wide to be a single exhuming block which is moving over a ramp. This therefore suggests the existence of several ramps and/or basement thrust ramps.

In summary, the regional cooling pattern illustrates that the exhumation pattern of the study area is episodic. During the late Oligocene to early Miocene, thrusting along the MCT and extrusion along the STD(1) exhumed the GHS rapidly from $\sim$20-30 km depth to shallow crustal depth resulting in cooling below the muscovite ^{40}Ar/^{39}Ar closure temperature by $\sim$21 to 15 Ma [Vannay et al., 2004; Schlup et al., 2011; Stübner et al., 2014]. Results of previous thermal modelling studies [Thiede et al., 2009; Stübner et al., 2018] suggest that low ($\sim$0.3 mm/yr) middle Miocene exhumation rates in central Himachal Himalaya can be attributed to a shallow dip of the MCT [Stübner et al., 2018]. This reveals two temporal and spatially varying stages of rock exhumation in the footwall of the STD, which we separated into an early phase (late Oligocene to early Miocene) referred to as STD(1) and a second late phase (middle to late Miocene) as STD(2). This second phase is constrained by ZFT and ZHe-data between 13-7 (Figure 4.6). In the Beas region the location of the STD is stable, in the Sutlej region the STD(2) is moving into the footwall (Figure 4.2). During the late Miocene – Pliocene exhumation due to accretion processes and stacking of crustal nappes along the MHT have lead to the development of the Lesser Himalayan duplex and the LKRW antiform to the south. During this time a major fault ramp has been established in the hanging wall of the Lesser Himalayan duplex [Vannay et al., 2004; Stübner et al., 2018]. Rapid exhumation above this ramp is reflected by a $\sim$40-km-wide belt of Pliocene ZFT, ZHe and AFT cooling ages northeast of the LKRW [Thiede et al., 2009; Schlup et al., 2011; Stübner et al., 2018 and this study]. These results agree with earlier interpretations that the periodicity of exhumation is caused by the passage of material points over ramp and flat segments of the basal detachment as well as out-of-sequence fault zone in the hanging wall resulting in variable rock uplift rates in space and time [Stübner et al., 2018].

Using the similar AGE2EDOT approach, Deeken et al. [2011] obtained exhumation rates of $\sim$1 mm/yr in the Dhauladar Range (cf., Figure 4.2, Figure 4.3) and $\sim$0.5 mm/yr in the Pir Panjal Range during the middle Miocene to Pliocene. This northward decrease in erosion rates is similar to the patterns obtained for the Beas Valley. Thiede et al. [2009] and Stübner et al. [2018] obtained exhumation rates of 2-3 mm/yr since the late Miocene-Pliocene in the Sutlej and Beas valleys, respectively. The higher erosion rates suggested by Stübner et al. [2018], compared to our estimates for the same area (2-3 mm/yr vs. ~1 mm/yr) may result from the different modeling approaches (Pecube vs. AGE2EDOT) and/or the different input data (ZHe vs. AFT).

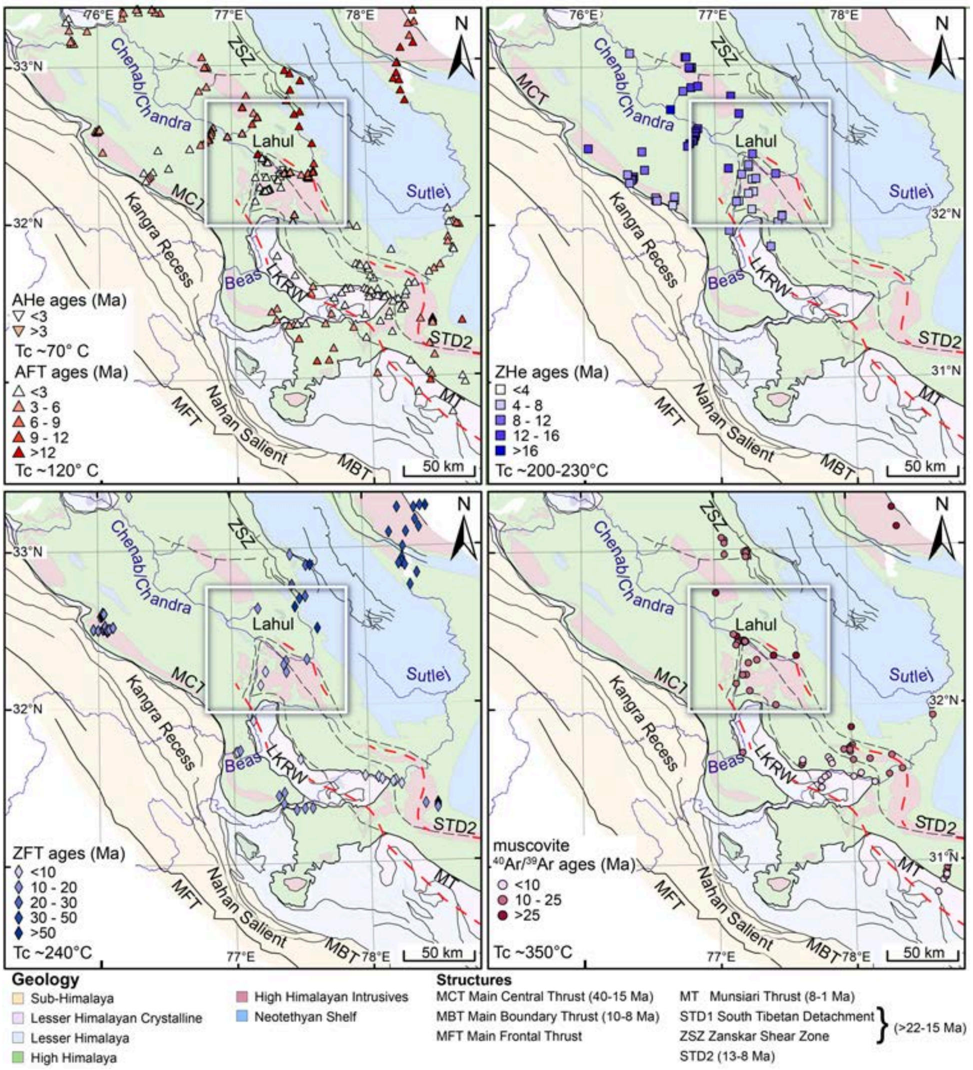

Figure 4.6: Overview of published and new thermochronometry data from the study area (rectangle) and adjacent regions. Data sources: Kumar et al. [1995], Dèzes et al. [1999], Lal et al. [1999], Jain et al. [2000], Schlup [2003]; Thiede et al. [2004], Vannay et al. [2004], Thiede et al. [2005], Thiede et al. [2006], Adams et al. [2009], Adlakha et al. [2013]; Stübner et al. [2014]; Stübner et al. [2017]; Thiede et al. [2017]; Stübner et al. [2018]. Closure temperatures (Tc) after Wolf et al. [1998], and Farley [2000] for apatite U/Th-He (AHe), Gleadow and Duddy [1981] for apatite fission track (AFT), Reiners et al. [2002] for zircon U/Th-He (ZHe), Brandon et al. [1998] for zircon fission track (ZFT), and Hodges [1991] for muscovite ^{40}Ar/^{39}Ar. LKRW= Larji-Kullu-Rampur window. Red dashed lines indicate extent of the belt of rapid exhumation and see text for definition.

4.5.2. Orogen-perpendicular transects

For a better understanding of the observed lateral variation in exhumation patterns in light of regional-scale deformation, we integrated our results with a compilation of previously published low-temperature thermochronometry data across northwestern India (Figure 4.6). We illustrate the lateral change in deformation along the transition zone between the Central and Western Himalaya using three approximately orogen-perpendicular transects, each 200 km in length and compile existing thermochronology data from a 50-km-wide swath (Figure 4.7, footprint of swath profiles shown in Figure 4.2A, topography and rainfall along swath profile shown in Figure 4.3). Although the transects are located only several tens of kilometers apart from each other, the topography, fault geometry, and exhumation patterns change significantly along strike in this part of the orogen. From west to east, the three transects are situated along the Dhauladar Range (Figure 4.7A), which resembles a typical Western Himalaya tectonic setting, the Beas Valley (Figure 4.7B), marking the transition zone, and the Sutlej Valley (Figure 4.7C), which resembles a typical Central Himalaya tectonic setting. The structural profiles are based on earlier work in the Dhauladar Range, Lahul/Beas, and Sutlej areas [Steck, 2003; Vannay et al., 2004; Deeken et al., 2011; Webb, 2013; Thiede et al., 2017; Stübner et al., 2018]. Note that we projected the thermochronology data from within each swath into the profiles, whereas structural boundaries are from the centerline. Where faults and geologic boundaries traverse the swaths obliquely, slight mismatches between structures and thermochronology data may occur.

In the Dhauladar Range (Figure 4.7A), young ZHe ages (<5 Ma), which constrain rapid Pliocene exhumation with rates of 2-3 mm/yr, are limited to a 40-km-wide zone, immediately north of the MBT [Deeken et al., 2011; Thiede et al., 2017]. Most of the MCT hanging wall is characterized by older ZHe (10-18 Ma) and AFT (∼3-10 Ma) ages, reflecting mean erosion rates of ∼0.5 mm/yr since ∼15 Ma [Thiede et al., 2017; Deeken et al., 2011]. In this transect, the PT_2 is neither defined as a major physiographic transition, nor is there a swath of young cooling ages or the existence of the STD(2) that would correspond to rapid exhumation in the orogenic interior as identified in the Beas and Sutlej transects (Figure 4.7).

Along the Beas transect (Figure 4.7B), which includes our study area, a ∼65-km-wide zone of high local relief corresponds approximately with the region northeast of the PT_2, which is less well defined here than farther to the southeast (i.e., Sutlej transect; figures 3B, 7C). The northeastern part of this zone coincides with a ∼35-km-wide band of young AFT (<3 Ma) and ZHe (<5 Ma) ages [this study; Schlup, 2003; Stübner et al., 2018]. Muscovite $^{40}Ar/^{39}Ar$ ages in this sector are significantly older (∼20 Ma) and have been attributed to Early Miocene extrusion between MCT and STD(1) [Stübner et al., 2014], suggesting that high exhumation rates were established within this topographic band in the late Miocene [Stübner et al., 2018]. Possible explanations for this rapid exhumation include thrusting over a mid-crustal ramp [c.f., Herman et al., 2010, and references therein], in combination with the growth of a Lesser Himalayan duplex, and/or thrusting (basement thrust ramp) along the MT [Stübner et al., 2018]. Although we argue above that an orographic effect accounts for the northward decrease in erosion rates and hence an increase in cooling ages, higher rainfall is probably not the only reason for rapid exhumation, because (1) the highest mean annual rainfall occurs ∼50 km southwest of the band of young cooling ages; (2) the band of young cooling ages coincides with the proposed location of an MHT ramp [Stübner et al., 2018] and the Lesser Himalayan duplex associated with the LKRW-antiform [Vannay and Grasemann, 2001; Webb, 2013]; and (3) a climate-driven mechanism does not readily explain the lateral changes in exhumation pattern from the Sutlej to the Dhauladar transects (Figure 4.6).

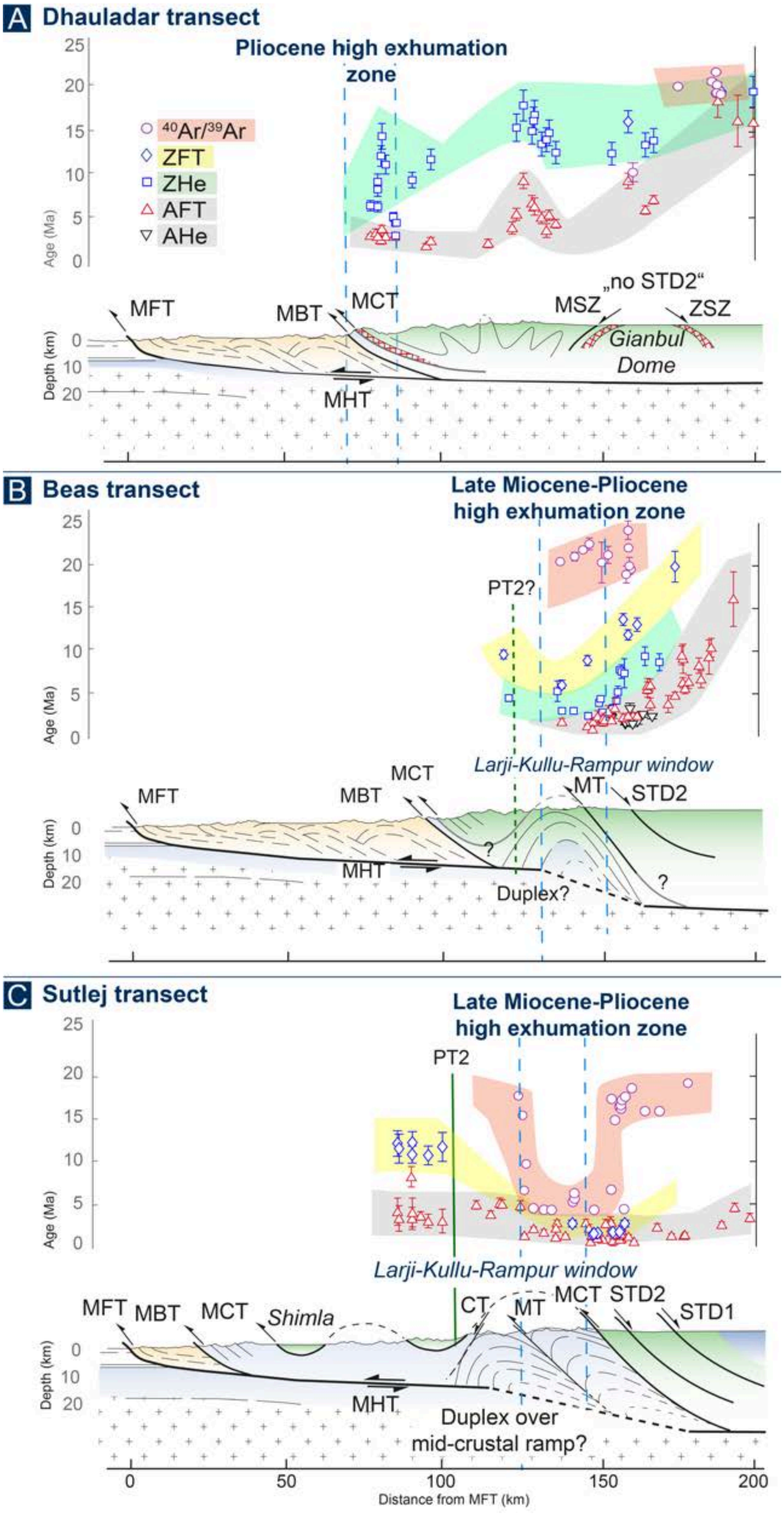

Figure 4.7: Transverse profiles across (A) the Dhauladar Range, (B) the Beas and Chandra valleys, and (C) the Sutlej Valley. In each transect, the upper panel shows the respective thermochronometer cooling ages [Kumar et al., 1995; Dèzes, 1999; Lal et al., 1999; Jain et al., 2000; Schlup, 2003; Thiede et al., 2004; Vannay et al., 2004; Thiede et al., 2005; Thiede et al., 2006; Adams et al., 2009; Stübner et al., 2014; Stübner et al., 2017; Thiede et al., 2017; Stübner et al., 2018]. The lower panel shows inferred subsurface geometry; beneath the Dhauladar Range a steeply dipping frontal ramp is proposed to cause rapid exhumation at the MBT [Thiede et al., 2017], where no evidence for STD(2) activity exists. In the Beas/Chandra valleys and the Sutlej Valley, combined deformation related to the growth of the Lesser Himalayan duplex occurs; here, rocks move over a mid-crustal ramp, and active faulting in the hanging wall leads to high local relief and rapid exhumation. Please note that the physiographic transition 2 (PT_2) is well defined in the Sutlej transect, but disappears farther northwest (see Figure 4.2C).

Along the Sutlej transect (Figure 4.7C) a zone of rapid late Miocene-Pliocene exhumation is reflected by a ~25 to 60-km-wide band of young AFT and ZFT ($\leq$5 Ma) and muscovite ^{40}Ar/^{39}Ar cooling ages (<8 Ma) between the MT and STD(2) [Jain et al., 2000; Vannay et al., 2004; Thiede et al., 2004, 2005, 2009]. Extrusion of Lesser Himalayan Crystalline rocks, accommodated by thrusting on the MT since the late Miocene [Caddick et al., 2007] and possibly assisted by normal-fault reactivation of the STD(2) in the MCT hanging wall, accounts for young cooling ages in the MCT footwall [Vannay et al., 2004]. However, Thiede et al. [2005; 2009] show that young cooling ages occur in a localized zone along the Sutlej River, which includes both MCT and STD(2) hanging and footwalls, and attribute cooling through the AFT closure temperature to protracted incision of the Sutlej River [c.f. Vannay et al., 2004]. Towards the southeast and northwest, the band of young AFT cooling ages is structurally bounded by the MT and STD(2), respectively; this suggests that the belt of young cooling ages in the Sutlej transect is related to the combined effect of tectonically driven exhumation over a mid-crustal ramp and/or duplex and sustained vigorous river incision [Vannay et al., 2004; Thiede et al., 2005].

From Garhwal to central Nepal (77°E-91°E), the PT_2 consistently delineates the boundary between a moderate-relief landscape and the slowly eroding (<1 mm/yr) Lesser Himalaya, and a high-relief, rapidly eroding (>1 mm/yr) High Himalaya [Hodges et al., 2001; Scherler et al., 2014; Godard et al., 2014; Morell et al., 2017]. The lateral changes in physiographic characteristics and exhumation rates between the Sutlej, Beas and Dhauladar transects since ~5-10 Ma document the lateral termination of the PT_2 in the northwestern Himalaya (Figure 4.2C). In the Sutlej and Beas transects, the high exhumation zone north of the PT_2 corresponds to tectonically driven rock uplift above an MHT ramp or duplex (Figure 4.7) [Stübner et al., 2018]. Singh et al. [2018] document earthquake moment-tensor solutions for a seismicity cluster at depths between 5 and 10 km within the LKRW of the Sutlej transect, which are consistent with ~30° NE-dipping fault planes in the Lesser Himalayan duplex. In contrast, the lower exhumation rates and older cooling ages throughout the Dhauladar transect have been attributed to a gently dipping MHT with no evidence for a ramp or a Lesser Himalayan duplex structures [Deeken et al., 2011; Thiede et al., 2017].

4.5.3. Potential causes for changes in tectonic style in the NW Himalaya

Various factors have been proposed to influence the tectonic style, pattern of deformation, and topography in the Himalaya in general. Amongst these are:

1) The far-field, plate-tectonic effects on the kinematics and the arcuate shape of the Himalaya result in westward-increasing obliquity in the convergence between India and Tibet, which ought to be associated with increasing partitioning of deformation [e.g., Styron et al., 2011; Kundu et al., 2014; Thakur et al., 2014; Whipp et al., 2014].

2) Because the amount of rainfall varies along strike of the mountain belt [e.g., Bookhagen and Burbank, 2006] from east to west, it may be assumed that erosion decreases westward and impacts the tectonic stress field, which may ultimately lead to different patterns of deformation [e.g., Willett, 1999].

3) Along-strike variations in the thickness of the Proterozoic sedimentary cover on the Indian margin may lead to variations in the style and pattern of sediment accretion and duplex formation [e.g., Raiverman et al., 1983; Rajendra Prasad et al., 2011].

4) Approximately northeast-trending ridges in the Indian basement form asperities that may affect deformation and exhumation patterns in the overthrusting orogenic wedge [Arora et al., 2012]. A related mechanism is the reactivation of pre-orogenic normal faults in the Indian basement, which may lead to the formation of lateral or oblique ramps in the basal thrust of the orogen [Powers et al., 1998; Dubey et al., 2004].

The above considerations may explain many salient features of Himalayan topography, structures, and exhumation patterns. However, a simple explanation for lateral variations, based on the presented data, is not yet possible. While some of the above factors are more likely to account for gradual and progressive along-strike changes (models 1 and 2), others are more likely to account for abrupt spatial variability (models 3 and 4). Because recent studies have suggested that tectonics – not climate – is the dominant control of the spatial pattern of erosion [e. g., Godard et al., 2014; Scherler et al., 2014; Olen et al., 2015], we focus on the scenarios (1), (3), and (4), which we consider to explain best the observed abrupt changes in geology, topography, and exhumation pattern from the Central to the Western Himalaya. In the following sections we discuss viable causes and mechanisms that may be responsible for lateral variations in tectonic style and exhumation patterns, considering the observed regional changes at the transition between the Central and the Western Himalaya.

The western termination of the PT_2 coincides with the prominent Kangra recess and a significant westward narrowing of the exposure of Lesser Himalayan rocks and a widening of the Sub-Himalaya at 77°E (Figure 4.1). Recesses and salients in mountain belts are commonly attributed to spatial variations in the thickness of sedimentary cover rocks that can be easily scraped off and incorporated into orogenic wedges [e.g., Macedo and Marshak, 1999]. The Proterozoic Vindhyan Supergroup covers large parts of the Indian basement and underlies much of the Indo-Gangetic foreland basin [e.g., Valdiya, 1995; Raiverman, 2002; Yin, 2006]. Based on seismic reflection data, Rajendra Prasad et al. [2011] demonstrate a northwestward decrease in the thickness of the Vindhyan formations and, in particular, a significant reduction in stratigraphic thickness from the Nahan salient (Sutlej transect) to the Kangra recess (Beas transect). These authors proposed that lateral variations in stratigraphic thickness and regional extent account for the salient–recess geometry at $\sim$77°E, which affects the mechanics within the Himalayan orogenic wedge [Macedo and Marshak, 1999]. These authors furthermore argue against a lateral basement ramp between the Kangra recess and the Nahan salient, for which they find no evidence in seismic reflection data [c.f. Powers et al., 1998]. Extending the argument of Rajendra Prasad et al. [2011] to regional scale, one could explain the change in tectonic style from the Central to the Western Himalaya, and the lateral termination of the PT_2 in northwestern Himalaya, if the Proterozoic units were generally thicker in the east compared to the west. Such a decrease of stratigraphic thickness of the Indian sedimentary cover could account not only for the reduced width of the LHS exposure west of 77°E, but also the shallower exhumation (i.e., the low-grade metamorphic Haimantas units west of Beas vs. the high-grade metamorphic core to the east) and lower exhumation rates in the northwestern Himalaya.

The influx of material into orogenic wedges is, however, controlled not only by the sediment thickness but also by the convergence rate [e.g., Dahlen, 1990]. It has been noted previously that the westward increase in the obliquity of the convergence direction between India and Tibet ought to be associated with increasing partitioning of deformation [e.g., Styron et al., 2011; Kundu et al., 2014; Thakur et al., 2014; Whipp et al., 2014]. The GPS-derived convergence rate between Tibet and India decreases from ∼20.2±1.1 mm/yr in central Nepal (∼83°E) to ∼18.5±1.8 mm/yr in the northwestern Himalaya (∼79°E) and ∼13.3±1.7 mm/yr in Kashmir (∼76°E) [Stevens and Avouac, 2015]. Kundu et al. [2014] determined ∼13.6 mm/yr frontal convergence in the northwestern Himalaya (∼76-78°E), which is oblique to the overall orientation of the Himalayan arc. Split into an arc-normal component of 11.8 mm/yr and an arc-parallel dextral component of 6.7 mm/yr; this estimate may imply an even stronger westward decrease in arc-normal convergence rates. A westward decrease in arc-normal convergence will have a similar effect as a westward decrease in the thickness of the sedimentary cover: the reduced material flux into the orogenic wedge may lead to reduced exhumation within the wedge to maintain the material-flux balance [e.g., Macedo and Marshak, 1999]. Sustained lower convergence rates would be associated with a westward decrease of the total amount of shortening. Although currently available data do not readily support the interpretation of a decrease of total shortening with increasing obliquity of the convergence direction [e.g., DeCelles et al., 2002; Bhattacharyya and Ahmed, 2016], we note that these estimates are notoriously difficult to obtain and fraught with uncertainties.

Finally, kinematic models of the evolution of the Himalayan orogenic wedge highlight two distinct phases; first, with long-distance overthrusting of the Tethyan Himalaya, followed by basal accretion and duplex formation leading to substantial amounts of shortening and crustal thickening [e.g., Robinson et al., 2001]. The activation of duplex structures may in fact be related to the thermal and rheological evolution of the orogen and the depth of the brittle-ductile transition [e.g., Avouac, 2007]. Within this context, the amount of crustal thickening and heating, which can be related to both total shortening and the thickness of cover rocks that are scraped off the lower plate, may reach a critical threshold at which duplex formation initiates. If this were true, the transition in tectonic style may be expected to migrate westward through time, and the formation of duplex structures were yet to follow in the western Himalaya.

In summary, the combination of both effects — the westward decreasing convergence rate and, consequently, total shortening, as well as potential thinning of the Proterozoic cover units — may account for the low exhumation documented in the northwestern Himalaya. However, neither of these effects predicts the relatively sharp transition from high exhumation and a well-defined PT_2 to the low exhumation as we have documented in the area between the Sutlej and Dhauladar transects. Future studies may reveal whether this sharp transition may be attributed, for example, to pre-existing structures or to some threshold mechanism that controls orogenic-wedge evolution.

4.6. Conclusions

We presented new AFT ages and field observations from northwestern India that constrain the spatial extent and structural characteristics of the western termination of the high-exhumation belt along strike of the Himalayan arc. Our newly obtained AFT data help to better delimit the spatial extent of those parts of the Himalaya that are characterized by young cooling ages and rapid exhumation ($\sim$1-2 mm/yr) of metamorphic core area of the Himalaya. This region is bounded to north and south by areas characterized by significantly older cooling ages, and therefore lower exhumation rates ($\leq$0.4 mm/yr). Our results suggest that the termination of the high-exhumation belt coincides with a northward-plunging crustal-scale antiform and major out-of-sequence basement thrust along the northwestern border of the Larji-Kullu-Rampur window. We interpret this crustal-scale antiform to be part of the Lesser Himalayan duplex structure. We discuss possible factors that help explain the transition in tectonic style from the Central to the Western Himalaya. We hypothesize that the combination of westward decreasing thickness in Indian cover sediments that are potentially available for underthrusting in the orogenic wedge, and westwardly decreasing arc-normal shortening, due to increasingly oblique convergence and strain partitioning, may be responsible for the inferred disappearance of a mid-crustal ramp, out-of-sequence basement thrust, and the formation of Lesser Himalayan duplexes.

Acknowledgements

This study was funded by DFG (Deutsche Forschungsgemeinschaft) grants to M. Strecker (STR 373/19-2; part of the graduate school GRK 1364) and R. Thiede (TH 1371/5-1) and DAAD-DST (PPP-India # 57035520) to R. Thiede and V. Jain. K. Stübner was funded by DFG grant STU 525/1-1 and the Excellence Initiative of the University of Tübingen. We thank V. Jain and T. Tsering Longpo for logistical support during the field seasons in India, P. Ballato, S. Dey and S. Olen for helpful discussions, and J. Faruhn for assistance with sample preparation. We also thank two anonymous reviewers and the AE S. Long for their comments that increased the quality of the manuscript significantly. Data on apatite fission-track cooling age calculation and rate calculations are provided in the supporting information of this manuscript.

5 Discussion

The aim of this study of the southern front of the Himalayan orogen in northwestern India was to better understand the processes that force landscape evolution on short and long timescales. At this specific location, both, climatic and tectonic processes strongly impact surface processes by creating pronounced topographic, rainfall and surface-process gradients due to the superposition of precipitation gradients parallel and perpendicular to the mountain belt. Moisture-bearing winds impacting the Himalaya are related to two atmospheric circulation systems: the ISM and the westerlies, enhancing fluvial but also glacial erosion along the windward flanks. In addition to the climatic impacts, this region is subjected to frequent large-magnitude earthquakes and deformation sustained over long timescales related to the ongoing convergence between India and Eurasia [e.g., Bilham et al., 2001 Avouac, 2015; Stevens and Avouac, 2015;]. In the study area, which spans from the southern humid mountain front of the Himalaya northward to the more arid parts of the Karakoram ranges, I studied landforms and low-temperature conditions of the exhumed rocks to assess the different processes that are responsible for the overall geomorphic and geologic evolution of the region.

In addition to the landscape-evolution aspects that I studied, my work has resulted in several methodological aspects that are associated with the use of the TCN-method. Therefore, the discussion is split into subchapters that focus on:

- The TCN-dating of landforms, although an established method in geochronology and geomorphology for many years, results in uncertainties in this study region, mainly occur due to the absence of a calibration site in the Himalaya and different scaling schemes (chapter 5.1).
- How the landscape developed on the short- and long-term by the influence of interacting climatic and tectonic drivers (in chapters 5.2 and 5.3).
- Finally, the findings of this study are set in context with further Himalayan studies on landscape evolution (in chapter 5.4).

5.1. Ambiguities in the use of the TCN-method

It has been shown that the use of recently available online calculators to obtain ^{10}Be derived exposure ages (e.g., CRONUS-Earth online calculator – University of Washington, CRONUS web calculators – University of Kansas) and the corresponding scaling schemes lead to a range of exposure ages for each sample. Even though additional calculators and calibrations for other parts of the world are available, for the Himalaya I only considered the CRONUS web and CRONUS-Earth online calculators. Borchers et al. [2016] established a new calibration data set, which is included in the CRONUS web calculator [Marrero et al., 2016], which also contains Lifton et al.'s [2014] latest scaling; this new calculator was used for age calculations presented in chapter 2. Borchers et al.'s [2016] calibration was also integrated in the current CRONUS-Earth online calculator v. 2.3, because of excessive (10%) production rates in the previous version 2.2 [https://cosmognosis.wordpress.com/2016/08/01/let-a-hundred-flowers-bloom/] (status February 2017).

In light of these issues I demonstrated in the Chandra Valley that using the newly CRONUS web calculator ages <25 ka may increase to 24% compared to Balco's calculator [Balco et al., 2008]. Similar issues are revealed in the Shyok data (Figure 5.1), where the obtained ages differ between the different used calculators and among the different scaling schemes. The corresponding values range between 11 and 38%. Interestingly, the most pronounced increase in ages results from the CRONUS-Earth online calculator v. 2.2 [Balco et al., 2008] compared to the CRONUS web calculator [Borchers et al., 2016; *Marrero et al., 2016*]. However, the oldest ages are obtained by the CRONUS web calculator, whereas the ages of obtained from the CRONUS-Earth online calculator (v. 2.3) are slightly younger. Interestingly, ages of the Lal/Stone time-dependent (Lm) scaling are remarkably similar to the ages obtained using the new scalings of Lifton et al. [2014] (Sa and Sf) and Lm ages scatter less than ages calculated from other scalings (Figure 5.1). However, the second observation is most likely owed to the fact that Lm depends

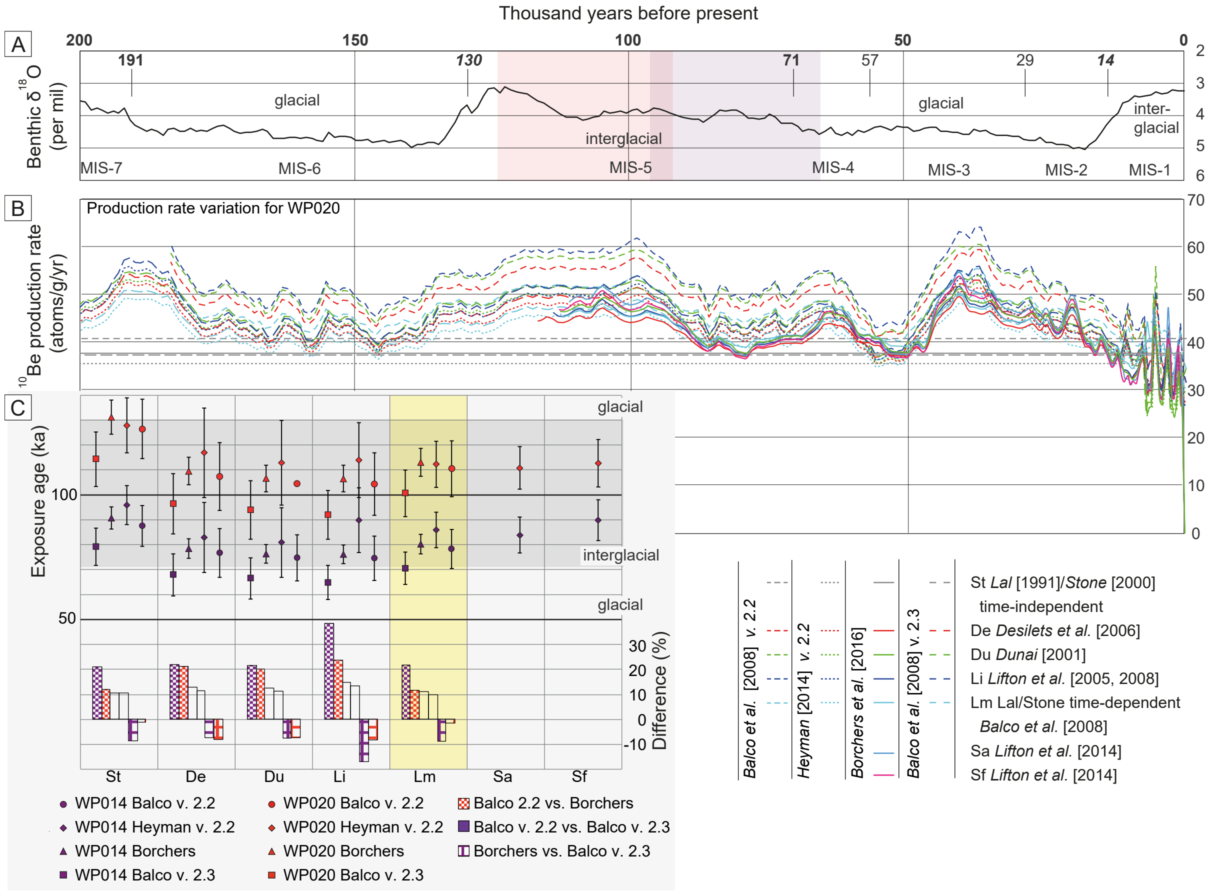

Figure 5.1: Comparison of production rates and exposure ages of two samples from the Shoyk area. A) Benthic δ^{18}O stack and Marine Isotope Stages (MIS) of Lisiecki and Raymo [2005] and glacial and interglacial phases during the last 200,000 years. Bold black numbers indicate onset of glacial periods, bold black numbers in italics indicate the onset of interglacial periods, respectively. Light red and purple boxes represent the age range of the two recalculated samples WP014 and WP020 derived from different CRONUS calculators as determined by different scaling schemes. B) Production rates according to the different scaling schemes and calibration sets of the CRONUS calculators used in this study (status February, 2017). C) Samples WP014 and WP020 recalculated according to the data published in chapter 3 with a bulk density of 2.7 g/cm^3 for WP014 and 2.0 g/cm^3 for WP020. Light grey box indicates the interglacial, the light yellow box highlights Lal/Stone time-dependent (Lm) ages.

on fewer parameters than the other scalings (see Table 1.1 for comparison). As shown in Figure 5.1 the increase of exposure ages is consistent with the decrease and adjustment of the ^{10}Be production rates. The magnitude of change in TCN ages has been discussed in earlier studies and is consistently around 30% [Lifton et al., 2014].

Because of these refinements due to better choice of calibration sites, scaling schemes and calculators, I would like to emphasize that the range of TCN-ages need to be considered with caution. Changes of 10% lead to different implications concerning possible global climatic impacts on glacial behavior and the formation of related landforms and deposits: e.g., an exposure age of 10 ka turns into 11 ka, whereas an exposure age of 100 ka increases to 110 ka. Such uncertainty and ambiguity may have lead to erroneous interpretations and the initially calculated ages may have been tied to a forcing event that is no longer viable. As illustrated in my study from the Chandra Valley the older ages obtained by the CRONUS web calculator shift the documented extensive glaciation towards the LGM (19–23 ka) [Mix et al., 2001; Lisiecki and Raymo, 2005] and furnishes information about post-LGM glacial behavior in the Himalaya by comparing it to global climate records. However, in the Shyok area the sample ages span over a much larger range than in the Chandra area and changes by 38% make a correlation with distinct events difficult. In my study this difficulty is illustrated by the ages of two surface samples (WP014, WP020) from Shyok. Sample WP014 stems from an erratic boulder on a moraine and yields ages between 65 to 96 ka and is therefore classified at the transition of a glacial to an interglacial period (red samples in Figure 5.1). In contrast to this, sample WP020 from a terrace surface is attributed to the middle of the interglacial period and the obtained ages range from 92 to 131 ka (purple colored samples in Figure 5.1). This is crucial, for example, when attributing aggradation and incision phases or glacial advances and retreats to external forcing mechanisms, such as insolation cycles.

5.2. Short-term TCN-exposure ages and landforms

In this study it has been suggested that during the LGM, prior to 20 ka, the Chandra Valley was covered by a voluminous valley glacier dated by well-preserved glacially polished bedrock ridges and previously dated boulders on moraines [Owen et al., 1996, 2001]. I showed that this valley glacier retreated very rapid and finally disappeared within a few thousand years after the onset of LGM deglaciation, possibly due to an increase in insolation. My study has been stimulated by the work of Owen et al. [1995, 1996, 1997, 2001] that postulated several glacial stages in this part of the Himalaya. In addition to the Himalayan studies mentioned in chapter 2, further ages from neighboring glaciated areas that were partly derived by other methods support extensive LGM glaciations in the monsoon-influenced high-mountain sectors and in the transition to the Transhimalaya such as the Sarchu Plain or the Goriganga Valley [e.g., Ali et al., 2013; Pinkey et al., 2015; Sharma et al., 2015]. In general, Himalayan analyses of past glacial extents have associated glacial cycles to enhanced mid-latitude westerlies and insolation-driven monsoonal activity [e.g., Benn and Owen, 1998; Finkel et al., 2003; Mölg et al., 2014; Sharma et al., 2016]. However, in the frame of my study I am unable to discuss the relation of glacial cycles to any one or another moisture bearing system, as proxy data helping to differentiate between the moisture sources are still missing.

In addition to the problems outlined above that result in a wide spread of potential ages depending on the use of a certain age calculator, the problem of unambiguously documented past glacial activity in this environment is exacerbated by the low preservation potential of glacial deposits and landforms, especially in the humid sectors of the orogen. More optimal conditions to derive such information exists in the arid internal parts [e.g., Seong et al., 2007; Owen and Dortch, 2014 and authors therein].

The capability of past Himalayan glaciers to carve deep valleys has led to the generation of deep valleys, which have provided accommodation space for eroded hillslope and outwash sediments throughout several glacial cycles. For example, at the confluence of the Chandra River and the Bara Shigri Glacier the glacial overdeepening is on the order of approx. 500 m and stores the corresponding amount of sediment [pers. commun. J. Mey, 2015]. However, the timing and the rate of aggradation are unknown; it is unclear at what time and over how many glacial cycles the trough had developed, and how old the sedimentary fill is. It has been proposed that the most extensive glaciations occurred before the LGM and therefore valleys were carved in the course of several glacial cycles, and some of the material must have been deposited pre-LGM [e.g., Owen and Dortch, 2014 and cited authors therein]. At Tandi, where the Bhaga River joins the Chandra River, an undated conglomeratic terrace possibly represents sediment accumulation from hillslopes and retransported glacigenic material likely related to reduced fluvial transport capacity during the Holocene.

In the Karakoram realm, where the Nubra Valley joins the Shyok Valley, large alluvial plains shape the character of the landscape caused by a glacial dam, which resulted in aggradation and incision due to frequent release of outburst floods into the Shoyk Valley (chapter 3). By means of ^{10}Be surface exposure-age determination and depth profiling combined with glacial landform mapping the chronological sequence within the Nubra and Shyok valleys could be determined.

I would like to emphasize the similarities between the two study areas. At both locations large and extensive valley glaciers have been described, whose erosive power lead to the formation of deeply carved valleys. Subsequently, these valleys were filled with sediments. Areas corresponding to changes in river gradient are located in the alluvial plains and often correlate with confluences of tributary valleys with the trunk streams; in some cases, the tributaries are still occupied by valley glaciers (see Figures 2.2, 3.13). In these areas deep incision occurs. This phenomenon is not only observed in the Shyok and Chandra valleys, but also in other orogen-parallel subsidiary valleys between the two study sites. Blöthe and Korup [2013] estimated valley fills of the northwestern Himalaya exceeding values of the central Himalaya in volume and in thickness. They attributed the sedimentary fills to the present glacier cover and mostly to mass wasting events on millennial timescales [Blöthe and Korup, 2013]. In this context outburst floods due to glacial-dam failure have also been proposed to have contributed to the aggradation of sediments downstream as described at both study sites [Coxon et al., 1996; chapter 3].

In light of my geomorphological field work, sedimentological observations, and regional facies relationships, I suggest that the sedimentary fills in the Chandra and Shyok valleys are mainly derived from mass wasting processes immediately following deglaciation until weakened and oversteepened hillslopes were adjusted to the post-glacial conditions [Porter and Orombelli, 1981; Ballantyne, 2002b; Vehling et al., 2016]. The envisaged processes of glacial overdeepening and subsequent filling may be applicable to other Himalayan valleys as well [Ballantyne, 2002a; Vehling et al., 2016]. These inferred relationships are important, especially against the backdrop of globally increasing temperatures, receding glaciers and increased sediment mobility [e.g., Bolch et al., 2012] that affect human life in mountainous regions [e.g., Bolch et al., 2012; Qiu, 2016].

5.3. Long-term exhumation and resulting landforms

In chapter 4, I presented new AFT ages that confirm and expand earlier exhumation studies [Schlup et al., 2003]; my results show a pronounced cooling-age gradient in the Chandra and Beas valley transect. High exhumation rates were obtained north and south of the Rothang Pass, which allows excluding orographic-rainfall effects on exhumation patterns, as the pass is a major drainage divide. It is suggested that the localized exhumation since late Miocene in the Chandra and Beas area is rather related to tectonically controlled processes that is tied to the belt of rapid exhumation in the area of the Lesser Himalayan Duplex expanding towards the Central Himalaya [e.g., Thöni et al., 2011; Webb et al., 2011; Stübner et al., 2014]. My data in compilation with further low-temperature cooling ages show and corroborate a significant change in the exhumation behavior from the Central to the Western Himalaya and underline the MHT segmentation [e.g., Powers et al., 1998; Deeken et al., 2011; Rajendra Prasad et al., 2011; Robert et al., 2011; Thiede et al., 2017]. In particular, a zone of high exhumation situated 100-150 km behind the MFT caused by the Lesser Himalayan Duplex is exposed from the Sutlej Region in the Central Himalaya to Trisuli Region in Central Nepal and steps towards the main mountain front in the Western Himalaya immediately west of Beas region.

A relation of the newly obtained AFT exhumation ages (1.70.2–10.01.1 Ma) to monsoon phases seems hardly to be established as climate proxy data have been interpreted in the way that monsoon phases weakened from 10 to ∼3.5 Ma and have been accelerating again since then [e.g., Clift et al, 2008]. This interpretation is in good agreement with recent studies in the Eastern Himalaya and Central Himalaya, where AFT determined recent rapid exhumation rates do not correspond with climate on the long-term [e.g., Abrahami et al., 2016; Landry et al., 2016; van der Beek, 2016]. Even tough, similarities between fluvial incision and long-term erosion have been observed in earlier studies [Lavé and Avouac, 2001]. My AFT data reveal erosion rates up to ∼1.85 mm/yr in the Chandra and Beas valleys in agreement with AHe measures [e.g., Adams et al., 2009]. These values lie within the range of incision rates that have been obtained from short-term TCN strath terrace dating along the Chandra River up to 13 mm/yr [Adams et al., 2009]. Nevertheless, it rather appears that the Pliocene AFT exhumation ages [e.g., Kumar et al., 1995; Schlup et al., 2003; Lal et al., 1999; Jain et al., 2000; Thiede et al., 2004; Vannay et al., 2004; Thiede et al., 2005; Herman et al., 2010; Deeken et al., 2011; Adlakha et al., 2013a; Abrahami et al., 2016; Landry et al., 2016; van der Beek et al., 2016] and kinematic models support a tectonic cause of exhumation [e.g., Bollinger et al., 2004; Bhattacharyya and Mitra, 2009; Mitra et al., 2010].

Although, the zone of young AFT cooling ages is observed almost continuously along strike of the whole Himalayan arc the tectonic underlying structure is still debated [e.g., Herman et al., 2010; Webb, 2013; Coutand et al., 2014; DeCelles et al., 2016; Mercier et al., 2017]. Many studies have been obtained in the Eastern Himalaya (i.e., Arunachal India or Bhutan), where AFT cooling ages vary from the MCT (∼6-9 Ma) towards the STD (∼2-3 Ma) partly coinciding with elevation increase between the two structures

[Adams et al., 2013; Adhlaka et al., 2013b, Grujic et al., 2006; Coutand et al., 2014, DeCelles et al., 2016]. In this part of the Himalaya it has been suggested that exhumation behavior is rather related to the flat-ramp-flat geometry of the MHT than to the surface traces of the major structures [Coutand et al., 2014] or precipitation [e.g., Grujic et al., 2006; Adlakha et al., 2013b, Adams et al., 2015]. Interestingly, present day rainfall peaks are documented several kilometers southward of the present day rapid exhumation [e.g., Bookhagen and Burbank, 2010]. In the Central Himalaya, which stretches from Nepal to our study area (∼77°E) Thiede and Ehlers [2013] have illustrated by a compilation of various low-temperature thermochronometry data, the extent of the belt of rapid exhumation in northwestern India. Based on balanced cross-sections and thermokinematic modelling this exhumation behavior has been attributed to the evolution the Lesser Himalayan Duplex above a midcrustal ramp or to out-of-sequence thrusting [e.g., Avouac, 2003; Bollinger et al., 2004; Herman et al., 2010; Robert et al., 2011; Célérier 2009a, Webb, 2013]. In contrast to this two scenarios, rapid exhumation in the Western Himalaya is focused at the southern front of the High Himalaya caused by a deep-seated ramp in vicinity of the MBT [Deeken et al., 2011, Adhlaka et al., 2013a, Thiede et al., 2017].

Fast exhumation is reflected in increasing topography and a reduction of stress in the valley walls [Willett et al., 2001]; factors that interact with climatic parameters [e.g., Willett, 1999] to promote mass wasting and fluvial incision [e.g., Ahnert, 1970; Schmidt and Montgomery, 1995] to modulate the Earth's surface. Therefore, it is of particular interest, which tectonic related landforms are observed along the Himalayan arc and how feedback mechanisms between tectonics and climate influence the landscape on the long-term.

The strongly dissected high local-relief area correlates with the belt of rapid exhumation along arc. Indeed, this zone coincides as well with the step in elevation from the Lesser to the High Himalaya at PT_2 [e.g., Hodges, 2000; Harvey et al., 2015; Morrell et al., 2015]. However, McQuarrie et al. [2014] state that topography is not directly reflecting the subsurface structure. In the Western and Eastern Himalaya topography rises steeply from the front and surprisingly releases high-elevation low-relief surfaces [e.g., Hodges, 2000; Adams et al., 2015; Adams et al., 2016; Faruhn, 2016]. In Bhutan, it is suggested that these low-relief surfaces are formed by sediment storage due to the uplift of an anticlinal crest because of back-tilting of the active fault [Adams et al., 2015]. Interestingly, in the Central Himalaya, where two-step topography dominates relict landscapes are observed as well resulting from a newly growing duplex because of a bend in the MHT [Hodges, 2000; Harvey et al., 2015]. As mentioned in chapter 5.2 within the Chandra and Beas valley morphology is mainly characterized by steep and highly incised valley walls. Present day rainfall patterns reveal the physiographic changes in topography along the Himalayan arc as the high ranges prevent the ISM moisture to travel into the orogen interior parts [e. g., Bookhagen and Burbank, 2010]. Hence, the Dhauladar Range established as orographic barrier to precipitation right at the High Himalayan front forcing denudation at the external flanks, leading to the reorganization of river networks and impeding of surface processes on the leeward side [Lavé and Avouac, 2001; Deeken et al., 2011; Adlakha et al., 2013a]. The Chenab River, which originates from the Chandra River, as well as the Sutlej River follow the Himalayan strike for several kilometers before they cut towards the foreland [e.g., Gosh et al., 2015]. Is this flow path a result of the uplifting High Himalaya above the midcrustal ramp? Or are the rivers just following other weak zones?

On the long-term an asymmetric evolution of the elevated area of high-relief above the midcrustal ramp at the orographic barrier is expected due to precipitation differences and unequal uplift above the midcrustal ramp [e.g., Willett, 1999; Willett et al., 2001]. Along the southern Himalayan ranges, it is suggested that climate drives and promotes valley wall denudation and therefore incision [e.g., Thiede et al., 2004; van der Beek et al., 2016].

5.4. Sediment evacuation and landscape forming processes

In the previous chapters I described processes that modulate the landscape in the northwestern Himalaya on short as well as on long timescales; these involve exhumation, glacial erosion, destabilization and denudation of valley walls, and sediment storage in glacial valleys (Figure 5.2). Present-day erosion and hillslope failure in the study area is most likely triggered by active tectonics, because here small to moderate earthquakes frequently occur (see Figure 4.3), the high relief landscape and precipitation delivered by the ISM and the westerlies (see Figure 1.8). Hovius et al. [2011] have described increased landsliding during Typhoon following earthquakes in Taiwan. This is in line with a study of Marc et al. [2015] who described co-seismic and post-seismic landslides delivering sediments to intermontane valleys. In addition, co-seismic landslides pose an instantaneous risk for populations living in high-mountain environments, as illustrated during the Gorkha earthquake in 2015, when the town of Langtang was buried underneath a large landslide [Marc et al., 2015; Qiu, 2016]. Furthermore, it has been suggested that post-seismic landslides keep the hazard level high [Marc et al., 2015].

As illustrated in the paraglacial cascade (Figure 5.2) sediment aggradation and slope failure constitute recurring events that may be triggered by both tectonic activity and climatic impacts along steep topography. Although the contributions of rainfall and seismicity regarding mass wasting are not yet clearly distinguishable, seismicity records [e.g., Avouac, 2003] and sedimentary archives indicate intensified monsoons [e.g., Bookhagen et al., 2005] point toward a coupling of both factors in these regions. In the realm of the processes that drive the sediment cascade in the High Himalaya and adjacent areas it seems that evacuation of stored sediments from of the Chandra Valley did not occur during the last 20 ka. In the intermontane valleys in the rain shadow of the peripheral Himalayan ranges, runoff related to precipitation, snow melt and glacial melt was obviously not sufficient enough to remove the para-glacially derived sediments and they thus remain transiently stored within the valleys for several thousands of years [e.g., Lane, 1955; Church and Ryder, 1972; Church and Slaymaker, 1989]. Wulf et al. [2012] document low present day river discharge within the upper catchment of the Chenab/Chandra River, but increases downstream as well coinciding with rainfall measurements [e.g., Bookhagen and Burbank, 2010]. This is in contrast to other mountainous regions such as the Southern Central Andes, where increased upstream discharge delivers sediments down valley causing rapid sediment aggradation, resulting in severe damage on infrastructure [Castino et al., 2016].

In landscapes subjected to variable tectonic and climate-driven influence (e.g., wind, rainfall, glaciers, seismicity) it is challenging to determine erosion rates [e.g., Munack et al., 2016; Ganti et al., 2016]; in Zanskar and Ladakh millennial erosion rates derived from ^{10}Be are lower than long-term exhumation rates [Munack et al., 2014]. The authors assumed this to be a reaction to climate fluctuations resulting

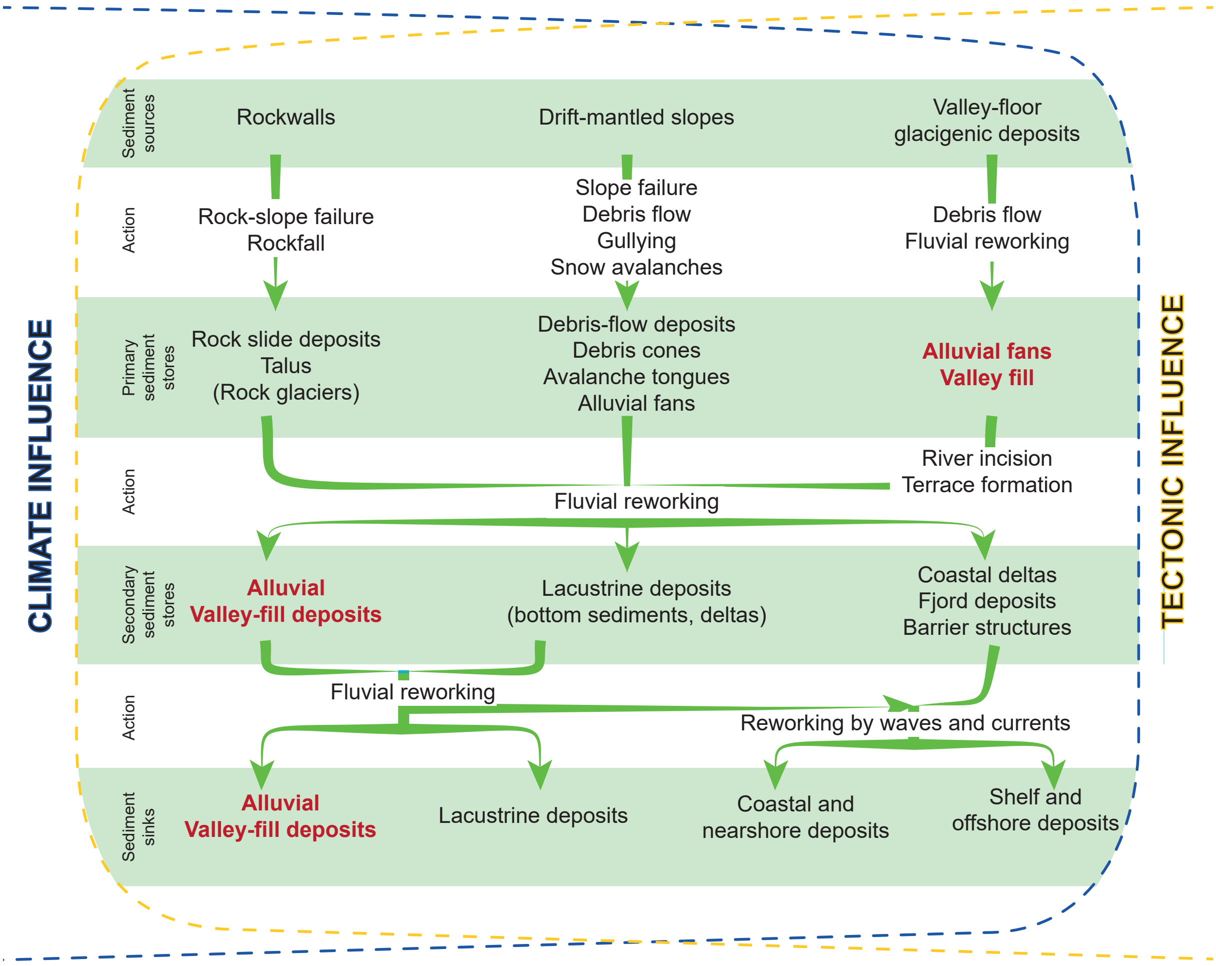

Figure 5.2: Source-to-sink mechanisms illustrated as paraglacial cascade in a tectonically active environment in the northwestern Himalaya. After the onset of deglaciation the sedimentary transport system reacts to climatic and tectonic influences by transporting sediments and storing sediments in the system. In red are the storing systems that are discussed in this thesis. Figure modified from Ballantyne [2002b].

in intensified and weakened erosion phases, respectively [Munack et al., 2014]. In this context, studies from the Himalayan interior and the Karakoram [e.g., Thiede and Ehlers, 2013; Scherler et al., 2014; Wallis et al., 2016; chapter 3] highlighted the dominance of glacial and/or tectonic processes over the impact of fluvial processes.

Close to the mountain front in the realm of the Sub-Himalaya Dey et al. [2016a] have described preserved Holocene and Late Pleistocene sediments that document multiple alternating sediment aggradation and incision phases in the Kangra basin during the last 50 ka. They propose that these deposits can be correlated with stronger and weaker ISM phases, respectively. In the Indus catchment similar late Pleistocene sedimentary infill and incision phases have been reported. They have been associated either with drainage impoundment or the effects of oscillating monsoon phases [e.g., Blöthe et al., 2014; Munack et al., 2016]. Whereas in the vicinity of the Tibetan plateau tectonic factors were not considered [Blöthe et al., 2014], there is some speculation if the unloading of sediments in the Sub-Himalayan orogenic wedge triggers the tectonic reorganization of the frontal wedge. The observed out-of-sequence thrusting of the Jawhalamuki thrust in the Kangra re-entrant has related to this [Dey et al., 2016b]. In this context it is interesting that I did not find evidence of active faults in the Chandra and Beas area, despite rapid exhumation since the late Miocene. However, surface traces of ruptures possibly not be detected because they are covered either by dense vegetation in the Beas Valley or colluvial sediment deposits in the Chandra Valley. Furthermore, not only sediment redistribution but also the loss of ice weight during deglaciation leads to reactivation of thrust faults [Ustaszewski et al., 2008; Turpeinen et al., 2008; Hampel et al., 2009] and isostatic uplift [e.g., Mey et al., 2016] and consequently, to changes in crustal stresses, which ultimately impacts the vulnerability of mountainous regions.

6 Conclusion & Outlook

In the framework of this study I tried to illustrate which short and long-term processes shaped the western Indian Himalayan landscape and lead to similar landforms. The western Indian Himalaya has been uplifting and actively exhuming since the Miocene leading to high local relief. My work and previous studies [Owen and Dortch, 2014 and references therein] assign several glaciations to the Lahul area, whose geomorphic and depositional vestiges dominate the landscape (e.g., overdeepened and U-shaped valleys, hanging tributary valleys, glacial deposits). Overdeepened glacial valleys were subsequently filled by fluvial gravel and sand or mass-wasting deposits released as a result of tectonic or climatic forcing.

Overall my studies have contributed 1) to a better understanding of late Pleistocene glaciations in the monsoonal-influenced northwestern Himalaya, and 2) to the debate about synchronicity of Himalayan glaciers with a midlatitude LGM deglaciation in the northern hemisphere. Furthermore, in the much broader context this study furnishes information about competing glacial and fluvial erosion, especially within the Chandra Valley.

On a larger, regional tectonic scale, I have described the termination of the Lesser Himalayan Duplex within the Chandra and Beas valleys using morphometric and geologic information. With the new data it was possible to describe the regional extent of major exhumation trends. Two alternative models were presented explaining possible causes for the drastic changes in exhumation patterns along the Himalayan arc. However, within the framework of the this study I was not able to finally solve this. Based on the archived results and experience, a reasonable next step could be the development of a numerical model to evaluate the consistency of the suggested models with the results of low-temperature thermochronometers and structures.

Bibliography

Abrahami, R., P. van der Beek, P. Huyghe, E. Hardwick, and J. Carcaillet (2016), Decoupling of long-term exhumation and short-term erosion rates in the Sikkim Himalaya, Earth and Planetary Science Letters, 433, 76-88, doi:10.1016/j.epsl.2015.10.039.

Adams, B., C. Dietsch, L. A. Owen, M. W. Caffee, J. Spotila, and W. C. Haneberg (2009), Exhumation and incision history of the Lahul Himalaya, northern India, based on (U-Th)/He thermochronometry and terrestrial cosmogenic nuclide methods, Geomorphology, 107(3-4), 285-299, doi:10.1016/j.geomorph.2008.12.017.

Ader, T. et al. (2012), Convergence rate across the Nepal Himalaya and interseismic coupling on the Main Himalayan Thrust: Implications for seismic hazard, Journal of Geophysical Research: Solid Earth, 117(B04403), doi:10.1029/2011JB009071.

Adlakha, V., K. A. Lang, R. C. Patel, N. Lal, and K. W. Huntington (2013b), Rapid long-term erosion in the rain shadow of the Shillong Plateau, Eastern Himalaya, Tectonophysics, 582, 76-83, doi:10.1016/j.tecto.2012.09.022.

Adlakha, V., R. C. Patel, N. Lal, Y. P. Mehta, A. K. Jain, and A. Kumar (2013a), Tectonics and climate interplay: exhumation patterns of the Dhauladar Range, Northwest Himalaya, Current SCIENCE, 104(11), 1551-1559.

Ahnert, F. (1970), Functional relationships between denudation, relief, and uplift in large, mid-latitude drainage basins, American Journal of Science, 268(3), 243-263, doi:10.2475/ajs.268.3.243.

Ali, K. F., and D. H. de Boer (2008), Factors controlling specific sediment yield in the upper Indus River basin, northern Pakistan, Hydrological Processes, 22, 3102-3114, doi:10.1002/hyp.6896.

Amante, C. and B.W. Eakins, 2009. ETOPO1 1 Arc-Minute Global Relief Model: Procedures, Data Sources and Analysis. NOAA Technical Memorandum NESDIS NGDC-24. National Geophysical Data Center, NOAA. doi:10.7289/V5C8276M [September 5, 2016].

Amundson, J., and N. Iverson (2006), Testing a glacial erosion rule using hang heights of hanging valleys, Jasper National Park, Alberta, Canada, Journal of Geoyphysical Research, 111, F01020, doi:10.1029/2005JF000359.

Anderson, R. S. (2005), Teflon peaks: the evolution of high local relief in glaciated mountain ranges, AGU Fall Meeting Abstracts, -1, 04.

Anderson, R. S., M. Dühnforth, W. Colgan, and L. Anderson (2012), Far-flung moraines: Exploring the feedback of glacial erosion on the evolution of glacier length, Geomorphology, 179, 269-285, doi:10.1016/j.geomorph.2012.08.018.

Annamalai, H., and J. M. Slingo (2001), Active/break cycles: diagnosis of the intraseasonal variability of the Asian Summer Monsoon, Climate Dynamics, 18(1), 85-102, doi:10.1007/s003820100161.

Applegate, P. J., N. M. Urban, K. Keller, and R. B. Alley (2009), Modeling the statistical distributions of cosmogenic exposure dates from moraines, Geosci. Model Dev. Discuss., 3(1), 293-307, doi:10.5194/gmdd-2-1407-2009-supplement.

Arendt, A. et al. (2012), Randolph Glacier Inventory: A Dataset of Global Glacier Outlines, version 2.0, Global Land Ice Measurement from Space, Boulder, Colorado.

Armijo, R., P. Tapponnier, and J. L. Mercier (1986), Quaternary extension in southern Tibet: Field observations and tectonic implications, Journal of Geophysical Research: Solid Earth, 91(B14), 13803-13872, doi:10.1029/JB091iB14p13803.

Arora, B. R., V. K. Gahalaut, and N. Kumar (2012), Structural control on along-strike variation in the seismicity of the northwest Himalaya, Journal of Asian Earth Sciences, 57, 15–24, doi: 10.1016/j.jseaes.2012.06.001.

Atwater, B. F. (1986), Pleistocene glacial-lake deposits of the Sanpoil River valley, northeastern Washington, Geological Survey Bulletin.

Avouac, J. P. (2003), Mountain building, erosion, and the seismic cycle in the Nepal Himalaya, Advances in Geophysics, 46, 1-80, doi:10.1016/S0065-2687(03)46001-9.

Avouac, J. P. (2007), Dynamic processes in extensional and compressional settings - mountain building: from earthquakes to geological deformation, Treatise on Geophysics, 6, 377-439.

Avouac, J. P., J. F. Dobremez, and L. Bourjot (1996), Palaeoclimatic interpretation of a topographic profile across middle Holocene regressive shorelines of Longmu Co (Western Tibet), Palaeogeography, Palaeoclimatology, Palaeoecology, 120(1-2), 93-104, doi:10.1016/0031-0182(96)88700-1.

Azam, M. F., P. Wagnon, C. Vincent, A. Ramanathan, A. Linda, and V. B. Singh (2014), Reconstruction of the annual mass balance of Chhota Shigri glacier, Western Himalaya, India, since 1969, Annals of Glaciology, 55(66), 69-80, doi:10.3189/2014AoG66A104.

Bai, D., M. J. Unsworth, M. A. Meju, X. Ma, and J. Teng (2010), Crustal deformation of the eastern Tibetan plateau revealed by magnetotelluric imaging, Nature, 3, 358-362, doi:10.1038/NGEO830.

Baker, V. R. (2009), High-Energy Megafloods: Planetary Settings and Sedimentary Dynamics, in Flood and Megaflood Processes and Deposits, pp. 1–15, Blackwell Publishing Ltd. doi:10.1002/9781444304299.ch1

Balco, G. (2004), The sedimentary record of subglacial erosion beneath the Laurentide Ice Sheet [Ph.D. thesis], Seattle, University of Washington.

Balco, G., J. Briner, R. C. Finkel, and J. A. Rayburn (2009), Regional beryllium-10 production rate calibration for late-glacial northeastern North America, Quaternary Geochronology, (4), 93–107, doi:10.1016/j.quageo.2008.09.001.

Balco, G., J. O. Stone, N. A. Lifton, and T. J. Dunai (2008), A complete and easily accessible means of calculating surface exposure ages or erosion rates from 10Be and 26Al measurements, Quaternary Geochronology, 3(3), 174-195, doi:10.1016/j.quageo.2007.12.001.

Ballantyne, C. K. (2002a), A general model of paraglacial landscape response, The Holocene, 12(3), 371–376, doi:10.1191/0959683602hl553fa.

Ballantyne, C. K. (2002b), Paraglacial geomorphology, Quaternary Science Reviews, 21(18-19), 1935-2017, doi:10.1016/S0277-3791(02)00005-7.

Barbarand, J., A. Carter, I. Wood, and T. Hurford (2003), Compositional and structural control of fission-track annealing in apatite, Chemical Geology, 1998(1-2), 107-137, doi:10.1016/S0009-2541(02)00424-2.

Barber, D. C. et al. (1999), Forcing of the cold event of 8,200 years ago by catastrophic drainage of Laurentide lakes, Nature, 400, doi:10.1038/22504.

Barnett, T. P., J. C. Adam, and D. P. Lettenmaier (2005), Potential impacts of a warming climate on water availability in snow-dominated regions, Nature, 438(7066), 303-309, doi:10.1038/nature04141.

Beaumont, C., R. A. Jamieson, M. H. Nguyen, and B. Lee (2001), Himalayan tectonics explained by extrusion of a low-viscosity crustal channel coupled to focused surface denudation, Nature, 414, 738–742, doi:10.1038/414738a.

Bendick, R., and R. Bilham (2001), How perfect is the Himalayan arc? Geology, 29(9), 791, doi:10.1130/0091-7613(2001)029<0791:HPITHA>2.0.CO;2.

Benn, D. I., and L. A. Owen (1998), The role of the Indian summer monsoon and the mid-latitude westerlies in Himalayan glaciation: review and speculative discussion, Journal of the Geological Society, 155, 353-363, doi:10.1144/gsjgs.155.2.0353.

Benn, D. I., and N. R. J. Hulton (2010), An ExcelTM spreadsheet program for reconstructing the surface profile of former mountain glaciers and ice caps, Computers Geosciences, 36(5), 605-610, doi:10.1016/j.cageo.2009.09.016.

Benn, D. I., T. Bolch, K. Hands, J. Gulley, A. Luckman, L. I. Nicholson, D. Quincey, S. Thompson, R. Toumi, and S. Wiseman (n.d.), Response of debris-covered glaciers in the Mount Everest region to recent warming, and implications for outburst flood hazards, Earth-Science Reviews, 114(1-2), 156-174.

Benn, D., and D. Evans (2010), Glaciers and glaciation, 2nd ed.

Benn, D., and F. Lehmkuhl (2000), Mass balance and equilibrium-line altitudes of glaciers in high-mountain environments, vol. 65-6, pp. 15-29.

Besse, J., and V. Courtillot (1988), Paleogeographic maps of the continents bordering the Indian Ocean since the Early Jurassic, Journal of Geophysical Research: Solid Earth, 93(B10), 11791–11808, doi:10.1029/JB093iB10p11791.

Bhattacharyya, K., and F. Ahmed (2016), Role of initial basin width in partitioning total shortening in the Lesser Himalayan fold-thrust belt: Insights from regional balanced cross-sections, Journal of Asian Earth Sciences, 116, 122–131, doi:10.1016/j.jseaes.2015.11.012.

Bhattacharyya, K., and G. Mitra (2009), A new kinematic evolutionary model for the growth of a duplex : an example from the Rangit duplex, Sikkim Himalaya, India, Gondwana Research, 16(3-4), 697-715, doi:10.1016/j.gr.2009.07.006.

Bhutiyani, M. R. (2000), Sediment load characteristics of a proglacial stream of Siachen Glacier and the erosion rate in Nubra valley in the Karakoram Himalayas, India, Journal of Hydrology, 227, 94-92, doi:10.1016/S0022-1694(99)00174-2.

Bierman, P., and E. J. Steig (1996), Estimating rates of denudation using cosmogenic isotope abundances in sediment, Earth Surface Processes and Landforms, 21(2), 125–139, doi:10.1002/(SICI)1096-9837(199602)21:2<125::AID-ESP511>3.0.CO;2-8.

Bilham, R., V. K. Gaur, and P. Molnar (2001), Himalaya Seismic Hazard, Science, 293(5534), 1442–1444, doi:10.1126/science.1062584.

Blanckenburg, von, F. (2005), The control mechanisms of erosion and weathering at basin scale from cosmogenic nuclides in river sediment, Earth and Planetary Science Letters, 237, 462-479, doi:10.1016/j.epsl.2005.06.030.

Blanckenburg, von, F., and J. K. Willenbring (2014), Cosmogenic Nuclides: Dates and Rates of Earth-Surface Change, Elements, 10(5), 341–346, doi:10.2113/gselements.10.5.341.

Blanckenburg, von, F., T. Hewawasam, and P. Kubik (2004), Cosmogenic nuclide evidence for low weathering and denudation in the wet, tropical highlands of Sri Lanka, Journal of Geoyph, 109, -, doi:10.1029/2003JF000049.

Blöthe, J. H., and O. Korup (2013), Millennial lag times in the Himalayan sediment routing system, Earth and Planetary Science Letters, 382, 38-46, doi:10.1016/j.epsl.2013.08.044.

Blöthe, J. H., H. Munack, O. Korup, A. Fülling, E. Garzanti, A. Resentini, and P. Kubik (2014), Late Quaternary valley infill and dissection in the Indus River, western Tibetan Plateau margin, Quaternary Science Reviews, 94, 102-119.

Bolch, T. et al. (2012), The State and Fate of Himalayan Glaciers, Science, 336(6079), 310-314, doi:10.1126/science.1215828.

Bollinger, L., P. Henry, and J. P. Avouac (2004), Thermal structure and exhumation history of the Lesser Himalaya in central Nepal, Tectonics, 23(5), doi:10.1029/2003TC001564.

Bonfiglioli, G., A. Ferro, and A. Mojoni (1961), Electron Microscope Investigation on the Nature of Tracks of Fission Products in Mica, J. Appl. Phys., 32(12), 2499, doi:10.1063/1.1728339.

Bookhagen, B. (2010), Appearance of extreme monsoonal rainfall events and their impact on erosion in the Himalaya, Geomatics, Natural Hazards and Risk, 1(1), 37-50, doi:10.1080/19475701003625737.

Bookhagen, B., and D. W. Burbank (2006), Topography, relief, and TRMM-derived rainfall variations along the Himalaya, Geophysical Research Letters, 33(8), 21, doi:10.1029/2006GL026037.

Bookhagen, B., and D. W. Burbank (2010), Towards a complete Himalayan hydrologic budget: The spatiotemporal distribution of snow melt and rainfall and their impact on river discharge, Journal of Geophysical Research, 115, doi:10.1029/2009JF001426.

Bookhagen, B., R. C. Thiede, and M. R. Strecker (2005), Late Quaternary intensified monsoon phases control landscape evolution in the northwest Himalaya, Geology, 33, 149-152, doi:10.1130/G20982.1.

Borchers, B., S. Marrero, G. Balco, M. Caffee, B. Goehring, N. Lifton, K. Nishiizumi, F. Phillips, J. Schaefer, and J. Stone (2016), Geological calibration of spallation production rates in the CRONUS-Earth project, Quaternary Geochronology, 31, 188-198, doi:10.1016/j.quageo.2015.01.009.

Brandon, M. T., M. K. Roden-Tice, and J. I. Garver (1998), Late Cenozoic exhumation of the Cascadia accretionary wedge in the Olympic Mountains, northwest Washington State, Geological Society of America, 110(8), 985–1009, doi:10.1130/0016-7606(1998)110<0985:LCEOTC>2.3.CO;2.

Braucher, R., E. T. Brown, D. L. Bourlès, and F. Colin (2003), In situ produced 10Be measurements at great depths: implications for production rates by fast muons, Earth and Planetary Science Letters, 211(3-4), 251-258, doi:10.1016/S0012-821X(03)00205-X.

Braucher, R., P. Del Castillo, L. Siame, A. J. Hidy, and D. L. Bourlès (2009), Determination of both exposure time and denudation rate from an in situ-produced 10Be depth profile: A mathematical proof of uniqueness. Model sensitivity and applications to natural cases, Quaternary Geochronology, 4(1), 56-67, doi:10.1016/j.quageo.2008.06.001.

Braun, J. (2002), Quantifying the effect of recent relief changes on age-elevation relationships, Earth and Planetary Science Letters, 200, 331-343, doi:10.1016/S0012-821X(02)00638-6.

Braun, J. (2010), Glaciers shield mountain tops, Nature, 467(7313), 281-282, doi:10.1038/467281b.

Bretz, J. H. (1969), The Lake Missoula Floods and the Channeled Scabland, The Journal of Geology, 77(5), 505-543.

Brocard, G. Y., P. A. Van Der Beek, and D. L. Bourlès (2003), Long-term fluvial incision rates and post-glacial river relaxation time in the French Western Alps from 10Be dating of alluvial terraces with assessment of inheritance, Earth and Planetary Science Letters, 209, 197-214

Brocklehurst, S. H., and K. X. Whipple (2002), Glacial erosion and relief production in the Eastern Sierra Nevada, California, Geomorphology, 42(1-2), 1-24, doi:10.1016/S0169-555X(01)00069-1.

Brocklehurst, S. H., and K. X. Whipple (2006), Assessing the relative efficiency of fluvial and glacial erosion through simulation of fluvial landscapes, Geomorphology, 75(3-4 ER -), 283-299.

Brown, E. T., R. F. Stallard, M. C. Larsen, G. M. Raisbeck, and F. Yiou (1995), Denudation rates determined from the accumulation of in situ-produced 10Be in the luquillo experimental forest, Puerto Rico, Earth and Planetary Science Letters, 129(1-4), 193-202, doi:10.1016/0012-821X(94)00249-X.

Brozovic, N., and D. W. Burbank (2000), Dynamic fluvial systems and gravel progradation in the Himalayan foreland, Geological Society of America.

Brummer, C. J., and D. R. Montgomery (2006), Influence of coarse lag formation on the mechanics of sediment pulse dispersion in a mountain stream, Squire Creek, North Cascades, Washington, United States, Water Resources Research, 42, W07412, doi:10.1029/2005WR004776.

Bull, W. B. (1991), Geomorphic responses to climatic change, New York, NY (United States); Oxford University Press, United States.

Burbank, D. W., A. D. Blythe, J. Putkonen, B. Pratt-Sitaula, E. Gabet, M. Oskin, A. Barros, and T. P. Ojha (2003), Decoupling of erosion and precipitation in the Himalayas, Nature, 426, 652–655, doi:10.1038/nature02187.

Burbank, D. W., and R. A. K. Tahirkeli (1985), The magnetostratigraphy, fission-track dating, and stratigraphic evolution of the Peshawar intermontane basin, northern Pakistan, Geological Society of America Bulletin, 96(4), 539–552, doi:10.1130/0016-7606(1985)96<539:TMFDAS>2.0.CO;2.

Burg, J. P., M. Guiraud, G. M. Chen, and G. C. Li (1984), Himalayan metamorphism and deformations in the North Himalayan Belt (southern Tibet, China), Earth and Planetary Science Letters, 69(2), 391–400, doi: 10.1016/0012-821X(84)90197-3.

Bürgisser, H. M., A. Gansser, and J. Pika (1982), Late Glacial lake sediments of the Indus valley area, northwestern Himalayas, Eclogae Geologicae Helvetiae, 75(1), 51-63. doi:10.5169/seals-165215

Caddick, M. J., M. J. Bickle, and N. Harris (2007), Burial and exhumation history of a Lesser Himalayan schist: Recording the formation of an inverted metamorphic sequence in NW India, Earth and Planetary Science Letters, 264(3-4), 375–390, doi:10.1016/j.epsl.2007.09.011.

Castino, F., B. Bookhagen, and M. R. Strecker (2016), River-discharge dynamics in the Southern Central Andes and the 1976–77 global climate shift, Geoph. Res. Lett., 43, 11,679–11,687, doi:10.1002/2016GL070868.

Cattin, R., and J. P. Avouac (2000), Modeling mountain building and the seismic cycle in the Himalaya of Nepal, Journal of Geophysical Research: Solid Earth, 105, 13389, doi:10.1029/2000JB900032.

Célérier, J., T. M. Harrison, and A. G. Webb (2009), The Kumaun and Garwhal Lesser Himalaya, India: Part 1. Structure and stratigraphy, Geological Society of America Bulletin, 121(9-10), 1262–1280, doi:10.1130/B26344.1.

Chadderton, L. T., and H. M. Montagu-Pollock (1963), Fission Fragment Damage to Crystal Lattices: Heat-Sensitive Crystals, Proceedings of the Royal Society A: Mathematical, Physical and Engineering Sciences, 274(1357), 239-252, doi:10.1098/rspa.1963.0127.

Charney, J. G. (1967), The Intertropical Convergence Zone and the Headley circulation of the atmosphere, Department of Meteorology, Massachusetts Institute of Technology.

Chevalier, M.-L., G. Hilley, P. Tapponnier, J. Van Der Woerd, J. Liu-Zeng, R. C. Finkel, F. J. Ryerson, H. Li, and X. Liu (2011), Constraints on the late Quaternary glaciations in Tibet from cosmogenic exposure ages of moraine surfaces, Quaternary Science Reviews, 30(5-6), 528-554, doi:10.1016/j.quascirev.2010.11.005.

Chew, D. M., and R. A. Spikings (2015), Geochronology and Thermochronology Using Apatite: Time and Temperature, Lower Crust to Surface, Elements, 11(3), 189-194, doi:10.2113/gselements.11.3.189.

Chmeleff, J., F. von Blanckenburg, K. Kossert, and D. Jakob (2010), Determination of the 10Be half-life by multicollector ICP-MS and liquid scintillation counting, Nuclear Instruments and Methods in Physics Research Section B: Beam Interactions with Materials and Atoms, 268(2), 192-199, doi:10.1016/j.nimb.2009.09.012.

Church, M., and J. M. Ryder (1972), Paraglacial Sedimentation: A Consideration of Fluvial Processes Conditioned by Glaciation, Geological Society of America Bulletin, 83(10), 3059, doi:10.1130/0016-7606(1972)83[3059:PSACOF]2.0.CO;2.

Church, M., and O. Slaymaker (1989), Disequilibrium of Holocene sediment yield in glaciated British Columbia, Nature, 337, 452-454, doi:10.1038/337452a0.

Clague, J. (2000), A review of catastrophic drainage of moraine-dammed lakes in British Columbia, Quaternary Science Reviews, 19(17-18), 1763-1783, doi:10.1016/S0277-3791(00)00090-1.

Clague, J. J., R. Barendregt, R. J. Enkin, and F. F. Foit (2003), Paleomagnetic and tephra evidence for tens of Missoula floods in southern Washington, Geology, 31(3), 247-250, doi:10.1130/0091-7613(2003)-031<0247:PATEFT>-2.0.CO;2.

Clarke, G., D. Leverington, J. Teller, and A. Dyke (2003), Superlakes, Megafloods, and Abrupt Climate Change, Science, 301, 922-923, doi:10.1126/science.1085921.

Clift, P. D., K. V. Hodges, D. Heslop, R. Hannigan, H. Van Long, and G. Calves (2008), Correlation of Himalayan exhumation rates and Asian monsoon intensity, Nature Geoscience, 1(12), 875-880, doi:10.1038/ngeo351.

Clift, P. D., R. Tada, and H. Zheng (2010), Monsoon evolution and tectonics-climate linkage in Asia: an introduction, Geological Society, London, Special Publications, 342(1), 1-4, doi:10.1144/SP342.1.

Copland, L., T. Sylvestre, M. P. Bishop, J. F. Shroder, Y. B. Seong, L. A. Owen, A. Bush, and U. Kamp (2011), Expanded and Recently Increased Glacier Surging in the Karakoram, Arctic, Antarctic, and Alpine Research, 43(4), 503-516, doi:10.1657/1938-4246-43.4.503.

Cornwell, K. (1998), Quaternary break-out flood sediments in the Peshawar basin of northern Pakistan, Geomorphology, 25(3-4), 225-248, doi:10.1016/S0169-555X(98)00061-0.

Cornwell, K., and S. Hamidullah (1992), Geomorphic evidence of catastrophic flooding along the middle Indus valley, Geol. Bull. Univ. Peshawar, 25, 113-121.

Costa, J. E., and R. L. Schuster (1988), The formation and failure of natural dams, Geological Society of America Bulletin, 100(7), 1054-1068, doi:10.1130/0016-7606(1988)100<1054:TFAFON> 2.3.CO;2.

Coutand, I., D. M. Whipp, D. Grujic, M. Bernet, M. G. Fellin, B. Bookhagen, K. R. Landry, S. K. Ghalley, and C. Duncan (2014), Geometry and kinematics of the Main Himalayan Thrust and Neogene crustal exhumation in the Bhutanese Himalaya derived from inversion of multithermochronologic data, Journal of Geophysical Research: Solid Earth, 119, 1446-1481, doi:10.1002/2013JB010891.

Coxon, P., L. A. Owen, and W. A. Mitchell (1996), A Late Quaternary catastrophic flood in the Lahul Himalayas, Journal of Quaternary Science, 11(6), 495-510, doi:10.1002/(SICI)1099-1417(199611/12)11:6<495::AID-JQS268>3.0.CO;2-M.

Cunningham, A. (1854), *Ladak,* physical, statistical, and historical with notices of the surrounding countries, Allen, London.

Célérier, J., T. M. Harrison, A. G. Webb, and A. Yin (2009a), The Kumaun and Garwhal Lesser Himalaya, India: Part 1. Structure and stratigraphy, Geological Society of America Bulletin, 121(9-10), 1262-1280, doi:10.1130/B26344.1.

Dahlen, F. A. (1990), Critical Taper Model of Fold-and-Thrust Belts and Accretionary Wedges, Annual Review of Earth and Planetary Sciences, 18, 55-99, doi:10.1146/annurev.ea.18.050190.000415.

Dahlen, F. A. (1990), Critical taper model of fold-and-thrust belts and accretionary wedges, Ann. Rev. Earth Planet. Sci., 18, 55-99.

Dahlen, F. A., and J. Suppe (1988), Mechanics, growth, and erosion of mountain belts, Geological Society of America Special Papers, vol. 218, pp. 161-178, doi:10.1130/SPE218-p161.

DeCelles, P. G., B. Carrapa, G. E. Gehrels, T. Chakraborty, and P. Ghosh (2016), Along-strike continuity of structure, stratigraphy, and kinematic history in the Himalayan thrust belt: The view from Northeastern India, Tectonics, 35(12), 2995–3027, doi:10.1002/2016TC004298.

DeCelles, P. G., G. E. Gehrels, J. Quade, T. P. Ojha, P. A. Kapp, and B. N. Upreti (1998), Neogene foreland basin deposits, erosional unroofing, and the kinematic history of the Himalayan fold-thrust belt, western Nepal, GSA Bulletin, 110(1), 2-21, doi:10.1130/0016-7606(1998)110<0002:NFBDEU>2.3.CO;2.

DeCelles, P. G., D. M. Robinson, and G. Zandt (2002), Implications of shortening in the Himalayan fold-thrust belt for uplift of the Tibetan Plateau, Tectonics, 21(6), 1061, doi:10.1029/2001TC001322.

Deeken, A., R. Thiede, and E. Sobel (2011), Exhumational variability within the Himalaya of northwest India, Earth and Planetary Science Letters, doi:10.1016/j.epsl.2011.02.045.

Derbyshire, E., L. Jijun, F. A. Perrott, X. Shuying, and R. S. Waters (1984), Quaternary glacial history of the Hunza Valley, Karakoram mountains, Pakistan, The International Karakoram Project, 2, 456-495.

Desilets, D., and M. Zreda (2001), On scaling cosmogenic nuclide production rates for altitude and latitude using cosmic-ray measurements, Earth and Planetary Science Letters, 193(1-2), 213-225, doi:10.1016/S0012-821X(01)00477-0.

Desilets, D., M. Zreda, and T. Prabu (2006), Extended scaling factors for in situ cosmogenic nuclides: New measurements at low latitude, Earth and Planetary Science Letters, 246(3-4), 265-276, doi:10.1016/j.epsl.2006.03.051.

Dewald, A. et al. (2013), CologneAMS, a dedicated center for accelerator mass spectrometry in Germany, Nuclear Instruments and Methods in Physics Research Section B: Beam Interactions with Materials and Atoms, 294, 18-23, doi:10.1016/j.nimb.2012.04.030.

Dey, S., R. C. Thiede, T. F. Schildgen, and H. Wittmann (2016a), Climate-driven sediment aggradation and incision since the late Pleistocene in the NW Himalaya, India, Earth and Planetary Science Letters, 449, 321-331, doi:10.1016/j.epsl.2016.05.050.

Dey, S., R. C. Thiede, T. F. Schildgen, H. Wittmann, B. Bookhagen, D. Scherler, and M. R. Strecker (2016b), Holocene internal shortening within the northwest Sub-Himalaya: Out-of-sequence faulting of the Jwalamukhi Thrust, India, Tectonics, doi:10.1002/2015TC004002.

Dèzes, P. J., J. C. Vannay, A. Steck, F. Bussy, and M. Cosca (1999), Synorogenic extension: Quantitative constraints on the age and displacement of the Zanskar shear zone (northwest Himalaya), Bulletin of the Geological Society of America, 111(3), 364–374, doi:10.1130/0016-7606(1999)111<0364:SEQCOT>2.3.CO;2.

Ding, Y., and D. R. Sikka (2006), Synoptic systems and weather, in The Asian Monsoon, pp. 131-201, Springer Berlin Heidelberg. doi:10.1007/3-540-37722-0_4

DiPietro, J. A., and K. R. Pogue (2004), Tectonostratigraphic subdivisions of the Himalaya: A view from the west, Tectonics, 23(5), doi:10.1029/2003TC001554.

Donelick, R. A. (2005), Apatite Fission-Track Analysis, Reviews in Mineralogy and Geochemistry, 58(1), 49–94, doi:10.2138/rmg.2005.58.3.

Dortch, J. M., L. A. Owen, and M. W. Caffee (2010), Quaternary glaciation in the Nubra and Shyok valley confluence, northernmost Ladakh, India, Quaternary Res, 74(1), 132-144, doi:10.1016/j.yqres.2010.04.013.

Dortch, J. M., L. A. Owen, and M. W. Caffee (2013), Timing and climatic drivers for glaciation across semi-arid western Himalayan-Tibetan orogen, Quaternary Science Reviews, 78, 188-208, doi:10.1016/j.quascirev.2013.07.025.

Dortch, J. M., L. A. Owen, L. M. Schoenbohm, and M. W. Caffee (2011a), Asymmetrical erosion and morphological development of the central Ladakh Range, northern India, Geomorphology, 135(1-2), 167-180, doi:10.1016/j.geomorph.2011.08.014.

Dortch, J. M., L. A. Owen, M. W. Caffee, and U. Kamp (2011b), Catastrophic partial drainage of Pangong Tso, northern India and Tibet, Geomorphology, 125(1), 109-121, doi:10.1016/j.geomorph.2010.08.017.

Drew, F. (1873), Alluvial and Lacustrine Deposits and Glacial Records of the Upper-Indus Basin, Quarterly Journal of the Geological Society, 29(1-2), 441-471, doi:10.1144/GSL.JGS.1873.029.01-02.39.

Dubey, A. K., S. S. Bhakuni, and A. D. Selokar (2004), Structural evolution of the Kangra recess, Himachal Himalaya: a model based on magnetic and petrofabric strains, Journal of Asian Earth Sciences, 24(2), 245–258, doi:10.1016/j.jseaes.2003.11.002.

Dunai, T. J. (2001), Influence of secular variation of the geomagnetic field on production rates of in situ produced cosmogenic nuclides, Earth and Planetary Science Letters, 193(1-2), 197-212, doi:10.1016/S0012-821X(01)00503-9.

Duncan, C., J. Masek, and E. Fielding; How steep are the Himalaya? Characteristics and implications of along-strike topographic variations, Geology, 31 (1): 75–78. doi: 10.1130/0091-7613(2003)031<0075:HSATHC>2.0.CO;2

Dunkl, I. (2002), Trackkey: a Windows program for calculation and graphical presentation of fission track data, Computers Geosciences, 28(1), 3–12, doi:10.1016/S0098-3004(01)00024-3.

Dunne, J., D. Elmore, and P. Muzikar (1999), Scaling factors for the rates of production of cosmogenic nuclides for geometric shielding and attenuation at depth on sloped surfaces, Geomorphology, 27(1-2), 3-11, doi:10.1016/S0169-555X(98)00086-5.

Dutt, S., A. K. Gupta, S. C. Clemens, H. Cheng, R. K. Singh, G. Kathayat, and R. L. Edwards (2015), Abrupt changes in Indian summer monsoon strength during 33,800 to 5500 years B.P, Geophysical Research Letters, 42(13), 5526-5532, doi:10.1002/2015GL064015.

Dyurgerov, M. B., and M. F. Meier (2005), Glaciers and the changing Earth system: a 2004 snapshot, Occasional Paper No. 58; Institute of Arctic and Alpine Research, University of Colorado.

Egholm, D. L., S. B. Nielsen, V. K. Pedersen, and J. E. Lesemann (2009), Glacial effects limiting mountain height, Nature, 460(7257), 884-U120, doi:10.1038/nature08263.

Ehlers, T. A. (2005), Crustal Thermal Processes and the Interpretation of Thermochronometer Data, Reviews in Mineralogy and Geochemistry, 58(1), 315–350, doi:10.2138/rmg.2005.58.12.

Elliott, J. R., R. Jolivet, P. J. González, J. P. Avouac, J. Hollingsworth, M. P. Searl, and V. L. Stevens (2016), Himalayan megathrust geometry and relation to topography revealed by the Gorkha earthquake, Nature, 9, doi:10.1038/NGEO2623.

Epard, J. L., Vannay, J. C., and Hunziker, J. C. (1995), Tertiary Himalayan structures and metarmorphism in the Kullu Valley (Mandi-Khoksar transect in the Western Himalaya) – Shikar-Beh-nappe and crystalline nappe, Schweiz. Mineral. Petrogr. Mitt. 75, 59-84, doi: 10.5169/seals-57144

Farley, K. A. (2000), Helium diffusion from apatite: General behavior as illustrated by Durango fluorapatite, Journal of Geophysical Research, 105(B2), 2903-2914, doi:10.1029/1999JB900348.

Farley, K. A., R. A. Wolf, and L. T. Silver (1996), The effects of long alpha-stopping distances on (U-Th)/He ages, Geochimica et Cosmochimica Acta, 60(21), 4223-4229, doi:10.1016/S0016-7037(96)00193-7.

Faruhn, J. (2016), 3D Thermokinematic modeling of the Dhauladar range, Himachal Pradesh, Northwest Himalaya, India, University of Potsdam, Masters'thesis

Ficker, von, H., and W. R. Rickmers (Eds.) (1932), Geologische Untersuchungen im Nordwestlichen Pamir-Gebiet und Mittleren Trans-Alai, D. Reimer, E. Vohsen, Berlin.

Finkel, R. C., L. A. Owen, P. L. Barnard, and M. W. Caffee (2003), Beryllium-10 dating of Mount Everest moraines indicates a strong monsoon influence and glacial synchroneity throughout the Himalaya, Geology, 31(6), 561-564, doi:10.1130/0091-7613(2003)031<0561:BDOMEM>2.0.CO;2.

Fleischer, R. L., P. B. Price, and R. M. Walker (1975), Nuclear Tracks in Solids: Principles and Applications, University of California Press.

Flint, R. F. (1971), Glaciation and Quaternary Geology, John Wiley and Sons, New York.

Flohn, H. (1957), Large-scale aspects of the summer monsoon in South and East Asia, J. Meteor. Soc. Japan, 75(180186), 6.

Fredin, O., B. Bergstrom, R. Eilertsen, L. Hansen, O. Longva, A. Nesje, and H. Sveian (2013), Glacial landforms and Quaternary landscape development in Norway, edited by L. Olsen, O. Fredin, and O. Olesen, Quaternary Geology of Norway Special Publication, 13, 5-25.

Fülöp, R. H. (2012), Quantifying the magnitude and timing of Holocene soil erosion events on parent materials of known age using in-situ cosmogenic C-14 and Be-10 depth-profiles, University of Glasgow.

Gadgil, S. (2003), The Indian Monsoon and its Variabilty, 31, 429-467, doi:10.1146/annurev.earth.31.100901.141251.

Galbraith, R. F. (1981), On statistical models for fission track counts, Journal of the International Association for Mathematical Geology, 13(6), 471–178, doi:10.1007/BF01034498.

Gallagher, K., R. Brown, and C. Johnson (1998), Fission track analysis and its application to geological problems, Annual Review of Earth and Planetary Sciences, 26(1), 519-572, doi:10.1146/annurev.earth.26.1.519.

Gansser, A. (1964), Geology of the Himalayas, Wiley-Interscience.

Ganti, V., C. von Hagke, D. Scherler, M. P. Lamb, W. W. Fischer, and J. P. Avouac (2016), Time scale bias in erosion rates of glaciated landscapes, Science Advances, 2(10), e1600204-e1600204, doi:10.1126/sciadv.1600204.

Gardner, J. S., and K. Hewitt (1990), A surge of Bualtar Glacier, Karakoram Range, Pakistan: a possible landslide trigger, Journal of Glaciology, 36(123), 159-162, doi:10.1017/S0022143000009394.

Gasse, F., J. C. Fontes, E. Van Campo, and K. Wei (1996), Holocene environmental changes in Bangong Co basin (Western Tibet). Part 4: Discussion and conclusions, Palaeogeography, Palaeoclimatology, Palaeoecology, 120(1-2), 79-92, doi:10.1016/0031-0182(95)00035-6.

Ghosh, P., S. Sinha, and A. Misra (2015), Morphometric properties of the trans-Himalayan river catchments: Clues towards a relative chronology of orogen-wide drainage integration, Patterns and rates of Cenozoic landscape change in orogenic and post-orogenic settings, 233, 127-141, doi:10.1016/j.geomorph.2014.10.035.

Gleadow, A. J. W., and I. R. Duddy (1981), A natural long-term track annealing experiment for apatite, Nuclear Tracks, 5(1-2), 169–174, doi:10.1016/0191-278X(81)90039-1.

Godard, V., D. L. Bourlès, F. Spinabella, D. W. Burbank, B. Bookhagen, G. Burch Fisher, A. Moulin, and L. Léanni (2014), Dominance of tectonics over climate in Himalayan denudation, Geology, 43(3), 243-246, doi:10.1130/G35342.1.

Godard, V., D. W. Burbank, D. L. Bourlès, B. Bookhagen, R. Braucher, and G. B. Fisher (2012), Impact of glacial erosion on 10Be concentrations in fluvial sediments of the Marsyandi catchment, central Nepal, Journal of Geophysical Research, 117(F3), F03013, doi:10.1029/2011JF002230.

Godin, L., and L. B. Harris (2014), Tracking basement cross-strike discontinuities in the Indian crust beneath the Himalayan orogen using gravity data-relationship to upper crustal faults, Geophysical Journal International, 198(1), 198-215, doi:10.1093/gji/ggu131.

Granger, D. E., J. W. Kirchner, and R. Finkel (1996), Spatially Averaged Long-Term Erosion Rates Measured from in Situ-Produced Cosmogenic Nuclides in Alluvial Sediment, The Journal of Geology, 104(3), 249-257, http://www.jstor.org/stable/30068190.

Green, P. F. (1981), A new look at statistics in fission-track dating, Nuclear Tracks, 5(1-2), 77–86, doi:10.1016/0191-278X(81)90029-9.

Grujic, D., I. Coutand, B. Bookhagen, S. Bonnet, A. Blythe, and C. Duncan (2006), Climatic forcing of erosion, landscape, and tectonics in the Bhutan Himalayas, Geology, 34(10), 801, doi:10.1130/G22648.1.

Gunn, J. P., H. J. Todd, and K. Mason (1930), The Shyok flood, 1929, Himalayan Journal, 2, 35-47.

Gutenberg, B., J. P. Buwalda, and R. P. Sharp (1956), Seismic explorations on the floor of Yosemite Valley, California, Geological Society of America Bulletin, 67(8), 1051-1078, doi:10.1130/0016-7606(1956)67[1051:SEOTFO]2.0.CO;2.

Haeberli, W. (1983), Frequency and characteristics of glacier floods in the Swiss Alps, Annals of Glaciology, 4, 85-90, doi:10.3198/1983AoG4-1-85-90.

Hampel, A., and R. Hetzel (2006), Response of normal faults to glacial?interglacial fluctuations of ice and water masses on Earth's surface, Journal of Geophysical Research, 111, B06406, doi:10.1029/2005JB004124.

Hampel, A., R. Hetzel, G. Maniatis, and T. Karow (2009), Three-dimensional numerical modeling of slip rate variations on normal and thrust fault arrays during ice cap growth and melting, Journal of Geophysical Research, 114(B8), B08406, doi:10.1029/2008JB006113.

Hancock, G. S., R. S. Anderson, O. A. Chadwick, and R. C. Finkel (1999), Dating fluvial terraces with and profiles: application to the Wind River, Wyoming, Geomorphology, 27(1-2), 41-60, doi:10.1016/S0169-555X(98)00089-0.

Harvey, J. E., D. W. Burbank, and B. Bookhagen (2015), Along-strike changes in Himalayan thrust geometry: Topographic and tectonic discontinuities in western Nepal, Lithosphere, 7(5), 511-518, doi:10.1130/L444.1.

Hedrick, K. A., Y. B. Seong, L. A. Owen, M. W. Caffee, and C. Dietsch (2011), Towards defining the transition in style and timing of Quaternary glaciation between the monsoon-influenced Greater Himalaya and the semi-arid Transhimalaya of Northern India, vol. 236, pp. 21-33, doi:10.1016/j.quaint.2010.07.023.

Herman, F. et al. (2010), Exhumation, crustal deformation, and thermal structure of the Nepal Himalaya derived from the inversion of thermochronological and thermobarometric data and modeling of the topography, Journal of Geophysical Research, 115(B6), doi:10.1029/2008JB006126.

Herman, F., and J. Braun (2008), Evolution of the glacial landscape of the Southern Alps of New Zealand: Insights from a glacial erosion model, Journal of Geophysical Research, 113, doi:10.1029/2007JF000807.

Herman, F., D. Seward, P. G. Valla, A. Carter, B. Kohn, S. D. Willett, and T. A. Ehlers (2013), Worldwide acceleration of mountain erosion under a cooling climate, Nature, 504(7480), 423-426, doi:10.1038/nature12877.

Herman, F., F. Beaud, J.-D. Champagnac, J. M. Lemieux, and P. Sternai (2011), Glacial hydrology and erosion patterns: A mechanism for carving glacial valleys, Earth and Planetary Science Letters, 310(3-4), 498-508, doi:10.1016/j.epsl.2011.08.022.

Herman, F., P. Copeland, J.-P. Avouac, L. Bollinger, G. Mahéo, P. Le Fort, S. Rai, D. Foster, A. P?cher, K. Stüwe, and P. Henry (2010), Exhumation, crustal deformation, and thermal structure of the Nepal Himalaya derived from the inversion of thermochronological and thermobarometric data and modeling of the topography, Journal of Geophysical Research, 115(B6), doi:10.1029/2008JB006126.

Herzschuh, U. (2006), Palaeo-moisture evolution in monsoonal Central Asia during the last 50,000 years, Quaternary Science Reviews, 25(1-2), 163-178, doi:10.1016/j.quascirev.2005.02.006.

Hewitt, K. (1982). Natural dams and outburst floods of the Karakoram Himalaya. IAHS, 138, 259-269.

Hewitt, K. (1998), Glaciers receive a surge of attention in the Karakoram Himalaya, Eos, Transactions American Geophysical Union, 79(8), 104-105, doi:10.1029/98EO00071.

Hewitt, K. (1999), Quaternary Moraines vs Catastrophic Rock Avalanches in the Karakoram Himalaya, Northern Pakistan, Quaternary Res, 51(3), 220-237, doi:10.1006/qres.1999.2033.

Hewitt, K. (2005), The Karakoram Anomaly? Glacier Expansion and the âœElevation Effect,â? Karakoram Himalaya, Mountain Research and Development, 25(4), 332-340, doi:10.1659/0276-4741(2005)025[0332:TKAGEA]2.0.CO;2.

Hewitt, K. (n.d.), Paraglacial rock slope failures, disturbance regimes, and transitional landscapes. Upper Indus Basin, northern Pakistan, in Periglacial and Paraglacial Processes and Environments, vol. 320, edited by J. Knight and S. Harrison, pp. 235-255, The Geological Society of London.

Hewitt, K., and J. Liu (2010), Ice-Dammed Lakes and Outburst Floods, Karakoram Himalaya: Historical Perspectives on Emerging Threats, Physical Geography, 31(6), 528-551, doi:10.1029/2007GL031426.

Hewitt, K., J. Gosse, and J. J. Clague (2011), Rock avalanches and the pace of late Quaternary development of river valleys in the Karakoram Himalaya, Geological Society of America Bulletin, 123, 1836-1850, doi:10.1130/B30341.1.

Heyman, J. (2014), Paleoglaciation of the Tibetan Plateau and surrounding mountains based on exposure ages and ELA depression estimates, Quaternary Science Reviews, 91, 30-41, doi:10.1016/j.quascirev.2014.03.018.

Heyman, J., A. P. Stroeven, J. M. Harbor, and M. W. Caffee (2011), Too young or too old: Evaluating cosmogenic exposure dating based on an analysis of compiled boulder exposure ages, Earth and Planetary Science Letters, 302(1-2), 71-80, doi:10.1016/j.epsl.2010.11.040.

Heyman, J., A. P. Stroeven, J. M. Harbor, and M. W. Caffee (2011), Too young or too old: Evaluating cosmogenic exposure dating based on an analysis of compiled boulder exposure ages, Earth and Planetary Science Letters, 302(1-2), 71-80, doi:10.1016/j.epsl.2010.11.040.

Hinderer, M. (2001), Late Quaternary denudation of the Alps, valley and lake fillings and modern river loads, Geodinamica Acta, 14(4), 231-263, doi:10.1080/09853111.2001.11432446.

Hintersberger, E., R. C. Thiede, and M. R. Strecker (2011), The role of extension during brittle deformation within the NW Indian Himalaya, Tectonics, 30(3), doi:10.1029/2010TC002822.

Hodges, K. V. (1991), Pressure-Temperature-Time Paths, Ann. Rev. Earth Planet. Sci., 19(1), 207–236, doi:10.1146/annurev.ea.19.050191.001231.

Hodges, K. V. (2000), Tectonics of the Himalaya and southern Tibet from two perspectives, Geological Society of America Bulletin, 112(3), 324–350, doi:10.1130/0016-7606(2000)112<324:TOTHAS>2.0.CO;2.

Hodges, K. V., J. M. Hurtado, and K. X. Whipple (2001), Southward extrusion of Tibetan crust and its effect on Himalayan tectonics, Tectonics, 20(6), 799–809, doi:10.1029/2001TC001281.

Hovius, N., P. Meunier, C.-W. Lin, H. Chen, Y.-G. Chen, S. Dadson, M.-J. Horng, and M. Lines (2011), Prolonged seismically induced erosion and the mass balance of a large earthquake, Earth and Planetary Science Letters, 304(3-4), 347-355, doi:10.1016/j.epsl.2011.02.005.

Huntington, K. W., T. A. Ehlers, K. V. Hodges, and D. M. Whipp (2007), Topography, exhumation pathway, age uncertainties, and the interpretation of thermochronometer data, Tectonics, 26(4), doi:10.1029/2007TC002108.

Hurford, A. J., and P. F. Green (1983), The zeta age calibration of fission-track dating, Chemical Geology, 41, 285–317, doi:10.1016/S0009-2541(83)80026-6.

Jain, A., D. Kumar, S. Singh, A. Kumar, and N. Lal (2000), Timing, quantification and tectonic modelling of Pliocene–Quaternary movements in the NW Himalaya: evidence from fission track dating, Earth and Planetary Science Letters, 179(3-4), 437–451, doi:10.1016/S0012-821X(00)00133-3.

Jamieson, S. S. R., M. W. Ewertowski, and D. J. A. Evans (2015), Rapid advance of two mountain glaciers in response to mine?related debris loading, Journal of Geoyph, 120(7), 1418-1435, doi:10.1002/2015JF003504.

Jarvis, A., H. I. Reuter, A. Nelson, and E. Guevara (2008), Hole-filled seamless SRTM data V4, International Centre for Tropical Agriculture (CIAT). Available from: http://srtm.csi.cgiar.org (Accessed 26 December 2008)

Jòhannesson, T., C. F. Raymond, and E. D. Waddington (1989a), A Simple Method for Determining the Response Time of Glaciers, in Glaciology and Quaternary Geology, vol. 6, pp. 343-352, Springer Netherlands, Dordrecht.

Jòhannesson, T., C. Raymond, and E. Waddington (1989b), Time-Scale for Adjustments of Glaciers to Changes in Mass Balance, Journal of Glaciology, 35(121), 355-369(15), doi:10.3198/1989JoG35-121-355-369.

Johnson, M. R. W. (1994), Culminations and domal uplifts in the Himalaya, Tectonophysics, 239(1-4), 139-147, doi:10.1016/0040-1951(94)90111-2.

Kääb, A., C. Huggel, L. Fischer, S. Guex, F. Paul, I. Roer, N. Salzmann, S. Schlaefli, K. Schmutz, and R. Schneider (2005), Remote sensing of glacier-and permafrost-related hazards in high mountains: an overview, Natural Hazards and Earth System Science, 5(4), 527-554, doi:10.5194/nhess-5-527-2005.

Kaplan, M. R., A. S. Hein, A. Hubbard, and S. M. Lax (2009), Can glacial erosion limit the extent of glaciation? Geomorphology, 103(2), 172-179, doi:10.1016/j.geomorph.2008.04.020.

Kelly, M. A., T. V. Lowell, P. J. Applegate, F. M. Phillips, J. M. Schaefer, C. A. Smith, H. Kim, K. C. Leonard, and A. M. Hudson (2013), A locally calibrated, late glacial 10Be production rate from a low-latitude, high-altitude site in the Peruvian Andes, Quaternary Geochronology, doi:10.1016/j.quageo.2013.10.007.

Ketcham, R. A., R. A. Donelick, and W. D. Carlson (1999), Variability of apatite fission-track annealing kinetics: III. Extrapolation to geological time scales, American Journal of Science, 84, 1235–1255, doi:10.2138/am-1999-0903.

Kleman, J., and C. Hättestrand (1999), Frozen-bed Fennoscandian and Laurentide ice sheets during the Last Glacial Maximum, Nature, 402(6757), 63–66, doi:10.1038/47005.

Kohl, C. P., and K. Nishiizumi (1992), Chemical isolation of quartz for measurement of in-situ -produced cosmogenic nuclides, Geochimica et Cosmochimica Acta, 56(9), 3583-3587, doi:10.1016/0016-7037(92)90401-4.

Kohn, M. J. (2014), Himalayan metamorphism and its tectonic implications, Ann. Rev. Earth Planet. Sci., 42(1), 381–419, doi:10.1146/annurev-earth-060313-055005.

Korschinek, G. et al. (2010), A new value for the half-life of 10Be by Heavy-Ion Elastic Recoil Detection and liquid scintillation counting, Nuclear Instruments and Methods in Physics Research Section B: Beam Interactions with Materials and Atoms, 268(2), 187-191, doi:10.1016/j.nimb.2009.09.020.

Korup, O. (2004), Landslide-induced river channel avulsions in mountain catchments of southwest New Zealand, Geomorphology, 63(1-2), 57-80, doi:10.1016/j.geomorph.2004.03.005.

Korup, O., and D. R. Montgomery (2008), Tibetan plateau river incision inhibited by glacial stabilization of the Tsangpo gorge, Nature, 455(7214), 786-789, doi:doi:10.1038/nature07322.

Korup, O., and F. Tweed (2007), Ice, moraine, and landslide dams in mountainous terrain, Quaternary Science Reviews, 26(25-28), 3406-3422, doi:10.1016/j.quascirev.2007.10.012.

Korup, O., D. R. Montgomery, and K. Hewitt (2010), Glacier and landslide feedbacks to topographic relief in the Himalayan syntaxes, Proceedings of the National Academy of Sciences, 107(12), 5317-5322, doi:10.1073/pnas.0907531107.

Kripalani, R. H. (2003), Indian Monsoon Variability in a Global Warming Scenario | SpringerLink, Nat Hazards, 29(2), 189-206, doi:10.1023/A:1023695326825.

Kuhn, M. (1995), The mass balance of very small glaciers, Zeitschrift für Gletscherkunde und Glaziologie, 31(1-2), 171-179.

Kumar, A., N. Lal, A. K. Jain, and R. B. Sorkhabi (1995), Late Cenozoic - Quaternary Thermo-Tectonic history of Higher Himalayan Crystalline (HHC) in Kishtwar-Padar-Zanskar region, NW Himalaya: Evidence from fission track ages, Journal Geological Society of India, 45, 375–391.

Kundu, B., R. K. Yadav, B. S. Bali, S. Chowdhury, and V. K. Gahalaut (2014), Oblique convergence and slip partitioning in the NW Himalaya: Implications from GPS measurements, Tectonics, 33, 2013–2014, doi:10.1002/2014TC003633.

Lague, D. (2005), Discharge, discharge variability, and the bedrock channel profile, Journal of Geophysical Research, 110(F4), F04006, doi:10.1029/2004JF000259.

Lal, D. (1991), Cosmic ray labeling of erosion surfaces: in situ nuclide production rates and erosion models, Earth and Planetary Science Letters, 104(2-4), 424-439, doi:10.1016/0012-821X(91)90220-C.

Lal, N., Y. P. Mehta, D. Kumar, A. Kumar, and A. K. Jain (1999), Cooling and exhumation history of the Mandi granite and adjoining tectonic units, Himachal Pradesh, and estimation of closure temperature from external surface of zircon, Geodynamic of the NW Himalaya, Gondwana Res. Group Mem, 6, 207–216.

Landry, K. R., I. Coutand, D. M. Whipp Jr., D. Grujic, and J. K. Hourigan (2016), Late Neogene tectonically driven crustal exhumation of the Sikkim Himalaya: Insights from inversion of multithermochronologic data, Tectonics, 35(3), 833-859, doi:10.1016/j.epsl.2015.10.026.

Lane, E. W. (1955), The importance of fluvial morphology in hydraulic engineering, Proceedings (American Society of Civil Engineers), 81.

Lang, K. A., K. W. Huntington, and D. R. Montgomery (2013), Erosion of the Tsangpo Gorge by megafloods, Eastern Himalaya, Geology, 41(9), 1003-1006, doi:10.1130/G34693.1.

Lang, T. J., and A. P. Barros (2004), Winter Storms in the Central Himalayas, Journal of the Meteorological Society of Japan, 82(3), 829-844, doi:10.2151/jmsj.2004.829.

Larson, K. P., L. Godin, and R. A. Price (2010), Relationships between displacement and distortion in orogens: Linking the Himalayan foreland and hinterland in central Nepal, Geological Society of America Bulletin, 122(7-8), 1116-1134, doi:10.1130/B30073.1.

Lavé, J., and J. P. Avouac (2001), Fluvial incision and tectonic uplift across the Himalayas of central Nepal, Journal of Geophysical Research, 106(B11), 26561–26,591, doi:10.1029/2001JB000359.

Le Fort, P. (1975), Himalayas: the collided range. Present knowledge of the continental arc, American Journal of Science, 275-A, 1-44.

Li, Y., N. Wang, X. Zhou, C. Zhang, and Y. Wang (2014), Synchronous or asynchronous Holocene Indian and East Asian summer monsoon evolution: A synthesis on Holocene Asian summer monsoon simulations, records and modern indices, Global and Planetary Change, 116, 30-40, doi:10.1016/j.gloplacha.2014.02.005.

Lifton, N. A., J. W. Bieber, J. M. Clem, M. L. Duldig, P. Evenson, J. E. Humble, and R. Pyle (2005), Addressing solar modulation and long-term uncertainties in scaling secondary cosmic rays for in situ cosmogenic nuclide applications, Earth and Planetary Science Letters, 239(1-2), 140-161, doi:10.1016/j.epsl.2005.07.001.

Lifton, N., T. Sato, and T. J. Dunai (2014), Scaling in situ cosmogenic nuclide production rates using analytical approximations to atmospheric cosmic-ray fluxes, Earth and Planetary Science Letters, 386, 149-160, doi:10.1016/j.epsl.2013.10.052.

Lüthi, M. P., and M. Funk (2011), Physics of Glaciers I, ETH lecture 651-4101-0, September 2011

Macedo, J., and S. Marshak (1999), Controls on the geometry of fold-thrust belt salients, Geological Society of America Bulletin, 111(12), 1808–1822, doi:10.1130/0016-7606(1999)111<1808:COTGOF>2.3.CO;2.

Mahesh, P., S. S. Rai, K. Sivaram, A. Paul, S. Gupta, R. Sarma, and V. K. Gaur (2013), One-Dimensional Reference Velocity Model and Precise Locations of Earthquake Hypocenters in the Kumaon–Garhwal Himalaya, Bulletin of the Seismological Society of America, 103(1), 328–339, doi:10.1785/0120110328.

Mancktelow, N. S., and B. Grasemann (1997), Time-dependent effects of heat advection and topography on cooling histories during erosion, Tectonophysics, 270(3-4), 167-195, doi:10.1016/S0040-1951(96)00279-X.

Marc, O., N. Hovius, P. Meunier, T. Uchida, and S. Hayashi (2015), Transient changes of landslide rates after earthquakes, Geology, 43(10), 883, doi:10.1130/G36961.1.

Marrero, S. M., F. M. Phillips, B. Borchers, N. Lifton, R. Aumer, and G. Balco (2015), Cosmogenic Nuclide Systematics and the CRONUS-calc Program, Quaternary Geochronology, doi:10.1016/j.quageo.2015.09.005.

Masarik, J., and R. C. Reedy (1995), Terrestrial cosmogenic-nuclide production systematics calculated from numerical simulations, Earth and Planetary Science Letters, 136(3-4), 381-395, doi:10.1016/0012-821X(95)00169-D.

Mason, K. (1929), Indus floods and Shyok glaciers, Himalayan Journal, 1, 10-29.

McFadden, L. D., S. G. Wells, and M. J. Jercinovich (1987), Influences of eolian and pedogenic processes on the origin and evolution of desert pavements, Geology, 15(6), 504-508, doi:10.1130/0091-7613(1987)15<504:IOEAPP>2.0.CO;2.

McQuarrie, N., and T. A. Ehlers (2015), Influence of thrust belt geometry and shortening rate on thermochronometer cooling ages: Insights from thermokinematic and erosion modeling of the Bhutan Himalaya, Tectonics, 34(6), 1055-1079, doi:10.1002/2014TC003783.

McQuarrie, N., T. Tobgay, S. P. Long, P. W. Reiners, and M. A. Cosca (2014), Variable exhumation rates and variable displacement rates: Documenting recent slowing of Himalayan shortening in western Bhutan, Earth and Planetary Science Letters, 386, 161-174, doi:10.1016/j.epsl.2013.10.045.

Mercier, J., J. Braun, and P. van der Beek (2017), Do along-strike tectonic variations in the Nepal Himalaya reflect different stages in the accretion cycle? Insights from numerical modeling, Earth and Planetary Science Letters, 472 IS -, 299–308, doi:10.1016/j.epsl.2017.04.041.

Mey, J., D. Scherler, A. D. Wickert, D. L. Egholm, M. Tesauro, T. F. Schildgen, and M. R. Strecker (2016), Glacial isostatic uplift of the European Alps, Nature Communications, 7, 13382, doi:10.1038/ncomms13382.

Mitra, G., K. Bhattacharyya, and M. Mukul (2010), The lesser Himalayan Duplex in Sikkim: Implications for variations in Himalayan shortening, Journal Geological Society of India, 75(1), 289-301, doi:10.1007/s12594-010-0016-x.

Mix, A., E. Bard, and R. Schneider (2001), Environmental processes of the ice age: land, oceans, glaciers (EPILOG), Quaternary Science Reviews, 20(4), 627-657, doi:10.1016/S0277-3791(00)00145-1.

Molnar, P., and P. England (1990), Late Cenozoic uplift of mountain ranges and global climate change: chicken or egg? Nature, 346, 29-34, doi:10.1038/346029a0.

Molnar, P., and J. M. Stock (2009), Slowing of India's convergence with Eurasia since 20 Ma and its implications for Tibetan mantle dynamics, Tectonics, 28(3), TC3001, doi:10.1086/428805.

Montgomery, D. R., B. Hallet, L. Yuping, N. Finnegan, A. Anders, A. Gillespie, and H. M. Greenberg (2004), Evidence for Holocene megafloods down the Tsangpo River gorge, southeastern Tibet, Quaternary Res, 62, 201-207, doi:10.1016/j.yqres.2004.06.008.

Morell, K. D., M. Sandiford, B. Kohn, A. Codilean, R.-H. Fülöp, and T. Ahmad (2017), Current strain accumulation in the hinterland of the northwest Himalaya constrained by landscape analyses, basin-wide denudation rates, and low temperature thermochronology, Tectonophysics, 721, 70–89, doi: 10.1016/j.tecto.2017.09.007.

Morell, K. D., M. Sandiford, C. P. Rajendran, K. Rajendran, A. Alimanovic, D. Fink, and J. Sanwal (2015), Geomorphology reveals active dŽcollement geometry in the central Himalayan seismic gap, Lithosphere, 7(3), 247-256, doi:10.1130/L407.1.

Mölg, T., F. Maussion, and D. Scherer (2014), Mid-latitude westerlies as a driver of glacier variability in monsoonal High Asia, Nature Climate Change, 4(January), 68-73, doi:10.1038/nclimate2055.

Munack, H., J. H. Blöthe, R. H. Fülöp, A. T. Codilean, D. Fink, and O. Korup (2016), Recycling of Pleistocene valley fills dominates 135 ka of sediment flux, upper Indus River, Quaternary Science Reviews, 149, 122-134, doi:10.1016/j.quascirev.2016.07.030.

Munack, H., O. Korup, A. Resentini, M. Limonta, E. Garzanti, J. H. Blöthe, D. Scherler, H. Wittmann, and P. W. Kubik (2014), Postglacial denudation of western Tibetan Plateau margin outpaced by long-term exhumation, Geological Society of America Bulletin, 126(11-12), 1580-1594, doi:10.1130/B30979.1.

Murari, M. K., L. A. Owen, J. M. Dortch, M. W. Caffee, C. Dietsch, M. Fuchs, W. C. Haneberg, M. C. Sharma, and A. Townsend-Small (2014), Timing and climatic drivers for glaciation across monsoon-influenced regions of the Himalayan-Tibetan orogen, Quaternary Science Reviews, 88, 159-182, doi:10.1016/j.quascirev.2014.01.013.

Najman, Y., M. Bickle, E. Garzanti, M. Pringle, D. Barfod, N. Brozovic, D. Burbank, and S. Ando (2009), Reconstructing the exhumation history of the Lesser Himalaya, NW India, from a multitechnique provenance study of the foreland basin Siwalik Group, Tectonics, 28(5), doi:10.1029/2009TC002506.

National Earthquake Information Center (NEIC), Catalog of Global Seismicity, http://earthquake.usgs.gov/earthquakes/search/, U.S. Geol. Surv. Earthquake Data Base, Reston, Va.

Ng, F., and S. Liu (2009), Temporal dynamics of a jökulhlaup system, Journal of Glaciology, 55(192), 651-665, doi:doi:10.3189/002214309789470897.

Nishiizumi, K., E. L. Winterer, C. P. Kohl, J. Klein, R. Middleton, D. Lal, and R. Arnold (1989), Cosmic ray production rates of 10Be and 26Al in quartz from glacially polished rocks, Journal of Geophysical Research: Solid Earth, 94(B12), 17907-17915, doi:10.1029/JB094iB12p17907.

Nye, J. F. (1976), Water Flow in Glaciers: Jökulhlaups, Tunnels and Veins, Journal of Glaciology, 17, 181-207, doi:10.1017/S002214300001354X.

O'Connor, J. E., and J. E. Costa (2004), The world's largest floods, past and present: their causes and magnitudes, US Geological Survey. Oerlemans, J. (1984), Numerical experiments on large-scale glacial erosion, GeoRef.

Olen , S., Bookhagen, B., HoffmannB., Sachse, D., Adhikari, D.., and Strecker, M.R., Understanding erosion rates at the Himalayan orogenic front: A case study from the Arun Valley, Nepal. Journal of Geophysical Research-Earth Surface 120, doi:10.1002/2014JF003410

Olen, S. M., B. Bookhagen, and M. R. Strecker (2016), Role of climate and vegetation density in modulating denudation rates in the Himalaya, Earth and Planetary Science Letters, doi:10.1016/j.epsl.2016.03.047.

Otto, J. C., L. Schrott, and M. Jaboyedoff (2009), Quantifying sediment storage in a high alpine valley (Turtmanntal, Switzerland), Earth Surface Processes and Landforms, doi:10.1002/esp.1856.

Ouimet, W. B., K. X. Whipple, L. H. Royden, Z. Sun, and Z. Chen (2007), The influence of large landslides on river incision in a transient landscape: Eastern margin of the Tibetan Plateau (Sichuan, China), Geological Society of America Bulletin, 119(11-12), 1462-1476, doi:10.1130/B26136.1.

Owen, L. A. (2009), Latest Pleistocene and Holocene glacier fluctuations in the Himalaya and Tibet, Quaternary Science Reviews, 28(21-22), 2150-2164, doi:10.1016/j.quascirev.2008.10.020.

Owen, L. A., and J. M. Dortch (2014), Nature and timing of Quaternary glaciation in the Himalayan-Tibetan orogen, Quaternary Science Reviews, 88, 14-54, doi:10.1016/j.quascirev.2013.11.016.

Owen, L. A., and J. M. Dortch (2014), Nature and timing of Quaternary glaciation in the Himalayan-Tibetan orogen, Quaternary Science Reviews, 88, 14-54, doi:10.1016/j.quascirev.2013.11.016.

Owen, L. A., E. Derbyshire, and S. Richardson (1996), The Quaternary glacial history of the Lahul Himalaya, northern India, Journal of Quaternary Science, 11(1), 25-42, doi:10.1002/(SICI)1099-1417(199601/02)11:1<25::AID-JQS209>3.0.CO;2-K.

Owen, L. A., L. Gualtieri, R. C. Finkel, M. W. Caffee, D. I. Benn, and M. C. Sharma (2001), Cosmogenic radionuclide dating of glacial landforms in the Lahul Himalaya, northern India: defining the timing of Late Quaternary glaciation, Journal of Quaternary Science, 16(6), 555-563, doi:10.1002/jqs.621.

Owen, L. A., M. W. Caffee, K. R. Bovard, R. C. Finkel, and M. C. Sharma (2006), Terrestrial cosmogenic nuclide surface exposure dating of the oldest glacial successions in the Himalayan orogen: Ladakh Range, northern India, GSA Bulletin, 118(3-4), 383-392, doi:10.1130/B25750.1.

Owen, L. A., M. W. Caffee, R. C. Finkel, and Y. B. Seong (2008), Quaternary glaciation of the Himalayan-Tibetan orogen, Journal of Quaternary Science, 23, 513-531, doi:10.1002/jqs.1203.

Owen, L. A., R. C. Finkel, P. L. Barnard, M. Haizhou, K. Asahi, M. W. Caffee, and E. Derbyshire (2005), Climatic and topographic controls on the style and timing of Late Quaternary glaciation throughout Tibet and the Himalaya defined by 10Be cosmogenic radionuclide surface exposure dating, Quaternary Science Reviews, 24(12-13), 1391-1411, doi:10.1016/j.quascirev.2004.10.014.

Owen, L. A., R. Robinson, D. I. Benn, R. C. Finkel, N. K. Davis, C. Yi, J. Putkonen, D. Li, and A. S. Murray (2009), Quaternary glaciation of Mount Everest, Quaternary Science Reviews, 28(15-16), 1412-1433, doi:10.1016/j.quascirev.2009.02.010.

Owen, L., R. Bailey, E. Rhodes, W. Mitchell, and P. Coxon (1997), Style and timing of glaciation in the Lahul Himalaya, northern India: A framework for reconstructing late Quaternary palaeoclimatic change in the western Himalayas, Journal of Quaternary Science, 12(2), 83-109, doi:10.1002/(SICI)1099-1417(199703/04)12:2<83::AID-JQS281>3.0.CO;2-P.

Pandey, M. R., R. P. Tandukar, J. P. Avouac, J. Lavé, and J. P. Massot (1995), Interseismic strain accumulation on the Himalayan crustal ramp (Nepal), Geophysical Research Letters, 22(7), 751–754, doi:10.1029/94GL02971.

Pant, R. K., N. R. Phadtare, L. S. Chamyal, and N. Juyal (2005), Quaternary deposits in Ladakh and Karakoram Himalaya: A treasure trove of the palaeoclimate records, Current Science, 88(11), 1789.

Penck, A. (1905), Glacial Features in the Surface of the Alps, The Journal of Geology, 13(1), 1-19.

Penck, A., and E. Brückner (1909), Die Alpen im Eiszeitalter, Tauschnitz.

Pfeffer, W. T. et al. (2014), The Randolph Glacier Inventory: a globally complete inventory of glaciers, Journal of Glaciology, 60(221), 537-552, doi:10.3189/2014JoG13J176.

Phartiyal, B., A. Sharma, P. Srivastava, and Y. Ray (2009), Chronology of relict lake deposits in the Spiti River, NW Trans Himalaya: Implications to Late Pleistocene-Holocene climate-tectonic perturbations, Geomorphology, doi:10.1016/j.geomorph.2009.02.018.

Phartiyal, B., A. Sharma, R. Upadhyay, and A. K. Sinha (2005), Quaternary geology, tectonics and distribution of palaeo- and present fluvio/glacio lacustrine deposits in Ladakh, NW Indian Himalaya–a study based on field observations, Geomorphology, 65(3-4), 241-256, doi:10.1016/j.geomorph.2004.09.004.

Phillips, F. M. et al. (2016), The CRONUS-Earth Project: A synthesis, Quaternary Geochronology, 31, 119-154, doi:10.1016/j.quageo.2015.09.006.

Phillips, R. J. (2008), Geological map of the Karakoram fault zone, Eastern Karakoram, Ladakh, NW Himalaya, Journal of Maps, 4(1), 21-37, doi:10.4113/jom.2008.98.

Phillips, W., V. Sloan, J. Shroder, P. Sharma, M. Clarke, and H. Rendell (2000), Asynchronous glaciation at Nanga Parbat, northwestern Himalaya Mountains, Pakistan, Geology, 28(5), 431-434, doi:10.1130/0091-7613(2000)28<431:AGANPN>2.0.CO;2.

Porter, S. C., and G. Orombelli (1981), Alpine Rockfall Hazards: Recognition and dating of rockfall deposits in the western Italian Alps lead to an understanding of the potential hazards of giant rockfalls in mountainous regions, American Scientist, 69, 67-75, http://www.jstor.org/stable/27850249

Post, A., and L. R. Mayo (1971), Glacier dammed lakes and outburst floods in Alaska, US Geological Survey Washington.

Powers, P. M., R. J. Lillie, and R. S. Yeats (1998), Structure and shortening of the Kangra and Dehra Dun reentrants, sub-Himalaya, India, Geological Society of America Bulletin, 110(8), 1010–1027, doi:10.1130/0016-7606(1998)110<1010:SASOTK>2.3.CO;2.

Pratt-Sitaula, B., and D. W. Burbank (2011), Topographic control of asynchronous glacial advances: A case study from Annapurna, Nepal, Geophysical Research Letters, 38, doi:10.1029/2011GL049940.

Pratt-Sitaula, B., M. Garde, D. W. Burbank, M. Oskin, A. Heimsath, and E. Gabet (2007), Bedload-to-suspended load ratio and rapid bedrock incision from Himalayan landslide-dam lake record, Quaternary Res, 68(1), 111-120, doi:10.1016/j.yqres.2007.03.005.

Preusser, F., J. M. Reitner, and C. Schlüchter (2010), Distribution, geometry, age and origin of overdeepened valleys and basins in the Alps and their foreland, Swiss Journal of Geoscience, 407-426, doi:10.1007/s00015-010-0044.

Putnam, A. E., G. H. Denton, J. M. Schaefer, D. J. A. Barrell, B. G. Andersen, R. C. Finkel, R. Schwartz, A. M. Doughty, M. R. Kaplan, and C. Schlüchter (2010), Glacier advance in southern middle-latitudes during the Antarctic Cold Reversal, Nature Geoscience, 3(10), 700-704, doi:10.1038/ngeo962.

Putnam, A. E., J. M. Schöefer, D. Barrell, M. Vandergoes, G. H. Denton, M. R. Kaplan, R. C. Finkel, R. Schwartz, B. M. Goehring, and S. E. Kelley (2010), In situ cosmogenic 10Be production-rate calibration from the Southern Alps, New Zealand, Quaternary Geochronology, 5(4), 392-409, doi:10.1016/j.quageo.20.

Qiu, J. (2016), Listening to landslides, Nature, 532, 428-431, doi:10.1038/532428a.

Raiverman, V. (2002), Foreland sedimentation in Himalayan tectonic regime: a relook at the orogenic process, Bishen Singh Mahendra Pal Sing, Dehra Dun.

Raiverman, V., S. V. Kunte, and A. Mukherjea (1983), Basin geometry, Cenozoic sedimentation and hydrocarbon prospects in northwestern Himalaya and Indo-Gangetic plains, Petroleum Asia Journal.

Rajendra Prasad, B., S. L. Klemperer, V. Vijaya Rao, H. C. Tewari, and P. Khare (2011), Crustal structure beneath the Sub-Himalayan fold–thrust belt, Kangra recess, northwest India, from seismic reflection profiling: Implications for Late Paleoproterozoic orogenesis and modern earthquake hazard, Earth and Planetary Science Letters, 308(1-2), 218–228, doi:10.1016/j.epsl.2011.05.052.

Rawat, S., A. K. Gupta, S. J. Sangode, P. Srivastava, and H. C. Nainwal (2015), Late Pleistocene-Holocene vegetation and Indian summer monsoon record from the Lahaul, Northwest Himalaya, India, Quaternary Science Reviews, 114, 167-181, doi:10.1016/j.quascirev.2015.01.032.

Reiners, P. W., and M. T. Brandon (2006), Using Thermochronology to Understand Orogenic Erosion, Ann. Rev. Earth Planet. Sci., 34(1), 419–466, doi:10.1146/annurev.earth.34.031405.125202.

Reiners, P. W., T. A. Ehlers, S. G. Mitchell, and D. R. Montgomery (2003), Coupled spatial variations in precipitation and long-term erosion rates across the Washington Cascades, Nature, 426, 645-647, doi: 10.1038/nature02111

Reiners, P. W., K. A. Farley, and H. J. Hickes (2002), He diffusion and (U-Th)/He thermochronometry of zircon: initial results from Fish Canyon Tuff and Gold Butte, Tectonophysics, 349(1-4), 297-308, doi:10.1016/S0040-1951(02)00058-6.

Richards, B. W., L. A. Owen, and E. J. Rhodes (2000), Timing of Late Quaternary glaciations in the Himalayas of northern Pakistan, Journal of Quaternary Science, 15(3), 283-297, doi:10.1002/(SICI)1099-1417(200003)15:3<283::AID-JQS525>3.0.CO;2-X.

Robert, X., P. van der Beek, J. Braun, C. Perry, and J.-L. Mugnier (2011), Control of detachment geometry on lateral variations in exhumation rates in the Himalaya: Insights from low-temperature thermochronology and numerical modeling, Journal of Geophsical Research: Solid Earth, 116(B5), 2156-2202, doi:10.1029/2010JB007893.

Roberts, M. J. (2005), Jökulhlaups: A reassessment of floodwater flow through glaciers, Rev. Geophys., 43(1), RG1002, doi:10.1029/2003RG000147.

Robinson, D. M., P. G. DeCelles, P. J. Patchett, and C. N. Garzione (2001), The kinematic evolution of the Nepalese Himalaya interpreted from Nd isotopes, Earth and Planetary Science Letters, 192(4), 507–521, doi: 10.1016/S0012-821X(01)00451-4.

Rolland, Y., A. P e cher, and C. Picard (2000), Middle Cretaceous back-arc formation and arc evolution along the Asian margin: the Shyok Suture Zone in northern Ladakh (NW Himalaya), Tectonophysics, 325(1-2), 145-173, doi:10.1016/S0040-1951(00)00135-9.

Royden, L. H., B. C. Burchfiel, and R. D. van der Hilst (2008), The Geological Evolution of the Tibetan Plateau, Science, 321(5892), 1054-1058, doi:10.1126/science.1155371.

Rupper, S., and M. Koppes (2010), Spatial patterns in Central Asian climate and equilibrium line altitudes, IOP Conf. Ser.: Earth Environ. Sci., 9(1), 012009, doi:10.1088/1755-1315/9/1/012009.

Saha, S., M. C. Sharma, M. K. Murari, L. A. Owen, and M. W. Caffee (n.d.), Geomorphology, sedimentology, and minimum exposure ages of streamlined subglacial landforms in the NW Himalaya, India, Boreas, doi:10.1111/bor.12153

Schelling, D., and K. Arita (1991), Thrust tectonics, crustal shortening, and the structure of the far-eastern Nepal Himalaya, Tectonics, 10(5), 851–862, doi:10.1029/91TC01011.

Scherler, D. (2014), Climatic limits to headwall retreat in the Khumbu Himalaya, eastern Nepal, Geology, 42(11), 1019-1022, doi:10.1130/G35975.1.

Scherler, D., B. Bookhagen, and M. R. Strecker (2014), Tectonic control on 10Be-derived erosion rates in the Garhwal Himalaya, India, J. Geophys. Res., 119, 83–105, doi:10.1002/2013JF002955.

Scherler, D., B. Bookhagen, and M. R. Strecker (2011a), Hillslope-glacier coupling: The interplay of topography and glacial dynamics in High Asia, Journal of Geophysical Research, 116, F02019, doi:10.1029/2010JF001751.

Scherler, D., B. Bookhagen, and M. R. Strecker (2011b), Spatially variable response of Himalayan glaciers to climate change affected by debris cover, Nature Geoscience, 4(3), 156-159, doi:10.1038/ngeo1068.

Scherler, D., B. Bookhagen, M. Strecker, F. von Blanckenburg, and D. Rood (2010), Timing and extent of late Quaternary glaciation in the western Himalaya constrained by 10Be moraine dating in Garhwal, India, Quaternary Science Reviews, 29(7-8), 815-831, doi:10.1016/j.quascirev.2009.11.031.

Schlup, M. (2003), Exhumation history of the western Himalaya: The Rupsha– Lahul–Kullu geochronological transect (NW India), PhD Thesis, University of Lausanne.

Schlup, M., A. Steck, A. Carter, M. Cosca, J.-L. Epard, and J. Hunziker (2011), Exhumation history of the NW Indian Himalaya revealed by fission track and 40Ar/39Ar ages, Journal of Asian Earth Sciences, 40, 344-350, doi: 10.1016/j.jseaes.2010.06.008.

Schmidt, K. M., and D. R. Montgomery (1995), Limits to Relief, Science, 270(5236), 617-620, doi:10.1126/science.270.5236.617.

Schrott, L., G. Hufschmidt, M. Hankammer, T. Hoffmann, and R. Dikau (2003), Spatial distribution of sediment storage types and quantification of valley fill deposits in an alpine basin, Reintal, Bavarian Alps, Germany, Geomorphology, 55(1-4), 45-63, doi:10.1016/S0169-555X(03)00131-4.

Schwanghart, W., and D. Scherler (2013), Short Communication: TopoToolbox 2-an efficient and user-friendly tool for Earth surface sciences, Earth Surface Dynamics Discussions, 1, 261-275, doi:10.5194/esurfd-1-261-2013.

Seitz, F. (1949), On the Distortion of Solids by Action of Fast Massive Particles, Discussions of the Faraday Society, 5, 271-282.

Seong, Y. B., L. A. Owen, C. Yi, and R. C. Finkel

(2009), Quaternary glaciation of Muztag Ata and Kongur Shan: Evidence for glacier response to rapid climate changes throughout the Late Glacial and Holocene in westernmost Tibet, Geological Society of America Bulletin, 121(3-4), 348-365, doi:10.1130/B26339.1.

Seong, Y. B., L. A. Owen, M. P. Bishop, A. Bush, P. Clendon, L. Copland, R. Finkel, U. Kamp, and J. F. Shroder Jr. (2007), Quaternary glacial history of the Central Karakoram, Quaternary Science Reviews, 26(25-28), 3384-3405, doi:10.1016/j.quascirev.2007.09.015.

Shakun, J. D., P. U. Clark, F. He, N. A. Lifton, Z. Liu, and L. Otto-Bliesner (2015), Regional and global forcing of glacier retreat during the last deglaciation, Nature Communications, 6:8059, doi:10.1038/ncomms9059.

Shi, Y., G. Yu, X. Liu, B. Li, and T. Yao (2001), Reconstruction of the 30–40kabp enhanced Indian monsoon climate based on geological records from the Tibetan Plateau, Palaeogeography, Palaeoclimatology, Palaeoecology, 169(1-2), 69-83, doi:10.1016/S0031-0182(01)00216-4.

Shreve, R. L. (1987), Blackhawk landslide, southwestern San Bernardino County, California, in Cordilleran Section of the Geological Society of America (Centennial Field Guide), edited by M. L. Hill, pp. 109-114.

Shroder, J. F. (1998), Slope failure and denudation in the western Himalaya, Geomorphology, 26(1-3), 81-105, doi:10.1016/S0169-555X(98)00052-X.

Shroder, J. F., M. S. Khan, R. D. Lawrence, I. P. Madin, and S. M. Higgins (1989), Quaternary glacial chronology and neotectonics in the Himalaya of northern Pakistan, Geological Society of America Special Papers, 232, 275-294, doi:10.1130/SPE232-p275.

Singh, R., Prasath, R. A., Paul., A., and Kumar, N. (2018), Earthquake swarm of Himachal Pradesh in northwest Himalaya and its seismotectonic implications, Physics of the Earth and Planetary Interiors, 275, 44-55, doi:10.1016/j.pepi.2018.01.002

Sklar, L., and W. E. Dietrich (1998), River Longitudinal Profiles and Bedrock Incision Models: Stream Power and the Influence of Sediment Supply, in Rivers Over Rock: Fluvial Processes in Bedrock Channels, pp. 237-260, American Geophysical Union.

Smith, J. A., G. O. Seltzer, D. L. Farber, D. T. Rodbell, and R. C. Finkel (2005), Early local Last Glacial Maximum in the Tropical Andes, Science, 308(5722), 678-681, doi:10.1126/science.1107075.

Snyder, N. P. (2003), Importance of a stochastic distribution of floods and erosion thresholds in the bedrock river incision problem, Journal of Geophysical Research, 108(B2), 2117, doi:10.1029/2001JB001655.

Sobel, E. R., and D. Seward (2010), Influence of etching conditions on apatite fission-track etch pit diameter, Chemical Geology, 271(1-2), 59-69, doi:10.1016/j.chemgeo.2009.12.012.

Sobel, E. R., and M. R. Strecker (2003), Uplift, exhumation and precipitation: tectonic and climatic control of Late Cenozoic landscape evolution in the northern Sierras Pampeanas, Argentina, Basin Research, 15(4), 431–451, doi:10.1038/35069099.

Srivastava, P., and G. Mitra (1994), Thrust geometries and deep structure of the outer and lesser Himalaya, Kumaon and Garhwal (India): Implications for evolution of the Himalayan fold?and?thrust belt, Tectonics, 13(1), 89–109, doi:10.1029/93TC01130.

Steck, A. (2003), Geology of the NW Indian Himalaya, Eclogae Geologicae Helvetiae, 96(2), 147–U13, doi:10.1007/s00015-003-1091-4.

Stenni, B., V. Masson-Delmotte, S. Johnsen, J. Jouzel, A. Longinelli, E. Monnin, R. R o thlisberger, and E. Selmo (2001), An Oceanic Cold Reversal During the Last Deglaciation, Science, 293(5537), 2074-2077.

Stevens, V. L., and J. P. Avouac (2015), Interseismic coupling on the main Himalayan thrust, Geophysical Research Letters, 42(14), 5828–5837, doi:10.1002/2015GL064845.

Stone, J. O. (2000), Air pressure and cosmogenic isotope production, Journal of Geophysical Research: Solid Earth, 105, 23753-23759, doi:10.1029/2000JB900181.

Strecker, M. R., G. E. Hilley, J. R. O. N. Arrowsmith, and I. Coutand (2003), Differential structural and geomorphic mountain-front evolution in an active continental collision zone: The northwest Pamir, southern Kyrgyzstan, Geological Society of America Bulletin, 115(2), 166-181, doi:10.1130/0016-7606(2003)115<0166:DSAGMF>2.0.CO;2.

Stübner, K., C. Warren, L. Ratschbacher, B. Sperner, R. Kleeberg, J. Pfänder, and D. Grujic (2017), Anomalously old biotite 40Ar/ 39Ar ages in the NW Himalaya, Lithosphere, 9(3), 366–383, doi:10.1130/L586.1.

Stübner, K., D. Grujic, I. Dunkl, R. Thiede, and P. Eugster (2018), Pliocene episodic exhumation and the significance of the Munsiari thrust in the northwestern Himalaya, Earth and Planetary Science Letters, 481, 273–283, doi: 10.1016/j.epsl.2017.10.036

Stübner, K., D. Grujic, R. R. Parrish, N. M. W. Roberts, A. Kronz, J. Wooden, and T. Ahmad (2014), Monazite geochronology unravels the timing of crustal thickening in NW Himalaya, Lithos, 210-211, 111–128, doi:10.1016/j.lithos.2014.09.024.

Stüwe, K., L. White, and R. Brown (1994), The influence of eroding topography on steady-state isotherms. Application to fission track analysis, Earth and Planetary Science Letters, 124(1-4), 63-74, doi:10.1016/0012-821X(94)00068-9.

Styron, R. H., M. H. Taylor, and M. A. Murphy (2011), Oblique convergence, arc-parallel extension, and the role of strike-slip faulting in the High Himalaya, Geosphere, 7(2), 582–596, doi:10.1130/GES00606.S1.

Sugden, D. E., and B. S. John (1976), Glaciers and landscape, E. Arnold.

Taylor, M., and A. Yin (2009), Active structures of the Himalayan-Tibetan orogen and their relationships to earthquake distribution, contemporary strain field, and Cenozoic volcanism, Geosphere, 5(3), 199-214, doi:10.1130/GES00217.1.

Thakur, V. C., M. Joshi, D. Sahoo, and N. Suresh (2014), Partitioning of convergence in Northwest Sub-Himalaya: estimation of late Quaternary uplift and convergence rates across the Kangra reentrant, North India, International Journal of Earth Sciences, 103, 1037–1056, doi:10.1007/s00531-014-1016-7.

Thiede, R., X. Robert, K. Stübner, S. Dey, and J. Faruhn (2017), Sustained out-of-sequence shortening along a tectonically active segment of the Main Boundary thrust: The Dhauladhar Range in the northwestern Himalaya, Lithosphere, 9(5), 715–725, doi:10.1130/L630.1.

Thiede, R. C., and T. A. Ehlers (2013), Large spatial and temporal variations in Himalayan denudation, Earth and Planetary Science Letters, 371-372, 278–293, doi:10.1016/j.epsl.2013.03.004.

Thiede, R. C., J. R. Arrowsmith, B. Bookhagen, M. McWilliams, E. R. Sobel, and M. R. Strecker (2006), Dome formation and extension in the Tethyan Himalaya, Leo Pargil, northwest India, GSA Bulletin, 118(5/6), 635–650, doi:10.1130/B25872.1.

Thiede, R. C., T. A. Ehlers, B. Bookhagen, and M. R. Strecker (2009), Erosional variability along the northwest Himalaya, Journal of Geoyphisical Research, 114, –, doi:10.1029/2008JF001010.

Thiede, R., B. Bookhagen, and J. Arrowsmith (2004), Climatic control on rapid exhumation along the Southern Himalayan Front, Earth and Planetary Science Letters, 222(3-4), doi:10.1016/j.epsl.2004.03.015.

Thiede, R., J. Arrowsmith, and B. Bookhagen (2005), From tectonically to erosionally controlled development of the Himalayan orogen, Geology, 33, 689–692, doi:10.1130/G21483AR.1.

Thomson, S. N., M. T. Brandon, J. H. Tomkin, P. W. Reiners, C. Vasquez, and N. J. Wilson (2010), Glaciation as a destructive and constructive control on mountain building, Nature, 467(7313), 313-317, doi:10.1038/nature09365.

Tovar, D.S., J. Shulmeister, and T. R. Davies (2008), Evidence for a landslide origin of New ZealandÕs Waiho Loop moraine, Nature Geoscience, 1(8), 524-526, doi:10.1038/ngeo249.

Trauth, M. H., R. A. Alonso, K. R. Haselton, R. L. Hermanns, and M. R. Strecker (2000), Climate change and mass movements in the NW Argentine Andes, Earth and Planetary Science Letters, 179(2), 243-256, doi:10.1016/S0012-821X(00)00127-8.

Tucker, G. E. (2004), Drainage basin sensitivity to tectonic and climatic forcing: implications of a stochastic model for the role of entrainment and erosion thresholds, Earth Surf Proc Land, 29(2), 185-205, doi:10.1002/esp.1020.

Turpeinen, H., A. Hampel, T. Karow, and G. Maniatis (2008), Effect of ice sheet growth and melting on the slip evolution of thrust faults, Earth and Planetary Science Letters, 269(1-2), 230-241, doi:10.1016/j.epsl.2008.02.017.

Tweed, F. S., and A. J. Russell (1999), Controls on the formation and sudden drainage of glacier-impounded lakes: implications for jökulhlaup characteristics, Progress in Physical Geography, 23(1), 79-110, doi:10.1177/030913339902300104.

Ustaszewski, M. E., A. Hampel, and O. A. Pfiffner (2008), Composite faults in the Swiss Alps formed by the interplay of tectonics, gravitation and postglacial rebound: an integrated field and modelling study, Swiss Journal of Geosciences, 101(1), 223-235, doi:10.1007/s00015-008-1249-1.

Valdiya, K. S. (1980), The two intracrustal boundary thrusts of the Himalaya, Tectonophysics, 66(4), 323–348, doi:10.1016/0040-1951(80)90248-6.

Valdiya, K. S. (1995), Proterozoic sedimentation and Pan-African geodynamic development in the Himalaya, Precambrian Research, 74(1-2), 35–55, doi:10.1016/0301-9268(95)00004-O.

van der Beek, P., C. Litty, M. Baudin, J. Mercier, X. Robert, and E. Hardwick (2016), Contrasting tectonically driven exhumation and incision patterns, western versus central Nepal Himalaya, Geology, 44(4), 327-330, doi:10.1130/G37579.1.

van der Beek, P., J. Van Melle, S. Guillot, A. Pêcher, P. W. Reiners, S. Nicolescu, and M. Latif (2009), Eocene Tibetan plateau remnants preserved in the northwest Himalaya, Nature Geoscience, 2(5), 364-368, doi:10.1038/ngeo503.

Vannay, J.-C., and B. Grasemann (2001), Himalayan inverted metamorphism and syn-convergence extension as a consequence of a general shear extrusion, Geological Magazine, 138(3), 253–276, doi:10.1017/S0016756801005313

Vannay, J.-C., B. Grasemann, R. Meinert, F. W, A. Carter, V. Baudraz, and M. Cosca (2004), Miocene to Holocene exhumation of metamorphic crustal wedges in the NW Himalaya: Evidence for tectonic extrusion coupled to fluvial erosion, Tectonics, 23(1), doi:10.1029/2002TC001429.

Vehling, L., J. Rohn, and M. Moser (2016), Quantification of small magnitude rockfall processes at a proglacial high mountain site, Gepatsch glacier (Tyrol, Austria), Zeitschrift für Geomorphologie, doi:10.1127/zfg_suppl/2015/S-00184.

Wagnon, P. et al. (2007), Four years of mass balance on Chhota Shigri Glacier, Himachal Pradesh, India, a new benchmark glacier in the western Himalaya, Journal of Glaciology, 53(183), 603-611, doi:10.3189/002214307784409306.

Waitt, R. B. (1985), Case for periodic, colossal jökulhlaups from Pleistocene glacial Lake Missoula, Geological Society of America Bulletin, 96(10), 1271-1286, doi:10.1130/0016-7606(1985)96<1271:CFPCJF>2.0.CO;2.

Walder, J. S., and J. E. Costa (1996), Outburst floods from glacier-dammed lakes: the effect of mode of lake drainage on flood magnitude, Earth Surface Processes and Landforms, 21(8), 701-723, doi:10.1002/(SICI)1096-9837(199608)21:8<701::AID-ESP615>3.0.CO;2-2.

Wallis, D., A. Carter, R. J. Phillips, A. J. Parsons, and M. P. Searl (2016), Spatial variation in exhumation rates across Ladakh and the Karakoram: New apatite fission track data from the Eastern Karakoram, NW India, Tectonics, 35, 704-721.

Ward, D. J., R. S. Anderson, and P. J. Haeussler (2012), Scaling the Teflon Peaks: Rock type and the generation of extreme relief in the glaciated western Alaska Range, Journal of Geophysical Research, 117(F1), doi:10.1029/2011JF002068.

Ward, D., and R. S. Anderson (2011), The use of ablation dominated medial moraines as samplers for 10Be derived erosion rates of glacier valley walls, Kichatna Mountains, AK, Earth Surfaces and Landforms, 36, 495-512, doi:10.1002/esp.2068.

Webb, A. A. G. (2013), Preliminary balanced palinspastic reconstruction of Cenozoic deformation across the Himachal Himalaya (northwestern India), Geosphere, 9, 572–587, doi:10.1130/GES00787.

Webb, A. A. G., A. Yin, T. M. Harrison, J. Célérier, and W. P. Burgess (2007), The leading edge of the Greater Himalayan Crystalline complex revealed in the NW Indian Himalaya: Implications for the evolution of the Himalayan orogen, Geology, 35(10), 955-958, doi:10.1130/G23931A.1.

Webb, A., A. Yin, T. M. Harrison, J. Célérier, G. Gehrels, C. E. Manning, and M. Grove (2011), Cenozoic tectonic history of the Himachal Himalaya (northwestern India) and its constraints on the formation mechanism of the Himalayan orogen, Geosphere, 7(4), 1013-1061, doi:10.1130/GES00627.1.

Webster, P. J., V. O. Magana, T. N. Palmer, J. Shukla, R. A. Tomas, M. Yanai, and T. Yasunari (1998), Monsoons: Processes, predictability, and the prospects for prediction, Journal of Geophysical Research, 103(C7), 14451-14510, doi:10.1029/97JC02719.

Wells, S. G., L. D. McFadden, J. Poths, and C. T. Olinger (1995), Cosmogenic 3He surface-exposure dating of stone pavements: Implications for landscape evolution in deserts, Geology, 23(7), 613-616, doi:10.1130/0091-7613(1995)023<0613:CHSEDO>2.3.CO;2.

Whipp, D. M., Jr., C. Beaumont, and J. Braun (2014), Feeding the "aneurysm": orogen-parallel mass transport into Nanga Parbat and the western Himalayan syntaxis, J. Geophys. Res., 119, doi:10.1002/2013JB010929.

Whipple, K. X., M. Shirzaei, K. V. Hodges, and J. R. Arrowsmith (2016), Active shortening within the Himalayan orogenic wedge implied by the 2015 Gorkha earthquake, Nature Geoscience, 9(9), 711–716, doi:10.1038/ngeo2797.

Willett, S. D. (1999), Orogeny and orography: The effects of erosion on the structure of mountain belts, Journal of Geophysical Research, 104(B12), 28957, doi:10.1029/1999JB900248.

Willett, S. D. (2010), Late Neogene Erosion of the Alps: A Climate Driver? Annual Review of Earth and Planetary Sciences, 38(1), 411-437, doi:10.1146/annurev-earth-040809-152543.

Willett, S. D., and M. T. Brandon (2002), On steady states in mountain belts,

Willett, S. D., R. Slingerland, and N. Hovius (2001), Uplift, shortening, and steady state topography in active mountain belts, American Journal of Science, 301, 455-485, doi:10.2475/ajs.301.45.455.

Wittmann, H., F. von Blanckenburg, T. Kruesmann, K. P. Norton, and P. W. Kubik (2007), Relation between rock uplift and denudation from cosmogenic nuclides in river sediment in the Central Alps of Switzerland, Journal of Geophysical Research: Earth Surface, 112, F04010, doi:10.1029/2006JF000729.

Wobus, C., A. Heimsath, K. Whipple, and K. Hodges (2005.), Active out-of-sequence thrust faulting in the central Nepalese Himalaya, Nature, 434, 1008-1011, doi:10.1038/nature03499.

Wobus, C. W., K. X. Whipple, and K. V. Hodges (2006), Neotectonics of the central Nepalese Himalaya: Constraints from geomorphology, detrital 40Ar/ 39Ar thermochronology, and thermal modeling, Tectonics, 25(4), TC4011, doi:10.1038/366557a0.

Wolf, R. A., K. A. Farley, and D. M. Kass (1998), Modeling of the temperature sensitivity of the apatite (U-Th)/He thermochronometer, Chemical Geology, 148(1-2), 105-114, doi:10.1016/S0009-2541(98)00024-2.

Wolman, M. G., and J. P. Miller (1960), Magnitude and frequency of forces in geomorphic processes, The Journal of Geology, 68(1), 54-74, doi:10.1086/626637.

Wu, C., K. D. Nelson, G. Wortman, S. D. Samson, Y. Yue, J. Li, W. S. F. Kidd, and M. A. Edwards (1998), Yadong cross structure and South Tibetan Detachment in the east central Himalaya (89°-90°E), Tectonics, 17(1), 28-45, doi:10.1029/97TC03386.

Wulf, H., B. Bookhagen, and D. Scherler (2010), Seasonal precipitation gradients and their impact on fluvial sediment flux in the Northwest Himalaya, Geomorphology, 118(1-2), 13-21, doi:10.1016/j.geomorph.2009.12.003.

Wulf, H., B. Bookhagen, and D. Scherler (2012), Climatic and geologic controls on suspended sediment flux in the Sutlej River Valley, western Himalaya, Hydrology and Earth System Science, 16, 2193-2217, doi:10.5194/hess-16-2193-2012.

Yin, A. (2006), Cenozoic tectonic evolution of the Himalayan orogen as constrained by along-strike variation of structural geometry, exhumation history, and foreland sedimentation, Earth-Science Reviews, 76(1-2), 1-131, doi:10.1016/j.earscirev.2005.05.004.

Säg Dank

I would like to thank Rasmus Thiede, Dirk Scherler and Tibi Codilean for their guidance during my doctoral studies at the University of Potsdam. Further I would to thank Manfred Strecker for the open door and to make it possible to attend exceptional opportunities during my time as doctoral student.

Lydia Olaka, Henry Wichura, Esther Hintersberger, Rasmus Thiede, Dirk Scherler and further persons involved into the Graduate School GRK 1364 are thanked for the organization of the excursions to Kenya and India, and workshops in Potsdam.

I would like to thank...

...Christine Fischer for her help coring OSL samples during night shifts and lab help.

...Tibi Codilean for introducing me into TCN method and sample preparation.

...Ed Sobel for his patient introduction and aid with the apatite fission-track method.

...Heiko Pingel for lab and Adobe Illustrator help.

...Hannes Faruhn for his help in apatite sample preparation.

...Walter Düsing, Franziska Scheffler, Taylor Schildgen, Steffi Tofelde for their help with cosmo sample preparation.

...Birgit Fabian for her help with Adobe Illustrator issues.

...big Tashi/Tashi 1 (Tsering Longpo), little Tashi/Tashi 2, Tashi from Batal, Tashi from Keylong, the Family of Tashi 1 and Tashi 2, Cherri and Amit in Manali for their big support during fieldwork.

...my office mates Anke, Vero, Fabiana, Fred, Johannes, Sebastian, Stephanie for cake, chocolate and coffee breaks and hours, but also fruitful discussions.

...Bernd, Franzi, Heiko, Jonathan, Alex, Michael for quality time.

...other group members and doctoral students Iris, Ricarda, Saptarshi, Jürgen, Clemens, Jan, Henry M., Swenja, Renjie, Giuditta, Steffi, Konstanze, Paolo, Görkem, Viktoria for discussions and support.

Danke Dani fürs Motivieren, Durchlesen, Ablenken, Aufbauen, Dasein.

Herzliche Dank a mini Familie und Fründ i de Schwiiz für Bsüech, Nochfroge und Schoggi.

Danke Grosi.

And he told stories, tracing with a finger in the dust,
of the immense and sumptuous ritual of avalanche-guarded cathedrals;
of processions and devil dances;
of changing of monks and nuns into swine;
of holy cities fifteen thousand feet in the air;
of intrigue between monastery and monastery;
of voices among the hills,
and of that mysterious mirage that dances on dry snow.

Kim Rudyard Kipling

APPENDICES

Appendix A

Reconstruction of the glacial extent and timing of the Chandra Valley Glacier

In Appendix A we list information we used to reconstruct the glacial timing and extent in the Chandra Valley.

- We also provide field photographs to emphasize the glacial features observed in the Chandra Valley, which are together with the ^{10}Be data the base of our reconstruction.
- References of Figure 2.3 will be listed in the following text part, full reference list is provided at the end of Appendix A.
- The datasets/tables contain information about our ^{10}Be concentrations and the re-calculated ^{10}Be data used in Figure 2.3 and the glacial striations.

A.1. Field photographs

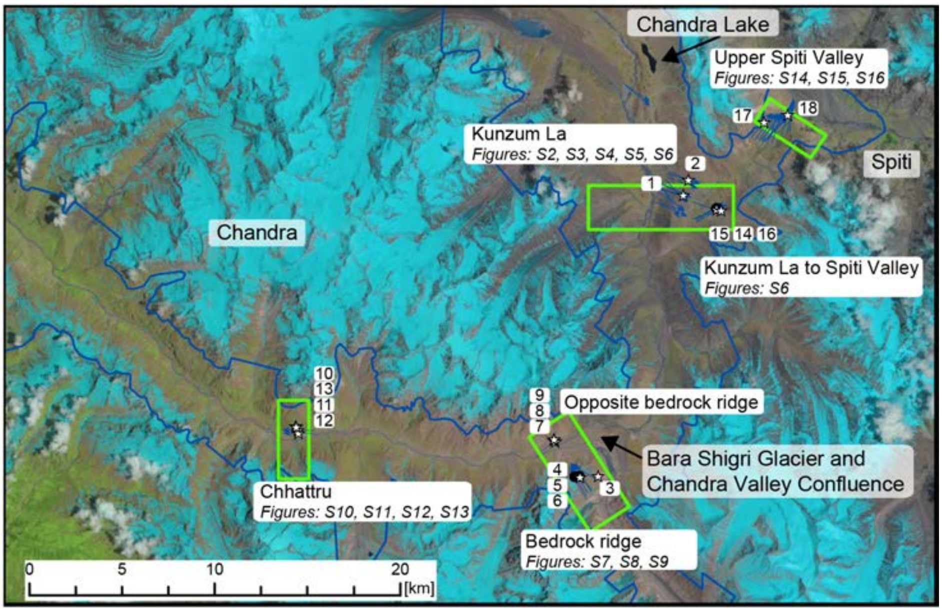

Figure A.1: Landsat 8 image of July, 2014 (data available from the U.S. Geological Survey http://glovis.usgs.gov/) with sampling areas indicated by green boxes. Sample numbers correspond to numbers in the Table A.1, Data Sets S1 and S2. Location names correspond to following photos of locations and glacial features.

Table A.1: Sampling locations in the Chandra Valley with sample number corresponding to Figure A.1

Nr.	Sample Name	Type[a]	Description	Location	Profile
1	WP051	pbs	Metagranite	Kunzum La	a - a’
2	PE13_01	pbs	Qtz vein	Kunzum La	a - a’
3	PE12_013	pbs	Metagranite	Bedrock ridge	b - b’
4	WP058	pbs	Metagranite	Bedrock ridge	b - b’
5	WP059	bos	Metagranite	Bedrock ridge	b - b’
6	WP057	bos	Metagranite	Bedrock ridge	b - b’
7	WP052	pbs	Qtz vein	Opposite bedrock ridge	b - b’
8	WP053	pbs	Metagranite	Opposite bedrock ridge	b - b’
9	WP054	pbs	Metagranite	Opposite bedrock ridge	b - b’
10	PE12_061	pbs	Qtz vein	Chhattru	c - c’
11	PE12_062	pbs	Metagranite	Chhattru	c - c’
12	PE12_063	pbs	Metagranite	Chhattru	c - c’
13	PE12_064	pbs	Metagranite, Qtz vein	Chhattru	c - c’
14	PE12_056	pbs	Qtz vein	Kunzum La to Spiti	-
15	PE12_057	bos	Qtz-sst	Kunzum La to Spiti	-
16	PE12_058	pbs	Qtz vein	Kunzum La to Spiti	-
17	PE13_02	pbs	Qtz-sst	Upper Spiti Valley	-
18	PE13_03	pbs	Qtz-sst	Upper Spiti Valley	-

[a] pbs = polished bedrock surface, bos = boulder on polished bedrock surface

Figure A.2: View from close to Chandratal (Chandra Lake) to Kunzum La in the south. From the front until Kunzum La, glacially polished bedrock surfaces are situated. The trimline, limit of polished and not overridden surfaces above, is clearly visible on the right valley side.

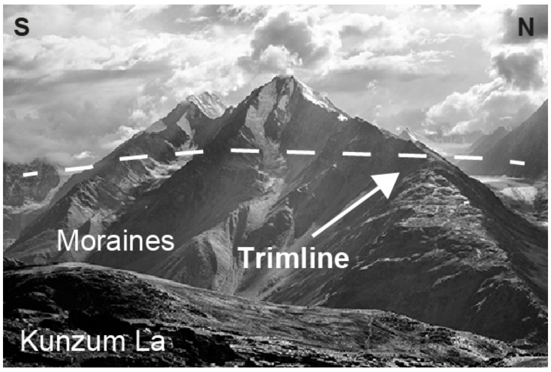

Figure A.3: STrimline across the valley seen from the Kunzum La.

Figure A.4: Glacial striations on a quartz vein at the Kunzum La.

Figure A.5: Sampling of a quartzite boulder on overridden surface from Kunzum La to Spiti.

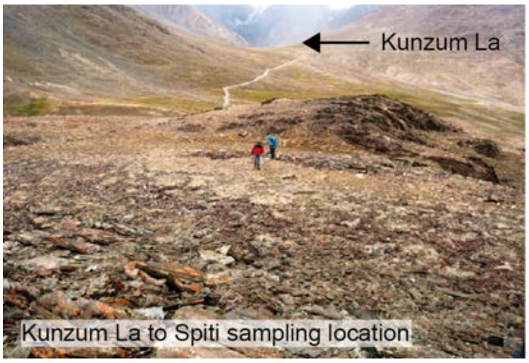

Figure A.6: In the foreground the sampling location from Kunzum La to Spiti situated on brittle bedrock, in the background the Kunzum La (Pass).

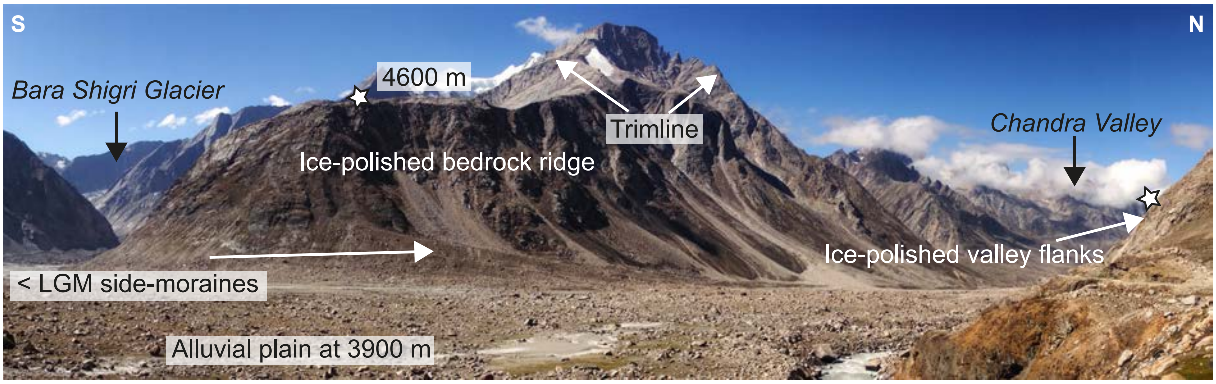

Figure A.7: Ice-polished bedrock ridge at confluence of Bara Shigri Glacier and the Chandra Valley: View from the road to the west. The polished back of the bedrock ridge is located 700 m above the current day valley floor. Stars indicate sampling locations (Photo: Franziska Hanf).

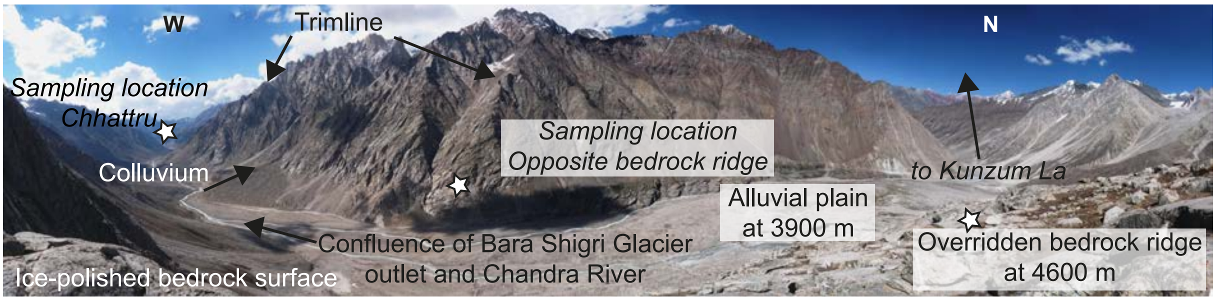

Figure A.8: View from the ice-polished bedrock ridge (Figure A.6 S6) at the confluence of the Bara Shigri Glacier and the Chandra Valley. On the right side view is to the north where the Kunzum La is located. On the left side view is into Chandra Valley, which is running from east to west. The sampling location at Chhattru is located 15 km valley down. Stars indicate sampling locations.

Figure A.9: Polished bedrock surface with glacial striations on the bedrock ridge.

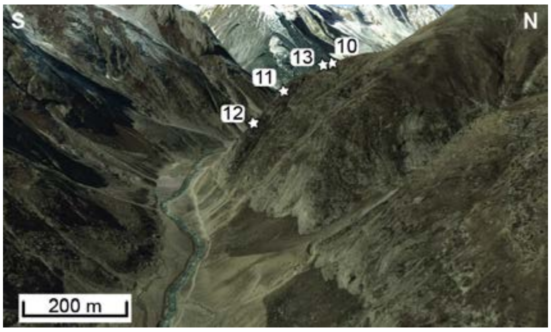

Figure A.10: Sampling location close to Chhattru, where the valley gets narrower. Number corresponds to sample number in the above table. Source: Google Earth.

Figure A.11: Sampling locations on ice-polished bedrock exposed approx. 700 m above current valley floor.

Figure A.12: Striations on valley wall indicating flow directions parallel to the strike of the valley.

Figure A.13: Close up of glacial striations on valley at the sampling site Chhattru.

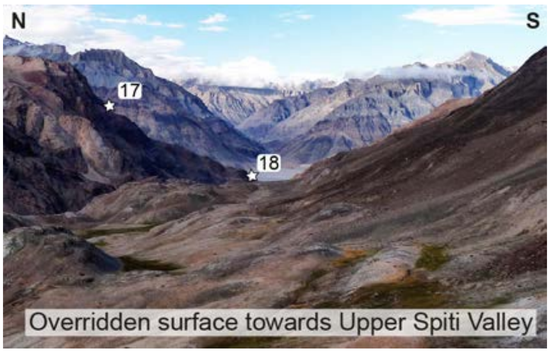

Figure A.14: Overridden landforms from Kunzum La into the Upper Spiti Valley. Stars indicate sampling location in the Upper Spiti Valley.

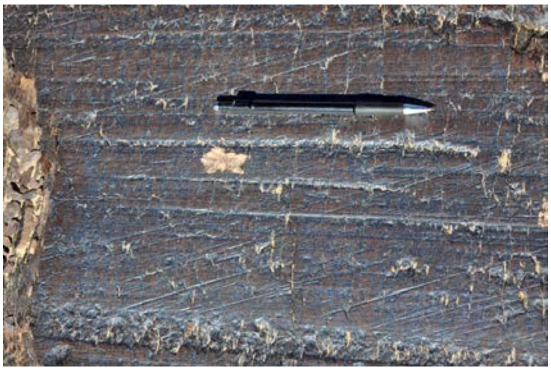

Figure A.15: Striations measured on quartzitic-sandstone with rock varnish around the location of sample 18.

Figure A.16: Overridden surface covered with glacial striations and rock varnish.

A.2. ^{10}Be ages and production rates comparison

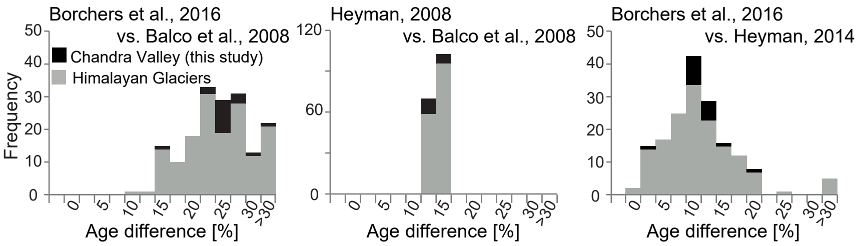

Figure A.17: Comparison of ^{10}Be exposure ages of Himalayan glaciers that were obtained by using the different calculators. Balco et al. [2008] and Heyman [2014] represent the Lal/Stone (2000) time-dependent ages, while Borchers et al. [2015] used LSD scaling [Lifton et al., 2014].

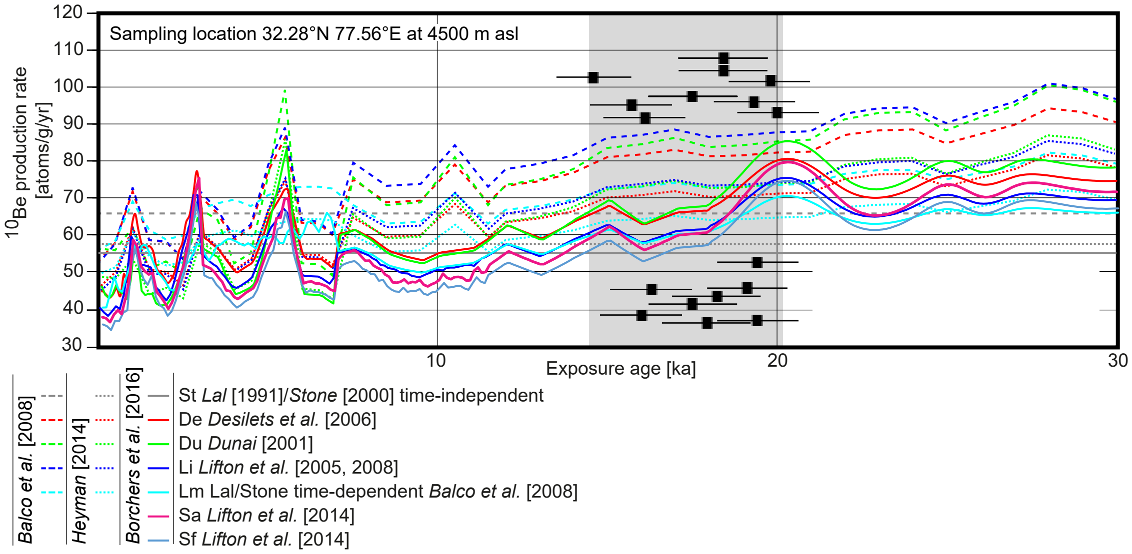

Figure A.18: Comparison of ^{10}Be production rates of a sampling location in the study area (32.28°N 77.56°E at 4500 m asl) by using different calibration sets and the ages of this study in the grey box (A.1). The production rate is lower in the newer calibration data sets. For the retreat history of the Chandra Valley glacier we used the Lifton et al. [2014] Sa scaling scheme.

A.3. References of Figure 2.3

Climate Proxies
NGRIP: Andersen et al. [2004]
Gulyia Ice core: Thompson et al. [1997]
Moisture: Herzschuh [2006]
Mamwluh Cave: Dutt et al. [2015]
Insolation: Berger and Loutre [1991]
Epica Ice Dome: Stenni et al. [2011]

Himalayan Glaciers
Baltoro Glacier, Karakorum: Seong et al. [2007]
Chandra Valley, NW Himalaya: Owen et al. [1996]; Owen et al. [2001], this study
Tons Glacier, Garhwal, NW Himalaya: Scherler et al. [2010]
Khumbu Glacier, Central Himalaya: Finkel et al. [2003], Owen et al. [2009]
Mailun Khola Glacier, Central Himalaya: Gayer et al. [2004], Gayer et al. [2006]
Rongbuk Glacier, Central Himalaya: Owen et al. [2009]

Northern Hemisphere Glaciers
Boulder Creek, North America: Ward et al. [2009]
Gurrenholm Dal, Greenland: Kelly et al. [2008]
Laurentide Ice Sheet, North America: Ullman et al. [2014]
Pinedale Ice Cap, North America: Licciardi et al. [2001], Licciardi and Pierce [2008]
Reuss Glacier, Alps : Reber et al. [2014]
Valais Glacier, Alps: Hadorn et al. [2002], Ivy-Ochs et al. [2004], Ivy-Ochs et al. [2008]

Southern Hemisphere Glaciers
Alacocha Glacier, Central Andes: Smith, [2005]
Lago Argentino, Patagonia: Kaplan et al. [2004]
Tres Lagunas, Central Andes: Zech et al. [2009]
Ohau Glacier, New Zealand: Putnam et al. [2013]
Pukaki Glacier New Zealand: Putnam et al. [2010], Kelley et al. [2014]

A.4. Data Set 1

Table A.2: Data Set 1: Comparison of ^{10}Be ages among different CRONUS calculators

Sample		Production rate		Lal(1991)/Stone(2000)	Production rate	Desilets et al. (2003,2006)	Dunai (2001)	Lifton et al. (2005)	Lal/Stone td	Lifton et al. (2014)	Lifton et al. (2014)
		muons	int. uncert.	Exposure age St	spallation	Exposure age De	Exposure age Du	Exposure age Li	Exposure age Lm	Expsosure age Sa	Exposure age Sf
Nr	Name	atoms/g/yr	yr	ka ±1σ	ka ±1σ	ka ±1σ	ka ±1σ	ka ±1σ	ka ±1σ	ka ±1σ	ka ±1σ
Borchers et al., 2016											
1	WP051	0.357		14.9 ±1.3	45.8	15.2 ±2.1	15.6 ±2.1	15.0 ±1.8	15.0 ±1.2	16.0 ±1.2	16.3 ±1.4
2	PE13_01	0.355		18.4 ±1.6	45.7	18.3 ±2.5	18.7 ±2.3	18.0 ±2.2	18.2 ±1.4	19.2 ±1.2	19.4 ±1.3
3	PE12_013	0.300		14.7 ±1.3	37.3	15.2 ±2.1	15.7 ±2.1	15.0 ±1.8	14.8 ±1.1	15.9 ±1.2	16.1 ±1.3
4	WP058	0.321		18.5 ±1.6	39.9	18.6 ±2.5	19.0 ±2.3	18.4 ±2.2	18.2 ±1.4	19.3 ±1.2	19.6 ±1.3
5	WP059	0.324		35.4 ±3.1	40.3	32.2 ±4.5	31.8 ±4.2	31.6 ±3.9	32.3 ±2.5	32.5 ±2.3	33.0 ±2.5
6	WP057	0.322		16.6 ±1.5	39.9	17.0 ±2.4	17.5 ±2.3	16.8 ±2.2	16.6 ±1.3	17.8 ±1.3	18.0 ±1.4
7	WP052	0.238		16.0 ±1.4	27.5	16.9 ±2.4	17.4 ±2.3	16.8 ±2.2	16.0 ±1.3	17.4 ±1.3	17.7 ±1.4
8	WP053	0.260		13.0 ±1.1	30.5	14.0 ±2.0	14.5 ±1.9	13.8 ±1.8	13.1 ±1.1	14.5 ±1.1	14.6 ±1.1
9	WP054	0.266		14.2 ±1.3	31.2	15.1 ±2.1	15.6 ±2.1	15.0 ±1.8	14.3 ±1.1	15.6 ±1.2	15.8 ±1.3
10	PE12_061	0.267		17.1 ±1.5	31.6	17.7 ±2.5	18.2 ±2.4	17.5 ±2.2	16.9 ±1.3	18.3 ±1.3	18.5 ±1.4
11	PE12_062	0.257		19.0 ±1.7	30.1	19.5 ±2.4	19.8 ±2.2	19.3 ±2.2	18.7 ±1.4	19.9 ±1.2	20.1 ±1.3
12	PE12_063	0.254		18.2 ±1.6	29.5	18.9 ±2.5	19.3 ±2.3	18.7 ±2.2	18.0 ±1.4	19.3 ±1.2	19.6 ±1.3
13	PE12_064	0.269		18.8 ±1.6	31.7	19.3 ±2.4	19.6 ±2.3	19.1 ±2.2	18.5 ±1.4	19.7 ±1.2	19.9 ±1.3
14	PE12_056	0.328		17.0 ±1.5	41.4	17.2 ±2.4	17.7 ±2.4	17.0 ±2.2	16.9 ±1.3	18.1 ±1.3	18.3 ±1.4
15	PE12_057	0.337		18.1 ±1.6	42.5	18.2 ±2.5	18.6 ±2.3	18.0 ±2.3	18.0 ±1.4	19.0 ±1.2	19.3 ±1.3
16	PE12_058	0.334		15.0 ±1.3	42.1	15.4 ±2.1	15.9 ±2.2	15.2 ±1.8	15.1 ±1.2	16.2 ±1.2	16.5 ±1.3
17	PE13_02	0.305		16.3 ±1.4	38.3	16.6 ±2.4	17.1 ±2.3	16.4 ±2.1	16.3 ±1.3	17.4 ±1.3	17.7 ±1.4
18	PE13_03	0.281		17.1 ±1.5	33.8	17.7 ±2.5	18.1 ±2.4	17.5 ±2.2	17.0 ±1.3	18.3 ±1.3	18.5 ±1.4

Continued on next page

Table A.2 – *Continued from previous page*

Sample		Production rate		Lal(1991)/Stone(2000)	Production rate	Desilets et al. (2003,2006)	Dunai (2001)	Lifton et al. (2005)	Lal/Stone td	Lifton et al. (2014)	Lifton et al. (2014)
		muons	int. uncert.	Exposure age St	spallation	Exposure age De	Exposure age Du	Exposure age Li	Exposure age Lm	Expsosure age Sa	Exposure age Sf
Nr.	Name	atoms/g/yr	yr	ka $\pm 1\sigma$	ka $\pm 1\sigma$	ka $\pm 1\sigma$	ka $\pm 1\sigma$	ka $\pm 1\sigma$	ka $\pm 1\sigma$	ka $\pm 1\sigma$	ka $\pm 1\sigma$
Heyman, 2014											
1	WP051	0.732	504	14.9 ±0.7	65.2	14.2 ±0.7	14.6 ±0.7	14.0 ±0.7	14.6 ±0.7		
2	PE13_01	0.734	605	18.5 ±0.9	65.0	17.1 ±0.8	17.3 ±0.8	16.7 ±0.8	17.8 ±0.9		
3	PE12_013	0.676	481	14.7 ±0.7	53.2	14.2 ±0.7	14.6 ±0.7	14.0 ±0.7	14.4 ±0.7		
4	WP058	0.673	607	18.5 ±0.9	57.0	17.4 ±0.9	17.6 ±0.9	17.0 ±0.8	17.8 ±0.9		
5	WP059	0.676	1150	35.5 ±1.7	57.4	30.3 ±1.5	29.9 ±1.5	29.5 ±1.4	32.1 ±1.6		
6	WP057	0.673	545	16.7 ±0.8	57.0	15.9 ±0.8	16.2 ±0.8	15.6 ±0.8	16.2 ±0.8		
7	WP052	0.585	530	16.1 ±0.8	39.3	15.8 ±0.8	16.1 ±0.8	15.6 ±0.8	15.6 ±0.8		
8	WP053	0.599	443	13.0 ±0.7	43.6	13.0 ±0.7	13.4 ±0.7	12.9 ±0.6	12.8 ±0.6		
9	WP054	0.608	475	14.2 ±0.7	44.6	14.2 ±0.7	14.5 ±0.7	14.0 ±0.7	13.9 ±0.7		
10	PE12_061	0.613	560	17.0 ±0.8	45.1	16.5 ±0.8	16.8 ±0.8	16.2 ±0.8	16.5 ±0.8		
11	PE12_062	0.6	618	19.0 ±0.9	43.0	18.2 ±0.9	18.4 ±0.9	17.9 ±0.9	18.2 ±0.9		
12	PE12_063	0.592	594	18.2 ±0.9	42.3	17.6 ±0.9	17.8 ±0.9	17.3 ±0.8	17.5 ±0.9		
13	PE12_064	0.61	613	18.8 ±0.9	45.3	17.9 ±0.9	18.2 ±0.9	17.6 ±0.9	18.0 ±0.9		
14	PE12_056	0.687	553	17.0 ±0.8	58.9	16.1 ±0.8	16.3 ±0.8	15.8 ±0.8	16.5 ±0.8		
15	PE12_057	0.698	601	18.2 ±0.9	60.4	17.0 ±0.8	17.3 ±0.8	16.7 ±0.8	17.6 ±0.9		
16	PE12_058	0.697	471	15.1 ±0.7	59.9	14.5 ±0.7	14.8 ±0.7	14.3 ±0.7	14.7 ±0.7		
17	PE13_02	0.686	554	16.3 ±0.8	54.5	15.5 ±0.8	15.8 ±0.8	15.3 ±0.8	15.9 ±0.8		
18	PE13_03	0.623	560	17.1 ±0.8	48.0	16.5 ±0.8	16.7 ±0.8	16.2 ±0.8	16.6 ±0.8		

Continued on next page

Table A.2 – *Continued from previous page*

Sample		Production rate		Lal(1991)/Stone(2000)	Production rate	Desilets et al. (2003,2006)	Dunai (2001)	Lifton et al. (2005)	Lal/Stone td	Lifton et al. (2014)	Lifton et al. (2014)
		muons	int. uncert.	Exposure age St	spallation	Exposure age De	Exposure age Du	Exposure age Li	Exposure age Lm	Expsosure age Sa	Exposure age Sf
Nr.	Name	atoms/g/yr	yr	ka ±1σ	ka ±1σ	ka ±1σ	ka ±1σ	ka ±1σ	ka ±1σ	ka ±1σ	ka ±1σ
Balco et al., 2008											
1	WP051	0.732	440	13.1 ±1.2	74.6	12.5 ±1.5	12.9 ±1.6	12.1 ±1.3	12.9 ±1.2		
2	PE13_01	0.734	529	16.2 ±1.5	74.4	15.1 ±1.9	15.4 ±1.9	14.5 ±1.5	15.8 ±1.4		
3	PE12_013	0.676	420	12.9 ±1.2	60.9	12.5 ±1.5	12.9 ±1.6	12.1 ±1.3	12.7 ±1.2		
4	WP058	0.673	530	16.2 ±1.5	65.2	15.3 ±1.9	15.7 ±1.9	14.8 ±1.5	15.8 ±1.4		
5	WP059	0.676	1004	31.0 ±2.9	65.7	26.9 ±3.3	26.7 ±3.3	25.7 ±2.7	28.7 ±2.6		
6	WP057	0.673	476	14.6 ±1.4	65.2	14.0 ±1.7	14.4 ±1.8	13.6 ±1.4	14.4 ±1.3		
7	WP052	0.585	463	14.0 ±1.3	45.0	13.9 ±1.7	14.3 ±1.8	13.5 ±1.4	13.9 ±1.3		
8	WP053	0.599	387	11.4 ±1.1	49.9	11.4 ±1.4	11.9 ±1.5	11.1 ±1.2	11.2 ±1.0		
9	WP054	0.608	415	12.5 ±1.2	51.1	12.4 ±1.5	12.8 ±1.6	12.1 ±1.3	12.3 ±1.1		
10	PE12_061	0.613	490	14.9 ±1.4	51.6	14.6 ±1.8	14.9 ±1.8	14.1 ±1.5	14.7 ±1.3		
11	PE12_062	0.6	540	16.6 ±1.5	49.2	16.1 ±2.0	16.4 ±2.0	15.6 ±1.6	16.2 ±1.5		
12	PE12_063	0.592	519	15.9 ±1.5	48.4	15.5 ±1.9	15.9 ±1.9	15.1 ±1.6	15.6 ±1.4		
13	PE12_064	0.61	536	16.4 ±1.5	51.9	15.8 ±1.9	16.2 ±2.0	15.3 ±1.6	16.0 ±1.5		
14	PE12_056	0.687	484	14.9 ±1.4	67.5	14.2 ±1.7	14.5 ±1.8	13.7 ±1.4	14.7 ±1.3		
15	PE12_057	0.698	525	16.0 ±1.5	69.2	15.1 ±1.9	15.4 ±1.9	14.5 ±1.5	15.6 ±1.4		
16	PE12_058	0.697	412	13.2 ±1.2	68.5	12.7 ±1.6	13.1 ±1.6	12.3 ±1.3	13.1 ±1.2		
17	PE13_02	0.686	484	14.3 ±1.3	62.4	13.7 ±1.7	14.1 ±1.7	13.3 ±1.4	14.1 ±1.3		
18	PE13_03	0.623	489	15.0 ±1.4	55.0	14.5 ±1.8	14.9 ±1.8	14.1 ±1.5	14.7 ±1.3		

A.5. Data Set 2

Table A.3: Data Set 2: Comparison of ^{10}Be ages used for the reconstruction

Fig.	Area and Publication	Sample	Latitude	Longitude	Elevation	Balco et al., 2008		Borchers et al., 2016		Heyman, 2014		Borchers vs. Heyman		Balco vs. Heyman		Balco vs. Borchers	
			+N,-S	+E, -W	m	Age (ka)	$\pm 1\sigma$	Age (ka)	$\pm 1\sigma$	Age (ka)	$\pm 1\sigma$	(%)	(ka)	(%)	(ka)	(%)	(ka)
3E	Chandra, India	L7	32.4	77.6	4340	13.2	1.4	16.5	1.6	14.9	1.1	11	1.6	13	1.7	25	3.3
	Owen et al.,1996	L8	32.5	77.6	4350	15.7	1.4	19.2	1.2	17.6	0.9	9	1.6	12	1.9	23	3.5
	Owen et al., 2001	L9	32.5	77.6	4350	14.7	1.4	18.1	1.4	16.6	1	9	1.5	12	1.8	23	3.4
		L10	32.3	77.2	2390	12.7	1.5	17	1.7	14.4	1.2	18	2.6	13	1.6	33	4.3
		L12	32.3	77.2	2415	11.6	1	15.5	1.2	13.1	0.6	18	2.4	13	1.5	34	3.9
		L15	32.3	77.2	2430	17.2	1.6	21.8	1.5	19.3	0.9	13	2.5	12	2.1	27	4.6
		L20	32.6	76.9	2865	9.8	1	13.1	1.2	11.1	0.7	18	2	13	1.3	34	3.3
		L21	32.6	76.9	2700	10.6	1.2	14.2	1.4	12	0.9	19	2.2	13	1.4	35	3.6
		L24	32.5	77	2985	3	0.3	3.9	0.4	3.4	0.2	15	0.5	12	0.4	29	0.9
		L25	32.5	77	2985	3.1	0.3	4.1	0.5	3.5	0.3	16	0.6	12	0.4	30	1
		L26	32.5	77	3050	14.1	1.3	18.2	1.4	15.8	0.9	15	2.4	12	1.8	30	4.1
		L27	32.5	77	2975	14.5	1.4	18.8	1.4	16.3	1	15	2.5	12	1.8	29	4.3
		L28	32.5	77	3000	12.3	1.1	16.2	1.3	14	0.7	16	2.2	13	1.6	31	3.9
		L29	32.5	77	2985	12.1	1.1	15.9	1.2	13.7	0.6	16	2.2	13	1.6	31	3.8
		L31	32.5	77.1	3020	10.5	0.9	14	1.1	11.9	0.5	18	2.1	13	1.4	33	3.5
		L32	32.5	77.1	3020	16.3	1.7	20.5	1.5	18.4	1.3	12	2.1	12	2	25	4.2
		L33	32.5	77.1	3036	17.8	1.6	22.1	1.5	20	0.9	10	2.1	13	2.2	24	4.3
		L37	32.4	77.6	4555	16.2	1.4	19.7	1.2	18.2	0.8	8	1.5	12	2	21	3.5
		L40	32.4	77.6	4780	14.7	1.3	18	1.3	16.5	0.8	9	1.5	12	1.8	22	3.3
		L41	32.4	77.6	4770	15.6	1.4	19	1.2	17.6	0.8	8	1.4	12	1.9	22	3.4

Continued on next page

Table A.3 – *Continued from previous page*

Fig. Area and Publication	Sample	Latitude	Longitude	Elevation	Balco et al., 2008		Borchers et al., 2016		Heyman, 2014		Borchers vs. Heyman		Balco vs. Heyman		Balco vs. Borchers	
		+N,-S	+E, -W	m	Age (ka)	±1σ	Age (ka)	±1σ	Age (ka)	±1σ	(%)	(ka)	(%)	(ka)	(%)	(ka)
	L42	32.4	77.6	4890	15.3	1.4	18.6	1.3	17.2	0.9	8	1.4	12	1.9	22	3.3
	L44	32.4	77.6	4070	12.7	1.1	16	1.2	14.3	0.7	12	1.7	13	1.7	26	3.3
	L49	32.4	77.6	4190	13.6	1.2	17	1.2	15.3	0.7	11	1.7	13	1.7	25	3.4
	L50	32.4	77.6	4070	15	1.3	18.7	1.2	16.9	0.8	11	1.8	12	1.9	25	3.7
Khumbu, Nepal	E5	27.89	86.82	4328	18.3	1.6	21.8	1.5	20.6	1	6	1.2	12	2.3	19	3.5
Finkel et al., 2003	E6	27.89	86.82	4433	15	1.3	18.5	1.3	16.9	0.7	10	1.6	12	1.8	23	3.5
	E7	27.89	86.82	4310	16	1.4	19.5	1.2	17.9	0.8	9	1.6	12	1.9	22	3.5
	E9	27.88	86.82	4401	22.4	2	26.1	1.8	25	1.1	4	1.1	12	2.6	17	3.7
	E10	27.88	86.82	4401	22.4	2	26.2	1.8	25	1.1	5	1.2	12	2.6	17	3.8
	E11	27.88	86.82	4401	22.4	2	26.2	1.8	25	1.1	5	1.2	12	2.6	17	3.8
	E71	27.91	86.81	4579	29.1	3	33.4	2.7	32.5	2.2	3	0.9	12	3.4	15	4.3
	E73	27.91	86.81	4557	15.5	1.4	18.9	1.3	17.4	0.8	9	1.5	12	1.9	22	3.4
	E77	27.92	86.81	4674	30.6	2.8	34.8	2.2	34.2	1.7	2	0.6	12	3.6	14	4.2
	E79	27.92	86.81	4624	9.6	0.8	12	0.9	10.8	0.5	11	1.2	13	1.3	26	2.5
	E80	27.92	86.81	4624	9.7	0.9	12.2	1.1	11	0.7	11	1.2	13	1.3	26	2.5
	E81	27.92	86.81	4628	9.8	0.9	12	1	11.1	0.6	8	0.9	13	1.3	23	2.2
	E82	27.92	86.81	4270	1.6	0.2	2	0.3	1.8	0.2	11	0.2	14	0.2	26	0.4
	E86	27.92	86.8	4739	74.1	6.5	86.4	7.9	84.5	3.5	2	1.9	14	10.3	17	12.3
	E88	27.93	86.8	5017	28	2.4	31.8	2.1	31.2	1.3	2	0.6	12	3.3	14	3.8
	E89	27.93	86.8	5021	28.7	2.6	32.5	2.3	32.1	1.6	1	0.4	12	3.4	13	3.8
Rongbuk, Nepal	Ron-34	28.15	86.85	5176	2	0.2	2.5	0.2	2.3	0.1	8	0.2	14	0.3	23	0.5
Owen et al., 2009	Ron-35	28.15	86.85	5180	1.4	0.1	1.8	0.2	1.6	0.1	9	0.1	13	0.2	24	0.3
	Ron-36	28.15	86.85	5164	1.4	0.1	1.7	0.1	1.6	0.1	9	0.1	13	0.2	23	0.3

Continued on next page

Table A.3 – *Continued from previous page*

Fig. Area and Publication	Sample	Latitude	Longitude	Elevation	Balco et al., 2008		Borchers et al., 2016		Heyman, 2014		Borchers vs. Heyman		Balco vs. Heyman		Balco vs. Borchers	
		+N,-S	+E, -W	m	Age (ka)	±1σ	Age (ka)	±1σ	Age (ka)	±1σ	(%)	(ka)	(%)	(ka)	(%)	(ka)
	Ron-25	28.14	86.85	5242	2.4	0.2	2.9	0.2	2.8	0.2	3	0.1	13	0.3	17	0.4
	Ron-26	28.14	86.85	5240	2.7	0.2	3.1	0.3	3.1	0.1	1	0	13	0.3	13	0.4
	Ron-27	28.14	86.85	5247	1	0.1	1.3	0.1	1.1	0.1	14	0.2	13	0.1	28	0.3
	Ron-28	28.14	86.85	5244	2.8	0.3	3.2	0.3	3.2	0.2	1	0	13	0.4	13	0.4
	Ron-29	28.14	86.85	5240	2.4	0.2	2.8	0.2	2.7	0.2	4	0.1	13	0.3	18	0.4
	Ron-30	28.14	86.85	5245	2.5	0.2	2.9	0.2	2.8	0.2	2	0.1	13	0.3	15	0.4
	Ron-31	28.14	86.85	5193	1.1	0.1	1.4	0.1	1.2	0.1	13	0.2	13	0.1	27	0.3
	Ron-32	28.14	86.85	5190	1	0.1	1.3	0.1	1.2	0.1	13	0.2	13	0.1	27	0.3
	Ron-33	28.14	86.85	5195	1.2	0.1	1.5	0.1	1.3	0.1	11	0.1	13	0.1	25	0.3
	Ron-2	28.2	86.83	5041	14.7	1.3	17.8	1.3	16.5	0.7	8	1.3	12	1.8	21	3.1
	Ron-3	28.2	86.83	5056	14.8	1.4	17.9	1.4	16.7	0.9	8	1.3	12	1.8	21	3.1
	Ron-4	28.2	86.83	5064	14.9	1.3	18.1	1.3	16.7	0.7	8	1.4	12	1.8	21	3.2
	Ron-5	28.2	86.83	5057	14.3	1.3	17.3	1.3	16.1	0.7	8	1.2	12	1.8	21	3
	Ron-6	28.2	86.83	5055	14.3	1.3	17.3	1.3	16	0.7	8	1.3	12	1.8	21	3
	Ron-7	28.2	86.83	5045	20.3	1.8	23.4	1.7	22.8	1	3	0.6	12	2.4	15	3.1
	Ron-8	28.2	86.83	5036	23	2	26.3	1.8	25.8	1.1	2	0.5	12	2.8	14	3.3
	Ron-9	28.2	86.83	5031	12.3	1.1	15	1.1	13.9	0.7	8	1.1	13	1.6	22	2.7
	Ron-10	28.2	86.83	5027	14.3	1.3	17.4	1.3	16.1	0.7	8	1.3	12	1.8	22	3.1
	Ron-11	28.2	86.83	5044	11.5	1	14.3	1.1	13.1	0.6	9	1.2	14	1.6	24	2.8
	Ron-12	28.2	86.83	5044	82.5	7.2	94.3	6.6	93.7	3.8	1	0.6	14	11.2	14	11.8
	Ron-13	28.2	86.83	5057	10.9	1	13.6	1.1	12.4	0.5	10	1.2	14	1.5	24	2.7
	Ron-67	28.2	86.83	5199	16.6	1.5	19.7	1.1	18.6	0.8	6	1.1	12	2	19	3.1
	Ron-14	28.25	86.82	4959	26.1	2.3	30	2	29.1	1.2	3	0.9	12	3	15	3.9

Continued on next page

Table A.3 – *Continued from previous page*

Fig. Area and Publication	Sample	Latitude	Longitude	Elevation	Balco et al., 2008		Borchers et al., 2016		Heyman, 2014		Borchers vs. Heyman		Balco vs. Heyman		Balco vs. Borchers	
		+N,-S	+E, -W	m	Age (ka)	±1σ	Age (ka)	±1σ	Age (ka)	±1σ	(%)	(ka)	(%)	(ka)	(%)	(ka)
	Ron-15	28.25	86.82	4954	21.4	1.9	24.6	1.6	23.9	1.1	3	0.7	12	2.5	15	3.2
	Ron-16	28.25	86.82	4957	25.1	2.3	28	2	28.1	1.3	0	-0.1	12	3	11	2.9
	Ron-17	28.25	86.82	4958	21.1	1.9	24.3	1.7	23.6	1	3	0.7	12	2.5	15	3.2
	Ron-18	28.25	86.82	4962	22.1	1.9	25.3	1.6	24.7	1	3	0.6	12	2.6	15	3.2
	Ron-19a	28.25	86.82	4935	17.2	1.5	20.3	1.1	19.3	0.8	5	1	12	2.1	18	3.1
	Ron-20	28.25	86.82	4935	24	2.1	27.4	1.8	26.9	1.2	2	0.5	12	2.9	14	3.4
	Ron-21	28.25	86.82	4943	24.1	2.1	27.4	1.8	27	1.1	2	0.4	12	2.9	14	3.3
	Ron-22	28.25	86.82	4933	17.3	1.5	20.4	1.1	19.4	0.9	5	1	12	2.1	18	3.1
	Ron-23	28.25	86.82	4921	24.5	2.2	27.9	1.9	27.4	1.3	2	0.5	12	2.9	14	3.4
	Ron-24	28.25	86.82	4927	26.5	2.3	30	2	29.6	1.2	1	0.4	12	3.1	13	3.5
Mailun Khola, Nepal	Mai 09	28.21	85.21	3510	11.2	1.4	14.4	1.6	12.7	1.2	13	1.7	13	1.5	29	3.2
Gayer et al., 2004	GA24a	28.23	85.19	4490	5	0.7	6	0.8	5.6	0.6	7	0.4	12	0.6	19	1
Gayer et al., 2006	GA55a	28.23	85.19	4446	9.2	1.3	11.7	1.6	10.4	1.2	12	1.3	14	1.2	27	2.5
	GA54a	28.23	85.19	4434	5.7	0.6	7	0.8	6.4	0.5	9	0.6	12	0.7	22	1.2
	MAI26a	28.21	85.19	4125	5.9	0.8	7	1	6.6	0.8	7	0.4	12	0.7	19	1.1
	GA95a	28.22	85.19	4150	7.1	0.9	9	1.3	8.1	0.8	11	0.9	13	0.9	26	1.9
	GA80a	28.24	85.2	4622	0.1	0	0.2	0.1	0.2	0	33	0.1	13	0	51	0.1
Garwhal, India	DS6-43	31.11	78.32	2661	8.6	0.7	11.7	0.9	9.8	0.4	19	1.9	14	1.2	36	3.1
Scherler et al., 2010	DS6-44	31.11	78.32	2661	12.9	1.1	16.8	1.2	14.5	0.6	16	2.3	13	1.7	31	3.9
	DS6-45	31.11	78.33	2720	16.3	1.4	20.6	1.2	18.3	0.7	12	2.3	12	2	26	4.3
	DS6-46	31.11	78.33	2725	16.4	1.4	20.7	1.2	18.4	0.7	13	2.3	12	2	27	4.3
	DS05-05B	31.15	78.43	3495	5.3	0.5	6.8	0.6	5.9	0.2	15	0.9	12	0.6	28	1.5
	DS6-61	31.15	78.43	3412	5.7	0.5	7.3	0.6	6.3	0.3	16	1	12	0.7	30	1.7

Continued on next page

Table A.3 – *Continued from previous page*

Fig. Area and Publication	Sample	Latitude	Longitude	Elevation	Balco et al., 2008		Borchers et al., 2016		Heyman, 2014		Borchers vs. Heyman		Balco vs. Heyman		Balco vs. Borchers	
		+N,-S	+E, -W	m	Age (ka)	±1σ	Age (ka)	±1σ	Age (ka)	±1σ	(%)	(ka)	(%)	(ka)	(%)	(ka)
	DS6-63	31.15	78.43	3516	5.3	0.5	6.8	0.6	5.9	0.2	15	0.9	12	0.6	28	1.5
	DS6-64	31.15	78.43	3504	5.3	0.5	6.8	0.6	5.9	0.3	15	0.9	12	0.6	28	1.5
	DS6-32	31.07	78.5	4071	0.2	0	0.3	0	0.3	0	32	0.1	13	0	50	0.1
	DS6-33	31.07	78.5	4046	0.2	0	0.3	0	0.2	0	32	0.1	13	0	50	0.1
	DS6-57	31.14	78.45	3636	0.3	0	0.4	0	0.3	0	33	0.1	13	0	51	0.1
	DS6-58	31.14	78.45	3623	0.8	0.1	1.2	0.1	0.9	0	23	0.2	13	0.1	38	0.3
	DS6-27A	31.12	78.38	3010	10.4	0.9	14	1	11.7	0.5	19	2.3	13	1.4	35	3.6
	DS6-27B	31.12	78.38	3010	13.8	1.2	17.8	1.2	15.5	0.6	15	2.3	13	1.7	29	4
	DS6-35	31.08	78.45	3642	0.5	0.1	0.8	0.1	0.6	0	31	0.2	12	0.1	47	0.3
	DS6-37	31.08	78.46	3658	9.5	0.8	12.4	0.9	10.8	0.4	15	1.7	13	1.3	31	2.9
	DS6-48	31.15	78.43	3544	7.6	0.7	10.1	0.8	8.6	0.4	17	1.4	14	1	33	2.5
	DS6-49	31.15	78.43	3514	7.7	0.7	10.2	0.8	8.7	0.4	17	1.5	14	1.1	33	2.5
Karakoram, northern Pakistan	K2-12	35.68	75.47	2950	16.4	1.4	19.8	1.2	18.5	0.7	7	1.3	13	2.1	21	3.4
Seong et al., 2007	K2-13	35.68	75.47	2952	16.9	1.5	20.3	1.3	19.1	0.9	6	1.2	13	2.1	20	3.4
	K2-14	35.68	75.48	2945	16.5	1.5	19.9	1.3	18.5	0.9	7	1.4	13	2.1	21	3.4
	K2-15	35.68	75.47	2950	16.4	1.5	19.8	1.3	18.5	0.9	7	1.3	13	2.1	21	3.4
	K2-16	35.68	75.47	2951	16.4	1.5	19.8	1.3	18.5	0.9	7	1.3	13	2.1	21	3.4
	K2-17	35.68	75.47	2950	16.4	1.5	19.8	1.3	18.5	0.9	7	1.3	13	2.1	21	3.4
	K2-18	35.68	75.47	2868	16.6	1.4	20.1	1.2	18.7	0.8	7	1.4	13	2.1	21	3.5
	K2-19	35.68	75.47	2865	15.0	1.4	18.5	1.4	16.9	0.9	10	1.6	13	1.9	23	3.5
	K2-23	35.72	75.52	2646	13.3	1.2	16.7	1.2	15	0.7	11	1.7	13	1.7	25	3.4
	K2-24	35.72	75.52	2631	12.8	1.1	16	1.2	14.4	0.7	11	1.6	13	1.7	25	3.2

Continued on next page

Table A.3 – *Continued from previous page*

Fig. Area and Publication	Sample	Latitude	Longitude	Elevation	Balco et al., 2008		Borchers et al., 2016		Heyman, 2014		Borchers vs. Heyman		Balco vs. Heyman		Balco vs. Borchers	
		+N,-S	+E, -W	m	Age (ka)	±1σ	Age (ka)	±1σ	Age (ka)	±1σ	(%)	(ka)	(%)	(ka)	(%)	(ka)
	K2-25	35.72	75.52	2631	12.4	1.1	15.6	1.1	14	0.7	11	1.6	13	1.6	26	3.2
	K2-26	35.72	75.52	2650	13.0	1.2	16.3	1.2	14.6	0.7	11	1.7	13	1.7	26	3.3
	K2-31	35.72	75.68	3164	10.8	0.9	14	1	12.2	0.5	14	1.8	13	1.4	30	3.2
	K2-32	35.72	75.67	3166	1.9	0.3	2.5	0.4	2.1	0.3	16	0.3	14	0.3	32	0.6
	K2-33	35.72	75.67	3052	11.0	1.0	14	1	12.5	0.6	12	1.5	13	1.5	27	3
	K2-48	35.67	75.8	3633	11.6	1.1	14	1	13.2	0.7	6	0.8	13	1.6	20	2.4
	K2-49	35.67	75.8	3631	11.9	1.1	14.5	1.1	13.4	0.7	8	1.1	13	1.6	22	2.6
	K2-50	35.67	75.8	3640	12.6	1.1	15.3	1.1	14.2	0.7	8	1.1	13	1.6	22	2.7
	K2-51	35.67	75.8	3644	11.6	1.1	14.2	1.1	13.1	0.6	8	1.1	13	1.6	23	2.6
	K2-52	35.67	75.8	3636	11.6	1.1	14.3	1.1	13.2	0.7	8	1.1	13	1.6	23	2.7
	K2-53	35.67	75.8	3643	12.5	1.1	15.2	1.1	14.2	0.7	7	1	13	1.6	21	2.7
	K2-54	35.67	75.8	3824	8.4	0.7	10.5	0.9	9.6	0.4	10	0.9	14	1.2	25	2.1
	K2-55	35.67	75.8	3825	12.4	1.1	15	1	14.1	0.6	7	0.9	13	1.6	21	2.6
	K2-56	35.67	75.8	3881	12.4	1.1	15	1	14	0.6	7	1	13	1.6	21	2.6
	K2-58	35.69	75.72	3879	12.2	1.2	14.8	1.1	13.8	0.8	7	1	13	1.6	21	2.6
	K2-59	35.69	75.72	3811	12.7	1.1	15.3	1.1	14.3	0.7	7	1	13	1.7	21	2.6
	K2-60	35.69	75.72	3031	12.0	1.1	15	1	13.5	0.6	11	1.5	13	1.6	25	3
	K2-61	35.69	75.72	3032	11.8	1.0	15	1	13.3	0.6	12	1.7	13	1.6	27	3.2
	K2-62	35.67	75.81	3017	11.2	1.1	14.1	1.2	12.7	0.8	11	1.4	13	1.5	26	2.9
	K2-63	35.67	75.81	2944	12.2	1.1	15.3	1.1	13.8	0.7	11	1.6	13	1.6	26	3.1
	K2-72	35.67	75.81	3113	13.0	1.1	15.4	1.1	14.7	0.6	5	0.7	13	1.7	18	2.4
	K2-73	35.67	75.81	3128	13.3	1.2	15.7	1.1	15	0.6	5	0.7	13	1.7	18	2.4
	K2-74	35.67	75.81	3122	13.4	1.2	15.9	1.1	15.1	0.6	5	0.8	13	1.7	19	2.5

Continued on next page

Table A.3 – *Continued from previous page*

Fig. Area and Publication	Sample	Latitude	Longitude	Elevation	Balco et al., 2008		Borchers et al., 2016		Heyman, 2014		Borchers vs. Heyman		Balco vs. Heyman		Balco vs. Borchers	
		+N,-S	+E, -W	m	Age (ka)	$\pm1\sigma$	Age (ka)	$\pm1\sigma$	Age (ka)	$\pm1\sigma$	(%)	(ka)	(%)	(ka)	(%)	(ka)
	K2-75	35.67	75.81	3113	13.1	1.2	15.5	1.1	14.8	0.7	5	0.7	13	1.7	18	2.4
	K2-76	35.7	75.95	3109	16.8	1.5	19.4	1.2	18.9	0.8	2	0.5	13	2.1	15	2.6
	K2-77	35.7	75.95	3106	13.7	1.2	16.2	1.2	15.4	0.7	5	0.8	13	1.8	18	2.5
	K2-78	35.7	75.95	4209	13.3	1.2	15.8	1.1	15.1	0.6	5	0.7	13	1.7	19	2.5
	K2-79	35.7	75.95	4213	12.7	1.1	15	1	14.3	0.6	5	0.7	13	1.7	18	2.3
	K2-80	35.7	75.95	4212	15.2	1.4	18.1	1.3	17.1	0.8	6	1	13	1.9	19	2.9
	K2-81	35.7	75.95	4215	15.6	1.4	18.5	1.3	17.6	0.8	5	0.9	13	2	18	2.9
	K2-82	35.7	75.95	4211	15.0	1.3	17.9	1.3	16.9	0.8	6	1	13	1.9	19	2.9
	K2-83	35.7	75.94	4211	41.3	3.6	44.5	3.2	46.3	2	-4	-1.8	12	5.1	8	3.3
	K2-84	35.7	75.96	4225	12.3	1.1	14.9	1.1	13.9	0.7	7	1	13	1.6	22	2.6
	K2-85	35.69	75.96	4221	12.6	1.2	15.2	1.2	14.2	0.8	7	1	13	1.7	21	2.6
	K2-65	35.69	75.96	3823	13.0	1.1	16.1	1.2	14.7	0.7	9	1.4	13	1.7	23	3.1
	K2-66	35.69	75.96	3821	5.4	0.6	6.8	0.8	6.1	0.4	12	0.7	12	0.7	26	1.4
	K2-67	35.69	75.96	3818	5.7	0.6	7.3	0.6	6.4	0.4	13	0.9	12	0.7	27	1.6
	K2-68	35.69	75.96	3779	6.0	0.6	7.7	0.7	6.8	0.4	13	0.9	12	0.7	27	1.6
	K2-69	35.69	75.94	3768	7.0	0.7	8.9	0.9	7.9	0.5	13	1	13	0.9	28	1.9
	K2-70	35.69	75.94	3766	6.1	0.6	7.8	0.7	6.9	0.4	13	0.9	12	0.8	27	1.6
	K2-86	35.69	75.94	3445	11.2	1.0	14	1	12.7	0.5	10	1.3	13	1.5	25	2.8
	K2-87	35.69	75.94	3442	11.9	1.1	14.7	1.1	13.5	0.7	9	1.2	13	1.6	24	2.8
	K2-88	35.69	75.93	3447	12.7	1.2	15.5	1.1	14.4	0.7	8	1.1	13	1.7	22	2.8
	K2-89	35.69	75.93	3441	11.2	1.0	14	1	12.8	0.5	10	1.2	13	1.5	24	2.8

Continued on next page

Table A.3 – *Continued from previous page*

Fig.	Area and Publication	Sample	Latitude	Longitude	Elevation	Balco et al., 2008		Borchers et al., 2016		Heyman, 2014		Borchers vs. Heyman		Balco vs. Heyman		Balco vs. Borchers	
			+N,-S	+E, -W	m	Age (ka)	±1σ	Age (ka)	±1σ	Age (ka)	±1σ	(%)	(ka)	(%)	(ka)	(%)	(ka)
3F	Animas Valley and San Juan Mountains, Colorado, USA	Baker's Bridge	37.47	-107.79	2155			20.3	1.4	19.3	0.9	5	1				
	Guido et al., 2007	Tacoma	37.56	-107.78	2285			17.2	1.4	16.2	0.8	6	1				
		Needleton	37.63	-107.69	2540			17.7	1.4	16.9	0.8	4	0.8				
		Molas Lake	37.74	-107.66	2828			32.7	2.4	33.2	1.5	-1	-0.5				
		Silverton	37.79	-107.67	2835			16.6	1.3	15.9	0.7	5	0.7				
		Highland Mary Lake	37.91	-107.58	3704			18.2	1.4	18.5	1	-2	-0.3				
		Elk Creek	37.71	-107.54	3871			12.9	1.1	13.1	0.6	-1	-0.2				
	Animas Valley and San Juan Mountains, Colorado, USA	GP4J-1	40.01	-105.67	3549			15.9	1.3	16.6	0.8	-4	-0.7				
	Ward et al., 2009	GP4J-2	40.01	-105.67	3521			16.2	1.3	17	0.8	-4	-0.8				
		GP4J-3	40.01	-105.68	3520			15.9	1.3	16.7	0.9	-5	-0.8				
		GP4J-4	40.01	-105.67	3484			15.8	1.3	16.5	0.8	-4	-0.7				
		GP4J-5	40.01	-105.67	3463			15.6	1.2	16.3	0.8	-4	-0.7				
		GP4J-6	40.01	-105.67	3451			15.7	1.3	16.3	0.9	-4	-0.6				
		GP4J-7	40.01	-105.67	3434			14.3	1.2	14.8	0.7	-4	-0.5				
		GP4J-10	39.97	-105.6	2904			16.8	1.4	17	0.8	-1	-0.2				
		GP4J-11	39.99	-105.62	3051			15.8	1.3	16.1	0.8	-2	-0.3				
		GP4J-16	39.96	-105.61	2909			19.1	1.6	19.5	1.2	-2	-0.4				
		GP4J-20	39.97	-105.68	3436			21.5	2.4	22.8	2.3	-6	-1.3				

Continued on next page

Table A.3 – *Continued from previous page*

Fig. Area and Publication	Sample	Latitude	Longitude	Elevation	Balco et al., 2008		Borchers et al., 2016		Heyman, 2014		Borchers vs. Heyman		Balco vs. Heyman		Balco vs. Borchers	
		+N,-S	+E, -W	m	Age (ka)	±1σ	Age (ka)	±1σ	Age (ka)	±1σ	(%)	(ka)	(%)	(ka)	(%)	(ka)
	GP4J-21	39.97	-105.66	3301			19.6	2.2	20.4	2.3	-4	-0.8				
	GP4J-22	39.97	-105.64	3106			19.8	2.4	20.5	2.5	-4	-0.7				
	GP4J-23	39.95	-105.58	2708			22	3	22.6	2.9	-3	-0.6				
	MB4J-0	39.96	-105.52	2590			23.3	3.4	23.7	3.3	-2	-0.4				
	33-JB-25	40	-105.64	3162			15.1	1.2	15.5	0.8	-2	-0.4				
	33-JB-30	40	-105.63	3421			18.9	1.4	19.8	1	-5	-0.9				
	JB03-28	40	-105.63	3362			16.9	1.3	17.6	0.8	-4	-0.7				
	JB03-29	40	-105.63	3464			45	3.5	48.8	2.2	-8	-3.8				
	99-t76b	40	-105.56	2982			24	1.8	25	1.1	-4	-1				
	DC-91-2	39.07	-106.3	2850			23.3	1.8	23.8	1.1	-2	-0.5				
	DC-91-3	39.07	-106.3	2810			23	1.9	23.4	1.3	-2	-0.4				
Pinedale ice cap, USA	8-A2	45.43	-110.7	1548			14.3	1.6	14.2	1.2	1	0.1				
Licciardi et al., 2001	8-B2	45.43	-110.71	1550			16.9	2.4	16.8	2	1	0.1				
	8-D1	45.43	-110.71	1545			18.2	1.8	18.1	1.2	0	0.1				
	8-F2	45.44	-110.7	1544			19.9	2.3	19.8	2	0	0.1				
	8-G2	45.44	-110.69	1529			21.6	2.5	21.6	2	0	0				
	8-I1	45.44	-110.69	1529			18.5	1.7	18.4	1.1	0	0.1				
	8-I2	45.44	-110.69	1529			19.6	2.3	19.6	1.9	0	0				
	8-J1	45.37	-110.69	1554			18.2	2.9	18.1	2.5	1	0.1				
	8-J2	45.37	-110.69	1554			20	2.6	19.9	2.3	0	0.1				
	8-K1	45.43	-110.69	1536			19.2	1.5	19.1	1	1	0.1				
	8-L1	45.37	-110.69	1554			14.6	1.9	14.5	1.6	1	0.1				
	8-L2	45.37	-110.69	1554			18.9	1.7	18.7	1.1	1	0.2				

Continued on next page

Table A.3 – *Continued from previous page*

Fig. Area and Publication	Sample	Latitude	Longitude	Elevation	Balco et al., 2008		Borchers et al., 2016		Heyman, 2014		Borchers vs. Heyman		Balco vs. Heyman		Balco vs. Borchers	
		+N,-S	+E, -W	m	Age (ka)	±1σ	Age (ka)	±1σ	Age (ka)	±1σ	(%)	(ka)	(%)	(ka)	(%)	(ka)
	8-M2	45.36	-110.69	1561			18.1	1.5	18	1	1	0.1				
	CH-1A	45.34	-110.7	1628			16.3	1.9	16.2	1.5	1	0.1				
	CH-2A	45.34	-110.7	1634			17.6	1.8	17.6	1.3	0	0				
	CH-3B	45.33	-110.7	1652			17.8	2.1	17.8	1.7	0	0				
	CH-6A	45.34	-110.71	1615			16.3	1.9	16.2	1.5	0	0.1				
	CH-6B	45.34	-110.71	1615			15.3	2.2	15.3	1.8	0	0				
	CH-8A	45.34	-110.7	1615			19.8	1.9	19.9	1.4	0	-0.1				
	CH-9B	45.34	-110.7	1618			19	2	19	1.5	0	0				
	CH-10B	45.34	-110.7	1612			21	2	21.2	1.5	-1	-0.2				
	CH-11B	45.34	-110.7	1615			18.1	1.6	18.1	1.1	0	0				
	DF-1A	45.04	-110.69	1811			15.8	1.4	15.9	0.9	-1	-0.1				
	DF-2B	45.04	-110.69	1811			14.5	1.8	14.6	1.5	0	-0.1				
	DF-3B	45.04	-110.69	1811			15.1	1.6	15.2	1.2	-1	-0.1				
	DF-4A	45.04	-110.69	1811			14.3	1.7	14.3	1.3	0	0				
	DF-5B	45.04	-110.69	1811			18.3	1.6	18.4	1	-1	-0.1				
	DF-6A	45.04	-110.69	1811			15.4	1.4	15.5	1	0	-0.1				
	DF-6B	45.04	-110.69	1811			17	1.9	17.1	1.4	0	-0.1				
	DF-7A	45.04	-110.69	1811			16.4	1.5	16.4	1	0	0				
	DF-8A	45.04	-110.69	1807			17.2	1.7	17.3	1.2	0	-0.1				
	DF-9B	45.04	-110.68	1804			15.1	1.2	15.2	0.8	0	-0.1				
	DF-10A	45.04	-110.68	1801			17.1	2.5	17.2	2.2	-1	-0.1				
	F-1A	45.06	-110.76	1583			19.2	2.6	19.2	2.2	0	0				
	F-3A	45.06	-110.76	1583			14.4	1.4	14.3	1	1	0.1				

Continued on next page

Table A.3 – *Continued from previous page*

Fig. Area and Publication	Sample	Latitude	Longitude	Elevation	Balco et al., 2008		Borchers et al., 2016		Heyman, 2014		Borchers vs. Heyman		Balco vs. Heyman		Balco vs. Borchers	
		+N,-S	+E, -W	m	Age (ka)	±1σ	Age (ka)	±1σ	Age (ka)	±1σ	(%)	(ka)	(%)	(ka)	(%)	(ka)
Pinedale ice cap, USA Licciardi and Pierce, 2008	F-3B	45.06	-110.76	1583			15.7	1.5	15.6	1	1	0.1				
	F-4A	45.06	-110.76	1584			14	2.2	13.9	1.9	1	0.1				
	F-6A	45.06	-110.76	1584			14.7	1.4	14.6	1	1	0.1				
	F-6B	45.06	-110.76	1584			16.3	1.6	16.2	1.1	0	0.1				
	F-9A	45.06	-110.76	1585			17.3	1.6	17.2	1.1	0	0.1				
	F-9B	45.06	-110.76	1585			17.8	1.6	17.7	1.1	1	0.1				
	F-10B	45.06	-110.76	1585			15.6	1.6	15.5	1.2	1	0.1				
	F-11A	45.06	-110.76	1584			14	1.9	13.9	1.5	1	0.1				
	CF-1	44.88	-109.25	1405			22.6	1.8	22.5	1	0	0.1				
	CF-2	44.88	-109.25	1405			21.2	1.6	21.1	0.9	1	0.1				
	CF-3	44.88	-109.25	1409			22	1.7	21.9	0.9	1	0.1				
	CF-4	44.88	-109.25	1409			21.7	1.6	21.6	0.9	1	0.1				
	CF-5	44.88	-109.25	1409			20.7	1.6	20.6	1	1	0.1				
	CF-6	44.88	-109.25	1412			21.1	1.6	21	1	0	0.1				
	CF-7	44.88	-109.25	1410			21.8	1.7	21.7	0.9	0	0.1				
	CF-8	44.87	-109.25	1413			19.1	1.5	18.9	0.9	1	0.2				
	CF-9	44.87	-109.25	1409			34	2.7	34	1.5	0	0				
	CF-10	44.87	-109.25	1411			21.6	1.7	21.5	0.9	1	0.1				
	CC-1	44.85	-109.64	2020			20.7	1.6	21.1	1	-2	-0.4				
	CC-2	44.85	-109.64	2019			18.9	1.5	19.2	0.8	-1	-0.3				
	CC-3	44.85	-109.62	1980			19.7	1.5	20	0.9	-1	-0.3				
	CC-4	44.86	-109.63	1999			19.7	1.5	20	0.8	-2	-0.3				
	CC-5	44.85	-109.63	1992			49	4	49.8	2	-2	-0.8				

Continued on next page

Table A.3 – *Continued from previous page*

Fig. Area and Publication	Sample	Latitude	Longitude	Elevation	Balco et al., 2008		Borchers et al., 2016		Heyman, 2014		Borchers vs. Heyman		Balco vs. Heyman		Balco vs. Borchers	
		+N,-S	+E, -W	m	Age (ka)	±1σ	Age (ka)	±1σ	Age (ka)	±1σ	(%)	(ka)	(%)	(ka)	(%)	(ka)
Ullman et al., 2014	JB-1	44.91	-110.37	1942			16.4	4.3	16.6	3.9	-1	-0.2				
	JB-2	44.91	-110.37	1941			16.1	1.3	16.2	0.7	-1	-0.1				
	JB-3	44.91	-110.38	1944			18.9	1.4	19.1	0.8	-1	-0.2				
	JB-4	44.91	-110.38	1907			15.9	1.3	16	0.7	-1	-0.1				
	JB-5	44.91	-110.38	1906			19	1.5	19.2	0.8	-1	-0.2				
	JB-7	44.92	-110.38	1897			16	1.3	16.1	0.7	-1	-0.1				
	JB-8	44.92	-110.38	1885			15.1	1.2	15.2	0.7	-1	-0.1				
	JB-9	44.92	-110.38	1886			18.1	1.5	18.3	0.9	-1	-0.2				
	JB-10	44.92	-110.38	1882			18.4	1.5	18.6	0.8	-1	-0.2				
	JB-11	44.92	-110.38	1886			16.2	1.3	16.3	0.7	-1	-0.1				
	RCLC-09-02	45.47	-91.54	449			24	2	22.9	1.3	5	1.1				
	RCLC-09-03	45.47	-91.53	449			21.7	1.8	20.7	1	5	1				
	RCLC-09-04	45.47	-91.53	440			52.3	4.5	50.3	2.4	4	2				
	RCLC-09-06	45.47	-91.53	461			26.9	2.3	25.7	1.5	5	1.2				
	RCLC-09-13	45.48	-91.53	505			48.9	4.1	47.2	2.1	4	1.7				
	RCLC-11-05	45.47	-91.53	444			25.3	2.2	24.2	1.4	5	1.1				
	RCLC-11-06	45.47	-91.53	410			26	2.2	24.8	1.4	5	1.2				
	RCLC-11-07	45.47	-91.53	432			32.2	2.6	30.8	1.6	5	1.4				
	RCLC-11-08	45.47	-91.53	428			25.8	2.1	24.6	1.2	5	1.2				
	RCLC-11-09	45.47	-91.53	439			68	5.6	65.7	2.9	3	2.3				
	RCLC-11-01	45.5	-91.39	514			21.6	1.8	20.6	1.2	5	1				
	RCLC-11-02	45.5	-91.39	482			20.6	1.6	19.6	1	5	1				
	GOG-11-01	46.29	-90.79	507			15.2	1.3	14.4	0.8	5	0.8				

Continued on next page

Table A.3 – *Continued from previous page*

Fig. Area and Publication	Sample	Latitude	Longitude	Elevation	Balco et al., 2008		Borchers et al., 2016		Heyman, 2014		Borchers vs. Heyman		Balco vs. Heyman		Balco vs. Borchers	
		+N,-S	+E, -W	m	Age (ka)	±1σ	Age (ka)	±1σ	Age (ka)	±1σ	(%)	(ka)	(%)	(ka)	(%)	(ka)
	GOG-11-02	46.29	-90.79	538			12.6	1.1	11.9	0.7	6	0.7				
	GOG-11-03	46.29	-90.79	538			12.7	1.1	12.1	0.7	5	0.6				
	GOG-11-04	46.29	-90.79	531			14	1.3	13.3	0.8	5	0.7				
	GOG-11-06	46.29	-90.79	518			18.1	3.5	17.2	3.2	5	0.9				
	GOG-11-07	46.29	-90.8	522			15	1.3	14.3	0.9	5	0.7				
	GOG-11-08	46.29	-90.8	524			15.1	1.4	14.4	0.9	5	0.7				
	GOG-11-09	46.29	-90.8	527			12.7	1.2	12.1	0.8	5	0.6				
	LCBC-11-01	45.23	-88.77	412			19	1.7	17.9	1.2	6	1.1				
	LCBC-11-02	45.23	-88.77	408			20.4	2.2	19.3	1.8	5	1.1				
	LCBC-11-03	45.23	-88.77	417			21	1.7	19.9	1.1	6	1.1				
	LCBC-11-04	45.23	-88.77	430			17.5	1.6	16.5	1.1	6	1				
	LCBC-11-05	45.23	-88.77	375			12.7	1.2	11.9	0.7	7	0.8				
Greenland	MKG-93	71.51	-24.94	790			0.8	0.1	0.8	0.1	-7	-0.1				
Kelly et al., 2008	MKG-94	71.51	-24.94	780			0.4	0.1	0.4	0.1	-5	0				
	MKG-95	71.51	-24.94	780			0.7	0.1	0.7	0.1	-7	-0.1				
	MKG-97	71.51	-24.94	778			0.3	0	0.3	0	-3	0				
	MKG-32	71.55	-24.9	709			11.3	0.9	11.8	0.5	-4	-0.5				
	MKG-33	71.55	-24.91	684			13	1.1	13.6	0.6	-4	-0.6				
	MKG-35	71.54	-24.89	610			14.5	1.2	15.2	0.7	-5	-0.7				
	MKG-36	71.54	-24.89	626			12	1	12.7	0.6	-6	-0.7				
	MKG-89	71.48	-24.81	375			11	1	12	0.6	-8	-1				
	MKG-90	71.48	-24.81	365			14.2	1.2	14.9	0.7	-5	-0.7				
	MKG-91	71.48	-24.81	348			17.8	1.5	18.9	0.9	-6	-1.1				

Continued on next page

Table A.3 – *Continued from previous page*

Fig. Area and Publication	Sample	Latitude	Longitude	Elevation	Balco et al., 2008		Borchers et al., 2016		Heyman, 2014		Borchers vs. Heyman		Balco vs. Heyman		Balco vs. Borchers	
		+N,-S	+E, -W	m	Age (ka)	±1σ	Age (ka)	±1σ	Age (ka)	±1σ	(%)	(ka)	(%)	(ka)	(%)	(ka)
	MKG-92	71.48	-24.81	330			11.8	1	12.3	0.6	-5	-0.6				
	MKG-98	71.51	-24.81	500			12.4	1.1	13	0.7	-5	-0.6				
	MKG-99	71.52	-24.82	515			47	3.8	52.2	2.3	-10	-5.2				
	MKG-100	71.51	-24.94	720			12.3	1.1	12.9	0.8	-4	-0.6				
	MKG-101	71.51	-24.94	720			11	1	11.4	0.6	-4	-0.4				
	MKG-102	71.51	-24.94	740			12	1	13.1	0.6	-8	-1.1				
	MKG-103	71.51	-24.94	750			11.1	0.9	11.6	0.5	-5	-0.5				
	MKG-104	71.51	-24.91	603			12	0.9	12.5	0.6	-4	-0.5				
	MKG-11	71.42	-24.77	345			13.5	1.2	14.2	0.7	-5	-0.7				
	MKG-12	71.42	-24.77	360			37	3.1	40.4	1.9	-8	-3.4				
	MKG-13	71.4	-24.72	129			18	1.5	19.3	0.9	-7	-1.3				
	MKG-14a	71.42	-24.71	134			19.1	1.6	20.5	0.9	-7	-1.4				
	MKG-15	71.41	-24.71	134			11.9	1	12.6	0.6	-5	-0.7				
	MKG-20	71.43	-24.67	215			13.2	1.1	14	0.6	-6	-0.8				
	MKG-21	71.43	-24.67	230			23.2	2.1	24.9	1.5	-7	-1.7				
	MKG-22	71.44	-24.67	317			13.9	1.1	14.6	0.6	-5	-0.7				
	MKG-24	71.44	-24.68	372			21.4	1.8	22.7	1.2	-6	-1.3				
	MKG-25	71.45	-24.68	385			59	4.9	67.2	3.3	-12	-8.2				
	MKG-26	71.45	-24.68	385			24	1.9	25.6	1.1	-6	-1.6				
	MKG-30	71.42	-24.68	124			15.2	1.2	16.2	0.7	-6	-1				
	MKG-07	71.42	-24.77	360			26	2.1	27.9	1.3	-7	-1.9				
	MKG-08	71.42	-24.77	360			38.5	3.1	42.2	2	-9	-3.7				
	MKG-09	71.44	-24.78	380			25.3	2.2	27.1	1.4	-7	-1.8				

Continued on next page

Table A.3 – *Continued from previous page*

Fig.	Area and Publication	Sample	Latitude	Longitude	Elevation	Balco et al., 2008		Borchers et al., 2016		Heyman, 2014		Borchers vs. Heyman		Balco vs. Heyman		Balco vs. Borchers	
			+N,-S	+E, -W	m	Age (ka)	±1σ	Age (ka)	±1σ	Age (ka)	±1σ	(%)	(ka)	(%)	(ka)	(%)	(ka)
		MKG-16	71.46	-24.68	478			89.1	7.3	108.4	5.7	-18	-19.3				
		MKG-19	71.44	-24.65	333			44.6	3.5	49.5	2.2	-10	-4.9				
		MKG-27	71.45	-24.67	375			26	2.3	27.9	1.5	-7	-1.9				
		MKG-28	71.44	-24.66	338			37	3	40.3	1.9	-8	-3.3				
	Alps	ER1	47.17	7.69	580			24.4	2.4	23.5	1.7	4	0.9				
	Ivy-Ochs et al., 2004	ER2	47.17	7.69	585			24.6	2.2	23.6	1.4	4	1				
	Ivy-Ochs et al., 2008	ER7	47.17	7.69	610			20.4	2.1	19.6	1.6	4	0.8				
		ER8	47.17	7.69	595			23.1	2.3	22.3	1.6	4	0.8				
	Alps	Reuss-20	47.35	8.31	502			19.2	1.7	18.5	1.1	4	0.7				
	Reber et al., 2014	Reuss-21	47.4	8.19	446			22.6	1.9	21.6	1.2	5	1				
		Reuss-22	47.4	8.19	475			23	2	21.9	1.3	5	1.1				
3G	Patagonia	LBA-01-05	-46.6	-71.04	438			18.6	1.5	17.8	0.9	5	0.8				
	Kaplan et al., 2004	LBA-01-06	-46.59	-71.94	438			21.7	2.4	20.9	1.8	4	0.8				
		LBA-98-78	-46.63	-71.04	454			21	1.7	20.2	1	4	0.8				
		LBA-98-97	-46.56	-71.03	430			21.5	1.8	20.7	1.1	4	0.8				
		LBA-98-98	-46.56	-71.03	430			23.4	1.9	22.5	1.1	4	0.9				
		LBA-98-120	-46.41	-71.07	510			25.4	2.2	24.5	1.3	4	0.9				
		LBA-98-123	-46.4	-71.07	510			25	2	23.8	1.1	5	1.2				
		LBA-98-135	-46.62	-70.96	439			26.8	2.2	26	1.2	3	0.8				
		LBA-01-22	-46.62	-70.95	452			26.7	2.1	25.9	1.2	3	0.8				
		LBA-01-60	-46.62	-70.95	439			29.4	2.5	28.5	1.5	3	0.9				
	Peru	AL001	-11.05	-75.9	4404			15.6	1.3	15.2	0.8	3	0.4				

Continued on next page

Table A.3 – *Continued from previous page*

Fig. Area and Publication	Sample	Latitude	Longitude	Elevation	Balco et al., 2008		Borchers et al., 2016		Heyman, 2014		Borchers vs. Heyman		Balco vs. Heyman		Balco vs. Borchers	
		+N,-S	+E, -W	m	Age (ka)	±1σ	Age (ka)	±1σ	Age (ka)	±1σ	(%)	(ka)	(%)	(ka)	(%)	(ka)
Smith et al., 2005	AL002	-11.05	-75.9	4409			14	1.2	13.6	0.7	3	0.4				
	AL003	-11.05	-75.9	4408			15.7	1.4	15.3	0.9	3	0.4				
	AL004	-11.05	-75.9	4412			29	2	29.4	1.2	-1	-0.4				
	AL005	-11.05	-75.89	4409			19.8	1.2	19.4	1	2	0.4				
	PE01-ALC-01	-11.05	-75.9	4401			18.9	1.3	18.4	1	3	0.5				
	PE01-ALC-02	-11.05	-75.9	4392			16.1	1.4	15.6	0.8	3	0.5				
	ZONG-00-01	-16.13	-68.2	3806			14.2	1.3	13.4	0.8	6	0.8				
	ZONG-00-02	-16.13	-68.2	3806			14.9	1.4	14.1	1	6	0.8				
	ZONG-00-03	-16.13	-68.2	3806			13.6	1.5	12.8	1	6	0.8				
	ZONG-00-04	-16.13	-68.2	3806			14.2	1.2	13.4	0.8	6	0.8				
	ZONG-00-05	-16.13	-68.2	3806			15	1.2	14.2	0.8	5	0.8				
	ZONG-00-06	-16.13	-68.19	3895			17.3	1.5	16.4	0.9	6	0.9				
	ZONG-00-07	-16.13	-68.19	3895			19.7	1.3	18.8	1.1	5	0.9				
	ZONG-00-08	-16.13	-68.19	3895			17.5	1.4	16.5	0.8	6	1				
	ZONG-00-09	-16.13	-68.19	3895			15.8	1.3	15.1	0.8	5	0.7				
	ZONG-00-10	-16.13	-68.19	4105			17	1.4	16.3	0.9	5	0.7				
	ZONG-00-11	-16.13	-68.19	4105			15.3	1.3	14.7	0.9	4	0.6				
	ZONG-00-12	-16.13	-68.19	4105			15.5	1.2	14.8	0.7	4	0.7				
	AL006	-11.07	-75.93	4390			20.3	1.2	20.1	0.9	1	0.2				
	AL007	-11.07	-75.93	4391			16.8	1.3	16.2	0.7	4	0.6				
	AL010	-11.07	-75.93	4384			19.6	1.2	19.2	0.9	2	0.4				
	PE01-ALC-03	-11.07	-75.93	4390			18.3	1.4	17.7	0.9	4	0.6				
	PE01-ALC-04	-11.07	-75.93	4390			18.9	1.3	18.3	0.9	3	0.6				

Continued on next page

Table A.3 – *Continued from previous page*

Fig. Area and Publication	Sample	Latitude	Longitude	Elevation	Balco et al., 2008		Borchers et al., 2016		Heyman, 2014		Borchers vs. Heyman		Balco vs. Heyman		Balco vs. Borchers	
		+N,-S	+E, -W	m	Age (ka)	±1σ	Age (ka)	±1σ	Age (ka)	±1σ	(%)	(ka)	(%)	(ka)	(%)	(ka)
	PE01-ALC-05	-11.07	-75.93	4383			23.3	1.7	23.3	1.1	0	0				
	PE01-ALC-06	-11.07	-75.93	4383			18.5	1.4	17.9	0.9	4	0.6				
	PE01-ALC-07	-11.07	-75.93	4389			29.8	2.2	29.8	1.4	0	0				
	PE01-ALC-23	-11.07	-75.94	4376			17.9	1.5	17.3	1	4	0.6				
	PE01-ALC-24	-11.07	-75.94	4374			17.8	1.6	17.1	1.2	4	0.7				
	PE01-ALC-25	-11.07	-75.94	4364			17.7	1.5	17.1	1	4	0.6				
	PE02-ALC-01	-11.07	-75.94	4377			17.9	1.6	17.3	1.2	3	0.6				
	PE02-ALC-05	-11.07	-75.94	4380			17.1	1.3	16.6	0.8	3	0.5				
	PE01-ANT-01	-11.03	-75.95	4292			18.3	1.4	17.6	0.9	4	0.7				
	PE01-ANT-02	-11.03	-75.95	4296			19.3	1.2	18.8	0.9	3	0.5				
	PE01-ANT-03	-11.03	-75.95	4281			19.2	1.2	18.6	0.9	3	0.6				
	PE01-ANT-04	-11.03	-75.96	4281			19.8	1.3	19.3	1.1	2	0.5				
	PE01-ANT-05	-11.03	-75.95	4279			17.3	1.4	16.7	0.8	4	0.6				
	PE01-ANT-06	-11.03	-75.95	4279			17.6	1.4	17	0.8	4	0.6				
	PE01-ANT-07	-11.03	-75.95	4286			18.6	1.3	18	0.9	3	0.6				
	PE01-CAL-01	-10.95	-75.99	4259			17.8	1.5	17.1	1	4	0.7				
	PE01-CAL-02	-10.95	-75.99	4255			17.1	1.4	16.5	0.9	4	0.6				
	PE01-CAL-03	-10.95	-75.99	4252			20.4	1.4	20	1.3	2	0.4				
	PE01-CAL-04	-10.95	-75.99	4256			17.1	1.4	16.5	0.9	4	0.6				
	PE01-CAL-05	-10.95	-75.99	4263			16	1.4	15.5	0.9	4	0.5				
	PE01-CAL-06	-10.95	-75.99	4269			17.9	2.4	17.2	2.1	4	0.7				
	PE01-CAL-07	-10.96	-75.99	4260			17	2	16.2	1.6	5	0.8				
	PE01-CAL-08	-10.96	-76	4255			18.4	1.4	17.7	0.9	4	0.7				

Continued on next page

Table A.3 – *Continued from previous page*

Fig. Area and Publication	Sample	Latitude	Longitude	Elevation	Balco et al., 2008		Borchers et al., 2016		Heyman, 2014		Borchers vs. Heyman		Balco vs. Heyman		Balco vs. Borchers	
		+N,-S	+E, -W	m	Age (ka)	$\pm 1\sigma$	Age (ka)	$\pm 1\sigma$	Age (ka)	$\pm 1\sigma$	(%)	(ka)	(%)	(ka)	(%)	(ka)
	PE01-CAL-09	-10.96	-76	4259			19	1.3	18.4	1	4	0.6				
	PE01-CAL-10	-10.96	-76	4265			20.6	1.3	20.3	1	1	0.3				
	PE01-CAL-11	-10.96	-76	4252			20	1.2	19.5	1	3	0.5				
	PE01-CAL-12	-10.96	-76	4256			22.3	2.4	22.2	2.1	0	0.1				
	PE01-CAL-13	-10.97	-76	4267			19.5	1.3	19	1	3	0.5				
	PE01-CAL-14	-10.97	-76	4254			20.4	1.2	20.1	1	1	0.3				
	MIL-00-15	-16.32	-68.14	4643			18.7	1.3	18.1	0.9	3	0.6				
	MIL-00-16 D	-16.32	-68.14	4643			9.8	1.3	9.8	0.8	0	0				
	MIL-00-17	-16.32	-68.14	4643			11.9	1.2	11.6	0.7	3	0.3				
	MIL-00-18	-16.32	-68.14	4643			11.6	1.1	11.3	0.6	2	0.3				
	ZONG-03-01	-16.14	-68.18	3489			21.2	1.6	20.4	1.3	4	0.8				
	ZONG-03-02	-16.14	-68.18	3500			19.5	1.2	18.4	0.9	6	1.1				
	ZONG-03-03	-16.14	-68.18	3503			15.6	1.2	14.6	0.7	7	1				
	ZONG-03-04	-16.14	-68.18	3503			9	1	8.7	0.5	4	0.3				
	ZONG-03-05	-16.14	-68.18	3505			16.6	1.4	15.6	0.8	7	1				
	ZONG-03-06	-16.13	-68.17	3417			19	1.4	17.7	0.9	7	1.3				
	ZONG-03-07	-16.13	-68.17	3408			18.8	1.4	17.5	1	7	1.3				
	ZONG-03-08	-16.13	-68.17	3399			6.3	0.4	6.1	0.4	3	0.2				
	ZONG-03-09	-16.13	-68.17	3393			18.1	1.3	16.8	0.8	8	1.3				
	ZONG-03-10	-16.13	-68.17	3391			6.9	0.4	6.7	0.4	2	0.1				
	ZONG-03-11	-16.13	-68.17	3383			4.2	0.4	3.9	0.3	8	0.3				
	ZONG-03-12	-16.13	-68.17	3386			13.8	1.1	12.8	0.6	8	1				
	PE01-ALC-26	-11.07	-75.94	4378			21.8	1.6	21.8	1.3	0	0				

Continued on next page

Table A.3 – *Continued from previous page*

Fig. Area and Publication	Sample	Latitude	Longitude	Elevation	Balco et al., 2008		Borchers et al., 2016		Heyman, 2014		Borchers vs. Heyman		Balco vs. Heyman		Balco vs. Borchers	
		+N,-S	+E, -W	m	Age (ka)	±1σ	Age (ka)	±1σ	Age (ka)	±1σ	(%)	(ka)	(%)	(ka)	(%)	(ka)
	PE01-ALC-27	-11.07	-75.94	4383			33.6	2.5	33.4	1.9	1	0.2				
	PE01-ALC-28	-11.07	-75.94	4388			33.1	2.6	33	1.9	0	0.1				
	PE01-ALC-29	-11.07	-75.94	4385			33.3	2.6	33.2	2	0	0.1				
	PE02-ALC-02	-11.07	-75.94	4377			26.4	1.9	26.5	1.3	0	-0.1				
	PE02-ALC-03	-11.07	-75.94	4382			19.7	1.2	19.3	1	2	0.4				
	PE02-ALC-04	-11.07	-75.94	4375			50.5	5.2	49.4	2.2	2	1.1				
	PE01-ANT-08	-11.04	-75.96	4275			28	2	28.3	1.3	-1	-0.3				
	PE01-ANT-09	-11.04	-75.96	4274			28	2	28.3	1.3	-1	-0.3				
	PE01-ANT-10	-11.04	-75.96	4267			29.6	2.1	29.4	1.3	1	0.2				
	PE01-ANT-11	-11.04	-75.96	4266			32.1	2.3	31.9	1.5	1	0.2				
	PE01-ANT-12	-11.04	-75.96	4269			31.4	2.2	31.3	1.4	0	0.1				
	PE01-ANT-13	-11.04	-75.96	4265			30.4	2.2	30.3	1.4	0	0.1				
	PE01-ANT-14	-11.04	-75.97	4264			26.8	1.9	26.7	1.2	0	0.1				
	PE01-ANT-15	-11.04	-75.97	4262			32.3	2.3	32.2	1.5	0	0.1				
	PE01-CAL-17	-10.97	-76.02	4315			33.9	2.3	33.7	1.6	1	0.2				
	PE01-CAL-18	-10.97	-76.02	4317			24.1	1.8	24	1.2	1	0.1				
	PE02-COL-01	-10.93	-75.94	4162			25.3	1.7	25.1	1.2	1	0.2				
	PE02-COL-02	-10.93	-75.94	4159			26	2	26	1.4	0	0				
	PE02-COL-03	-10.93	-75.94	4168			25.4	1.8	25.2	1.3	1	0.2				
	PE02-COL-04	-10.93	-75.94	4164			23.6	1.8	23.4	1.2	1	0.2				
	PE02-COL-05	-10.93	-75.94	4176			186	11	177.5	10	5	8.5				
	PE02-COL-07	-10.93	-75.94	4208			25.8	1.8	25.7	1.2	0	0.1				
	MIL-00-01	-16.4	-68.18	4594			32.2	2.3	32.1	1.4	0	0.1				

Continued on next page

Table A.3 – *Continued from previous page*

Fig. Area and Publication	Sample	Latitude	Longitude	Elevation	Balco et al., 2008		Borchers et al., 2016		Heyman, 2014		Borchers vs. Heyman		Balco vs. Heyman		Balco vs. Borchers	
		+N,-S	+E, -W	m	Age (ka)	±1σ	Age (ka)	±1σ	Age (ka)	±1σ	(%)	(ka)	(%)	(ka)	(%)	(ka)
	MIL-00-02	-16.4	-68.18	4594			30.8	2.2	30.6	1.4	1	0.2				
	MIL-00-03 D	-16.4	-68.18	4594			27	1.9	27	1.2	0	0				
	MIL-00-04	-16.4	-68.18	4594			34.4	2.3	34.3	1.8	0	0.1				
	MIL-00-05	-16.4	-68.18	4594			17.1	1.3	16.6	0.8	3	0.5				
	MIL-00-06	-16.4	-68.18	4594			18.9	1.3	18.3	0.8	3	0.6				
	MIL-00-07	-16.4	-68.18	4591			27.9	1.9	27.9	1.3	0	0				
	MIL-00-08	-16.4	-68.19	4595			25.6	1.8	25.5	1.2	0	0.1				
	MIL-00-09	-16.4	-68.19	4595			25.3	1.8	25.2	1.4	0	0.1				
	MIL-00-10	-16.4	-68.19	4595			26.6	1.9	26.5	1.3	0	0.1				
	MIL-00-11	-16.4	-68.19	4595			24.1	1.7	24.1	1.1	0	0				
	MIL-00-12	-16.4	-68.19	4595			24.9	1.7	24.7	1.1	1	0.2				
	MIL-00-13	-16.4	-68.19	4595			29.2	2.1	29.1	1.3	0	0.1				
	MIL-00-14	-16.4	-68.19	4576			27.9	1.9	27.9	1.3	0	0				
NW Argentina Zech et al., 2009	LG11	-22.2	-65.12	4454			18.8	1.4	18.1	1	4	0.7				
	LG15	-22.2	-65.12	4469			16.7	1.5	16.1	1	4	0.6				
	LG21	-22.2	-65.12	4485			21.2	1.6	20.9	1.4	1	0.3				
	LG22	-22.2	-65.11	4509			22.1	1.9	21.9	1.4	1	0.2				
	LG23	-22.2	-65.12	4506			104.1	7.1	100.9	4.9	3	3.2				
	LG25	-22.2	-65.12	4478			15.9	1.4	15.4	0.8	3	0.5				
	LG31	-22.19	-65.1	4480			16.3	1.5	15.8	1	3	0.5				
	LG33	-22.18	-65.1	4471			18	1.6	17.3	1.1	4	0.7				
	LG41	-22.19	-65.1	4454			15.3	1.2	14.8	0.8	4	0.5				
	LG42	-22.19	-65.1	4454.5			15.5	1.7	15	1.3	4	0.6				

Continued on next page

Table A.3 – *Continued from previous page*

Fig. Area and Publication	Sample	Latitude	Longitude	Elevation	Balco et al., 2008		Borchers et al., 2016		Heyman, 2014		Borchers vs. Heyman		Balco vs. Heyman		Balco vs. Borchers	
		+N,-S	+E, -W	m	Age (ka)	±1σ	Age (ka)	±1σ	Age (ka)	±1σ	(%)	(ka)	(%)	(ka)	(%)	(ka)
	LG51	-22.2	-65.12	4453			18.7	1.5	17.9	1.1	4	0.8				
	LG52	-22.2	-65.12	4444			17.4	1.4	16.7	0.9	4	0.7				
	LG53	-22.2	-65.12	4437			87.4	9.6	84.5	5.7	3	2.9				
	LG61	-22.19	-65.13	4300			80.4	9.5	77.9	5.2	3	2.5				
	LG62	-22.19	-65.13	4316			176	16	164.8	8.1	7	11.2				
	LG63	-22.19	-65.13	4320			117	9	112.3	5.5	4	4.7				
	LG64	-22.19	-65.13	4329			78.6	7.8	76.4	3.7	3	2.2				
	LG65	-22.19	-65.13	4331			170	20	161	10.8	6	9				
	LG72	-22.19	-65.12	4379			13.2	1.2	12.8	0.6	3	0.4				
	LG73	-22.19	-65.12	4375			14.4	1.2	13.8	0.7	4	0.6				
	LG76	-22.19	-65.12	4377			18.7	1.4	17.9	1	4	0.8				
	LG81	-22.2	-65.12	4425			17	1.4	16.3	0.9	4	0.7				
	LG83	-22.2	-65.14	4421			15.6	1.3	15	0.8	4	0.6				
	LG92	-22.21	-65.11	4573			12.9	1.2	12.6	0.7	3	0.3				
	LG93	-22.21	-65.11	4561			14	1.2	13.6	0.8	3	0.4				
	LG95	-22.2	-65.11	4563			55.2	5.7	54.3	3.2	2	0.9				
New Zealand	BH-07-08	-43.85	170.11	584.8			14.3	1.2	13.7	0.6	4	0.6				
Putnam et al., 2010	BH-07-09	-43.86	170.11	588.6			14.4	1.2	13.8	0.6	4	0.6				
	BH-06-02	-43.82	170.11	747.3			13.1	1.1	12.8	0.6	2	0.3				
	BH-06-03	-43.82	170.11	681.3			12.6	1.1	12.2	0.6	3	0.4				
	BH-06-04	-43.82	170.11	688.8			13	1	12.2	0.6	6	0.8				
	BH-06-05	-43.81	170.11	765.6			12.6	1.1	12.2	0.6	3	0.4				
	BH-06-06	-43.81	170.1	765.1			13.1	1.1	12.8	0.6	3	0.3				

Continued on next page

Table A.3 – *Continued from previous page*

Fig. Area and Publication	Sample	Latitude	Longitude	Elevation	Balco et al., 2008		Borchers et al., 2016		Heyman, 2014		Borchers vs. Heyman		Balco vs. Heyman		Balco vs. Borchers	
		+N,-S	+E, -W	m	Age (ka)	±1σ	Age (ka)	±1σ	Age (ka)	±1σ	(%)	(ka)	(%)	(ka)	(%)	(ka)
	BH-06-07	-43.81	170.1	772.9			12.8	1.1	12.4	0.6	3	0.4				
	BH-07-10	-43.85	170.11	578.7			12.8	1.1	12.3	0.6	4	0.5				
	BH-07-11	-43.85	170.11	577.7			16	2	15.5	1.6	3	0.5				
	BH-07-12	-43.85	170.11	583.6			13.2	1.1	12.7	0.6	4	0.5				
	BH-07-13	-43.84	170.11	679.1			13.6	1.1	13.2	0.6	3	0.4				
	BH-07-14	-43.84	170.11	674.9			13.6	1.1	13.1	0.6	4	0.5				
	BH-07-15	-43.84	170.11	674.9			13.3	1.1	12.9	0.6	3	0.4				
	BH-07-16	-43.84	170.11	671.5			13.6	1.1	13.1	0.6	4	0.5				
	BH-07-17	-43.83	170.11	674.3			13.1	1.1	12.6	0.6	4	0.5				
	BH-07-18	-43.83	170.11	673.2			13.6	1.2	13.1	0.6	4	0.5				
	BH-06-09	-43.81	170.11	634.9			13.4	1.3	12.9	0.9	4	0.5				
	BH-06-10	-43.81	170.11	607.6			13.3	1.2	12.8	0.6	4	0.5				
	BH-06-11	-43.82	170.11	612.3			13.2	1.1	12.7	0.6	4	0.5				
	BH-06-12	-43.82	170.11	629.6			13.6	1.2	13.1	0.7	4	0.5				
	BH-06-13	-43.82	170.11	606.2			13.5	1.2	13	0.6	4	0.5				
	KIWI631	-43.82	170.11	605.5			13.6	1.2	13.1	0.6	4	0.5				
	KIWI632	-43.82	170.11	603.7			12.9	1.1	12.4	0.5	4	0.5				
	MR-09-01	-43.57	170.61	1064.4			13.2	1.1	13	0.6	1	0.2				
	MR-09-02	-43.57	170.61	1057.3			13	1	12.9	0.5	1	0.1				
	MR-09-03	-43.57	170.61	1056.9			13	1	13.2	0.5	-2	-0.2				
New Zealand	OH-07-04	-44.3	169.99	605.2			128	11	124.4	5.6	3	3.6				
Putnam et al., 2013	OH-07-44	-44.3	170	615.4			149	13	144.7	6.2	3	4.3				
	OH-07-45	-44.3	170	621.1			138	12	133.7	6.8	3	4.3				

Continued on next page

Table A.3 – *Continued from previous page*

Fig. Area and Publication	Sample	Latitude	Longitude	Elevation	Balco et al., 2008		Borchers et al., 2016		Heyman, 2014		Borchers vs. Heyman		Balco vs. Heyman		Balco vs. Borchers	
		+N,-S	+E, -W	m	Age (ka)	±1σ	Age (ka)	±1σ	Age (ka)	±1σ	(%)	(ka)	(%)	(ka)	(%)	(ka)
	OH-06-60a	-44.35	169.9	599			33.9	2.7	33	1.6	3	0.9				
	OH-06-61	-44.35	169.89	600			32.9	2.7	32	1.5	3	0.9				
	OH-06-62	-44.35	169.9	586			29.5	2.4	28.6	1.4	3	0.9				
	OH-06-63	-44.34	169.9	590			33.4	2.9	32.4	1.7	3	1				
	OH-07-01	-44.29	169.98	579			32.1	2.6	31.1	1.5	3	1				
	OH-07-16	-44.32	169.96	569.1			28.6	2.4	27.7	1.5	3	0.9				
	OH-07-18	-44.32	169.97	564.5			26.6	2.2	25.8	1.4	3	0.8				
	OH-07-19	-44.32	169.98	554.5			31.4	2.6	30.4	1.6	3	1				
	OH-07-21	-44.32	169.95	570.5			32.1	2.7	31.2	1.6	3	0.9				
	OH-07-26	-44.34	169.83	680			29.3	2.4	28.5	1.4	3	0.8				
	OH-06-04	-44.26	169.98	592.1			17.7	1.4	17.1	0.8	4	0.6				
	OH-06-05	-44.26	169.98	591.6			22	1.8	21.4	1	3	0.6				
	OH-06-16	-44.25	169.97	582.2			22.5	1.8	21.9	1	3	0.6				
	OH-06-18	-44.25	169.97	585.9			22.3	1.8	21.7	1	3	0.6				
	OH-06-44	-44.32	169.95	581.8			23	2	22.4	1.2	3	0.6				
	OH-06-45	-44.32	169.95	574.2			24	2	23.3	1.1	3	0.7				
	OH-06-46	-44.33	169.94	572.5			22.8	1.9	22.1	1	3	0.7				
	OH-06-50	-44.33	169.94	573.9			24	2	23	1.1	4	1				
	OH-06-59	-44.33	169.89	605			22.3	1.9	21.7	1	3	0.6				
	OH-06-72	-44.33	169.89	602			21.9	1.8	21.3	1.1	3	0.6				
	OH-06-73	-44.33	169.89	603			22.3	1.9	21.7	1.2	3	0.6				
	OH-07-08	-44.3	169.96	582.2			24	2	23	1.2	4	1				
	OH-07-10	-44.3	169.96	583.4			22.9	1.8	22.1	1	3	0.8				

Continued on next page

Table A.3 – *Continued from previous page*

Fig. Area and Publication	Sample	Latitude	Longitude	Elevation	Balco et al., 2008		Borchers et al., 2016		Heyman, 2014		Borchers vs. Heyman		Balco vs. Heyman		Balco vs. Borchers	
		+N,-S	+E, -W	m	Age (ka)	±1σ	Age (ka)	±1σ	Age (ka)	±1σ	(%)	(ka)	(%)	(ka)	(%)	(ka)
	OH-07-11	-44.3	169.96	581.7			20.1	1.6	19.5	1	3	0.6				
	OH-07-13	-44.31	169.96	577.5			22.1	1.8	21.5	1.1	3	0.6				
	OH-07-14	-44.31	169.96	576.9			23.2	1.9	22.5	1.1	3	0.7				
	OH-07-15	-44.31	169.96	575.5			22.9	1.9	22.2	1.1	3	0.7				
	OH-07-31	-44.33	169.88	620			22.3	1.9	21.7	1.1	3	0.6				
	OH-07-33	-44.33	169.88	618			23.7	1.9	23.1	1.1	3	0.6				
	OH-07-34	-44.33	169.88	618			23.5	1.9	22.8	1.1	3	0.7				
	OH-07-36	-44.33	169.88	613			23.7	1.9	23	1.2	3	0.7				
	OH-07-37	-44.33	169.88	613			22.4	1.8	21.8	1	3	0.6				
	OH-07-38	-44.33	169.89	606			22.1	1.8	21.6	1	2	0.5				
	OH-07-39	-44.32	169.87	614			21.6	1.8	21.1	1	3	0.5				
	OH-07-40	-44.32	169.88	612			22.3	1.8	21.6	1.1	3	0.7				
	OH-07-41	-44.32	169.88	612			22.6	1.8	21.9	1.1	3	0.7				
	OH-06-08	-44.28	169.94	557.3			20.2	1.6	19.6	0.9	3	0.6				
	OH-06-10	-44.28	169.98	561.4			18.4	1.5	17.8	0.9	4	0.6				
	OH-06-11	-44.28	169.94	559			18.4	1.6	17.8	0.9	3	0.6				
	OH-06-13	-44.27	169.94	561.2			18.7	1.5	18.1	0.8	3	0.6				
	OH-06-14	-44.27	169.93	564.1			17.7	1.5	17.1	0.8	3	0.6				
	OH-06-15	-44.27	169.93	546.3			18.7	1.5	18.1	0.8	3	0.6				
	OH-06-22	-44.3	169.9	583.5			18.7	1.5	18.1	0.9	3	0.6				
	OH-06-23	-44.3	169.9	583.6			18.8	1.5	18.1	0.9	4	0.7				
	OH-06-24	-44.3	169.9	578.3			19	1.6	18.3	0.9	4	0.7				
	OH-06-26	-44.3	169.9	575.3			18.7	1.5	18.1	0.9	3	0.6				

Continued on next page

Table A.3 – *Continued from previous page*

Fig. Area and Publication	Sample	Latitude	Longitude	Elevation	Balco et al., 2008		Borchers et al., 2016		Heyman, 2014		Borchers vs. Heyman		Balco vs. Heyman		Balco vs. Borchers	
		+N,-S	+E, -W	m	Age (ka)	±1σ	Age (ka)	±1σ	Age (ka)	±1σ	(%)	(ka)	(%)	(ka)	(%)	(ka)
	OH-06-27	-44.3	169.91	579.2			19.4	1.5	18.8	0.9	3	0.6				
	OH-06-31	-44.29	169.93	546.8			18.7	1.5	18.1	0.8	3	0.6				
	OH-06-84	-44.3	169.88	586.2			18.1	1.5	17.4	0.8	4	0.7				
	OH-06-85	-44.3	169.88	582.9			18.9	1.5	18.2	0.9	4	0.7				
	OH-06-86	-44.3	169.89	581			18.8	1.5	18.1	0.9	4	0.7				
	OH-06-90	-44.31	169.89	580			17.8	1.5	17.1	0.8	4	0.7				
	OH-06-92	-44.31	169.88	580			17.9	1.5	17.3	0.8	3	0.6				
	OH-06-95	-44.3	169.87	591			18.9	1.5	18.3	0.9	3	0.6				
	OH-06-96	-44.3	169.86	598			17.5	1.5	17	0.9	3	0.5				
	OH-06-25	-44.3	169.9	575.7			18	1.5	17.4	0.8	3	0.6				
	OH-06-28	-44.29	169.9	554.8			17.4	1.5	16.7	0.8	4	0.7				
	OH-06-29	-44.29	169.91	550.1			18	1.5	17.4	0.8	3	0.6				
	OH-06-78	-44.29	169.88	540			18.3	1.5	17.7	0.8	3	0.6				
	OH-06-79	-44.29	169.88	539.2			19.7	1.6	19.1	0.9	3	0.6				
	OH-06-80	-44.28	169.88	539			18.4	1.4	17.6	0.8	4	0.8				
	OH-06-88	-44.3	169.89	569.9			17.8	1.4	17.1	0.8	4	0.7				
	OH-10-01	-44.07	169.87	721.9			17.3	1.3	16.7	0.7	3	0.6				
	OH-10-02	-44.07	169.87	718.8			17.1	1.4	16.6	0.7	3	0.5				
	OH-10-03	-44.07	169.87	718.2			18	1.4	17.4	0.7	3	0.6				
	OH-10-04	-44.07	169.87	694			18.4	1.5	17.9	0.9	3	0.5				
	OH-10-05	-44.07	169.87	722.3			17.2	1.4	16.6	0.7	3	0.6				
	OH-10-06	-44.07	169.87	722.3			17.1	1.4	16.7	0.7	3	0.4				
	OH-10-07	-44.16	169.81	644.3			18	1.4	17.3	0.7	4	0.7				

Continued on next page

Table A.3 – *Continued from previous page*

Fig.	Area and Publication	Sample	Latitude	Longitude	Elevation	Balco et al., 2008		Borchers et al., 2016		Heyman, 2014		Borchers vs. Heyman		Balco vs. Heyman		Balco vs. Borchers	
			+N,-S	+E, -W	m	Age (ka)	±1σ	Age (ka)	±1σ	Age (ka)	±1σ	(%)	(ka)	(%)	(ka)	(%)	(ka)
		OH-10-08	-44.17	169.81	622.4			11.6	1	11.3	0.5	3	0.4				
	New Zealand	Kiwi-9106	-43.97	170.25	794			17.6	1.5	17.1	0.8	3	0.5				
	Kelley et al., 2014	Kiwi-984	-43.97	170.26	825			18.3	1.8	17.8	1.4	3	0.5				
		Kiwi-9107	-43.97	170.25	796			19	1.5	18.5	0.9	3	0.5				
		Kiwi-9103	-43.98	170.25	812			20.3	1.6	19.8	0.9	2	0.5				
		Pl-07-04	-43.97	170.25	795			20.9	1.7	20.4	1.1	2	0.5				
		Pl-08-19	-44	170.26	794			19.8	1.5	19.3	0.8	2	0.5				
		Pl-08-37	-43.91	170.23	950			19.8	1.5	19.4	0.8	2	0.4				
		Pl-08-15	-44	170.27	790			20.1	1.5	19.6	0.9	3	0.5				
		Pl-08-36	-43.91	170.23	951			20.3	1.6	19.9	0.9	2	0.4				
		Pl-08-21	-44.03	170.26	777			20.6	1.5	20.1	0.9	3	0.5				
		Pl-08-18	-44.01	170.27	776			20.8	1.6	20.2	0.8	3	0.6				
		Pl-08-14	-44	170.27	801			20.7	1.6	20.2	0.8	2	0.5				
		Pl-08-20	-44.01	170.26	769			20.9	1.6	20.5	0.9	2	0.4				
		Kiwi-992	-43.96	170.25	857			21	1.7	20.5	1	2	0.5				
		Pl-08-16	-44	170.27	781			21	1.6	20.5	0.9	3	0.5				
		Pl-08-13	-43.99	170.27	801			21	1.6	20.6	0.9	2	0.4				
		Kiwi-990x	-43.97	170.26	847			21.8	1.7	21.4	0.9	2	0.4				
		Kiwi-990	-43.97	170.26	847			22.1	1.7	21.6	1	2	0.5				
		Kiwi-981	-43.99	170.26	819			22	1.8	21.6	1	2	0.4				
		Pl-08-17	-44	170.27	785			24	1.9	23.4	1	2	0.6				
		Pl-08-05	-43.96	170.26	838			37.7	2.9	37.1	1.5	2	0.6				
		Kiwi-986	-43.96	170.26	861			38	3	37.7	1.7	1	0.3				

Continued on next page

Table A.3 – *Continued from previous page*

Fig. Area and Publication	Sample	Latitude	Longitude	Elevation	Balco et al., 2008		Borchers et al., 2016		Heyman, 2014		Borchers vs. Heyman		Balco vs. Heyman		Balco vs. Borchers	
		+N,-S	+E, -W	m	Age (ka)	±1σ	Age (ka)	±1σ	Age (ka)	±1σ	(%)	(ka)	(%)	(ka)	(%)	(ka)
	Pl-08-02	-43.97	170.27	809			42.4	3.3	41.7	1.8	2	0.7				
	Pl-08-01	-43.97	170.27	806			39	3	38.3	1.6	2	0.7				
	Kiwi-985	-43.96	170.26	864			42.7	3.3	42.1	1.7	1	0.6				
	Pl-08-39	-43.92	170.24	942			40.2	3.1	39.7	1.7	1	0.5				
	Pl-08-38	-43.91	170.23	968			37.8	2.9	37.3	1.5	1	0.5				
	Kiwi-979	-43.97	170.26	840			38	3	37.5	1.7	1	0.5				
	Kiwi-980	-43.96	170.26	865			43	3.4	42.4	1.8	1	0.6				

A.6. Data Set 3: Glacial striations measured in the Lahul area

Table A.4: Data Set 3: Measured Striations in the Lahul Area

Longitude	Latitude	Northing	Easting	Altitude	Surface	Azimut
77.5677	32.2787	3574218.4000	741830.3300	4545		330
77.5676	32.2806	3574433.6301	741815.4665	4580		330
77.5681	32.2816	3574540.1091	741860.0466	4590		328
77.5689	32.2822	3574610.3373	741933.7723	4600		320
77.5701	32.2825	3574651.9370	742049.0919	4590		330
77.5696	32.2843	3574852.1944	741997.1619	4550		302
77.6485	32.4078	3588724.3625	749088.5336	4565	200/44	70
77.6501	32.4076	3588709.3356	749243.2892	4588	278/25	60
77.6500	32.4093	3588893.0337	749222.7293	4605	160/28	55
77.6516	32.4091	3588876.9467	749379.3917	4620	120/50	66
77.6497	32.4092	3588885.6112	749205.3385	4597	250/20	110
77.6497	32.4092	3588885.6112	749205.3385	4597	250/20	60
77.6286	32.4120	3589146.0000	747207.9800	4597		137
77.6294	32.4167	3589663.8000	747272.8000	4597		105
77.6303	32.4168	3589679.5000	747351.9500	4615		137
77.6309	32.4181	3589823.4000	747406.3800	4695		114
77.6289	32.4085	3588756.9000	747239.9600	4717		114
77.6300	32.4170	3589697.0000	747321.0000	4750		105
77.4063	32.3065	3576948.8740	726560.2526	4010		270
77.4071	32.3052	3576807.4123	726634.0981	3960		270
77.4186	32.7517	3626351.1000	726598.9300			134
77.4210	32.7545	3626663.9000	726814.5500			142
77.4214	32.7546	3626679.5000	726844.9500			136
77.4214	32.7556	3626791.0000	726847.9300			148
77.4178	32.7513	3626302.0000	726518.0100			110
77.4218	32.7534	3626548.0000	726889.9600			135
77.4218	32.7535	3626561.0000	726890.0400			138
77.4218	32.7536	3626563.0000	726885.9600			140
77.4218	32.7536	3626567.0000	726891.0200			144
77.4216	32.7544	3626651.9000	726867.9900			140
77.4221	32.7541	3626617.3218	726916.4069	4915		145
77.4217	32.7536	3626562.9372	726881.7419	4910		144
77.4214	32.7557	3626794.8832	726845.1198	4920		158
77.4197	32.7564	3626869.0187	726680.9450	4910		144
77.6265	32.4105	3588974.0679	747014.4707	4653	232/40	152
77.6265	32.4105	3588974.0679	747014.4707	4653	120/20	105
77.6279	32.4123	3589181.2745	747140.2449	4637	195/10	125

Continued on next page

Table A.4 – *Continued from previous page*

Longitude	**Latitude**	**Northing**	**Easting**	**Altitude**	**Surface**	**Azimut**
77.6314	32.4174	3589746.6520	747457.8953	4758	335/05	115
77.6350	32.4216	3590221.3601	747782.0999	4782	020/50	110
77.6363	32.4234	3590431.4066	747898.8240	4810	015/65	105
77.6357	32.4237	3590463.9307	747837.3081	4819	229/35	112
77.6955	32.4550	3594067.0000	753381.0000	4164		10
77.6963	32.4565	3594235.6417	753451.0248	4132		7
77.6881	32.4497	3593466.3752	752701.9892	4316	040/05	35
77.6881	32.4497	3593466.3752	752701.9892	4316	040/05	17
77.6887	32.4487	3593352.7871	752757.1495	4301	280/10	45
77.6884	32.4494	3593431.2920	752727.1732	4316	105/10	40
77.6862	32.4498	3593469.7548	752514.8570	4390	100/05	40
77.6862	32.4498	3593469.7548	752514.8570	4390	100/05	21
77.6851	32.4499	3593482.6364	752413.1774	4425	293/10	30
77.6840	32.4505	3593541.6843	752311.1735	4473	335/02	33
77.6820	32.4503	3593519.5612	752118.6739	4494	110/10	35
77.6801	32.4507	3593559.7757	751944.0583	4568	120/60	40
77.6937	32.4539	3593940.6336	753215.5427	4163	140/05	38
77.6937	32.4539	3593940.6336	753215.5427	4163	140/05	18
77.6076	32.4893	3597668.5000	745017.8300	4278		70
77.6075	32.4890	3597633.0000	745012.0300	4284		64
77.6097	32.4638	3594844.4086	745291.0168	4296	230/25	130
77.6096	32.4653	3595013.6465	745274.8752	4336	340/10	125

References

Andersen, K. K. et al. (2004), High-resolution record of Northern Hemisphere climate extending into the last interglacial period, Nature, 431(7005), 147-151, doi:10.1038/nature02805.

Balco, G., J. O. Stone, N. A. Lifton, and T. J. Dunai (2008), A complete and easily accessible means of calculating surface exposure ages or erosion rates from 10Be and 26Al measurements, Quaternary Geochronology, 3(3), 174-195, doi:10.1016/j.quageo.2007.12.001.

Berger, A., and M. F. Loutre (1991), Insolation values for the climate of the last 10 million years, Quaternary Science Reviews, 10(4), 297-317, doi:10.1016/0277-3791(91)90033-Q.

Borchers, B., S. Marrero, G. Balco, M. Caffee, B. Goehring, N. Lifton, K. Nishiizumi, F. Phillips, J. Schaefer, and J. Stone (2016), Geological calibration of spallation production rates in the CRONUS-Earth project, Quaternary Geochronology, 31, 188-198, doi:10.1016/j.quageo.2015.01.009.

Desilets, D., M. Zreda, and T. Prabu (2006), Extended scaling factors for in situ cosmogenic nuclides: New measurements at low latitude, Earth and Planetary Science Letters, 246(3-4), 265-276, doi:10.1016/j.epsl.2006.03.051.

Dunai, T. J. (2001), Influence of secular variation of the geomagnetic field on production rates of in situ produced cosmogenic nuclides, Earth and Planetary Science Letters, 193(1-2), 197-212, doi:10.1016/S0012-821X(01)00503-9.

Dutt, S., A. K. Gupta, S. C. Clemens, H. Cheng, R. K. Singh, G. Kathayat, and R. L. Edwards (2015), Abrupt changes in Indian summer monsoon strength during 33,800 to 5500 years B.P, Geophysical Research Letters, 42(13), 5526-5532, doi:10.1002/2015GL064015.

Finkel, R. C., L. A. Owen, P. L. Barnard, and M. W. Caffee (2003), Beryllium-10 dating of Mount Everest moraines indicates a strong monsoon influence and glacial synchroneity throughout the Himalaya, Geology, 31(6), 561-564, doi:10.1130/0091-7613(2003)031<0561:BDOMEM>2.0.CO;2.

Gayer, E., J. Lavé, R. Pik, and C. France-Lanord (2006), Monsoonal forcing of Holocene glacier fluctuations in Ganesh Himal (Central Nepal) constrained by cosmogenic 3He exposure ages of garnets, Earth and Planetary Science Letters, 252(3-4), 275-288, doi:10.1016/j.epsl.2006.09.040.

Gayer, E., R. Pik, J. Lavé, C. France-Lanord, D. Bourles, and B. Marty (2004), Cosmogenic 3He in Himalayan garnets indicating an altitude dependence of the 3 He/10Be production ratio, Earth and Planetary Science Letters, 229(1-2), 91-104, doi:10.1016/j.epsl.2004.10.009.

Hadorn, P., N. Thew, G. R. Coope, G. Lemdahl, I. Hajdas, and G. Bonani (2002), Equilibres et ruptures dans les écosystèmes depuis 20 000 ans en Europe de l'Ouest, edited by H. Richard and A. Vignot, Collection Annales Littéraires: Serié Environment, Sociétés et achéologie, 3, 75-90.

Herzschuh, U. (2006), Palaeo-moisture evolution in monsoonal Central Asia during the last 50,000 years, Quaternary Science Reviews, 25(1-2), 163-178, doi:10.1016/j.quascirev.2005.02.006.

Heyman, J. (2014), Paleoglaciation of the Tibetan Plateau and surrounding mountains based on exposure ages and ELA depression estimates, Quaternary Science Reviews, 91, 30-41, doi:10.1016/j.quascirev.2014.03.018.

Ivy-Ochs, S., H. Kerschner, A. Reuther, F. Preusser, K. Heine, P. W. Kubik, and C. Schlüchter (2008), Chronology of the last glacial cycle in the European Alps, Journal of Quaternary Science, 23(6-7), 550-573, doi:10.1002/jqs.1202.

Ivy-Ochs, S., J. M. Schäfer, P. W. Kubik, H.-A. Synal, and C. Schlüchter (2004), Timing of deglaciation on the northern Alpine foreland (Switzerland), Eclogae Geologicae Helvetiae, 97(1), 47-55, doi:10.1007/s00015-004-1110-0.

Kaplan, M. R., R. P. Ackert, B. S. Singer, D. C. Douglass, and M. D. Kurz (2004), Cosmogenic nuclide chronology of millennial-scale glacial advances during O-isotope stage 2 in Patagonia, GSA Bulletin, 116(3/4), 308-321, doi:10.1130/B25178.1.

Kelley, S. E., M. R. Kaplan, J. M. Scefer, B. G. Andersen, D. J. A. Barrell, A. E. Putnam, G. H. Denton, R. Schwartz, R. C. Finkel, and A. M. Doughty (2014), High-precision 10Be chronology of moraines in the Southern Alps indicates synchronous cooling in Antarctica and New Zealand 42,000 years ago, Earth and Planetary Science Letters, 405, 194-206, doi:10.1016/j.epsl.2014.07.031.

Kelly, M. A., T. V. Lowell, B. L. Hall, J. M. Schäfer, R. C. Finkel, B. M. Goehring, R. B. Alley, and G. H. Denton (2008), A 10Be chronology of lateglacial and Holocene mountain glaciation in the Scoresby Sund region, east Greenland: implications for seasonality during lateglacial time, Quaternary Science Reviews, 27(25-26), 2273-2282, doi:10.1016/j.quascirev.2008.08.004.

Lal, D. (1991), Cosmic ray labeling of erosion surfaces: in situ nuclide production rates and erosion models, Earth and Planetary Science Letters, 104(2-4), 424-439, doi:10.1016/0012-821X(91)90220-C.

Licciardi, J. M., and K. L. Pierce (2008), Cosmogenic exposure-age chronologies of Pinedale and Bull Lake glaciations in greater Yellowstone and the Teton Range, USA, Quaternary Science Reviews, 27(7-8), 814-831, doi:10.1016/j.quascirev.2007.12.005.

Licciardi, J. M., P. U. Clark, E. J. Brook, K. L. Pierce, M. D. Kurz, D. Elmore, and P. Sharma (2001), Cosmogenic 3He and 10Be chronologies of the late Pinedale northern Yellowstone ice cap, Montana, USA, Geology, 29(12), 1095-1098.

Lifton, N. A., J. W. Bieber, J. M. Clem, M. L. Duldig, P. Evenson, J. E. Humble, and R. Pyle (2005), Addressing solar modulation and long-term uncertainties in scaling secondary cosmic rays for in situ cosmogenic nuclide applications, Earth and Planetary Science Letters, 239(1-2), 140-161, doi:10.1016/j.epsl.2005.07.001.

Lifton, N., D. F. Smart, and M. A. Shea (2008), Scaling time-integrated in situ cosmogenic nuclide production rates using a continuous geomagnetic model, Earth and Planetary Science Letters, 268(1-2), 190-201, doi:10.1016/j.epsl.2008.01.021.

Lifton, N., T. Sato, and T. J. Dunai (2014), Scaling in situ cosmogenic nuclide production rates using analytical approximations to atmospheric cosmic-ray fluxes, Earth and Planetary Science Letters, 386, 149-160, doi:10.1016/j.epsl.2013.10.052.

Owen, L. A., E. Derbyshire, and S. Richardson (1996), The Quaternary glacial history of the Lahul Himalaya, northern India, Journal of Quaternary Science, 11(1), 25-42.

Owen, L. A., L. Gualtieri, R. C. Finkel, M. W. Caffee, D. I. Benn, and M. C. Sharma (2001), Cosmogenic radionuclide dating of glacial landforms in the Lahul Himalaya, northern India: defining the timing of Late Quaternary glaciation, Journal of Quaternary Science, 16(6), 555-563, doi:10.1002/jqs.621.

Putnam, A. E., J. M. Schäfer, D. Barrell, M. Vandergoes, G. H. Denton, M. R. Kaplan, R. C. Finkel, R. Schwartz, B. M. Goehring, and S. E. Kelley (2010), In situ cosmogenic 10Be production-rate calibration from the Southern Alps, New Zealand, Quaternary Geochronology, 5(4), 392-409, doi:10.1016/j.quageo.20.

Putnam, A. E., J. M. Schäfer, G. H. Denton, D. J. A. Barrell, S. D. Birkel, B. G. Andersen, M. R. Kaplan, R. C. Finkel, R. Schwartz, and A. M. Doughty (2013), The Last Glacial Maximum at 44°S documented by a 10Be moraine chronology at Lake Ohau, Southern Alps of New Zealand, Quaternary Science Reviews, 62, 114-141, doi:10.1016/j.quascirev.2012.10.034.

Reber, R., A. Naki, S. Ivy-Ochs, D. Tikhomirov, R. Burkhalter, C. Zahno, A. Lüthold, P. W. Kubik, C. Vockenhuber, and C. Schlüchter (2014), Timing of retreat of the Reuss Glacier (Switzerland) at the end of the Last Glacial Maximum, Swiss Journal of Geosciences, 107(2), 293-307, doi:10.1007/s00015-014-0169-5.

Scherler, D., B. Bookhagen, M. Strecker, F. von Blanckenburg, and D. Rood (2010), Timing and extent of late Quaternary glaciation in the western Himalaya constrained by 10Be moraine dating in Garhwal, India, Quaternary Science Reviews, 29(7-8), 815-831, doi:10.1016/j.quascirev.2009.11.031.

Seong, Y. B., L. A. Owen, M. P. Bishop, A. Bush, P. Clendon, L. Copland, R. Finkel, U. Kamp, and J. F. Shroder Jr. (2007), Quaternary glacial history of the Central Karakoram, Quaternary Science Reviews, 26(25-28), 3384-3405, doi:10.1016/j.quascirev.2007.09.015.

Smith, J. A., G. O. Seltzer, D. L. Farber, D. T. Rodbell, and R. C. Finkel (2005), Early Local Last Glacial Maximum in the Tropical Andes, Science, 308(5722), 678-681, doi:10.1126/science.1107075.

Stenni, B. et al. (2011), Expression of the bipolar see-saw in Antarctic climate records during the last deglaciation, Nature Geoscience, 4, 46-49, doi:10.1038/ngeo1026.

Stone, J. O. (2000), Air pressure and cosmogenic isotope production, Journal of Geophysical Research: Solid Earth, 105, 23753-23759, doi:10.1029/2000JB900181.

Thompson, L. G., T. Yao, M. E. Davis, K. A. Henderson, E. Mosley-Thompson, P. N. Lin, J. Beer, H.-A. Synal, J. Cole-Dai, and J. F. Bolzan (1997), Tropical climate instability: The last glacial cycle from a Qinghai-Tibetan ice core, Science, 276(5320), 1821-1825, doi:10.1126/science.276.5320.1821.

Ullman, D. J., A. E. Carlson, A. N. LeGrande, F. S. Anslow, A. K. Moore, M. Caffee, K. M. Syverson, and J. M. Licciardi (2014), Southern Laurentide ice-sheet retreat synchronous with rising boreal summer insolation, Geology, 43(1), 23-26, doi:10.1130/G36179.1.

Ward, D. J., R. S. Anderson, Z. S. Guido, and J. P. Briner (2009), Numerical modeling of cosmogenic deglaciation records, Front Range and San Juan mountains, Colorado, Journal of Geophysical Research: Earth Surface, 114(F01026), 2156-2202, doi:10.1029/2008JF001057.

Zech, J., R. Zech, P. W. Kubik, and H. Veit (2009), Glacier and climate reconstruction at Tres Lagunas, NW Argentina, based on 10Be surface exposure dating and lake sediment analyses, Palaeogeography, Palaeoclimatology, Palaeoecology, 284(3-4), 180-190, doi:10.1016/j.palaeo.2009.09.023.

Appendix B

Ice-dams and Outburst Floods

The supplementary data of chapter 3 containing

- Figures B.1-B.3 containing information about the recalculated ^{10}Be-depth profile modeling
- Table B.1 contains the recalculated ^{10}Be-exposure ages by Dortch et al. [2010]
- Table B.2 contains glacial striation measurements

are presented here.

B.1. Figures B.1-B.3 containing information about the recalculated ^{10}Be-depth profile modeling

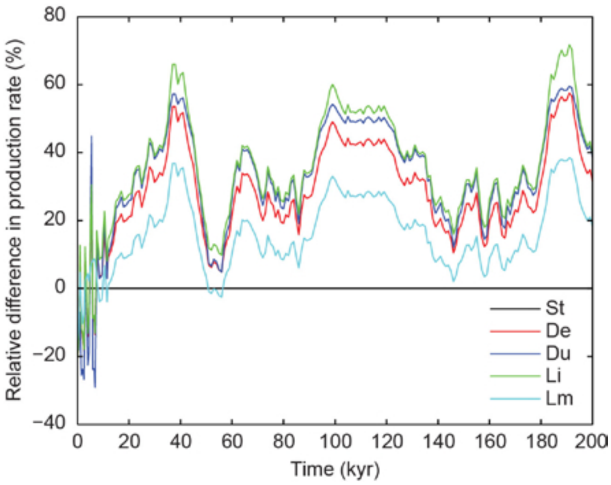

Figure B.1: Relative differences of instantaneous production rates during the past 200 kyr in the study area, according to the production rate scaling models available in the CRONUS online calculator [Balco et al., 2008]. St=time-independent Lal/Stone scaling; De=timedependent Desilets et al. scaling; Du=time-dependent Dunai scaling; Li=time-dependent Lifton et al. scaling; Lm=time-dependent form of the Lal/Stone scaling. See Balco et al. [2008] for details and references on the different scaling models.

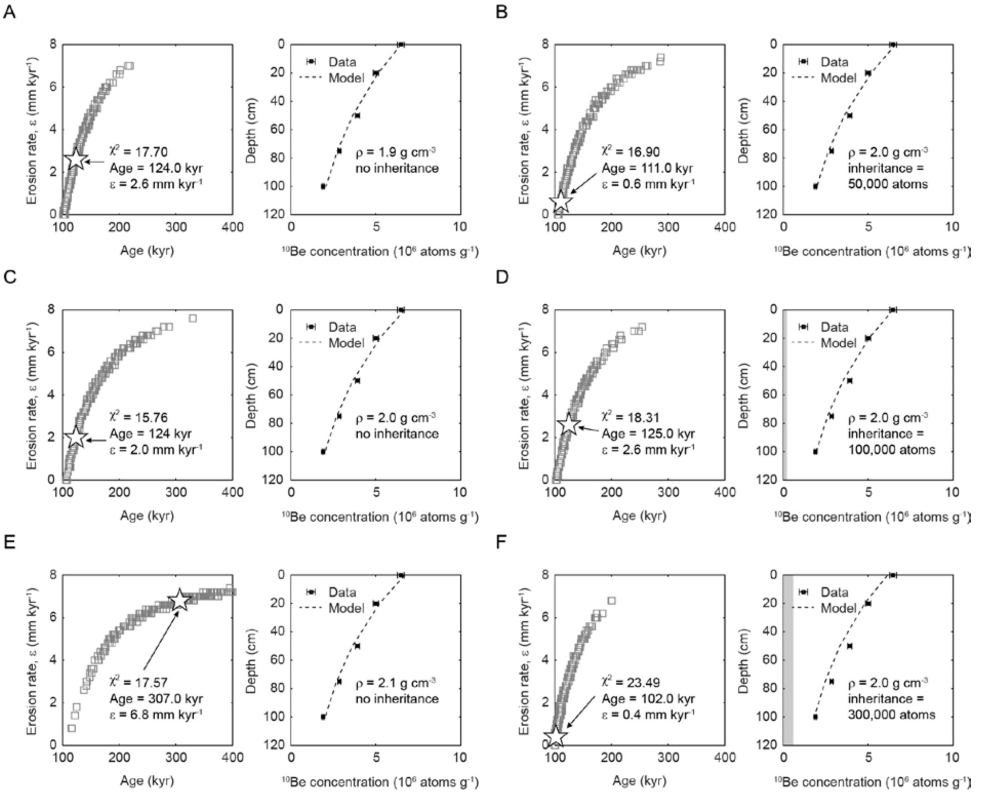

Figure B.2: Best-fit ^{10}Be depth-profile modeling results for the till plain at the Shyok-Nubra confluence, showing the effect of different densities, given no inheritance (A, C, E), and the effect of different inheritances for a fixed density of 2.0 g/cm^3 (B, D, F). In each panel, the left plot shows the best-fit results from 200 Monte Carlo runs, the right plot shows modeled (dashed line) and measured (solid squares) ^{10}Be concentrations and their 2-σ total analytical uncertainties (error bars). Gray bars indicate the assumed inherited concentration. The ultimate best-fit solution is indicated with a star in the left plot of each panel and the corresponding modeled ^{10}Be-depth profile is shown in the right plot of each panel.

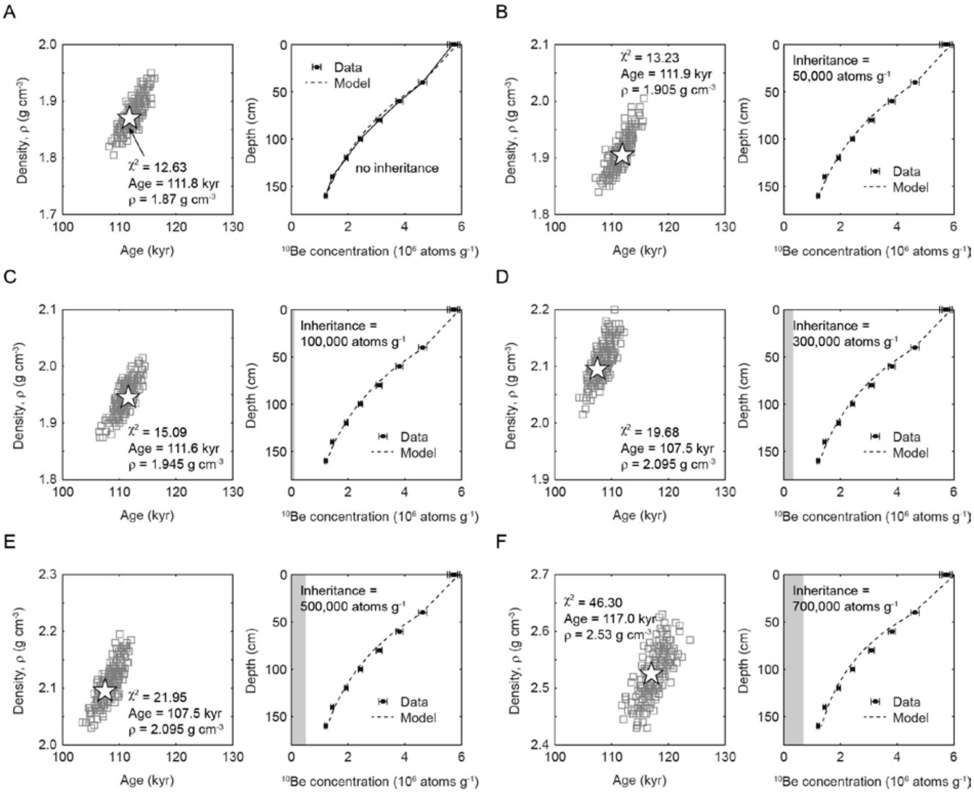

Figure B.3: ^{10}Be depth-profile modeling results for the terrace surface near Agham and different scenarios of inherited concentrations: (A) no inheritance, (B) 50,000 atoms/g, (C) 100,000 atoms/g, (D) 300,000 atoms/g, (E) 500,000 atoms/g, (F) 700,000 atoms/g. Symbols are as in Figure B.2. Reasonable fits can be achieved with each inheritance scenario, but the misfit (χ^2) between the modeled and measured data increases with increasing inheritances. Note the different scaling on the y-axis of the left plots.

B.2. Table B.1: Recalculated ^{10}Be-exposure ages by Dortch et al., (2010)

Table B.1: Surface exposure ages, based on data published in Dortch et al. [2010], recalculated with the CRONUS online calculator [Balco et al., 2008]. All uncertainties on model ages refer to the external errors; 'St', 'De', 'Du', 'Li', and 'Lm' refer to the different production rate scaling models [Balco et al., 2008]. See Dortch et al. [2010] for further sample details. Ages from the last column ('Lm') were be used to compare with our new data.

Sample Name	St	De	Du	Li	Lm
	Age (kyr)	Age (kyr)	Age (kyr)	Age (kyr)	Age (kyr)
NU-1	85.1 ± 7.7	73.8 ± 8.9	72.0 ± 8.7	70.2 ± 7.1	75.9 ± 6.6
NU-2	66.8 ± 6.8	58.4 ± 7.6	57.2 ± 7.4	55.4 ± 6.2	60.0 ± 5.9
NU-3	47.6 ± 4.6	41.4 ± 5.2	40.8 ± 5.1	39.9 ± 4.3	42.2 ± 3.9
NU-4	80.5 ± 7.3	69.5 ± 8.5	68.0 ± 8.2	66.4 ± 6.8	71.8 ± 6.3
NU-5	48.1 ± 5.0	41.8 ± 5.5	41.2 ± 5.4	40.2 ± 4.6	42.6 ± 4.3
NU-6	43.0 ± 4.3	38.2 ± 4.9	37.6 ± 4.8	36.8 ± 4.1	38.7 ± 3.8
NU-7	61.8 ± 5.6	53.7 ± 6.5	52.4 ± 6.3	50.8 ± 5.2	55.1 ± 4.8
NU-8	47.0 ± 4.3	41.0 ± 5.0	40.4 ± 4.9	39.5 ± 4.1	41.7 ± 3.7
NU-9	25.5 ± 2.4	24.4 ± 3.1	24.3 ± 3.0	23.6 ± 2.5	24.3 ± 2.3
NU-10	48.0 ± 4.5	41.8 ± 5.1	41.2 ± 5.0	40.2 ± 4.2	42.5 ± 3.8
NU-11	28.7 ± 2.8	27.1 ± 3.4	26.9 ± 3.4	26.2 ± 2.8	27.1 ± 2.6
NU-12	32.2 ± 3.1	30.0 ± 3.7	29.7 ± 3.7	28.9 ± 3.1	30.1 ± 2.8
NU-13	118.6 ± 10.9	99.0 ± 12.2	96.6 ± 11.8	94.7 ± 9.8	103.9 ± 9.3
NU-14	112.8 ± 10.8	94.9 ± 11.9	92.6 ± 11.6	90.5 ± 9.7	99.5 ± 9.3
NU-15A	35.2 ± 3.3	31.7 ± 3.9	31.4 ± 3.9	30.6 ± 3.2	32.6 ± 3.0
NU-15B	37.8 ± 3.8	33.7 ± 4.3	33.3 ± 4.3	32.5 ± 3.6	34.7 ± 3.4
NU-16	163.9 ± 16.2	132.4 ± 17.0	128.3 ± 16.4	125.5 ± 13.7	140.8 ± 13.5
NU-17	147.3 ± 13.7	119.8 ± 14.8	116.5 ± 14.3	114.1 ± 11.9	126.6 ± 11.4
NU-18	111.3 ± 11.5	93.8 ± 12.3	91.4 ± 11.9	89.3 ± 10.1	98.3 ± 9.9
NU-19	155.7 ± 19.1	126.1 ± 18.6	122.4 ± 17.9	119.8 ± 15.7	133.6 ± 16.1
NU-20	70.5 ± 6.6	61.5 ± 7.6	60.4 ± 7.4	58.6 ± 6.1	63.2 ± 5.7
NU-21	86.3 ± 8.0	74.5 ± 9.2	72.8 ± 8.9	70.9 ± 7.4	76.9 ± 7.0
NU-23	87.0 ± 8.0	75.3 ± 9.3	73.6 ± 9.0	71.7 ± 7.4	77.6 ± 7.0
NU-24	112.0 ± 10.4	96.3 ± 11.9	94.0 ± 11.6	92.1 ± 9.6	99.1 ± 8.9
NU-25	46.6 ± 4.4	40.7 ± 5.0	40.1 ± 4.9	39.2 ± 4.1	41.4 ± 3.8
NU-26	50.6 ± 5.2	43.6 ± 5.7	42.9 ± 5.6	41.9 ± 4.7	44.6 ± 4.4
NU-27	124.8 ± 11.8	103.4 ± 12.9	100.8 ± 12.5	98.8 ± 10.4	108.8 ± 10.0
NU-28	121.1 ± 11.2	100.7 ± 12.4	98.3 ± 12.0	96.3 ± 10.0	105.8 ± 9.4
NU-29	142.6 ± 13.3	116.2 ± 14.4	113.1 ± 14.0	110.8 ± 11.6	122.7 ± 11.1
NU-30	132.4 ± 12.3	108.9 ± 13.4	106.1 ± 13.0	103.9 ± 10.8	114.7 ± 10.3

B.3. Table B.2: Glacial striations measurements

Table B.2: Glacial striation measurements. Note that the azimuth of the striation does usually not correspond to the flow direction of the glacier, because most striations were measured on the upglacier side of roches moutonnées, hence plunging in an up-valley direction. Readings refer to several measurements at one site, and relative ages are inferred from cross-cutting relationships.

			Reading 1		Reading 2		Reading 3		
Lat (°N)	Lon (°E)	Elevation (m a.s.l.)	Azimuth (°)	Plunge (°)	Azimuth (°)	Plunge (°)	Azimuth (°)	Plunge (°)	Relative Age
34.543866	77.563636	3300	50	5					
34.543891	77.563746	3300	54	0					
34.543909	77.563746	3300	60	10					
34.543918	77.563725	3300	53	2					
34.544235	77.56368	3300	26	5					
34.544242	77.563746	3300	25	30					
34.544384	77.563572	3244	222	12					
34.544551	77.563607	3240	206	24					
34.568243	77.619189	3166	14	14	350	20			
34.569902	77.650878	3999	340	17					
34.570069	77.649412	3936	325	12	330	15	326	30	
34.574583	77.633295	3441	190	5					
34.574923	77.626045	3257	180	13					
34.575544	77.627373	3296	1		1				
34.57867	77.628127	3276	30	28	21	30	20	40	
34.672166	77.405306	3329	114	10					
34.672175	77.404764	3344	302	6	72	2			
34.67219	77.40498	3333	72	2					
34.672223	77.405177	3329	104	9					
34.672229	77.405185	3340	104	9	114	10			
34.67224	77.404741	3329	302	6					
34.695559	77.308948	3490	16	10	198	7	4	12	
34.695812	77.308889	3499	5	1					
34.71681	77.242239	3255	145	7					
34.71681	77.242239	3255	154	12					
34.71681	77.242239	3255	136	3					
34.717598	77.242533	3286	155	10					old
			184	23					interm.
			210	36					young
34.72522	77.569422	3198	340						

References

Balco, G., Stone, J.O., Lifton, N.A., and Dunai, T.J., 2008, A complete and easily accessible means of calculating surface exposure ages or erosion rates from 10Be and 26Al measurements: Quaternary Geochronology, v. 3, p. 174–195.

Dortch, J.M., Owen, L.A., and Caffee, M.W., 2010, Quaternary glaciation in the Nubra and Shyok valley confluence, northernmost Ladakh, India: Quaternary Research, v. 74, p. 132-144.

Appendix C

Apatite Fission Track results

C.1. Apatite Fission Track results

The individual samples of chapter 4 are presented in the following data sheets (see also Table 4.1). Where available the radial plots are shown on the top, and age vs. D_{par} graphs at the bottom. The listed results were obtained with TRACKKEY (v. 4.2) [Dunkl, 2002].

Sample Name

Irradiation code

Ns	Number of spontaneous tracks in the apatite
Ni	Number of induced tracks in the mica
Area	Number of microscope squares of the counted area in the sample.
RhoS	Density of the spontaneous tracks in 10^5 tracks/cm^2
RhoI	Density of the induced tracks in 10^5 tracks/cm^2
Pooled Age	The pooled gives the ratio of total counts of spontaneous and induced tracks, in age$\pm 1\sigma$ in Ma.
Mean Age	The arithmetic mean age, in age $\pm 1\sigma$in Ma
Central Age	The central age gives the geometric mean of the population, in $\pm 1\sigma$ in Ma, calculated after Galbraith and Laslett [1993]
Chi-sq	χ^2 value according to Green [1981]
P(%)	Probability of χ^2 for degrees of freedom where equals the number of grains - 1.
Dispersion	The relative standard deviation of the population ages after Galbraith and Laslett [1993].
RhoD	Track density in 10^5 tracks/cm^2
Nd	Number of the induced tracks counted on the U standards.
U Standard	CN 5
Zeta (ζ)	ζ-factor $\pm 1\sigma$
D_{par}	Length of etch pit in the apatite situated parallel to the c-axis. Corrected after Sobel and Seward [2010]
StDev	

Sample RT11-39

Irradiation code UP136_12

Ns	62
Ni	1295
Area	821
RhoS	0.775
RhoI	16.179
Pooled Age	8.0 ± 1.2
Mean Age	12.3 ± 2
Central Age	9.1 ± 1.7
Chi-sq	25.4
P(%)	4.48
Dispersion	0.37
RhoD	8.68
Nd	3661
U Standard	CN 5
Zeta ± 1σ	386.1 ± 27.8 counted by PE
Dpar	1.50
StDev	0.24

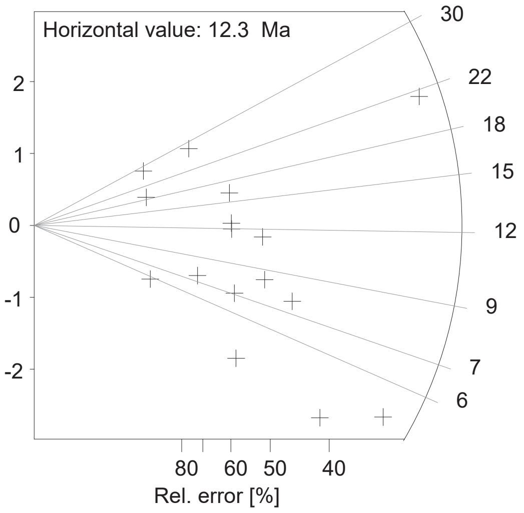

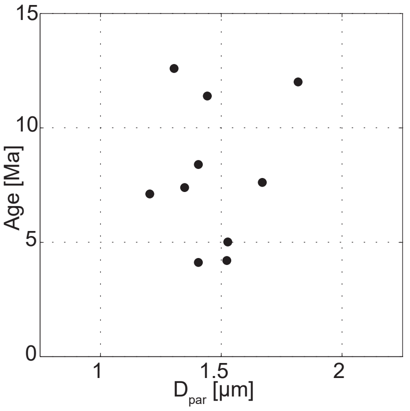

Sample RT11-28

Irradiation code UP136_13

Ns	289
Ni	4997
Area	2078
RhoS	1.427
RhoI	24.666
Pooled Age	9.6 ± 0.9
Mean Age	9.9 ± 0.9
Central Age	10.0 ± 1.1
Chi-sq	50.04
P(%)	2.21
Dispersion	0.25
RhoD	8.61
Nd	3661
U Standard	CN 5
Zeta ± 1σ	386.1 ± 27.8 counted by PE
Dpar	1.56
StDev	0.27

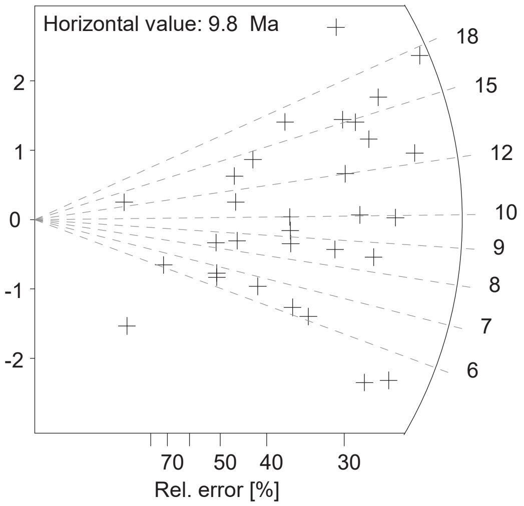

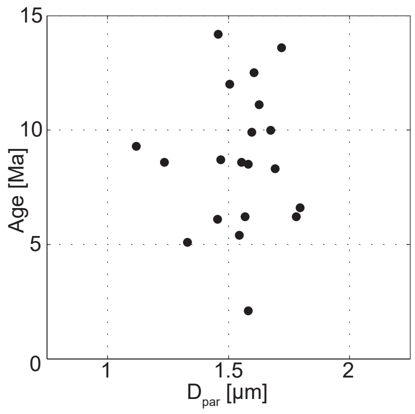

Sample RT11-29

Irradiation code UP136_14

Ns	67
Ni	1263
Area	1021
RhoS	0.673
RhoI	12.688
Pooled Age	8.7 ± 1.3
Mean Age	10.6 ± 1.5
Central Age	9.3 ± 1.5
Chi-sq	31.99
P(%)	15.82
Dispersion	0.33
RhoD	8.53
Nd	3661
U Standard	CN 5
Zeta ± 1σ	386.1 ± 27.8 counted by PE
Dpar	1.57
StDev	0.17

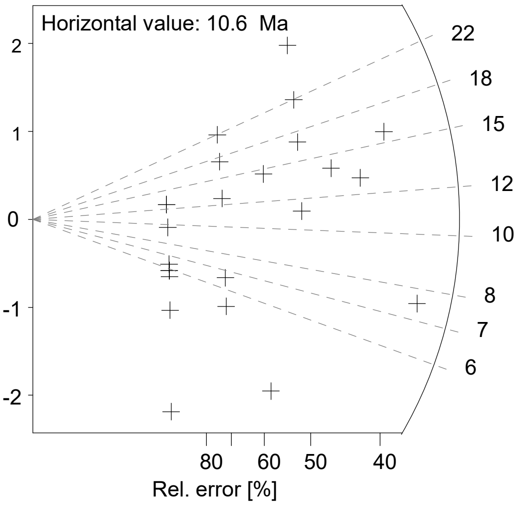

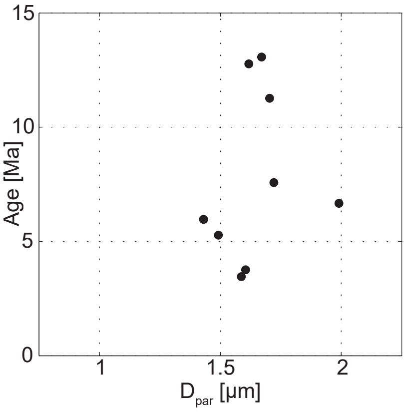

Sample RT11-30

Irradiation code UP136_15

Ns	70
Ni	2189
Area	1391
RhoS	0.516
RhoI	16.142
Pooled Age	5.2 ± 0.7
Mean Age	6.7 ± 1.3
Central Age	5.2 ± 0.7
Chi-sq	42.11
P(%)	19.04
Dispersion	0.02
RhoD	8.46
Nd	3661
U Standard	CN 5
Zeta ± 1σ	386.1 ± 27.8 counted by PE
Dpar	1.62
StDev	0.29

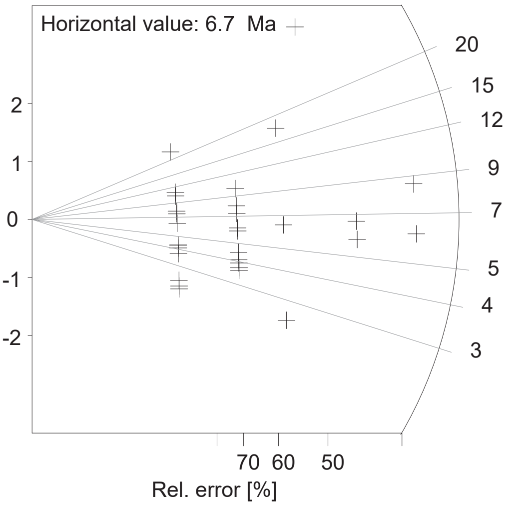

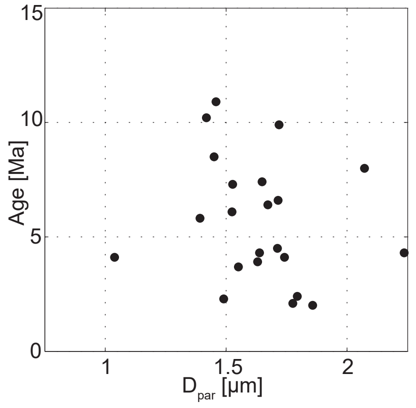

Sample PE12_014

Irradiation code UP137_1

Ns	316
Ni	7257
Area	3132
RhoS	1.035
RhoI	23.766
Pooled Age	6.3 ± 0.6
Mean Age	7.0 ± 0.6
Central Age	6.3 ± 0.6
Chi-sq	47.25
P(%)	14.45
Dispersion	0.12
RhoD	7.46
Nd	2962
U Standard	CN 5
Zeta ± 1σ	386.1 ± 27.8 counted by PE
Dpar	1.74
StDev	0.30

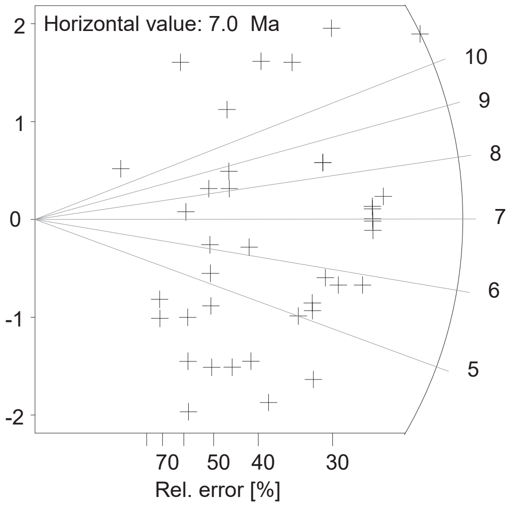

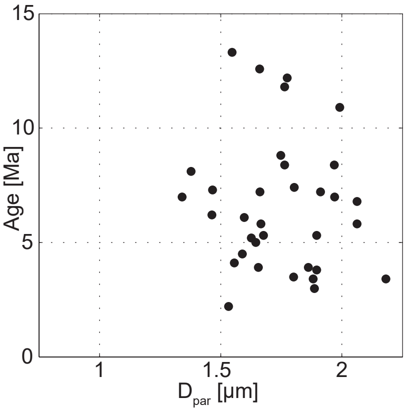

Sample PE12_015

Irradiation code UP137_2

Ns	200
Ni	3215
Area	1414
RhoS	1.451
RhoI	23.322
Pooled Age	8.9 ± 0.9
Mean Age	10.5 ± 1.0
Central Age	9.1 ± 1.0
Chi-sq	38.16
P(%)	24.64
Dispersion	0.20
RhoD	7.43
Nd	2962
U Standard	CN 5
Zeta ± 1σ	386.1 ± 27.8 counted by PE
Dpar	1.65
StDev	0.30

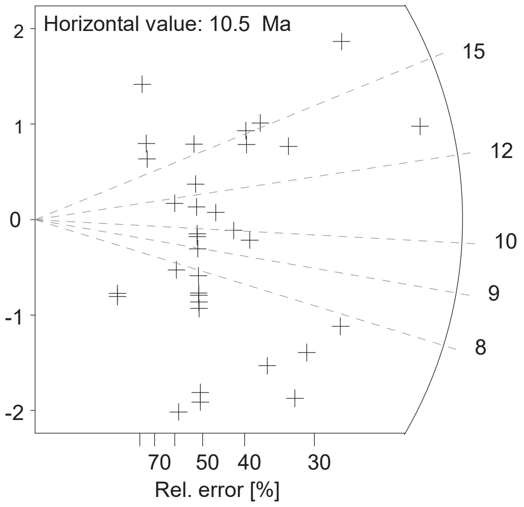

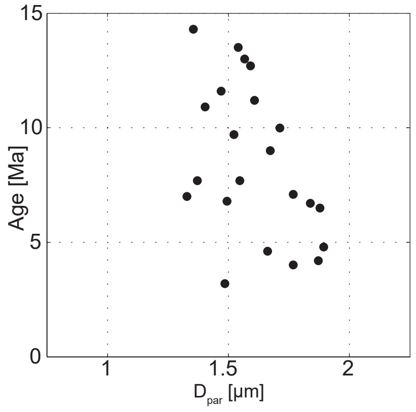

Sample PE12_017

Irradiation code UP137_4

Ns	234
Ni	5975
Area	2509
RhoS	0.957
RhoI	24.427
Pooled Age	5.6 ± 0.6
Mean Age	7.4 ± 1.6
Central Age	5.6 ± 0.6
Chi-sq	41.4
P(%)	17.9
Dispersion	0.05
RhoD	7.37
Nd	2962
U Standard	CN 5
Zeta ± 1σ	386.1 ± 27.8 counted by PE
Dpar	1.63
StDev	0.26

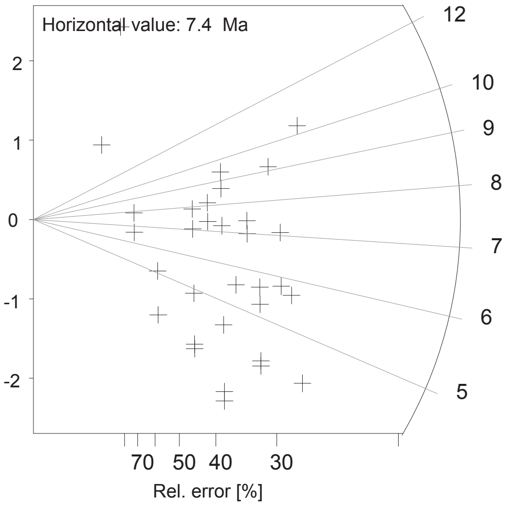

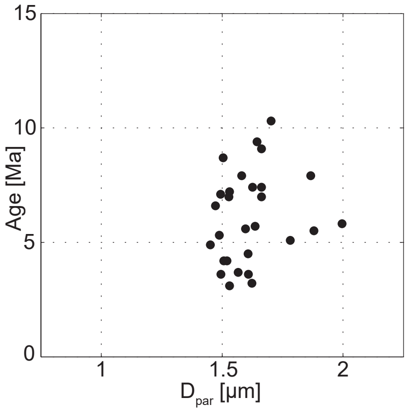

Sample PE12_021

Irradiation code UP137_6

Ns	252
Ni	4286
Area	1164
RhoS	2.221
RhoI	37.768
Pooled Age	8.3 ± 0.8
Mean Age	8.6 ± 0.7
Central Age	8.3 ± 0.9
Chi-sq	26.79
P(%)	14.12
Dispersion	0.14
RhoD	7.31
Nd	2962
U Standard	CN 5
Zeta ± 1σ	386.1 ± 27.8 counted by PE
Dpar	1.65
StDev	0.29

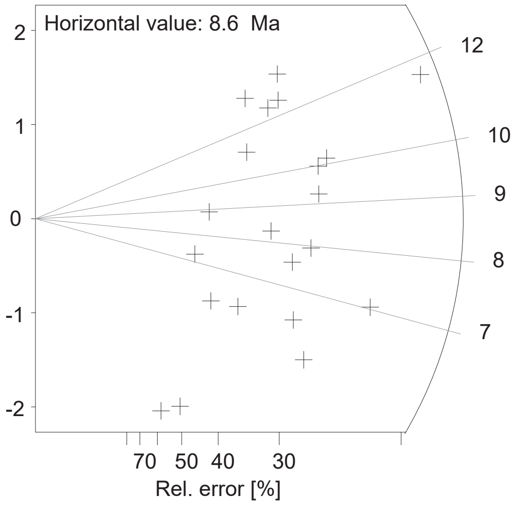

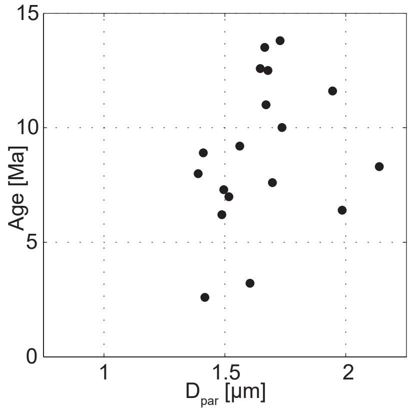

Sample PE12_047

Irradiation code UP137_8

Ns	104
Ni	1073
Area	2618

RhoS	0.407
RhoI	4.204

Pooled Age	13.6 ± 1.7
Mean Age	16.3 ± 2
Central Age	14.4 ± 2

Chi-sq	49.83
P(%)	13.71
Dispersion	0.33

RhoD	7.25
Nd	2962
U Standard	CN 5

Zeta ± 1σ	386.1 ± 27.8 counted by PE

Dpar	1.51
StDev	0.28

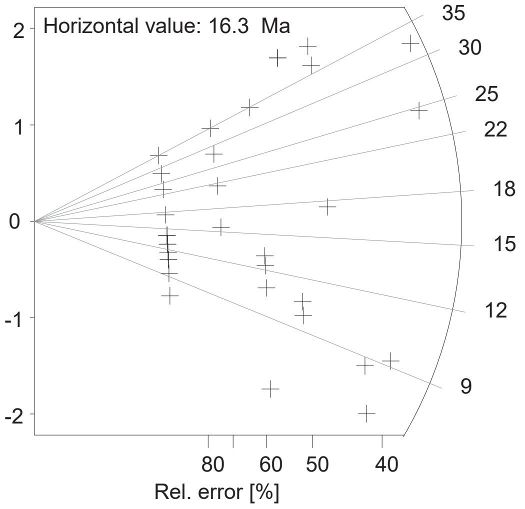

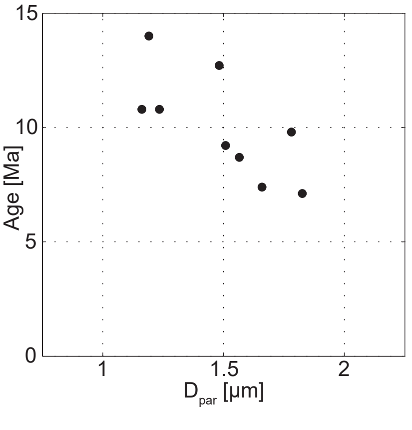

Sample PE12_053

Irradiation code UP137_9

Ns	73
Ni	4364
Area	2753
RhoS	0.272
RhoI	16.259
Pooled Age	2.3 ± 0.3
Mean Age	2.4 ± 0.3
Central Age	2.3 ± 0.3
Chi-sq	31.06
P(%)	81.38
Dispersion	0.06
RhoD	7.22
Nd	2962
U Standard	CN 5
Zeta ± 1σ	386.1 ± 27.8 counted by PE
Dpar	1.69
StDev	0.25

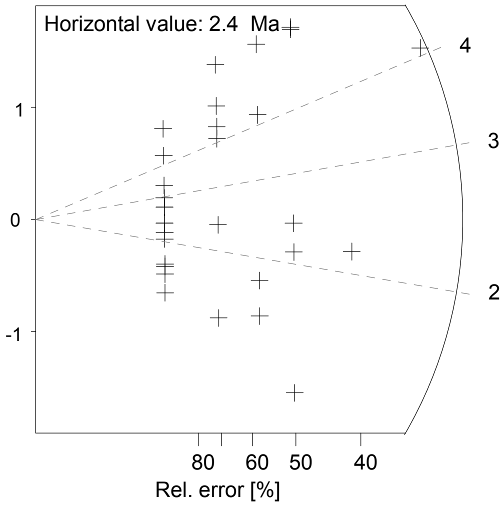

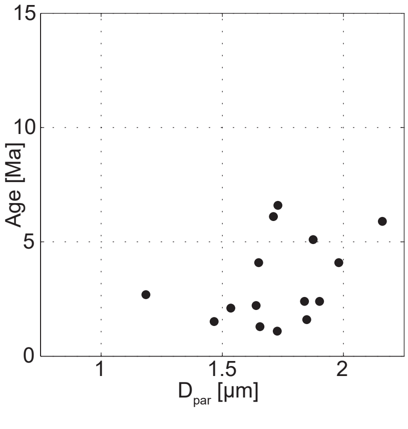

Sample PE12_054

Irradiation code UP137_10

Ns	37
Ni	1400
Area	1533
RhoS	0.248
RhoI	9.367
Pooled Age	3.7 ± 0.7
Mean Age	3.7 ± 0.4
Central Age	3.7 ± 0.7
Chi-sq	8.12
P(%)	99.94
Dispersion	0
RhoD	7.19
Nd	2962
U Standard	CN 5
Zeta $\pm 1\sigma$	386.1 ± 27.8 counted by PE
Dpar	1.53
StDev	0.36

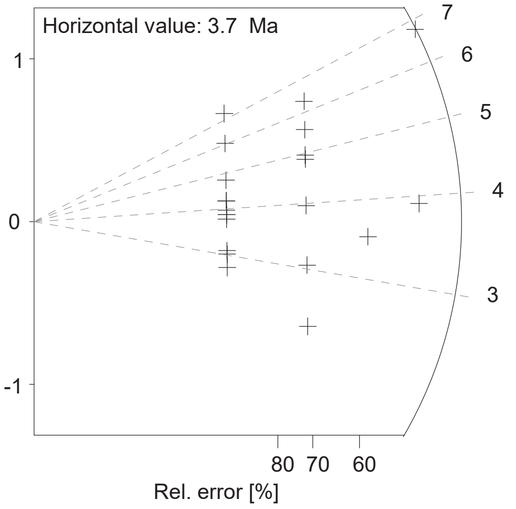

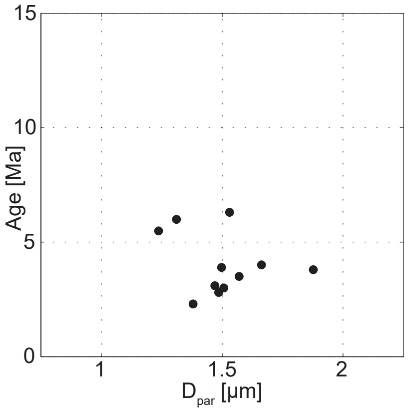

Sample PE12_059

Irradiation code UP137_11

Ns	155
Ni	3360
Area	1972
RhoS	0.806
RhoI	17.477
Pooled Age	6.1 ± 0.7
Mean Age	8.4 ± 1.1
Central Age	6.4 ± 0.8
Chi-sq	46.36
P(%)	6.14
Dispersion	0.21
RhoD	7.16
Nd	2962
U Standard	CN 5
Zeta ± 1σ	386.1 ± 27.8 counted by PE
Dpar	1.63
StDev	0.31

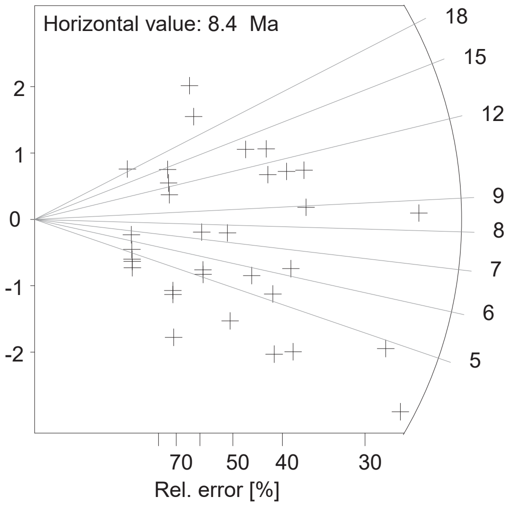

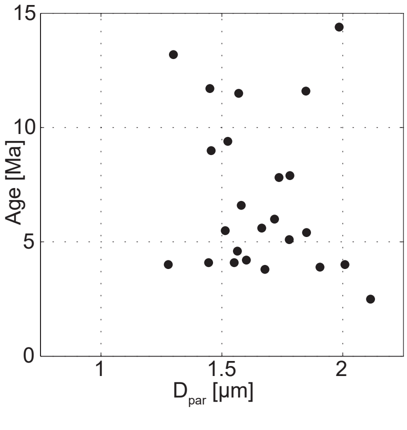

Sample PE12_065

Irradiation code UP137_12

Ns	108
Ni	2494
Area	3298
RhoS	0.336
RhoI	7.757
Pooled Age	6.0 ± 0.7
Mean Age	6.7 ± 0.7
Central Age	6.0 ± 0.7
Chi-sq	43.03
P(%)	42.68
Dispersion	0.14
RhoD	7.13
Nd	2962
U Standard	CN 5
Zeta ± 1σ	386.1 ± 27.8 counted by PE
Dpar	1.64
StDev	0.32

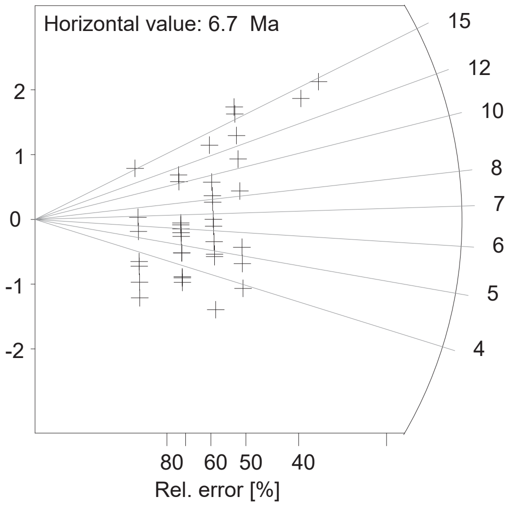

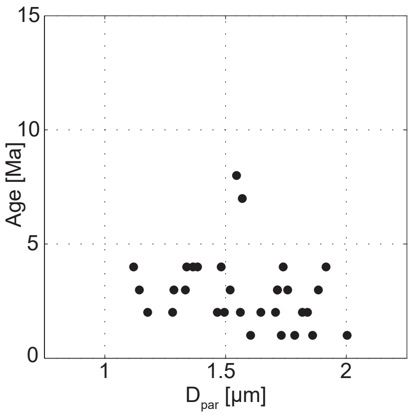

Sample PE12_066

Irradiation code UP140_14

Ns	43
Ni	1232
Area	1642
RhoS	0.269
RhoI	7.696
Pooled Age	7.2 ± 1.2
Mean Age	8.7 ± 1.3
Central Age	7.3 ± 1.3
Chi-sq	28.42
P(%)	59.96
Dispersion	0.15
RhoD	10.682
Nd	4529
U Standard	CN 5
Zeta ± 1σ	386.1 ± 27.8 counted by PE
Dpar	1.87
StDev	0.37

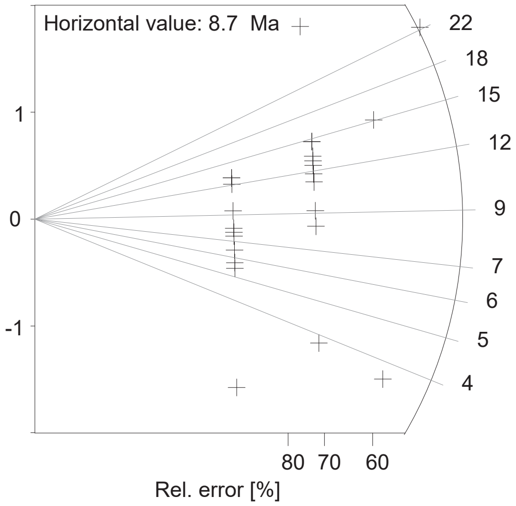

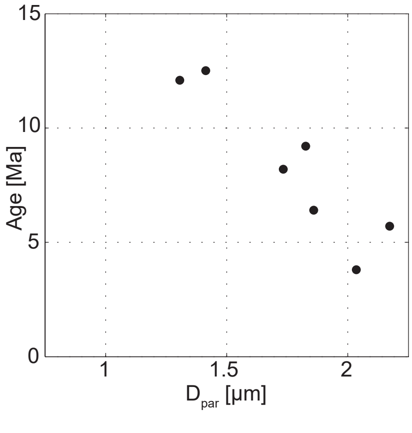

Sample PE12_068

Irradiation code UP137_14

Ns	64
Ni	1491
Area	1147
RhoS	0.572
RhoI	13.333
Pooled Age	5.9 ± 0.9
Mean Age	8.9 ± 5.9
Central Age	5.9 ± 0.9
Chi-sq	43.75
P(%)	6.41
Dispersion	0.15
RhoD	7.07
Nd	2962
U Standard	CN 5
Zeta ± 1σ	386.1 ± 27.8 counted by PE
Dpar	1.52
StDev	0.23

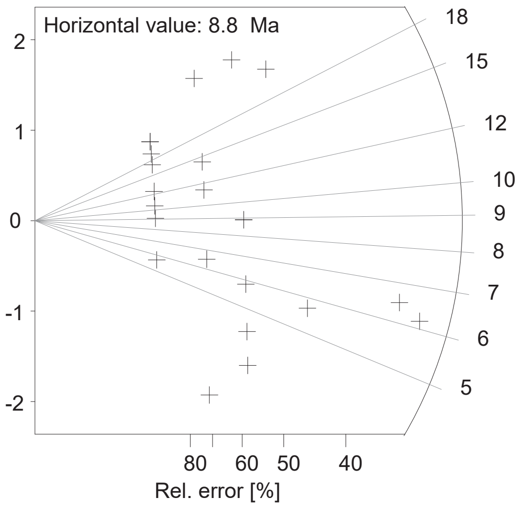

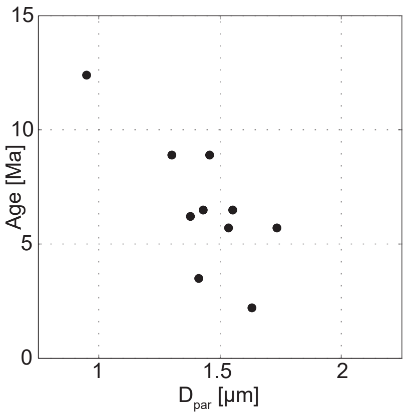

Sample RT11-31

Irradiation code UP137_15

Ns	42
Ni	1549
Area	910

RhoS	0.473
RhoI	17.46

Pooled Age	3.7 ± 0.6
Mean Age	4.3 ± 0.7
Central Age	3.7 ± 0.6

Chi-sq	23.84
P(%)	96.46
Dispersion	0

RhoD	7.04
Nd	2962
U Standard	CN 5

Zeta ± 1σ	386.1 ± 27.8 counted by PE

Dpar	1.46
StDev	0.26

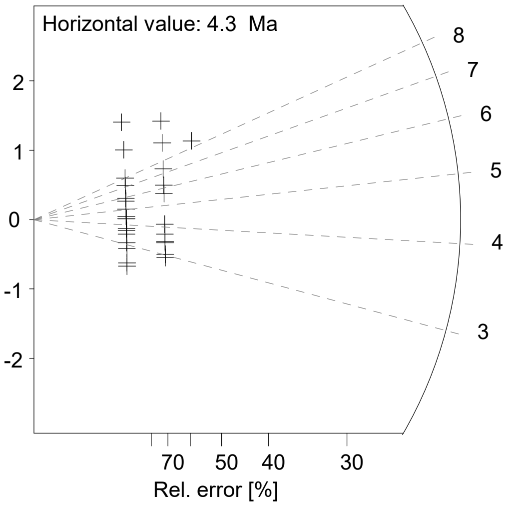

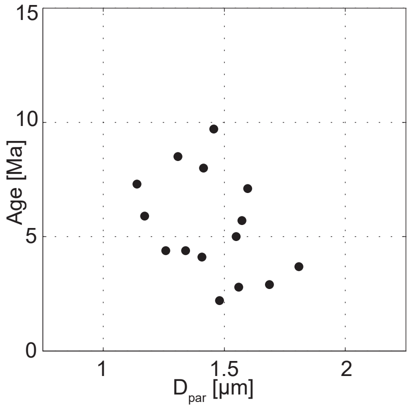

Sample B03B4

Irradiation code -

Ns	127
Ni	4671
Area	2764
RhoS	0.464
RhoI	17.07
Pooled Age	3.8 ± 0.4
Mean Age	3.8 ± 0.5
Central Age	3.8 ± 0.4
Chi-sq	77.12
P(%)	53.89
Dispersion	0.03
RhoD	7.215
Nd	7887
U Standard	CN 5
Zeta ± 1σ	389.1 ± 6.8 counted by KS
Dpar	-
StDev	-

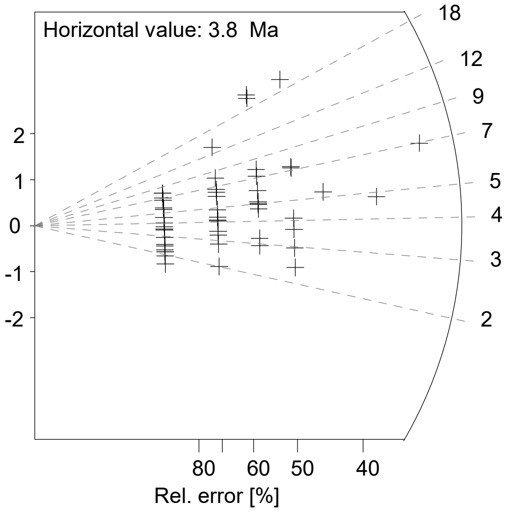

Sample 804C1

Irradiation code -

Ns	465
Ni	7060
Area	2084

RhoS	2.254
RhoI	34.219

Pooled Age	9.3 ± 0.5
Mean Age	9.4 ± 0.5
Central Age	9.3 ± 0.5

Chi-sq	60.69
P(%)	41.46
Dispersion	0.05

RhoD	7.267
Nd	7887
U Standard	CN 5

Zeta ± 1σ	389.1 ± 6.8 counted by KS

Dpar	-
StDev	-

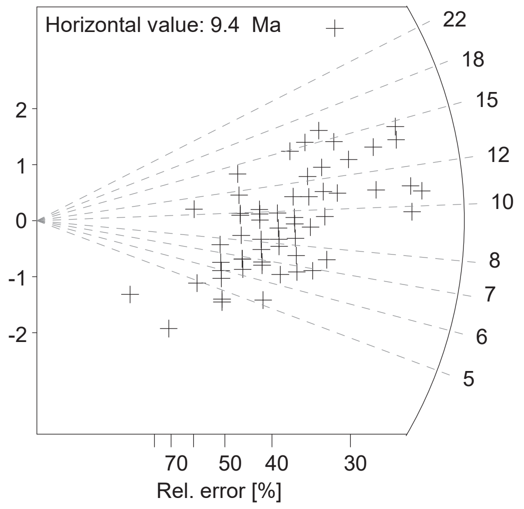

Sample 807A1

Irradiation code -

Ns	119
Ni	7006
Area	6740
RhoS	0.178
RhoI	10.5
Pooled Age	2.4 ± 0.2
Mean Age	3.6 ± 0.6
Central Age	2.5 ± 0.3
Chi-sq	226.81
P(%)	0.0
Dispersion	0.46
RhoD	7.319
Nd	7887
U Standard	CN 5
Zeta ± 1σ	389.1 ± 6.8 counted by KS
Dpar	-
StDev	-

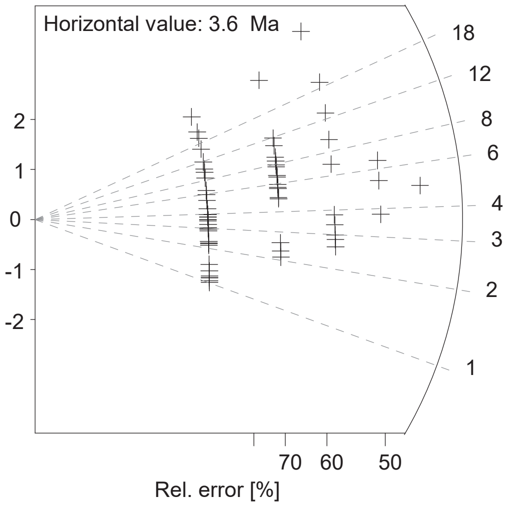

Sample 823G1

Irradiation code -

Ns	66
Ni	5766
Area	6480
RhoS	0.103
RhoI	8.988
Pooled Age	1.7 ± 0.2
Mean Age	1.7 ± 0.2
Central Age	1.7± 0.2
Chi-sq	167.47
P(%)	72.15
Dispersion	0.12
RhoD	7.424
Nd	7887
U Standard	CN 5
Zeta ± 1σ	389.1 ± 6.8 counted by KS
Dpar	-
StDev	-

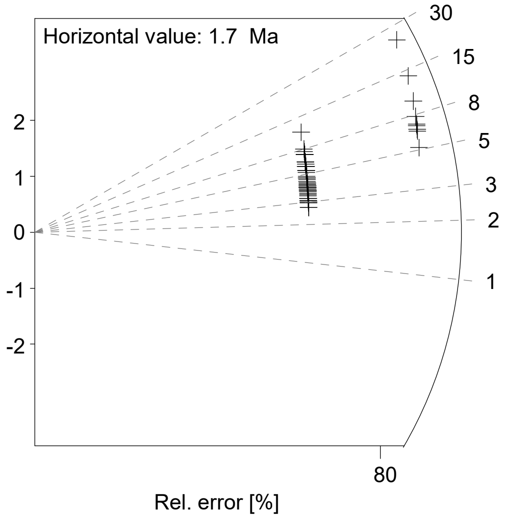

Sample 010A1

Irradiation code -

Ns	120
Ni	10309
Area	8716
RhoS	0.139
RhoI	11.947
Pooled Age	1.7 ± 0.2
Mean Age	1.7 ± 0.2
Central Age	1.7± 0.2
Chi-sq	121.14
P(%)	42.82
Dispersion	0.22
RhoD	7.581
Nd	7887
U Standard	CN 5
Zeta ± 1σ	389.1 ± 6.8 counted by KS
Dpar	-
StDev	-

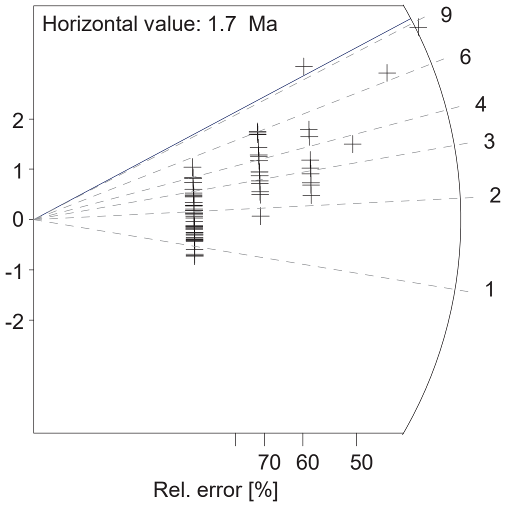

Sample 010D1

Irradiation code -

Ns	84
Ni	5819
Area	6444
RhoS	0.132
RhoI	9.121
Pooled Age	2.1 ± 0.2
Mean Age	2.6 ± 0.3
Central Age	2.2 ± 0.3
Chi-sq	238.85
P(%)	0.16 Dispersion
0.62	
RhoD	7.633
Nd	7887
U Standard	CN 5
Zeta ± 1σ	389.1 ± 6.8 counted by KS
Dpar	-
StDev	-

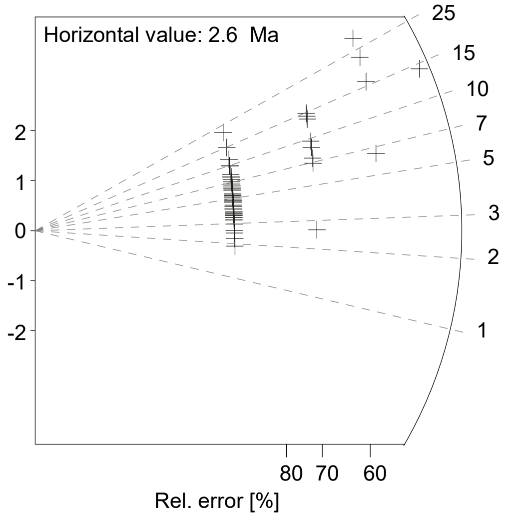

Sample 011B1

Irradiation code -

Ns	128
Ni	6503
Area	6480

RhoS	0.2
RhoI	10.137

Pooled Age	2.9± 0.3
Mean Age	3.1 ± 0.4
Central Age	3.0 ± 0.3

Chi-sq	231.71
P(%)	0.49
Dispersion	0.57

RhoD	7.685
Nd	7887
U Standard	CN 5

Zeta ± 1σ	389.1 ± 6.8 counted by KS

Dpar	-
StDev	-

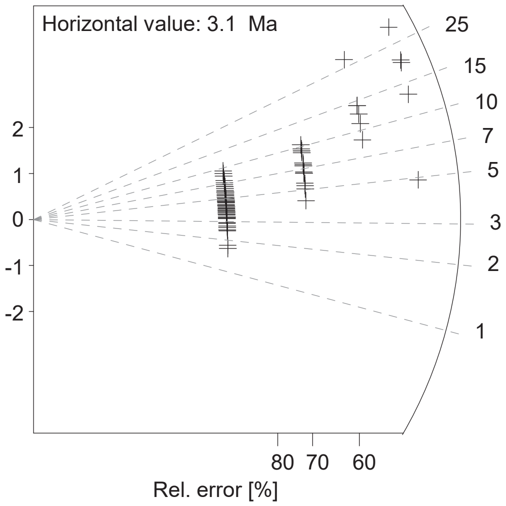

Sample 011D1

Irradiation code -

Ns	53
Ni	4303
Area	3932
RhoS	0.136
RhoI	11.054
Pooled Age	1.9 ± 0.3
Mean Age	2.1 ± 0.3
Central Age	1.9 ± 0.3
Chi-sq	66.6
P(%)	11.65
Dispersion	0.42
RhoD	7.738
Nd	7887
U Standard	CN 5
Zeta ± 1σ	389.1 ± 6.8 counted by KS
Dpar	-
StDev	-

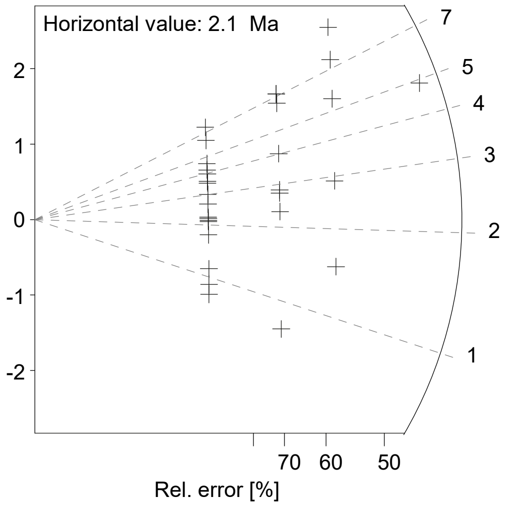

Sample 011E1

Irradiation code -

Ns	65
Ni	4361
Area	2880
RhoS	0.228
RhoI	15.295
Pooled Age	2.3± 0.3
Mean Age	2.4 ± 0.4
Central Age	2.3 ± 0.3
Chi-sq	115.16
P(%)	0.5
Dispersion	0.74
RhoD	7.79
Nd	7887
U Standard	CN 5
Zeta ± 1σ	389.1 ± 6.8 counted by KS
Dpar	-
StDev	-

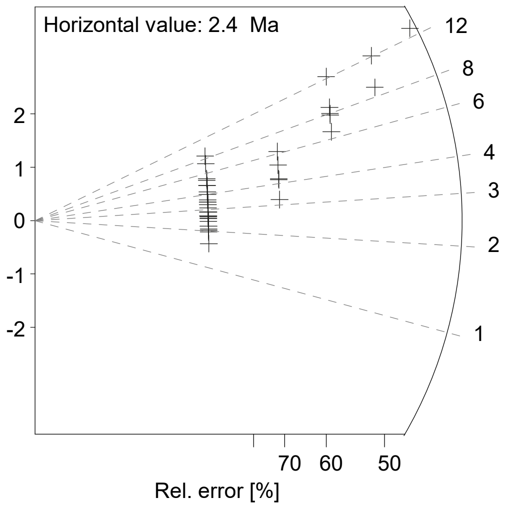

Sample 014B2

Irradiation code -

Ns	42
Ni	1907
Area	5788
RhoS	0.073
RhoI	3.328
Pooled Age	3.4 ± 0.5
Mean Age	3.7 ± 0.6
Central Age	3.5 ± 0.6
Chi-sq	122.21
P(%)	53.1
Dispersion	0.51
RhoD	7.842
Nd	7887
U Standard	CN 5
Zeta ± 1σ	389.1 ± 6.8 counted by KS
Dpar	-
StDev	-

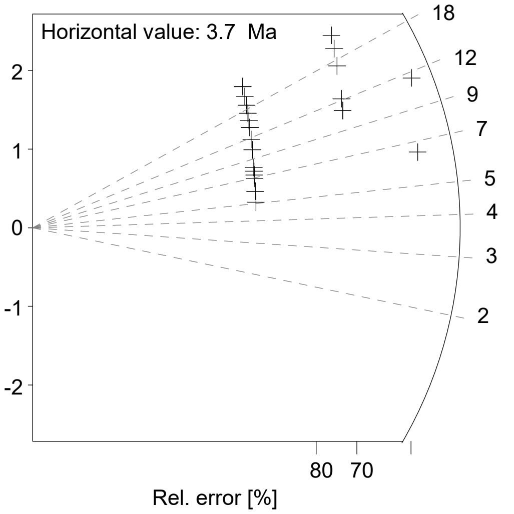

C.2. Erosion rate calculation

Table C.1: Mean erosion rates derived from AGE2EDOT with a surface geothermal gradient of 35 °C/km and layer thickness of 10 km

Surface geothermal gradient (°C/km)	35								
κ (km^2/Myr)	28.6			43			50		
Ht (κ/Myr)	11.5	28.7	43	11.5	28.7	43	11.5	28.7	43
L: 10 km	L10_1	L10_2	L10_3	L10_4	L10_5	L10_6	L10_7	L10_8	L10_9

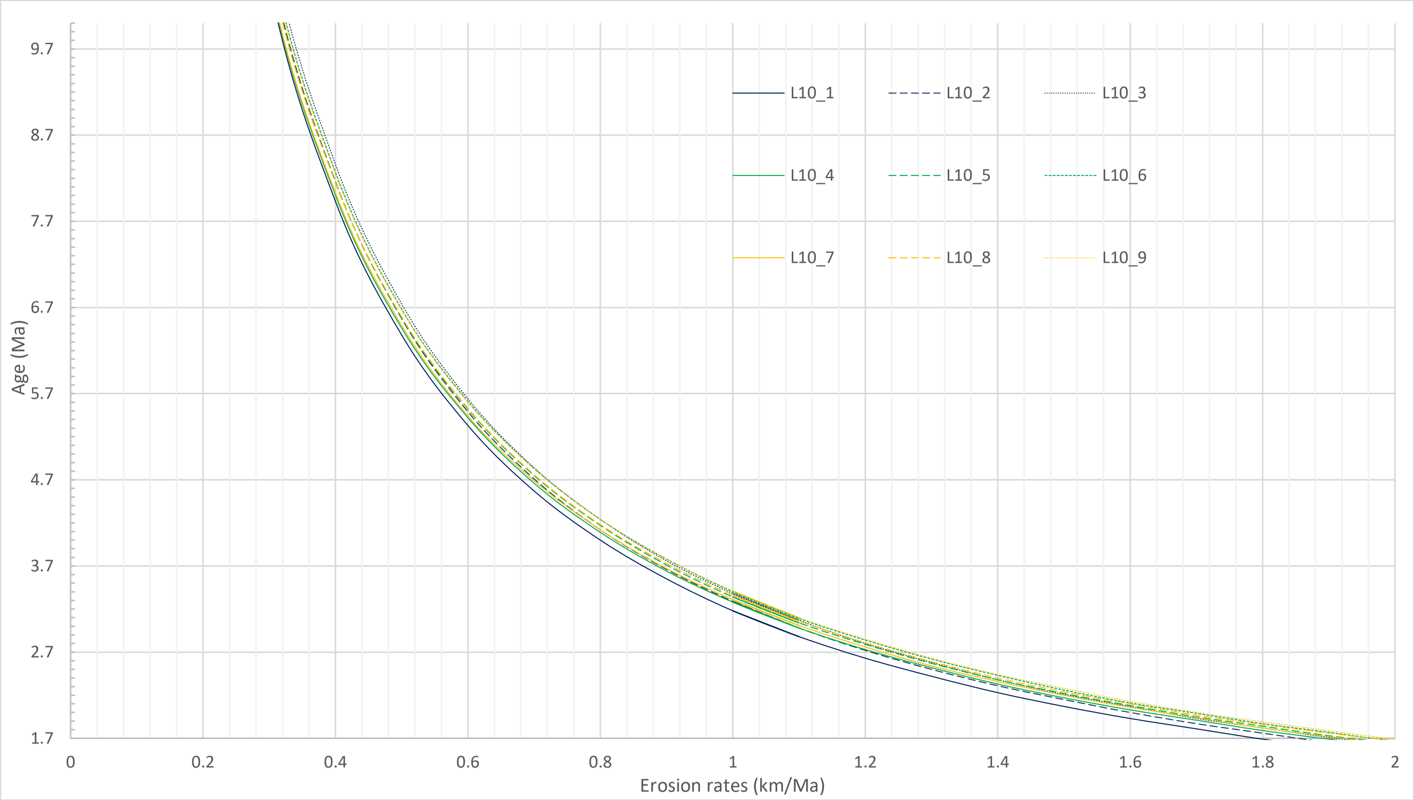

Table C.2: Mean erosion rates derived from AGE2EDOT with a surface geothermal gradient of 35 °C/km and layer thickness of 20 km

Surface geothermal gradient (°C/km)	35								
κ (km^2/Myr)	28.6			43			50		
Ht (κ/Myr)	11.5	28.7	43	11.5	28.7	43	11.5	28.7	43
L: 20 km	L20_1	L20_2	L20_3	L20_4	L20_5	L20_6	L20_7	L20_8	L20_9

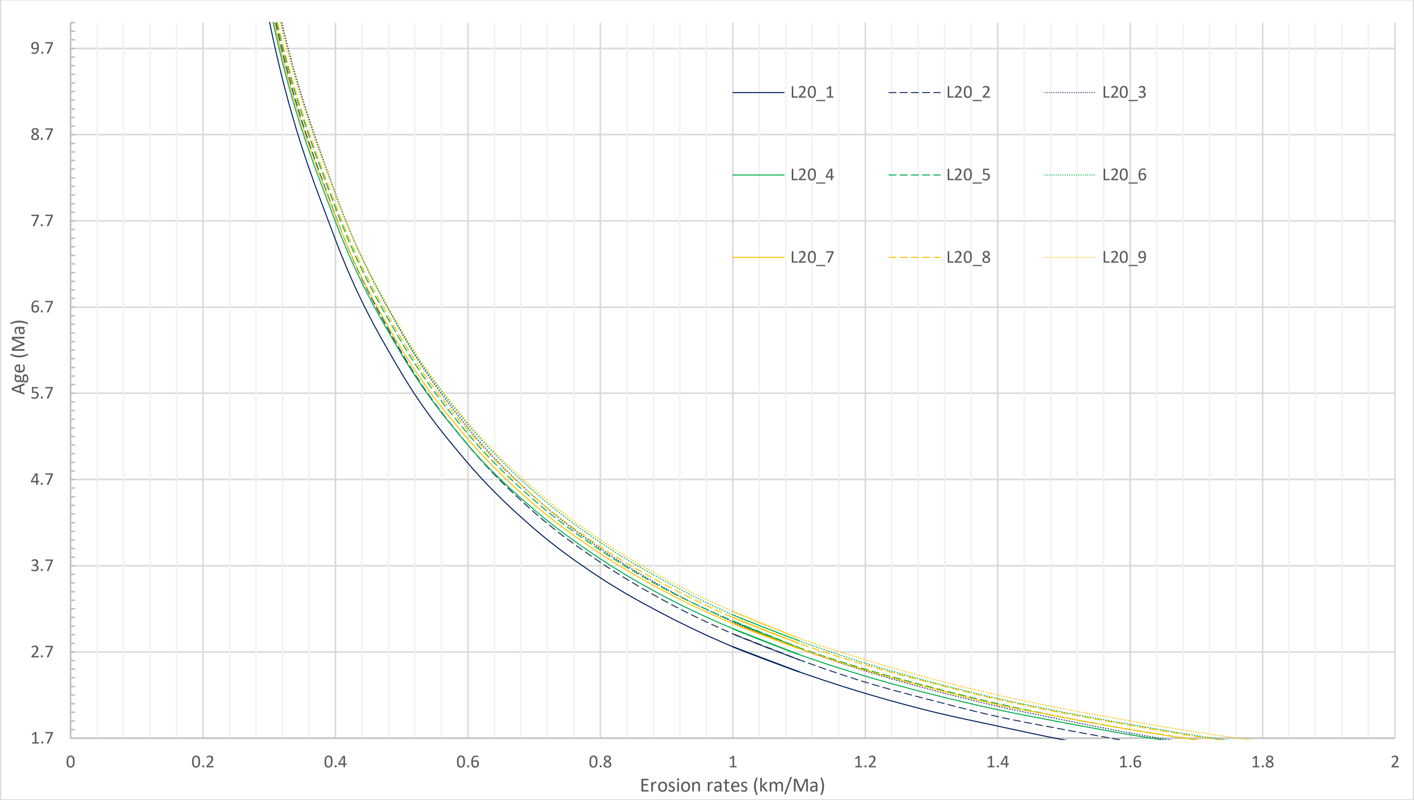

Table C.3: Mean erosion rates derived from AGE2EDOT with a surface geothermal gradient of 35 °C/km and layer thickness of 30 km

Surface geothermal gradient (°C/km)	35								
κ (km^2/Myr)	28.6			43			50		
Ht (κ/Myr)	11.5	28.7	43	11.5	28.7	43	11.5	28.7	43
L: 30 km	L30_1	L30_2	L30_3	L30_4	L30_5	L30_6	L30_7	L30_8	L30_9

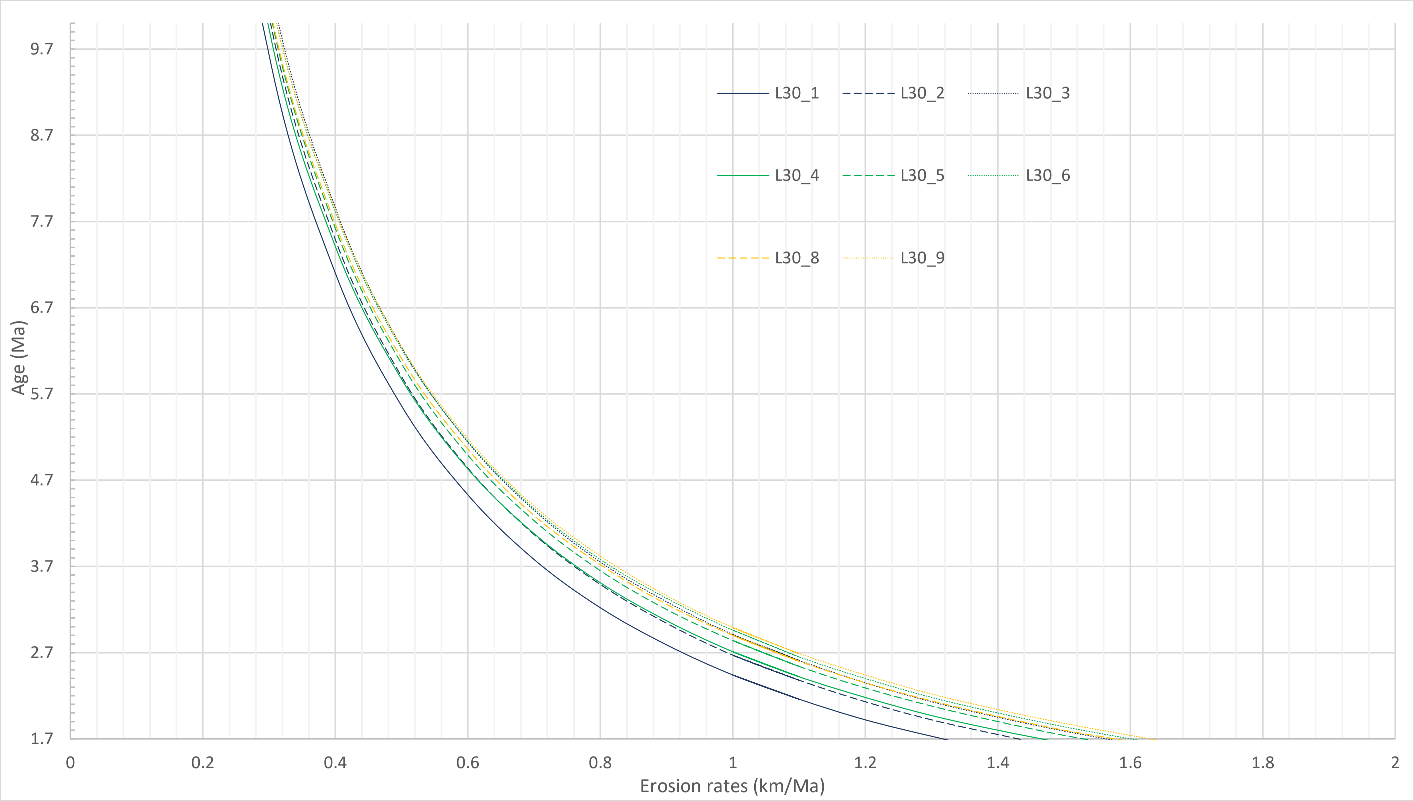

C.3. Advection calculation

Table C.4: RESPTIME calculations - sudden onset of erosion from 0 to 2 km/Myr and response of the closure isotherm for a surface goethermal gradient of 35 °C/km and layer thickness of 10, 20, and 30 km

Surface geothermal gradient (°C/km)	35								
κ (km^2/Myr)	28.6			43			50		
Ht (κ/Myr)	11.5	28.7	43	11.5	28.7	43	11.5	28.7	43
L: 10 km	R10_1	R10_2	R10_3	R10_4	R10_5	R10_6	R10_7	R10_8	R10_9
L: 20 km	R20_1	R20_2	R20_3	R20_4	R20_5	R20_6	R20_7	R20_8	R20_9
L: 30 km	R30_1	R30_2	R30_3	R30_4	R30_5	R30_6	R!0_7	R30_8	R30_9

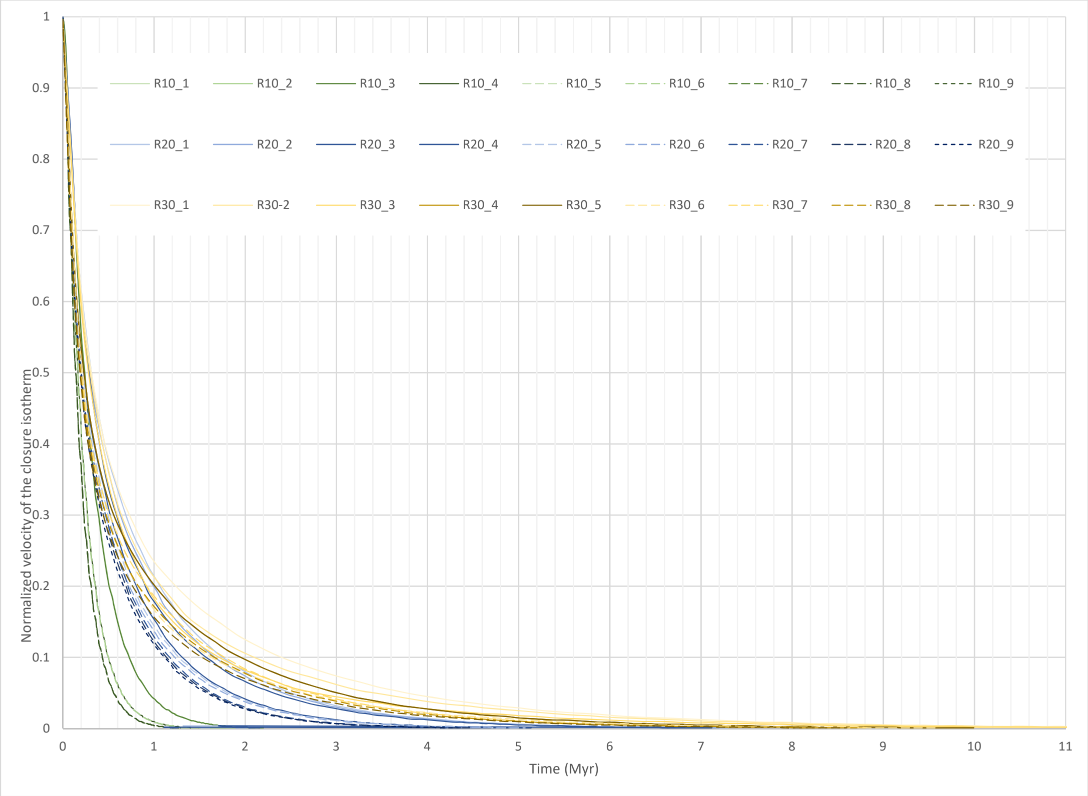

References

Dunkl, I. (2002), Trackkey: a Windows program for calculation and graphical presentation of fission track data, Computers Geosciences, 28(1), 3-12, doi:10.1016/S0098-3004(01)00024-3.

Galbraith, R. F., and G. M. Laslett (1993), Statistical models for mixed fission track ages, Nuclear Tracks and Radiation Measurements, 21(4), 459-470, doi:10.1016/1359-0189(93)90185-C.

Green, P. F. (1981), A new look at statistics in fission-track dating, Nuclear Tracks, 5(1-2), 77-86, doi:10.1016/0191-278X(81)90029-9.

Sobel, E. R., and D. Seward (2010), Influence of etching conditions on apatite fission-track etch pit diameter, Chemical Geology, 271(1-2), 59-69, doi:10.1016/j.chemgeo.2009.12.012.